

**Experimental and numerical investigations on the generation of
3-D hemispherical micro features using reverse micro EDM**

By

**TRIBENI ROY
ENGG01201404026**

Bhabha Atomic Research Centre, Mumbai

*A thesis submitted to the
Board of Studies in Engineering Sciences*

*In partial fulfilment of requirements
for the degree of*

DOCTOR OF PHILOSOPHY

of

HOMI BHABHA NATIONAL INSTITUTE



February 2019

STATEMENT BY AUTHOR

This dissertation has been submitted in partial fulfillment of requirements for an advanced degree at Homi Bhabha National Institute (HBNI) and is deposited in the Library to be made available to borrowers under rules of the HBNI.

Brief quotations from this dissertation are allowable without special permission, provided that accurate acknowledgement of source is made. Requests for permission for extended quotation from or reproduction of this manuscript in whole or in part may be granted by the Competent Authority of HBNI when in his or her judgment the proposed use of the material is in the interests of scholarship. In all other instances, however, permission must be obtained from the author.

Tribeni Roy

(Tribeni Roy)

DECLARATION

I, hereby declare that the investigation presented in the thesis has been carried out by me. The work is original and has not been submitted earlier as a whole or in part for a degree / diploma at this or any other Institution / University.

Tribeni Roy

(Tribeni Roy)

List of publications arising from the thesis

Journals

1. **T. Roy**, D. Datta, R. Balasubramaniam, “Numerical Modelling, Simulation and Fabrication of 3-D hemi-spherical convex micro features using Reverse Micro EDM”, *Journal of Manufacturing Processes*, Vol. 32, pp. 344-356, 2018. <https://doi.org/10.1016/j.jmapro.2018.02.018>
2. **T. Roy**, D. Datta, R. Balasubramaniam, “Numerical modelling and simulation of surface roughness of 3-D micro hemisphere generated by Reverse Micro-EDM” *International Journal of Advanced Manufacturing Technology*, Vol. 97, Issue 1-4, pp. 979-992, 2018. <https://link.springer.com/article/10.1007%2Fs00170-018-1971-4>
3. **T. Roy**, A. Sharma, D. Datta, R. Balasubramaniam, “Molecular dynamics study on the effect of discharge on adjacent craters on micro EDMed surface”, *Precision Engineering*, Vol. 52, pp. 469-476, 2018. <https://doi.org/10.1016/j.precisioneng.2018.02.005>
4. **T. Roy**, D. Datta, R. Balasubramaniam, “Reverse Micro EDMed 3-D Hemispherical Protruded Micro Feature: Microstructural and Mechanical Characterization”, *Materials Research Express*, Vol. 6, pp. 036513, 2018. <https://doi.org/10.1088/2053-1591/aaf490>
5. **T. Roy**, R. Balasubramaniam, “Effect of various factors influencing the generation of hemispherical micro features using non-conformal RMEDM” – accepted in *Journal of Micromanufacturing*, SAGE, 2019. <https://doi.org/10.1177/2516598419829593>
6. **T. Roy**, A. Sharma, D. Datta, R. Balasubramaniam, “Molecular dynamics simulation of single discharge and dimensionless correlation with actual material removal in micro-EDM” – accepted in *Molecular Simulation*, Taylor & Francis, 2019. <https://doi.org/10.1080/08927022.2019.1626988>
7. **T. Roy**, R. Balasubramaniam, “Fabrication, characterization and comparative analysis of mechanical properties of micro features generated by reverse micro EDM” – accepted in *Microsystem Technologies*, Springer, 2019
8. **T. Roy**, D. Datta, R. Balasubramaniam, “Debris based discharge segregation in reverse micro EDM” – *Measurement*, Elsevier, under 3rd review
9. **T. Roy**, R. Balasubramaniam, “Understanding the role of debris in generating 3-D hemispherical convex micro feature by reverse micro EDM” – *Journal of Manufacturing Science and Engineering*, ASME, under 1st review
10. **T. Roy**, R. Balasubramaniam, “Influence of ion rich discharge channel on unusually high discharging points in Reverse Micro Electrical Discharge Machining” – manuscript submitted to *International Journal of Advanced Manufacturing Technology*, Springer
11. **T. Roy**, P.S. Sarkar, D. Datta, R. Balasubramaniam, “Characterization of recast layer thickness on micro textured surface with varying aspect ratio generated by reverse micro EDM and its effect on surface roughness” – *manuscript ready for submission*

Conferences

1. **T. Roy**, P.S. Sarkar, D. Datta and R. Balasubramaniam, “Recast layer thickness characterization of array of micro features using X-Ray micro computed tomography” in *International Conference on Advances in Thermal System, Materials and Design Engineering*, VJTI Mumbai, 2017, pp. 1-5. <http://dx.doi.org/10.2139/ssrn.3101416>
2. **T. Roy**, S. Sundaram, P. Ranjan, R. Balasubramaniam, “Prediction of Material Removal in Single Spark Micro-EDM using Multiple Linear Regression and CART”, in *International Conference on Precision, Meso, Micro and Nano Engineering*, IITM, Chennai, 2017, pp. 571-574. ISBN: 978-93-80689-28-9.
3. **T. Roy**, D. Datta, R. Balasubramaniam, “Pulsed Electric Field Based Material Removal in Micro Electrical Discharge Machining” in *COMSOL Conference*, Bangalore 2016
4. **T. Roy**, D. Datta, R. Balasubramaniam, “Study on the fabrication of micro pillars of varying height and shape simultaneously using Reverse Micro Electrical Discharge Machining,” in *International Conference on Precision, Meso, Micro and Nano Engineering*, Mumbai, 2015

Tribeni Roy

(Tribeni Roy)

Dedicated

To

My mother (*Maa*), Sister (*Didibhai*),

Brother in law (*Tanmoy*) and Niece (*Mummum*)

ACKNOWLEDGEMENTS

At the very outset, I would like to express my sincere gratitude towards my supervisor, Dr. R. Balasubramaniam (Bala sir) who has guided me immensely during the entire course of my research work. Apart from research work, I also discussed various problems that I faced during this time to which he listened carefully and also gave valuable suggestions. He also encouraged me to undertake various courses at different organizations in India conducted by national as well as international scientists which has helped me a great deal during my research work. I am also grateful to Revathi madam (Bala sir's wife) who considered me as their family member and also invited me during various occasions and encouraged me to be integral part of those occasions.

I am very thankful to Dr. D. Datta, my co-supervisor who has guided me during my Ph.D. and also introduced me to newer techniques in statistical modelling which will help me in my future endeavour. I would also like to thank Dr. Prabhat Ranjan who has provided valuable inputs during both simulation as well as experiments. He also provided key inputs during writing research papers and also suggested various ideas for my research work. I am also indebted to Mr. Ashwin Rathod, Mr. Shivam Mishra and Mrs. Shrinkhla Ghildiyal who constantly motivated me during my Ph.D. and also helped me during signal processing of discharges. I am also very thankful to Mr. N. V. Surendran, Mr. Chandan Behera, Mr. Ramraverndra Nagar and Mr. Lalchand who have helped me during experimentation and also shared their experience on operation of different micro manufacturing operations and characterization techniques. Their experience have helped me to learn a lot about various problems that I encountered during experiments and how to overcome it. I would also like to thank Mrs. Sushama Joshi, Mr. J.K. Nandan, Mr. Shankar Valmiki, Mr. Tarun Dewangan, Mr. B.G. Kori, Mr. Abhay Chaturvedi and Mr. T.P. Sabharwal for their immense support during my course of research work.

I would also like to thank Dr. K. V. Mani Krishna, Dr. N. Naveen Kumar, Mr. Nachiket Keskar (Polishing and etching, FIB, SEM), Dr. P.S. Sarkar, Mr. Nirmal, Mr. Manoj, (X-Ray micro computed tomography) and Prof. P. Pant (Nano indentation, IITB) for allowing me to use their respective characterisation facilities.

I am deeply obligated to Prof. Suhas Joshi, Prof. Rakesh Mote and Prof. Salil Kulkarni under whom I have learnt the basics of Ultra precision machining and Finite and boundary element methods during my coursework at IIT Bombay. I am also thankful to Prof. Johnson Samuel (Rensselaer Polytechnic Institute, USA) and Prof. Sachin Mastud (VJTI, Mumbai) for sharing their knowledge during GIAN workshop on “Micro/ Meso -Scale Manufacturing Technologies” and also to Prof. Satish Bukkapatnam (Texas A&M University, USA) and Prof. Ramesh Babu (IIT Madras) for helping me to learn the basics of machine learning techniques in manufacturing during the GIAN course on “Data Science for Smart Manufacturing”.

I shall forever be grateful to Dr. B. K. Dutta (former Dean, HBNI and also the Chairman of my doctoral committee), who allowed me to pursue my Ph.D. knowing that I shall not be availing fellowship. He constantly motivated me to finish my Ph.D. as early as possible. I am also thankful to other members of the doctoral committee (Dr. J. Chattopadhyay, Dr. T. A. Dwarakanath and Dr. I. A. Khan) who provided valuable inputs in improving my research work. I am also very much thankful to Mr. S. K. Singh, Warden who went out of the rule book to provide me accommodation in New Bachelor’s Hostel for the first two years and subsequently in Annapurna for the next two years.

I wholeheartedly thank my lab mate and flat mate Mr. Anuj Sharma for helping me out in every possible way whenever I needed him. I would also like to extend my sincere thanks to my flat mates (Dr. Shankar Rao, Mr. Abhishek Kaushik and Mr. Rahul Kumar) and my research peers Mr. Vinod Belwanshi and Mr. Ashish Shelke. I also thank my DGFS 2014 batchmates (Mr. Pankaj Jadhav, Mr. Vivekananda Sinha, Mr. Eagle Tarpara, Mr. Shrenik Patel,

Mr. Suryakant Gautam, Mr. Shantaram Dond and Mr. Suman Paik) for their constant support and motivation during my Ph.D.

I am also thankful to European Society for Precision Engineering and Nanotechnology (euspen) and Heidenhain GmbH for providing me Heidenhain Scholarship Award due to which I was able to attend the euspen's 18th International Conference & Exhibition at Venice, Italy in 2018.

Friends and family were and always will be constant motivation for me. I would like to specially thank Mr. Aniket Das who also happens to my friend since kindergarten and family members (Mrs. Sunanda Das (Moni aunty), Mr. Rabindra Das (Rabi uncle), Mrs. Suchitra Das (Rubu didi), Mr. H. Sujit Singh (Sujit uncle), Mrs. Ankita Das (Rima), Mr. Gaurav Aniket, Ms. Udit Das (Rayna), Mr. Shivshankar Das (Bhomval), Ms. Srishty Das (Bonu)) for motivating me since day one of my Ph.D.

CONTENTS

	Page No:
Synopsis	i-iii
List of figures	iv-viii
List of tables	ix
List of nomenclatures and abbreviations	x-xii
CHAPTER	
1 INTRODUCTION	1-10
1.1 Relevance and motivation	2
1.2 Objectives	6
1.3 Organization of the thesis	9
2 LITERATURE SURVEY	11-28
2.1 Introduction	12
2.2 Surface texturing	12
2.3 RMEDM as a top down process for generation of micro features	14
2.3.1 Material removal mechanism	16
2.3.2 Effect of debris on machining	18
2.3.3 Discharges during machining	19
2.3.4 Recast layer and its effect on surface roughness	21
2.3.5 Analysis of surface roughness	23
2.4 Gap area	24
2.5 Scope of research work	25
3 MOLECULAR DYNAMICS SIMULATION AND EXPERIMENTAL ANALYSIS OF MATERIAL REMOVAL MECHANISM	29-56
3.1 Introduction	30
3.2 Molecular dynamics simulation during single discharge in RMEDM	30
3.2.1 MDS methodology	31

3.2.2	Material removal mechanism and recast layer formation due to single discharge	34
3.2.3	Crystal structure distortion due to single discharge	39
3.3	Molecular dynamics simulation of multiple discharges in RMEDM	41
3.3.1	Material removal mechanism during multiple discharges	42
3.3.2	Size of craters during multiple discharges	45
3.3.3	Qualitative comparison of craters formation during multiple discharges in RMEDM	46
3.4	Dimensionless correlation between MDS and experimental results	47
3.4.1	Dimensionless ratio (R_{MDS}) of specific material removal from MDS	47
3.4.2	Dimensionless ratio (R_{expt}) of specific material removal from experiments	49
3.4.3	Proposed dimensionless correlation (k')	51
3.5	Summary	55

4 SEGREGATION OF DISCHARGES USING FEA 57-78

SIMULATION AND EXPERIMENTAL CORRELATION

4.1	Introduction	58
4.2	Segregation of discharges in RMEDM (numerical model and simulation)	58
4.2.1	Primary, secondary and higher order discharges	58
4.2.2	Discharges with unusually high discharging points	63
4.3	Segregation of discharges in RMEDM (experimental)	69
4.3.1	Number of primary, secondary and higher discharges and comparison with numerical model	73
4.3.2	Unusual discharges during machining and its comparison with numerical model	75
4.4	Summary	77

5	SHAPE GENERATION MECHANISM AND SURFACE ROUGHNESS ANALYSIS OF 3-D HEMISPHERICAL MICRO FEATURE	79-124
5.1	Introduction	80
5.2	Numerical model and simulation of shape of 3-D hemispherical micro feature	80
5.2.1	Governing Equations	81
5.2.2	Geometry of the model	81
5.2.3	Boundary conditions	84
5.2.4	Role of debris in shape generation	88
5.3	Surface roughness analysis based on piecewise de- trending of simulated shape	102
5.3.1	Two equal segments	105
5.3.2	Four equal segments	106
5.3.3	Six equal segments	107
5.4	Experimental analysis of 3-D hemispherical micro feature using RMEDM	108
5.4.1	Shape generation of 3-D hemispherical convex micro feature	108
5.4.2	Surface roughness measurements on the 3-D hemispherical convex micro feature	110
5.5	Model validation for shape and surface roughness of 3- D hemispherical convex micro feature	112
5.6	Fabrication of arrayed micro features	115
5.6.1	Array of 3-D hemispherical micro features	116
5.6.2	Fabrication of protruded micro features with different shapes and height	118
5.7	Summary	121
6	MECHANICAL AND MICROSTRUCTURAL CHARACTERIZATION OF MICRO FEATURES GENERATED BY RMEDM FOR RECAST LAYER AND HAZ	125-150
6.1	Introduction	126

6.2	Destructive characterization for determination of recast layer and HAZ of 3-D hemispherical micro feature	126
6.2.1	Preparation and characterization of samples for nano indentation	126
6.2.2	Nano indentation system	127
6.2.3	Microstructural characterization and determination of recast layer thickness	128
6.2.4	Mechanical properties of recast layer and heat affected zone (HAZ)	131
6.2.5	Qualitative analysis of residual stress	136
6.2.6	Comparative analysis of mechanical properties of micro features	138
6.3	Non-destructive characterization for determination of discharge affected layer	144
6.4	Summary	148
7	CONCLUSIONS & SCOPE FOR FUTURE WORK	151-156
7.1	Conclusion	152
7.1.1	Scientific contributions	154
7.2	Scope for future work	154
	REFERENCES	157-166

SUMMARY

3-D shape of micro features especially hemispherical shaped features are preferred in many applications, however, fabrication of such features are very difficult by single stage manufacturing process. On the other hand, Reverse micro EDM (RMEDM) is a well-established process for generating 2.5-D micro features. Based on the results of the preliminary experiments, it is proposed that suitable tool modification in RMEDM can lead to generation of 3-D hemispherical micro features. Hence, to understand the mechanism of 3-D hemispherical shape generation of micro features using RMEDM, this research work was carried out.

The present research work includes an exhaustive study on the feasibility of RMEDM process in generating 3-D hemispherical shaped micro feature. Atomistic and continuum modelling and simulation were carried out to understand the mechanism behind shape generation while experimental analysis supported the validation of the simulation results as well as in extending the capability of RMEDM process in generating arrayed micro features of similar and dissimilar aspect ratios.

Molecular dynamics simulation was carried out using single and multiple discharges in RMEDM to understand the mechanism of material removal. Further, the effect of discharge on the distortion of crystal structure was also studied. MDS results showed that the percentage of material removed by melting (~ 60%) and vaporisation (~ 40%) during a single discharge remained nearly constant at low spark energies (0.165 μ J and 5 μ J). A dimensionless correlation was found out between MDS and experimental results that relates the ratio between specific material removal at higher spark energy to that at lower spark energy. This correlation was further used as an input to numerical modelling and simulation for determining the material removal during shape generation of 3-D hemispherical micro feature.

The effect of debris in dielectric on increasing depth of machining is unavoidable and it alters the behaviour of the discharge. In view of this, segregation of discharges was carried out in the presence of debris. It was found that the ratio of material removal by abnormal discharges (presence of debris) was five times that of normal discharges (absence of debris). This ratio was found to be the most influential factor in determining the shape of micro feature by numerical modelling and simulation. Also, multiphysics modelling and simulation showed that large amount of debris deposition on the cathode is responsible for creating large proportion of secondary and higher order discharges (abnormal discharges) on the workpiece leading to shaping of 3-D hemispherical convex micro feature.

Analysis of surface roughness values obtained from simulation revealed that larger crater sizes formed on sides of micro feature were due to the occurrences of secondary and higher order discharges leading to higher surface roughness on the sides as compared to the base and the tip of micro feature.

Mechanical characterization of the 3-D hemispherical micro feature showed that the recast layer had the highest hardness followed by the hardened layer of HAZ. The soft layer had the least hardness as compared to parent material. Recast layer formation on the 3-D hemispherical micro feature substantially increased the elastic modulus as compared to parent material. The soft layer of HAZ had the least elastic modulus. Qualitative analysis of residual stress based on the loading and unloading portion of the load-displacement curves obtained by nano indentation indicated that the recast layer comprises of compressive residual stresses while the soft layer of HAZ had tensile residual stresses as compared to the parent material.

RMEDM process capability was further extended to fabricate arrayed micro features of similar aspect ratio as well as different aspect ratio of micro features using suitable tool modifications. Measurement of discharge affected layer thickness on arrayed micro features carried out using non-destructive technique X-Ray micro computed tomography (XMCT)

revealed that thickness of discharge affected layer increases with increase in height of micro feature on the array.

LIST OF FIGURES

Fig. No.	Title	Page No.
1.1	(a) Micro wells (cavities) (b) Positive micro feature (protrusion on the surface)	3
1.2	Schematic of RMEDM	3
2.1	Flowchart for various discharges observed in a voltage pulse	20
2.2	Research Plan for Ph.D.	28
3.1	(a) 3D view (b) top view and (c) sliced view of MD model of workpiece	32
3.2	Material removal process on workpiece at spark energy of 0.165 μJ	35
3.3	Material removal process on workpiece at spark energy of 5 μJ	36
3.4	Material removal at 2.5 ps in the form of atoms with spark energy (a) 0.165 μJ (b) 5 μJ	37
3.5	Material removal mechanism at different spark energies	37
3.6	Schematic of crater characteristics	38
3.7	Crater formation at spark energy (a) 0.165 μJ (b) 5 μJ	38
3.8	Formation of amorphous layer during single spark at energy (a-b) 0.165 μJ (c-d) 5 μJ	39
3.9	Number of atoms in the amorphous layer	40
3.10	(a) Discharges separated by spark diameter ($2r$) (separate craters) (b) Discharges coinciding at the periphery (craters coinciding) (c) Discharges overlapping (craters overlapping)	41
3.11	Melting and vaporization taking place on (a) separate craters (b) craters coinciding (c) craters overlapping at time intervals 5 ps, 23.5 ps and 40 ps	42
3.12	Effect of 2nd discharge on 1st crater in case of overlapping craters	43
3.13	Crater and recast layer formation in (a) separate craters (b) craters coinciding (c) craters overlapping	44
3.14	Crater depth and diameter obtained during discharge in all three cases	45
3.15	(a) Separate craters (b) Craters coinciding (c) Overlapping of craters (d) SEM image of surface obtained from RMEDM	46
3.16	Simulated specific material removal at different spark energies	48

3.17	Crater formation with spark energy (a) 0.165 μ J (b) 5 μ J	49
3.18	Actual material removal at different spark energies	50
3.19	Qualitative comparison of specific material removal between MDS and experiments (for equal spacing of different energies along X-axis)	51
3.20	Grain boundaries on workpiece	52
3.21	Dimensionless correlation between MDS and experimental results	54
4.1	Types of discharges in RMEDM	59
4.2	Equivalent capacitance in case of (a) no debris (b) single debris adhered to either cathode or anode or in the discharge channel (c) debris adhering to both electrodes (d) multiple peaks with debris in dielectric	60
4.3	Electric field intensity due to normal and abnormal discharges	62
4.4	Typical schematic of a discharge	63
4.5	Dissociation of neutral molecule of dielectric in discharge channel	64
4.6	Ion and electron in discharge channel	65
4.7	Ion in discharge channel	67
4.8	Change in voltage at A due to presence of ions and electrons	68
4.9	Change in voltage at A due to presence of ions	69
4.10	ED-07 Micro EDM setup	70
4.11	Voltage profiles recorded at (a) 0.2 mm (b) 0.6 mm and (c) 1.0 mm traverse depth in RMEDM ((Magnified view of * in Fig. 4.11 (a & b)))	71
4.12	(a) Secondary and (b) Higher order discharge obtained during machining in RMEDM	72
4.13	Number of discharges during RMEDM at different traverse of anode	73
4.14	Maximum discharging points obtained in simulation and experiments	75
4.15	Comparison of simulated and experimental results for voltage profiles	76
5.1	2-D axisymmetric geometry (obtained after $t = 0.1$ s)	81
5.2	Flowchart for simulation of shape and surface roughness of 3-D hemispherical convex micro feature	83

5.3	Change in voltage with respect to time	84
5.4	Effect of buoyancy on debris	88
5.5	Value of ' k_0 ' obtained through simulations	89
5.6	Geometry during (a) Stage I (b) Stage II (c) Stage III (d) Stage IV of RMEDM process	90
5.7	Profile of micro feature during initial discharges (with and without cathode wear)	91
5.8	Stage I (a) Uniform distribution of debris (b) Pressure contour for plasma implosion (c) Movement of debris (d) Electric field enhancement due to debris	92
5.9	Mass of debris deposited on worn out portion on cathode during Stage I	93
5.10	Pressure contour during Stage II	95
5.11	Mass of debris deposited on straight portion of cathode during Stage II	96
5.12	Pressure contour and velocity field during Stage III	97
5.13	Stage III (a) Mass of debris deposited on tapered portion of cathode (b) Velocity of debris	98
5.14	Mass of debris deposited on straight portion of cathode during Stage III	98
5.15	Pressure contour and velocity field during Stage IV	99
5.16	Mass of debris deposited on tapered portion of cathode during Stage IV	99
5.17	Mass of debris deposited on straight portion of cathode during Stage IV	100
5.18	(a) Debris particle velocity corresponding to its mass (diameter) (b) Velocity of debris during Stage IV	100
5.19	(a) Simulated profile of cathode during Stage IV (b) SEM image of worn out cathode	101
5.20	Segment of simulated shape showing crater formation and surface roughness on the profile	104
5.21	Best fit curve for (a) linear (b) quadratic (c) cubic	104
5.22	Two equal segments of surface profile of anode	105
5.23	Surface roughness prediction using two segments of profile of anode	105
5.24	Four equal segments of surface profile of anode	106

5.25	Surface roughness prediction using four segments of profile of anode	106
5.26	Six equal segments of surface profile of anode	107
5.27	Surface roughness prediction using six segments of profile of anode	107
5.28	(a) Schematic of RMEDM process (b) Optical and (c) SEM image of 3-D hemispherical micro feature fabricated by RMEDM	109
5.29	Shape of anode generated due to various traverse of anode downwards	110
5.30	SEM micrographs of (a) Side (b) Tip and (c) Base of the convex micro hemispherical profile	111
5.31	(a) 3-D hemispherical convex micro feature (b) Surface roughness on the fabricated micro feature	111
5.32	Experimental and simulated shape of micro feature corresponding to anode traverse of (a) 0.095 mm (b) 0.8 mm	112
5.33	Comparison of final shape of micro feature obtained with experiment and simulation	113
5.34	Comparison of simulated and experimental results for surface roughness	114
5.35	Secondary and higher order erosion on 3 – D hemispherical convex micro feature	115
5.36	Array of 5 by 5 3-D hemi-spherical convex micro features using RMEDM	116
5.37	(a) Symmetrical profile of 3-D hemi-spherical convex micro feature (b) Surface roughness obtained for various profile at different location	116
5.38	Best fit curve for Surface Roughness	117
5.39	Protruded micro features corresponding to different hole depths using RMEDM	118
5.40	Protruded micro features of different shape and height	119
5.41	(a) Shape of micro features generated using RMEDM (b) Shape of micro feature corresponding to 0.1 mm hole depth and 1.2 mm traverse	119
5.42	Feature height vs Anode traverse	120
5.43	(a) XMCT image of isometric and (b) top views (c) SEM image of 5 by 5 fabricated protruded micro features generated by non-conformal RMEDM	121
6.1	Polished 3-D hemispherical convex micro feature mounted on polymeric transparent mould	127
6.2	Location of one set of nano indents on etched micro feature	128
6.3	Grain structure of etched micro feature	128

6.4	Magnified view of a portion of the micro feature	129
6.5	Schematic of formation of recast layer and HAZ in a single crater	129
6.6	Recast layer on micro feature (a) Near the tip (b) Near the base	130
6.7	Thickness of recast layer on the micro feature (16 sample points)	130
6.8	Schematic of micro feature showing the location of nano indents with recast layer and HAZ	132
6.9	Loading and unloading curves for nano-indents made on parent material, recast layer (N1) and near the centre (N6) of the fabricated 3-D hemispherical protruded micro feature	132
6.10	Variation of hardness on the fabricated 3-D hemispherical protruded micro feature	134
6.11	Variation of elastic modulus on the fabricated 3-D hemispherical protruded micro feature	135
6.12	Schematic of 3-D hemispherical protruded micro feature showing the recast layer, hardened and soft layer of HAZ	135
6.13	Loading curves for indents made to a maximum depth of 200 nm with different residual stresses	137
6.14	Ending part of unloading curves for indents made to a maximum depth of 200 nm with different residual stress states	137
6.15	Optical microscopic images of protruded micro features corresponding to tapered blind hole depth of (a) 0.1 mm (b) 0.3 mm	138
6.16	EBSD images of protruded micro features corresponding to tapered blind hole depth of (a) 0.1 mm (b) 0.3 mm	139
6.17	Typical loading-unloading curves for protruded micro features corresponding to nano indent N ₃	140
6.18	Comparison of maximum indentation load of the protruded micro features	141
6.19	Comparison of hardness of the protruded micro features	142
6.20	Typical discharge profile for same time interval during machining of (a) 3-D hemispherical convex micro feature corresponding to 0.1 mm hole depth (b) micro feature corresponding to 0.3 mm hole depth	142
6.21	Comparison of elastic modulus of the protruded micro features	143
6.22	Schematic of different slices of micro features for determining recast layer thickness	146
6.23	Sliced images of micro features corresponding to (a) Section A-A (b) Section B-B (c) Section C-C	147
6.24	Thickness of recast layer at different sections	148

LIST OF TABLES

Table No.	Title	Page No.
3.1	Parameters for simulation	34
3.2	Computational parameters for simulation	41
3.3	Values of R_{MDS} and R_{expt} for different ratios of discharge energies	53
4.1	Parameters for simulation	61
4.2	Simulations parameters	66
4.3	Materials and Operating Parameters	70
5.1	Parameters for simulation	88
5.2	Comparative analysis of different stages of machining	103
6.1	Parameters for conducting XMCT	145

NOMENCLATURE

E	Electric Field (V/m)
E_{th}	Threshold electric field (V/m)
V	Electric potential (V)
D	Electric displacement (C/m ²)
ρ_V	Space charge density (C/m ³)
ρ_f	Density of fluid (kg/m ³)
ρ	Density of solid (kg/m ³)
u	Flow velocity (m/s)
t	Time (s)
t_{on}	Pulse on time (ns)
t_{off}	Pulse off time (ns)
z	Cylindrical coordinate in vertical direction
p	Pressure of fluid (Pa)
μ	Dynamic viscosity (Pa.s)
F	Volume Force (N)
p_{plasma}	Plasma implosion pressure (Pa)
r	Position
I	Identity matrix
ϵ_0	Permittivity of free space
F_D	Drag Force (N)
F_B	Buoyancy Force (N)
F_E	Electrostatic Force (N)
F_{P-P}	Particle – Particle interaction force (N)
F_{P-W}	Particle – wall interaction force (N)
F_M	Weight of particle (N)
d_p	Diameter of debris particle (μm)

r_p	Radius of debris particle (μm)
u_p	Debris velocity (m/s)
R	Resistance (Ω)
C	Capacitance (F)
σ	Finite distance at which the inter-particle potential is zero
n	Charge multiplication factor
Z	Charge number
e	Charge on an electron (C)
δ	Dirac delta function
r_j	Position vector of j^{th} particle
ε	Depth of the potential well

ABBREVIATION

2.5-D	Two dimension with constant thickness along the third dimension
3-D	Three dimension
DE	Discharge energy
FEA	Finite element analysis
MDS	Molecular dynamics simulation
MEDM	Micro electrical discharge machining
RMEDM	Reverse micro electrical discharge machining
SMR	Specific material removal
XMCT	X-Ray micro computed tomography

CHAPTER 1

INTRODUCTION

1.1 Relevance and Motivation

Recent innovations in the area of micro-nano manufacturing have led to improvement in surface properties by surface texturing. With an ever increasing demand for smaller and faster computing systems, the microelectronics industry has seen a paradigm shift in the size of smallest possible lateral dimensions that can be generated on silicon wafer. Lithography has extensively been used for this purpose for more than two decades. Apart from semiconductor industry, surface texturing has found tremendous improvement in various fields of study. Friction between two mating surfaces reduces due to lubrication retention in the micro sized pockets (textures); this also leads to texturing of tool rake surface for machining. Texturing has also led to an improvement in surface wettability (super hydrophobicity) and this has found wider application in anti-biofouling, anti-sticking of snow for windows and antennas, self-cleaning windows etc. Surface texturing has also helped in defining suitable micro environments for cell-based culture systems. Osseointegrative properties of biomedical implants have seen an improvement due to texturing. The application area has increased many folds in the last decade due to incorporation of textures on the surface. Apart from conventional lithography process, several other manufacturing process have also been scaled down appropriately in order to add/remove material to achieve micro/nano sized features. This has helped tremendously to manufacture micro/nano textures of small-medium-high aspect ratios on metals, polymers and ceramics.

Though the requirement of textures in the form of micro wells (cavities) on the surface (**Fig. 1.1 (a)**) have their specific applications, many applications nowadays require the usage of positive textures (protruding from the surface) (**Fig. 1.1 (b)**) and hence, research works are being carried out in this area of generation of different aspect ratios of protruded micro features by bottom up processes that include chemical deposition, layer by layer deposition, sol-gel method, etc. as well as by top down approaches that include LIGA, photolithography, micro



Fig. 1.1: (a) Micro wells (cavities) (b) Positive micro feature (protrusion on the surface)

milling and reverse micro EDM (RMEDM). Aspect ratios of bottom up processes are comparatively low. Among the top down approaches, photolithography is time consuming and consists of multiple stages of processing. Micro milling can generate single protruding micro feature at a time and is not a parallel manufacturing process. LIGA is a very costly process although it can fabricate the highest aspect ratio of micro features (~500:1) on polymers. RMEDM on the other hand is capable of generating moderate to high aspect ratio of protruding micro features on metals. It is one of the variants of the EDM process. EDM is a nonconventional machining process wherein material removal takes place from the targeted location on electrode by virtue of high thermal energy generated as a result of electrical discharge occurring between two electrodes (assigned anode and cathode) submerged in a dielectric medium [1–3]. In case of RMEDM, cathode is in the form of a metal plate with a through hole generated by a suitable micro manufacturing process and is fixed to the table. A solid metal rod (anode), held vertically on a column is then traversed through the plate with

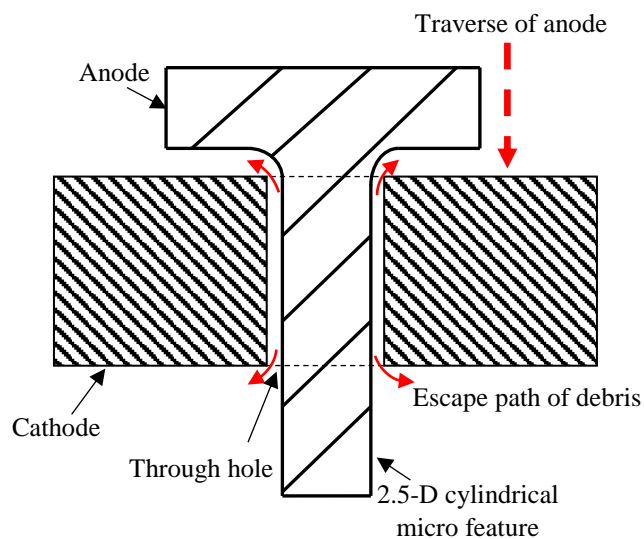


Fig. 1.2: Schematic of RMEDM

suitable feed rate (**Fig. 1.2**). Due to electrical discharges occurring between cathode and anode, material removal takes place from both anode and cathode at locations that are in proximity to each other; however, more amount of material removal takes place on anode and less on cathode. The remaining portion of anode is intact and passes through the hole. This process can simultaneously produce single or arrayed micro features depending on the number of holes incorporated on the flat plate. The shape of micro feature generated by RMEDM are conformal to the shape of the hole and therefore, 2.5-D micro features are generated by this process. Most of the manufacturing processes including RMEDM are capable of generating 2.5-D protruded micro features, however, for many applications like metallic dies for lens let arrays, solar cells, superhydrophobic surfaces etc., 3-D protruded micro features are required.

Results of preliminary experiments have shown that tool modification in RMEDM can result in 3-D shape generation. However, theoretical and experimental investigations are required in order to understand the physical phenomena behind 3-D shape generation using RMEDM. As RMEDM operates at very small scales with pulse times of few ns, it is very difficult to observe experimentally various phenomena like the mechanism of material removal during discharges, effect of discharge on the material, etc. Modelling and simulation at the atomic scale can throw light on the mechanisms occurring at very short time scales in RMEDM like molten material expulsion, amount of vaporization, crystal structure distortion etc. due to discharges.

It is very well known that the presence of debris in the dielectric alters the discharge profiles thereby affecting the machining process in a destructive way. It has been conclusively stated by researchers that debris removal is necessary in order to have a stable machining in RMEDM. The role of debris in generation of 3-D shapes especially hemispherical has not been explicitly researched till now. The presence of debris creates abnormal discharges in the machining zone. To understand the role of debris, it is necessary to determine the location of

such discharges, their effect on machining and subsequently to understand the mechanism of shape generation based on these factors. Therefore, numerical and experimental investigations are required to ascertain the role of debris as either constructive or destructive from the view point of shape generation.

Also, the properties of the generated 3-D shaped micro features influence its performance during application. For example, the surface roughness and lay pattern dictates the adhesion properties which are important for fluidic applications (fuel cell, super hydrophobic surfaces), shape and size accuracies affects the optical behaviour (lens let array), surface hardness and elastic behaviour affects tribological behaviour (bearings), etc. Therefore, studying the properties of micro features is also equally important as the generation of the micro features.

The motivation behind the current research work is to have a thorough understanding of the mechanism of 3-D shape generation especially protruding hemispherical shaped micro feature using RMEDM. Till date, RMEDM has only been used to generate 2.5-D cylindrical micro features. Therefore, enhancing and establishing the capability of existing RMEDM to generate 3-D shaped micro features is another motivation of this research work as this can open up newer avenues for researchers and industries for the generation of desired 3-D shaped micro features using this technique for various application. With modified tool shape in RMEDM, the process behaviour becomes more complex as debris play a crucial role. Enhancing the knowledge about the effects of debris on the process, both on the theoretical as well as experimental front, is also a motivation for this research work. From the material point of view, effect of discharges on the material has not been explicitly studied. This requires atomistic scale modelling which is explored very little till date. Atomistic scale modelling (Molecular dynamics simulation) has very recently come up in the area of manufacturing. Hence, another motivation for this research work is to demonstrate the feasibility of using MDS to study

behaviour of material during discharge as continuum scale cannot predict the mechanisms occurring at very short time scales in RMEDM.

After carrying out extensive literature survey, it was found that there is dearth of scientific knowledge and understanding about 3-D hemispherical shape generation RMEDM, continuum scale modelling for process behaviour incorporating debris and atomistic modelling to study material behaviour during discharge. Hence, research gap areas were identified and the objectives of this study are summarized as follows.

1.2 Objectives

The primary objective of the current research work is to understand the mechanism of shape generation of 3-D hemispherical convex micro feature using RMEDM. In order to achieve this, knowledge regarding the process behaviour and the behaviour of material during process is essential. In view of this, the various objectives of the present research work are summarised as follows.

1. Atomic scale modelling or molecular dynamics simulation (MDS) to understand the mechanism of material removal during single and multiple discharges in RMEDM. Single discharge modelling helps in understanding various aspects of the process such as formation of recast layer, melting and vaporization at different discharge energies, distortion of crystal structure due to discharge etc. Multiple discharge modelling at atomic scale can throw light on the changes in crater size due to subsequent discharges in RMEDM.
2. Establish a correlation between molecular dynamics simulation and experimental results for material removal in RMEDM. Since, MDS is carried out at atomic scale and experiments occur at micro scale, it becomes very difficult to validate the simulation results with actual values. Hence, in this study an attempt was made to correlate the

MDS results with experimentally obtained values for material removal during single discharge. This correlation shall further be used during determination of shape generation using numerical modelling.

3. Understand the effect of debris on the discharge profiles in RMEDM and segregation of discharges based on numerical and experimental correlation. Though the segregation of discharges have been studied previously, however, the effect of debris on the change in discharge profile with increasing machining depth in RMEDM needs deeper understanding. An attempt has been made to numerically study the effect of debris on the discharges and further correlate with experimentally observed discharges.
4. Multiphysics modelling and simulation to study the process behaviour of RMEDM incorporating debris during shape generation of 3-D hemispherical convex micro feature. This study is carried out to understand the multiple physical phenomena viz. effect of electric field during discharge and subsequent heat transfer to electrodes, flow of dielectric and various forces on debris responsible for its movement, agglomeration and adhesion leading to shape generation of 3-D hemispherical convex micro feature. Though material removal from both anode (workpiece) and cathode (tool) were considered in the model, more emphasis was laid on studying the shape generation of 3-D hemispherical convex micro feature (anode) as it is the main objective of the current research work.
5. Surface roughness analysis of the 3-D hemispherical micro feature based on simulated shape and experimental validation. The surface roughness of simulated shape of micro feature can be determined by piecewise de-trending technique and the values shall be validated with actual values of surface roughness. This study can confirm the effect of debris on surface roughness at specific locations on the micro feature.

6. Experimental investigations on the generation of single and arrayed micro features of similar and dissimilar aspect ratios using RMEDM. Apart from generation of single 3-D hemispherical micro feature, an attempt is also made to extend the capability of the RMEDM process in generating arrayed micro features of similar as well as dissimilar aspect ratios.
7. Study and characterization of recast layer, residual stresses and mechanical properties of 3-D hemispherical micro feature. In order to use the generated micro features for its intended application, it is important to determine the mechanical properties of the micro features. It is also equally important to determine the extent of formation of recast layer and heat affected zone which is considered detrimental in case of discharge based surfaces.
8. Comparison of mechanical properties of 3-D hemispherical micro feature with that of higher aspect ratio micro feature generated by the same process. Prior knowledge of mechanical properties of micro feature with different aspect ratio can help in understanding how the debris play a role during generation of different aspect ratio of micro features.
9. Study and characterization of discharge affected layers on arrayed micro features of dissimilar aspect ratio. Determination of discharge affected layers (recast layer + HAZ) on arrayed micro features is very difficult by conventional metallography. An attempt has, therefore, been made here to characterize and further study the discharge affected layers on arrayed micro features based on suitable non-destructive characterization technique.

1.3 Organisation of the thesis

Chapter 1 provides a glimpse of the general background of the area of this research work, relevance and motivation for carrying out this research work along with the research objectives.

Chapter 2 is devoted for the literature survey pertaining to application perspectives of surface texturing as well as RMEDM as a top down process for generation of protruded micro features and its various aspects. It also briefs about the research gap and the scope of the current work.

Chapter 3 provides an in-depth understanding of the material removal mechanism during single and multiple discharges in RMEDM based on molecular dynamics simulation (MDS). Experiments for single discharge were also conducted to establish a dimensionless correlation of specific material removal between MDS and experiments.

Chapter 4 presents the effects of debris on discharges and the segregation of discharges in RMEDM. This was carried out in order to understand their effect at various machining depths in RMEDM. Segregation of discharges carried out using numerical model based on electric field intensity is correlated experimentally with the discharge voltage captured during machining.

Chapter 5 deals with the contribution of abnormal discharges towards generation of 3-D hemispherical convex micro feature using numerical model. Also the role of debris leading to generation of these abnormal discharges which in turn generates the desired shape has also been explained. Simulated shape of micro feature was divided into various sections and surface roughness of each section was carried out based on piecewise de-trending of shape. The effect of secondary and higher order discharges on surface roughness is also discussed in this chapter. Further, fabrication aspects of 3-D hemispherical convex micro feature using RMEDM is also described. Surface roughness analysis of the fabricated micro feature was carried out.

Validation of numerical models for shape and surface roughness of 3-D hemispherical convex micro feature is also shown in this chapter. The RMEDM process with modified tool has been extended to generate array of 3-D hemispherical convex micro features as well as arrayed micro features with different size and shapes simultaneously.

Chapter 6 investigates the determination of thickness of discharge affected layers (recast layer and heat affected zone) of single and arrayed micro features using destructive/non-destructive techniques. Further, the comparison of mechanical properties viz. hardness, elastic modulus and residual stress of the recast layer, HAZ and parent material (unaffected by discharges) were also carried out. Also, mechanical properties viz. hardness and elastic behaviour of single 3-D hemispherical convex micro feature were compared with a protruded micro feature having different height and shape fabricated by RMEDM process.

Chapter 7 summarizes the completed work in the form of concluding remarks and specifies areas of future work.

---x---

CHAPTER 2

LITERATURE SURVEY

2.1 Introduction

This chapter covers the research activities carried out by various researchers in the areas of surface texturing, RMEDM as a manufacturing process for generation of protruded micro features and its different aspects. Based on the literature survey, research gaps have been identified and scope of this research work is also presented.

2.2 Surface texturing

Surface texturing has led to many advancements in the field of surface engineering. Micro and nano scale textures are being used extensively for enhancement of various properties of engineering surfaces. Fields of application include tribology, micro fluidics, surface wettability, tool design, bio-medical and many more. The effect of shape of micro feature has found to play a key role in enhancing surface properties required for specific application.

Imran et al. [4] compared the effect of different geometrical shapes of micro features on the performance of friction reduction. Their study led to the conclusion that triangular shaped micro features produced the lowest co-efficient of friction. Geometric shape of micro features also effect the hydrodynamic pressure generated between conformal contacting surfaces [5]. Yu et al. found that the best load carrying capacity of contacting surfaces was shown by ellipse dimples perpendicular to the sliding direction. Friction performance on laser textured steel surfaces can be improved by incorporating multi-dimple textured patters viz. circles and triangles, and circles and squares as compared to un-textured or single textured patterns on surfaces [6]. Obikawa et al. [7] studied the effect of four different types of micro features on coated tool face in order to have better lubrication conditions thereby improving machinability. Results indicated that one-directional grooves parallel to the cutting edge and square dot shape of micro features on the tool face effectively improved the machining conditions. Triangular shaped cross-section of micro pillars fabricated on micro channels were

found to enhance heat transfer co-efficient particularly at high velocities as compared to circular, diamond shaped cross-section of pillars or on micro channel without pillars [8]. The effect of different cross sectional shapes viz. rectangular, circular, triangular and cross shaped micro pillars on PDMS surface on the contact angle was studied by theoretical and experimental techniques [9]. It was found that apparent contact angle monotonically increases with a decrease in surface area at the top of micro feature. Most of the geometrical shape discussed above are 2.5-D micro features (constant cross-section along length).

Of all the possible shapes of micro features, 3-D hemispherical micro features find wide application in various fields of surface engineering viz. tribological, micro lens let arrays, solar cells, energy conversion devices, heat transfer applications and many more. Chang et al. [10] fabricated 3-D hemispherical micro lens let arrays with respect to a silicon mould using photolithography and etching in multiple steps. Bhattacharjee et al. [11] studied the DLVO (Derjaguin-Landau-Verwey-Overbeek) interaction potential on a surface considering both hemispherical protrusion as well as depression to model an actual rough surface. Surface element integration technique showed that repulsive interaction energy reduces significantly which depends on the size and frequency of the hemispherical protrusions and depressions. Zhang et al. [12] developed a super hydrophobic surface with water contact angle 163° using hemispherical protruded micro features using ZnAl-LDH-laurate hybrid film on substrate. Structural integrity and hydrophobicity led to good corrosive properties of the film which sustained longer immersion period (31 days) in 3.5% NaCl solution at room temperature without any structural changes. Il'inkov et al. [13] experimentally studied the heat transfer on a surface with hemispherical protrusions at the turbulent flow regime. Results showed that by increasing the number of hemispherical protrusions upto a certain point (ratio of the total surface area with hemispherical protrusions to the area of surface without protrusions = 0.24), the average heat transfer increases; while increasing the number of hemispherical protrusions

beyond that point, the average heat transfer gradually decreases. Yadav et al. [14] enhanced the heat transfer and friction factor during turbulent flow of air through a rectangular duct containing hemispherical protrusions as compared to a smooth duct. Li et al. [15] found that by incorporating low aspect ratio micro/nano hemispherical protrusions on ultrathin GaAs solar cells, light can be absorbed higher than 90% in regime of high photon energy density of the solar spectrum for GaAs. Liu et al. [16] performed numerical investigations to determine the effect of hemispherical protrusions on flow and heat transfer in dimpled cooling channels. The averaged local heat transfer of dimpled surface was greatly increased due to the hemispherical protrusions that were positioned ahead of the dimples. Also, these hemispherical protrusions caused downward flows and thereby helped in reducing the extent of recirculating flows in the dimples.

Micro and nano textures/features can be generally of two types (**Fig. 1.1**) viz. negative (cavities on the surface) and positive (protruding from the surface). Negative textures are fabricated by top down processes like micro drilling [17–19], micro EDM (MEDM) [20–25], micro ECM [26–28], laser micro machining [29–31], etc. Positive textures (protruded micro features), on the other hand can be fabricated by top down processes that include LIGA [32,33], photolithography [34–36], etc. as well as by bottom up processes like chemical deposition, layer by layer deposition, sol-gel method, etc. Of all the processes, micro EDM is one such process which not only generates a negative recess on the surface but one of its variants i.e. reverse MEDM (RMEDM) can generate protruded 2.5-D micro textures of medium to high aspect ratio on the surface.

2.3 RMEDM as a top down process for generation of micro features

RMEDM is a variant of MEDM and is used for the fabrication of medium to high aspect ratio positive micro features. In this process, a flat plate with single or multiple through holes

acts as cathode. Anode is in the form of a solid cylindrical rod which is traversed downwards (or upwards) into the tool (cathode). Material removal from anode (mostly) due to discharges between anode and cathode leads to shaping of anode in the form of cylindrical micro feature (**Fig. 1.2**). The aspect ratio of micro feature depends on the traverse of anode. This process is used to generate medium to high aspect ratio of micro features.

Kim et al. [37] have demonstrated the process capability of RMEDM and also studied the effect of machining parameters viz. voltage and capacitance on the process stability. Zeng et al. [38] further improved the RMEDM process by using ultrasonic vibrations to the tool (cathode). This not only improved the surface finish of the workpiece but also reduced machining time by almost 2.5 times. Further insight into the RMEDM process also showed that machining time reduces with increasing voltage and capacitance in the already developed ultrasonically assisted RMEDM process [39]. Hwang et al. fabricated array of 40 x 40 (1600 pins of $\text{\O}30 \mu\text{m}$, length $625 \mu\text{m}$, and pitch $100 \mu\text{m}$) on WC over $6.8 \times 6.8 \text{ mm}^2$ area using RMEDM [40]. Peng et al. [41] fabricated complex micro features of high aspect ratio using a combination of deposition using RMEDM followed by selective removal using MEDM. Mujumdar et al. [42] fabricated micro rods of similar length but different diameters using RMEDM process wherein, the work piece on which features are to be generated is made as anode and is plunged into cathode which has single or multiple through holes on it. Taguchi based parametric analysis on micro rods fabricated by RMEDM were carried out by Mastud et al. [43]. It was found that better erosion rate and surface finish were obtained using lower thickness of flat plate (tool). Debris modelling in vibration assisted RMEDM showed that higher local debris velocities and oscillatory motion due to flow reversal reduces the debris agglomeration leading to higher normal discharges [44]. This enhances material removal leading to feasibility in fabrication of arrayed micro features using this process. Mastud et al.

have also shown that using vibration assisted RMEDM process, hydrophobic surfaces with arrayed micro pillars (40-50 μm in diameter spaced at 35 μm) can be fabricated [45].

2.3.1. Material removal mechanism

Prediction of material removal by experiments at increased machining time becomes difficult due to presence of debris causing randomness in the MEDM process [46]. Also, extremely small spark gap [47] and discharge duration (ns to few μs) [48] makes it difficult to observe the phenomena occurring at such small scales during machining. Due to this complexity, modelling and simulation provide a better insight into fundamentals of the process at smaller scales. Dhanik and Joshi [49] predicted the amount of material removed in a single pulse discharge with the help of an analytical model. The breakdown phenomena during discharge has also been explained. Yeo et al. [50] developed an electro-thermal model to estimate the size of micro crater formed due to single discharge in MEDM. Low energy discharges were considered for developing the model and maximum error obtained during validation with experimental results was 6.6%. Tang and Yang [51] developed a thermo-hydraulic coupled numerical model in EDM to study the discharge crater formation using finite element method (FEM). They found that the metal removal efficiency was 0.04 since most of the molten material re-solidified and adhered on the electrode. Jeong and Min [52] developed a 2-D model incorporating tool wear to study the material removal process in EDM drilling. The developed model was able to predict the change in shape of tool and workpiece with an error of 13%. Somashekhar et al. [53] numerically modelled MEDM process for multiple discharges to determine temperature distribution on the workpiece during discharge. The model predicts that temperature during pulse on time rises along both normal and axial directions of workpiece and faster decrease in temperature during pulse off time due to surface convection. Tan and Yeo [54] developed a model incorporating the effect of multiple discharges and

thereby formation of overlapped craters in MEDM was studied. This approach for modelling overlapping craters showed good agreement based on maximum surface roughness obtained from simulated and experimental results. Feng et al. [55] constructed overlapped craters using non-uniform model of single crater. The developed method was able to correlate the size of actual overlapped clusters. Most of the work related to numerical and/or analytical models are based on continuum mechanics which considers material to be uniform. Hence, the discrete effects taking place at atomistic level during pulse discharges cannot be predicted using numerical/analytical models. To understand mechanisms occurring due to mechanical and thermal actions on materials at atomic/molecular scale, molecular dynamics simulation (MDS) is used [56–58]. Material removal mechanism in single discharge MEDM process was studied by Yang et al. [59] with the help of MDS. Material removal efficiency was found to be low in MDS since most of the molten material re-solidified and adhered to workpiece. Similar results were also observed by Yue and Yang during single discharge process in MDS wherein most of the molten material re-solidifies and only a small amount of material is removed [60]. The behaviour of single discharge on different planes viz. {100}, {110}, and {111} was studied by Yue and Yang [61] using MDS. Different orientation of crystal did not have any substantial effect on melting and re-solidification. However, defects were found in the workpiece (stacking faults, dislocations etc.) after discharge. Another study was carried out by Yue and Yang [62] where material removal and bubble dynamics behaviours were studied based on single pulse discharge in deionized water using MDS. The study led to the conclusion that material removal took place during discharge as well as after discharge. A comparison of material removal in gas and inside deionized water showed that the amount of material removed was higher in case of deionized water as dielectric. Residual stress on electrode surface using EDM was studied by Yang et al. [63]. Results indicated that on the electrode surface, stresses were tensile while

it became compressive on the inner part indicating ease of crack formation in the re-solidified layer.

Both numerical as well as molecular dynamics simulation were carried out by researchers to study the material removal mechanism. Though numerical modelling can provide an estimate about the amount of material removal, it cannot predict the defects occurring in the crystal structure due to occurrence of discharges. Hence, molecular dynamics simulation proves to be appropriate from the point of view of understanding material removal mechanism as well as determination of the effect of discharges on the discharges surface.

2.3.2. Effect of debris on machining

A longer normal discharge time coupled with higher material removal makes it makes RMEDM an efficient machining process as compared to micro EDM (MEDM) [64]. The process capability of RMEDM is greatly affected at high machining depths as debris accumulation in the discharge gap leads to frequent short circuit and abnormal discharges. This in turn results in high surface roughness [64], taper formation [42], debris adhesion [65] etc. Debris, therefore, play a key role in defining the machining output in terms of shape, size and surface finish of the parts manufactured. Mastud et al. [44] found that incorporating vibration to tool electrode reduces localised debris agglomeration which in turn reduces the occurrences of short circuit and arcing. Wang et al. [66] studied the flow of debris in the machining gap in MEDM. Numerical results suggested that secondary discharges increase at the bottom portion of the gap where the number of debris particles increase with increase in machining depth. Tanjilul et al. [67] developed a simultaneous flushing and vacuum assisted debris removal system in deep hole EDM drilling. The developed setup led to improvement in drilling time as well as reduction in surface roughness. Liao et al. [68] found that on increasing the jump height of tool electrode by 1/4th of machining depth, debris removal becomes easier. Wang and Han

[69] also led to similar conclusion that with appropriate tool electrode jump height and speed, most of the debris can be removed from the bottom gap. Cetin et al. [70] compared the effect of low and high electrode jump of tool electrode with respect to flushing of debris. Simulation results indicate that lower electrode jump do not pump enough fluid to remove debris, thereby, debris rich regions in the machining zone lead to secondary discharges as compared to high electrode jump where debris removal occurs effectively.

Debris, therefore, is found to play a destructive role during machining and hence different techniques were studied to effectively remove them from the machining zone.

2.3.3. Discharges during machining

At high machining depths, the capability of RMEDM significantly deteriorates. This is due to frequent short circuit and generation of abnormal discharges leading to defects such as taper formation on anode, high surface roughness, debris adhesion on electrode etc. These defects limit the usage of fabricated structures in their relevant fields of application. Efforts were made by Wu et al. [71] to stabilize the sparking process and thereby increase the machining rate in EDM by introducing an adaptive control system based on minimum-variance and pole-placement coupled control law (MVPPC). Zhou et al. [72] further improved the control system by developing a two-step-ahead prediction (TP) control law which not only stabilized the EDM process but also produced burn free machined features.

Various pulse discriminating (PD) systems have been developed to detect the occurrence of normal discharge, abnormal discharge or short circuit. Some of the PD systems were developed based on voltage signals [73], whereas some others were based on current signals captured during real time machining [74]. Few studies also showed usage of acoustic emission signals for monitoring of discharges [75–77]. Tee et al. [78] segregated different pulses in EDM with a rotating electrode using simultaneous comparison of the gap voltage and

current signals with respective thresholds. Kao and Shih [79] monitored voltage and current in sub-nanoseconds duration wherein pre-discharging current occurred before the onset of a full discharge. Also, a ringing effect was observed at the end of a discharge, which is very difficult to determine using nano or sub-microsecond monitoring. Mahardika et al. [65] proposed a monitoring system in MEDM wherein the number of discharge pulses during flat head and shape up machining were recorded. An analysis of discharge pulses gives the effect of above machining types on material removal and tool wear. Liao et al. [73] developed an online PD system to monitor various pulses in MEDM process, which determines the percentage of different discharges as well as the occurrence of short circuit during an actual discharge. Nirala et al. [80] developed a PD system that is based on voltage as well as current signals. They found that the current signals underestimate the percentage of normal discharges and overestimate the total number of discharges. Hence, they concluded that online monitoring using voltage pulses provides better insight into the machining process. Nirala et al. [81] developed a virtual discharge pulse based PD system for identification of different discharges during continuous machining in MEDM. Different types of discharges were segregated depending on the percentage of open circuit voltage (OCV) and on the discharging points of each pulse.

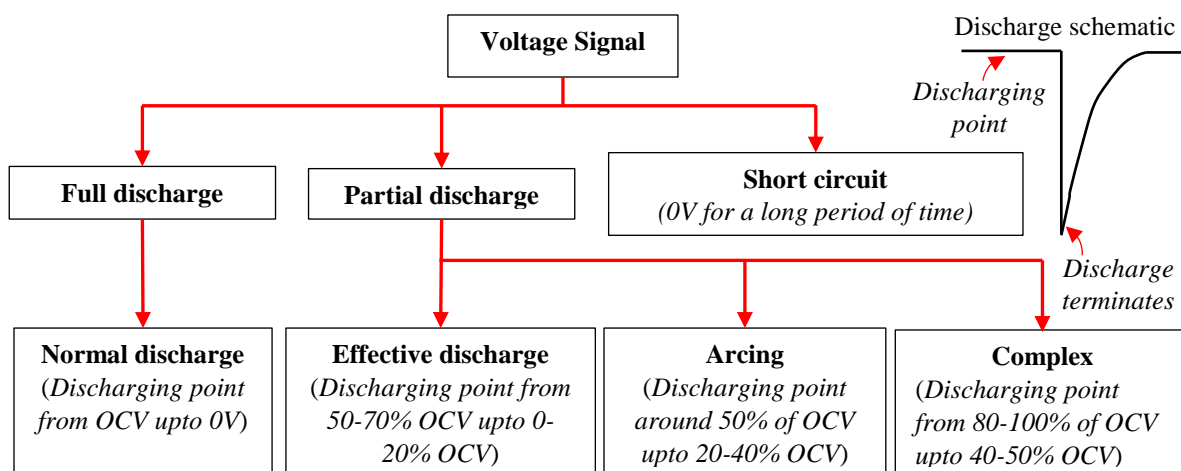


Fig. 2.1: Flowchart for various discharges observed in a voltage pulse

Characteristics of voltage pulses observed in MEDM by previous researchers can be summarised as shown in **Fig. 2.1**. Though most of the discharges observed in MEDM also holds good during RMEDM process [82], there are some unusual discharges which occur from very high discharging points, well above the OCV. This was observed during machining of Inconel 718 using wire EDM [83].

2.3.4. Recast layer and its effect on surface roughness

During each discharge, material is removed in molten and/or vaporized form. A portion of the molten material re-solidifies and adheres to the electrode surface. This layer has different chemical and metallurgical properties as compared to the base material [84]. Based on the energy of discharges, the recast layer thickness can be small or large [85]. The recast layer also contain micro cracks that can be visualised from the cross-sections of the tool/workpiece [86]. Thao and Joshi have analysed the surfaces of EDM and micro EDM through split hole trials and concluded that micro hardness reduces from EDM to micro EDM [87]. The recast layer degrades the quality of the original surface [88] and hence different techniques are employed for its removal viz. lapping, grinding, polishing etc. As the size and shape of the micro feature changes owing to these finishing processes, measurement of recast layer is a pre-requisite before adopting any additional technique for its removal. Destructive technique viz. metallography is mostly carried out to measure the thickness of recast layer. This technique though provides good result but the fabricated feature is destroyed and cannot be further used. Recast layer also affects the surface roughness of the surface [88]. Empirical equations were established by Ramasawmy et al. [89] relating recast layer thickness and 3D surface texture parameters viz. amplitude, spatial and volume. Results showed a better correlation of average recast layer thickness and spatial parameter i.e. density of summits of the surface among all the 3D surface texture parameters. Yildiz et al [84] have shown the correlation of surface roughness

with recast layer and concluded that there is a linear relation between the two. Yildiz [90] also developed thermal and 3-D finite element models for predicting recast layer thickness in EDM. On comparing with experimental results, it was found that prediction by finite element model was better. Guu et al. [91] experimentally investigated the effect of machining parameters on recast layer thickness and surface roughness of AISI D2 tool steel using kerosene as a dielectric. Results indicated that both surface roughness and recast layer thickness are directly proportional to input power of EDM. Gil et al [92] developed an experimental model for correlating various input parameters to surface roughness and thickness of recast layer on micro ED milled surface of a micro pin. The model reveals that for a particular energy, both surface roughness and thickness of recast layer show a similar trend. This also indicates a direct correlation between surface roughness and thickness of recast layer. A parametric analysis based on response surface methodology (RSM) was carried out by Kumar et al. [93] to determine the effect of various input parameters on recast layer in wire EDM. Results indicated that pulse on time was the most dominant factor that affected recast layer. Vignesh et al. [94] compared the recast layer thickness formed on AISI 202 stainless steel by using two different pulse generators viz. transistor pulse generator and iso current pulse generator. It was found that transistor pulse generator produced larger recast layer thickness. Kaneko and Furutani [95] machined molybdenum (Mo) with titanium (Ti) electrode using EDM to generate surface without any cracks in the recast layer as well as parent material. With positive electrode polarity and increased discharge current, sliced images of cross-sections of Mo showed that cracks escalated in the recast layer as well as in the base material. However, with negative electrode polarity, no cracks were observed in either the recast layer or the base material. Most of the research work have been carried out on determination of recast layer thickness and/or surface roughness either on flat surfaces after proper treatment or on single micro feature viz. micro pins.

The presence of recast layer affects the surface roughness of the generated surface. Hence, determination of extent of recast layer is very important especially in RMEDM where surface finish of the generated surface is one of the key characteristics.

2.3.5. Analysis of surface roughness

Though primary erosion is the main phenomena for material removal in RMEDM, the degree of abnormal discharges increases with increasing depth of micro features. Abnormal discharges cause erosion at random places leading to higher surface roughness at localised areas where debris accumulation is more [66]. Kiran and Joshi [96] developed surface roughness prediction model in MEDM by taking into account of pure dielectric as well as the inclusion of debris in dielectric. Their model indicated that inclusion of debris in dielectric predicted surface roughness better than the case without dielectric. A thermal model of surface roughness was developed by Salonitis et al [97] based on various input parameters of die sinking EDM. Two overlapping craters were considered for determining average surface roughness of the model. Kurnia et al [98] developed a surface roughness model for MEDM process wherein prediction of surface roughness was calculated based on crater geometry found from electro-thermal model. Effect of overlapping of craters, pockmarks, micro-cracks, and reattachment of debris were considered in the model. Abbasi et al. [99] predicted surface roughness of HSLA steel machined by wire-cut EDM using regression analysis. Results showed that apart from individual parameters (pulse-on time, pulse ratio, power, wire speed and discharge gap) responsible for effecting the surface roughness, interaction between process parameters also played a key role. Kiyak et al [100] experimentally studied the effect of discharge energy density (changing electrode diameters) on surface roughness in EDM. They found that increase in discharge energy density had a detrimental effect on surface roughness.

Presence of debris also affects surface roughness in addition to recast layer. Therefore, previous research works were aimed at reducing the surface roughness by properly flushing the debris.

2.4 Gap area

Based on literature survey, specific gap areas in the field of surface texturing and RMEDM have been identified based on which the scope of this current research work was found out.

- a) As the tool used in RMEDM is a flat plate with through holes (mostly circular), only 2.5-D cylindrical micro features can be fabricated. 3-D shaped micro features namely hemispherical, conical, pyramidal etc. were not attempted using the existing RMEDM process.
- b) Though few studies have been carried out to investigate the material removal mechanism in discharge based machining process, most of these have been carried out using single discharge only. No experimental validation or correlation have been obtained between MDS results with experimental results for single discharge. During actual machining, numerous discharges occur leading to shaping of micro feature. Therefore, single discharge studies are not enough to study the overall mechanism of material removal in RMEDM. Also, the effect of discharge on the crystal structure have also not been carried out till date.
- c) The destructive role of debris during machining has been studied in detail by various researchers. Research works have been carried out to improve the flushing conditions so that debris removal becomes easier. However, the constructive role of debris in EDM and especially in the generation of various shapes of micro features (hemispherical, conical, pyramidal etc.) has not been studied. Moreover, there is a lack of scientific understanding

of the various forces on debris that govern their movements in the dielectric and subsequently their behaviour towards change in discharge phenomena.

- d) Segregation of discharges have been carried out experimentally in literature based on voltage and/or current values obtained by signals. As RMEDM employs RC circuit, pulse discharges are governed by the charging of the capacitor. There is a lack of understanding of the effect of charging/discharging of capacitor based on inclusion of debris in the dielectric which leads to abnormal discharges.
- e) Apart from effect of debris, multiple physical processes occur simultaneously in RMEDM which makes modelling and simulation of generation of specific shape of micro features very difficult. Subsequently, surface roughness analysis of the simulated shape also becomes difficult as location of discharges due to debris varies at different portion of micro feature for various traverse of anode/depth of machining.
- f) Experimental analysis have been carried out for generating similar aspect ratio of arrayed micro features. However, certain applications require the usage of varying aspect ratio of arrayed micro features and fabrication of such varying aspect ratio of micro features have not been studied and reported.
- g) Characterization of micro features for recast layer, heat affected zone (HAZ) and their mechanical properties have been carried out mostly on flat surfaces but not on protruded micro features. As conventional metallography techniques for determination of recast layer and HAZ is difficult for arrayed micro features, alternate techniques are not explored and reported.

2.5 Scope of research work

Based on research gaps highlighted in *Section 2.4*, the scope for this research work has been identified and listed below:

- a) Study and development of technique for generating 3-D micro features especially hemispherical shape using RMEDM based on suitable tool modification.
- b) Single discharge studies using MDS are capable of throwing light on the material removal mechanism. Further, information about the change in crystalline structure of the workpiece during discharge can also be studied using MDS. Though it is very difficult to validate MDS and experimental results since both operate at different scales (MDS – nano, experiments – micro), an attempt to establish a dimensionless correlation between experimental and MDS results will be made.
- c) Multiple discharge studies in MDS can explain the phenomena of movement of molten material during discharge and help in understanding the formation of craters of various sizes which eventually lead to difference in surface roughness at various locations.
- d) The effect of debris on the charging and discharging of capacitor leading to transition of discharge phenomena at increased machining depths needs further investigation both numerically as well as experimentally. Subsequently the role of debris in generation of 3-D hemispherical shaped micro feature using RMEDM needs further exploration.
- e) Suitable process model needs to be developed that can explain the multiple physical phenomena responsible for shape generation and surface roughness of the 3-D hemispherical shaped micro features. Appropriate validation of shape and surface roughness also needs to be carried out.
- f) Experimental investigations are required for generating arrayed micro features of different aspect ratio. To achieve this, tool modification in RMEDM has to be established for single micro feature generation and then subsequently arrayed micro features of similar and dissimilar aspect ratio of micro features can be attempted.
- g) Metallography and etching can be carried out for single micro feature which can be used to visualize and determine recast layer, HAZ, parent material and subsequently their

mechanical properties by suitable techniques. For arrayed micro features, however, metallography is not possible. Hence, a non-destructive method has to be employed which can visualize the internal structure of the micro feature in order to gain insight in the discharge affected layers.

In view of this, various activities that have been carried out in this study are shown in Fig. 2.2.

---x---

Research Plan

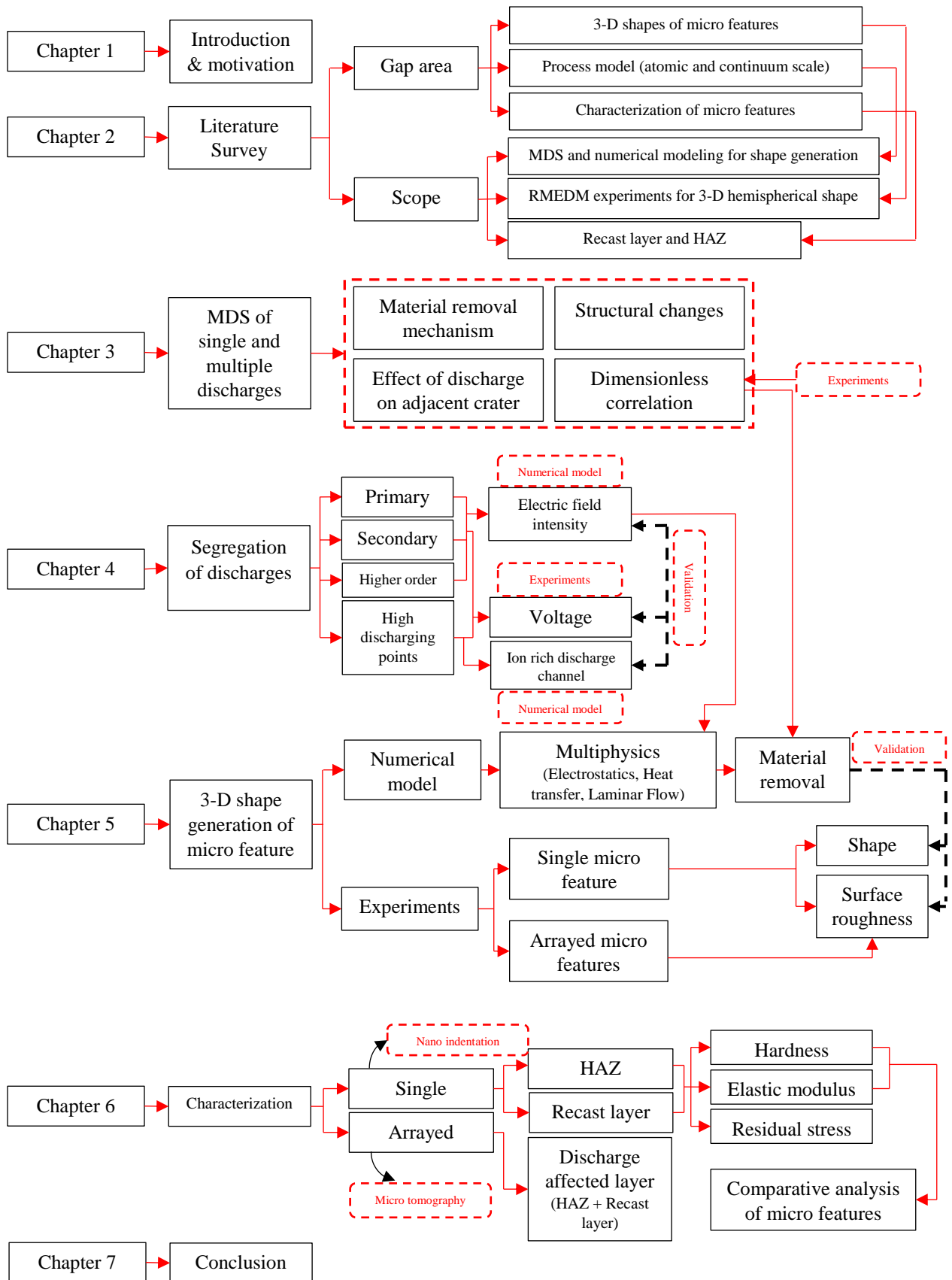


Fig. 2.2: Research Plan for Ph.D.

CHAPTER 3

MOLECULAR DYNAMICS SIMULATION AND EXPERIMENTAL ANALYSIS OF MATERIAL REMOVAL MECHANISM

3.1 Introduction

Discharges during MEDM including RMEDM occur at time scales of few ns and length scales of few μm . At such small scales, it is very difficult to experimentally observe the material removal mechanism, formation of recast layer and other discrete effects such as crystal structure distortion during RMEDM. Continuum scale modelling is also limited by the very short time and length scales of discharges in RMEDM. Molecular dynamics simulation (MDS), on the other hand, is used to study mechanisms occurring at the atomic scale. This chapter, therefore, investigates the mechanism of material removal during single discharge in RMEDM using MDS. The actual process, however, have numerous discharges leading to formation of the micro feature. To understand the behaviour of multiple discharges during RMEDM, two different discharges were considered depending on their relative location of occurrences on the surface. Apart from studying the material removal mechanism for multiple discharges, crater diameter, height as well as recast layer thickness have been compared. Further, a new method is proposed that provides a dimensionless correlation between MDS and experiments for specific material removal at different discharge energies in RMEDM.

3.2 Molecular dynamics simulation during single discharge in RMEDM

Molecular Dynamics Simulation (MDS) is extensively used for studying the mechanisms occurring due to mechanical and thermal actions on materials at the atomic scale [56–58]. Although it is known from literature that material removal takes place by melting and vaporisation, accurate estimation of them at lower energy levels are not reported. Moreover, MDS is not extensively used for this aspect. This section deals with determining the percentage of material removal by melting and vaporisation at two different discharge energies viz. low and high energy levels of RMEDM using MDS and their comparison. In addition, various other aspects such as formation of recast layer, change in crystal structure due to discharge and formation of crater have also been studied.

3.2.1 MDS methodology

An atomistic model has been developed to understand various aspects of single discharge viz. the percentage of material removed by melting and vaporisation, formation of recast layer, change in crystal structure due to discharge and formation of crater. The assumptions that are taken for simplifying the model are as follows:

- a) Due to computational limitations, the geometry of the model has been scaled down to tens of nm.
- b) Heat source has been assumed in the form of circular Gaussian heat source
- c) Only the workpiece was considered (anode). Tool (cathode) was not considered in the model.
- d) Radiation and convection heat losses are negligible
- e) The working gap is taken to be vacuum for simplicity [101].

3.2.1.1 *Geometry of the model*

The geometry used in MDS is shown in **Fig. 3.1**. Monocrystalline copper was used as workpiece with dimensions 100 Å wide (X-axis orientation), 100 Å long (Y-axis orientation) and height of 100 Å (Z-axis orientation). In order to prevent the workpiece from unexpected movements during material removal, boundary atoms (atoms with zero movement) with thickness 4 Å were applied on all the sides (**Fig. 3.1 (a)**) except the top face where discharge occurs. Adjacent to boundary layer atoms, thermostat atoms of thickness 4 Å (**Fig. 3.1 (b)**) were distributed whose temperature remained fixed at 300 K during simulation to ensure adequate heat conduction in the workpiece. The rest of the geometry comprised of Newtonian

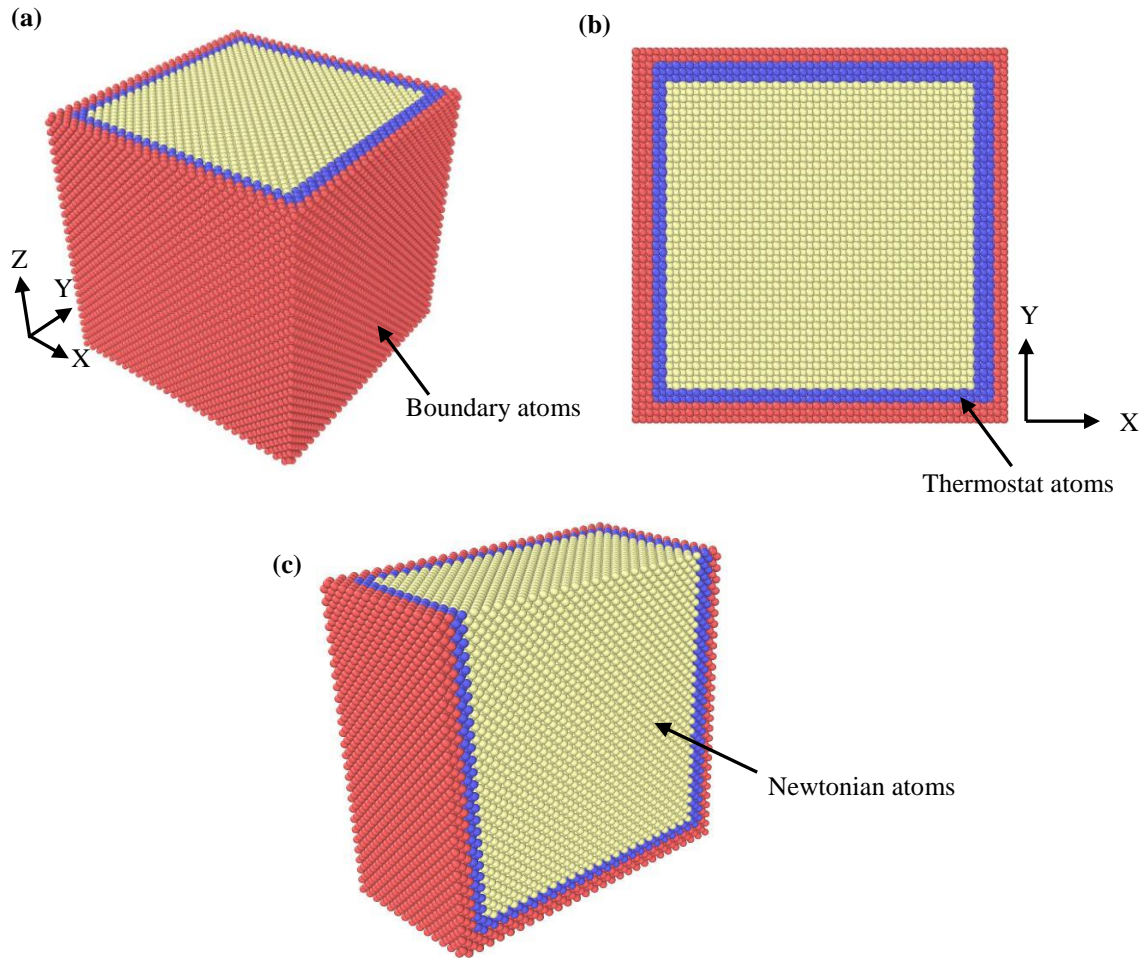


Fig. 3.1: (a) 3D view (b) top view and (c) sliced view of MD model of workpiece

atoms (**Fig. 3.1 (c)**) that obey Newton's second law. The initial temperature was set to 300 K. Discharge occurs on the top surface of the geometry which was assigned free boundary condition. Non-periodic and shrink wrapped boundary conditions were used for simulation.

3.2.1.2 Heat source in single discharge

Plasma channel consists of ions, electrons and neutral particles. The diameter of plasma channel changes with time. For simplicity, during single discharge, the plasma column is assumed to be a circular Gaussian heat source [61] whose radius expands linearly with time and the heat source was applied at the centre of the top surface of workpiece to imitate the heat flux from the plasma column. The Gaussian heat source can be expressed as shown in **Eq. 3.1**.

$$q(r) = q_m e^{(-ar^2)} \quad (3.1)$$

where, r is the distance from the centre of discharge column, $q(r)$ is the heat flux density at radius r , q_m is the heat flux density at the centre of plasma channel and a is the heat source concentration factor.

The temperature distribution in the workpiece during simulation was calculated using **Eq. 3.2**.

$$T = \frac{2K_e}{3Nk} \quad (3.2)$$

where, K_e is the total kinetic energy of the atom group, N is the number of atoms, and k is the Boltzmann constant.

3.2.1.3 Potential function

Embedded-atom method (EAM) potential [102] was used for interaction between copper atoms. In this study, the embedded-atom method [13] was employed to express the interatomic potential in the copper structure. The total energy E_t of an elemental system in EAM can be expressed as shown in **Eq. 3.3**.

$$E_t = \frac{1}{2} \sum_{i \neq j} V(r_{ij}) + \sum_i F_i(\rho_i) \quad (3.3)$$

where, V is a pair potential as a function of distance r_{ij} between atoms i and j , and F_i is the embedding energy as a function of the host electron density ρ_i induced at site i by all other atoms in the system.

MDS was carried out using Large-scale Atomic/Molecular Massively Parallel Simulator (LAMMPS) [103]. Very low discharge energies viz. 0.165 μJ and 5 μJ (discharge energies used for generating 3-D hemispherical convex micro feature) were used for simulation. Simulation parameters used are shown in **Table 3.1**. Heat flux density was calculated based on the applied discharge energy ($\frac{1}{2}CV^2$) and the pulse on time (ns) obtained

Table 3.1: Parameters for simulation

Parameters	Values
Maximum heat flux density at the centre of arc column	• 0.020 GeV/ps (0.165 μ J) • 0.624 GeV/ps (5 μ J)
Spark radius	12.5 Å
Discharge duration	5 ps
Relaxing time	15 ps
Total calculation time	20 ps
Potential	Embedded-atom method

from preliminary experiments. Units ‘metal’ was used for this study in LAMMPS where unit of energy used is in eV. Appropriate conversion in units from μ J/s to GeV/ps were done before simulation. The ratio of spark radius to lateral dimensions of workpiece carried out by Yang et al. [59] was ~ 0.138 . Keeping this in mind, the spark radius was estimated in terms of the length of the workpiece and hence spark radius was used as 12.5 Å (ratio between spark radius and lateral dimensions of workpiece ~ 0.125). The discharge duration (5 ps) was kept similar to that used by Yang et al. [59] (4.8 ps). The relaxation time used in this study was based on some initial simulations wherein it was found that at 15 ps, stabilisation of crater formation occurs. Though the spark radius and discharge duration has been scaled down in order to simulate the discharge process using MDS, the actual spark energies used during experiments have been used for simulation after appropriately converting their units.

Visualisation and analysis of atomistic data obtained from LAMMPS was done using OVITO [104], a 3D open source visualization software. Local structural changes that occurred during and after single discharge was characterized using common neighbor analysis (CNA), which is an efficient method to segregate atoms in crystalline systems considering relevant phases and defects occurring in the workpiece [105].

3.2.2 Material removal mechanism and recast layer formation due to single discharge

The process of material removal at different discharge energies are shown in **Figs. 3.2 – 3.3**. Cross sectional views of workpiece at different time steps and top view of the workpiece

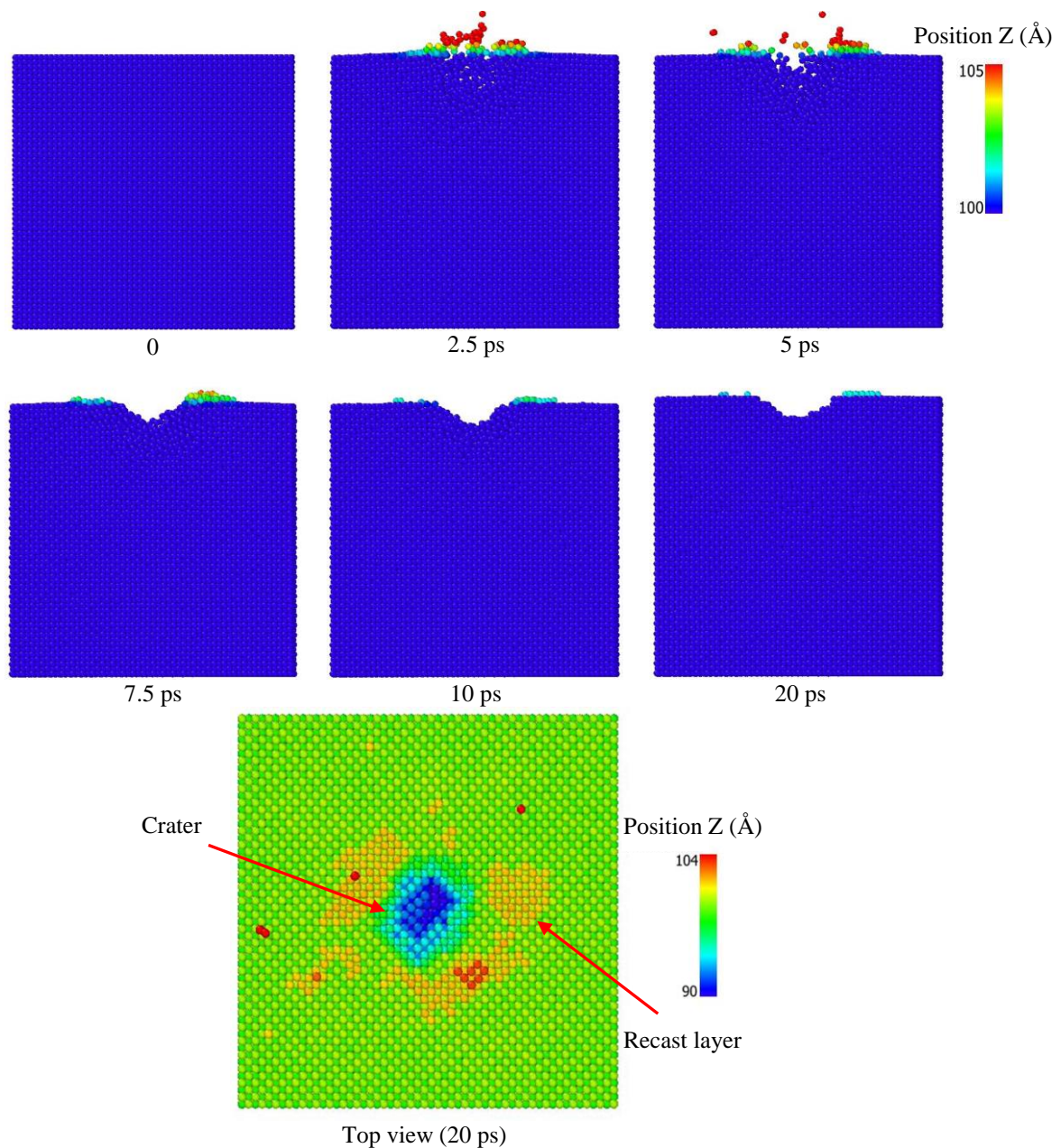


Fig. 3.2: Material removal process on workpiece at spark energy of $0.165 \mu\text{J}$

at the end of simulation are shown. The process of material removal and formation of crater due to single discharge in MEDM were simulated using parameters shown in **Table 3.1**. It can be seen that during the discharge duration from 0 ps to 5 ps (**Figs. 3.2 – 3.3**), material removal from workpiece starts immediately. This is in coherence with Yue and Yang [62] where they have attributed high extreme pressure as the cause for this spontaneous material removal. With high discharge energy and constant spark radius, specific energy in case of $5 \mu\text{J}$ will be higher

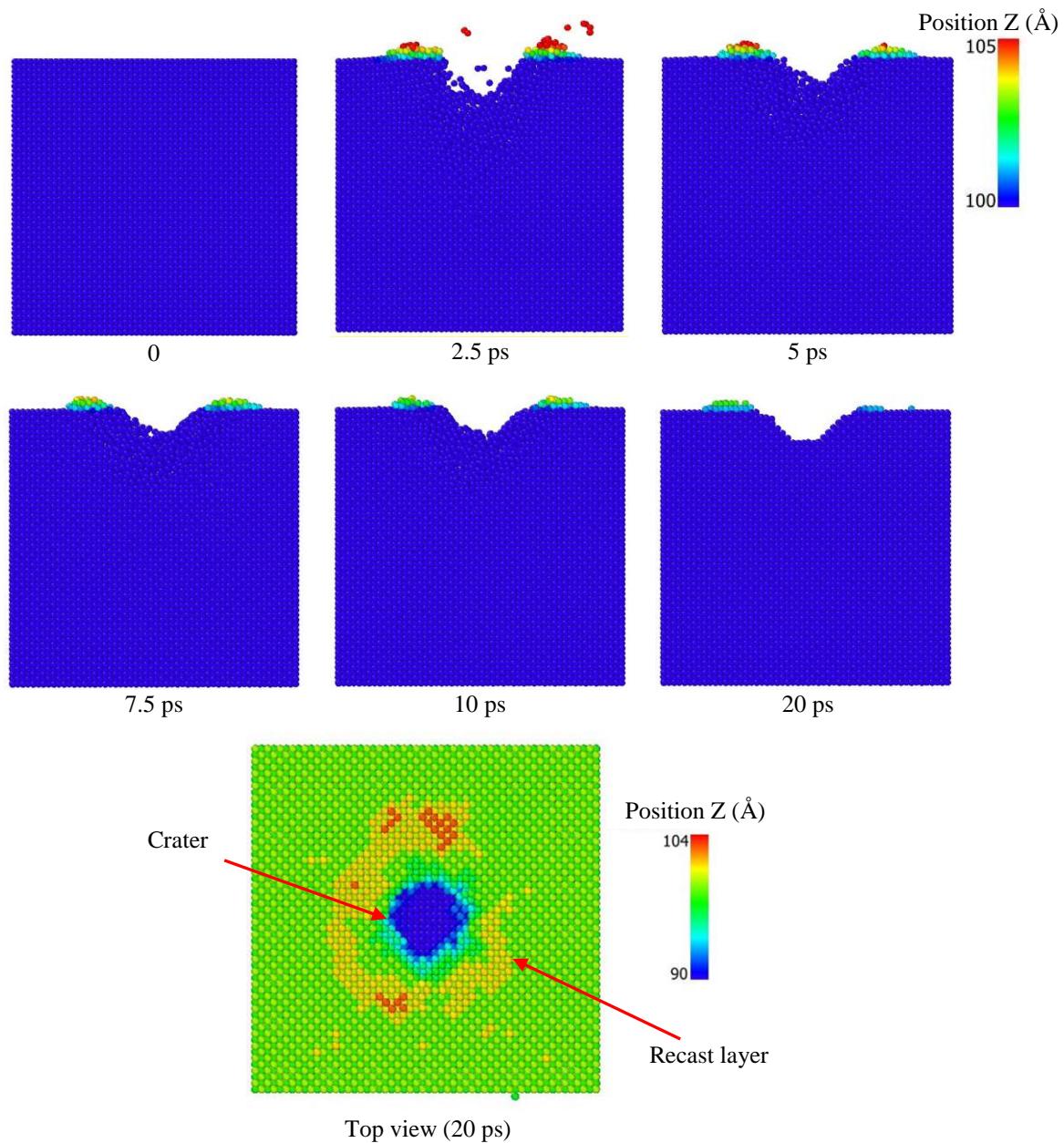


Fig. 3.3: Material removal process on workpiece at spark energy of $5 \mu\text{J}$

due to which material removal occurs earlier (**Fig. 3.3**) as compared to the case with low discharge energy (**Fig. 3.2**). Position of Z-axis has been used as reference since it gives an indicator of the crater dimensions as well as recast layer thickness after discharge for both the cases. Melting and vaporisation are the two primary modes of material removal. Due to application of heat source, atoms starts vibrating and expulsion of material occurs whenever the temperature of atoms exceeds melting ($T_{melt} = 1355 \text{ K}$) and vaporisation ($T_{vap} =$

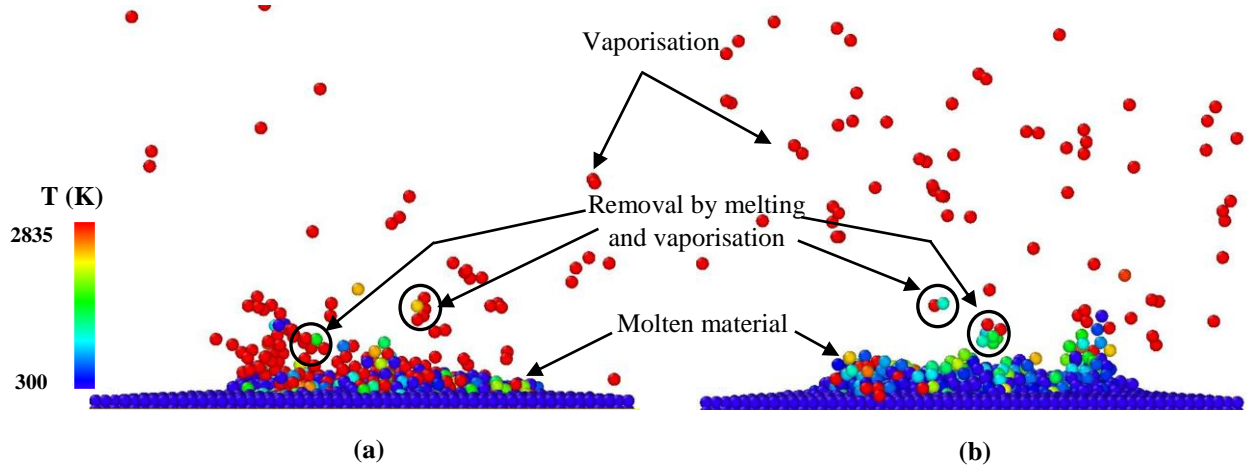


Fig. 3.4: Material removal at 2.5 ps in the form of atoms with spark energy (a) 0.165 μJ (b) 5 μJ

2835 K) temperature of workpiece (**Fig. 3.4**). Craters are formed on the workpiece at the end of discharge (**Figs. 3.2 – 3.3**).

Wong et al. [47] in their study on single discharge material removal in MEDM found that at discharge energy of 23.50 μJ , 20% of molten material is vaporised and removed from machining zone thereby increasing net material removal efficiency. Melting and vaporisation

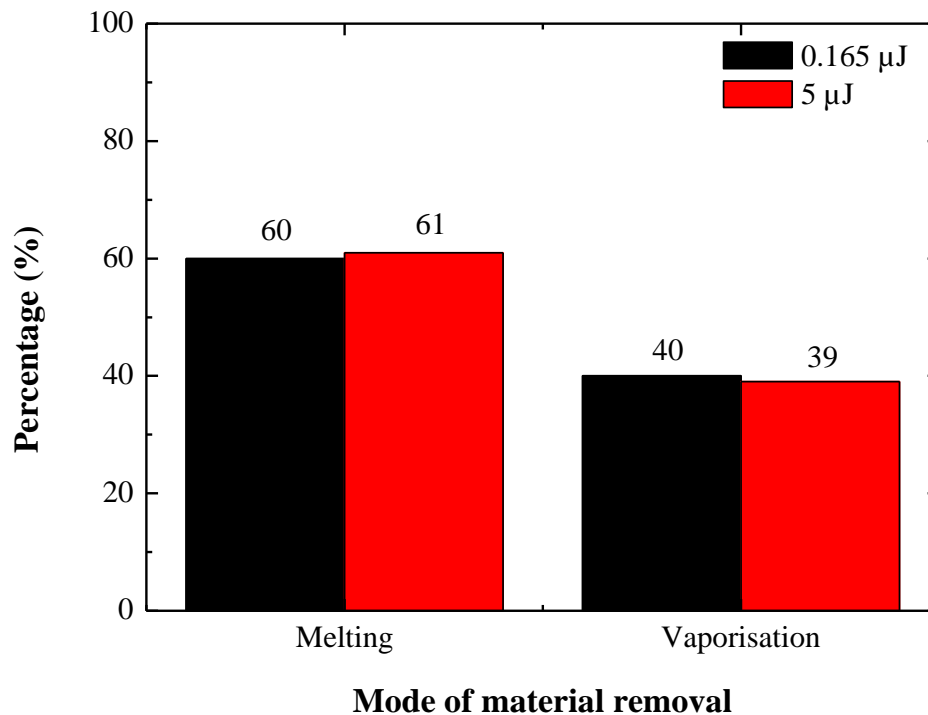


Fig. 3.5: Material removal mechanism at different spark energies

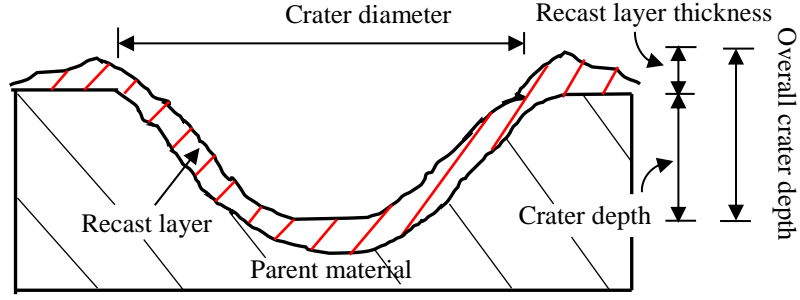


Fig. 3.6: Schematic of crater characteristics

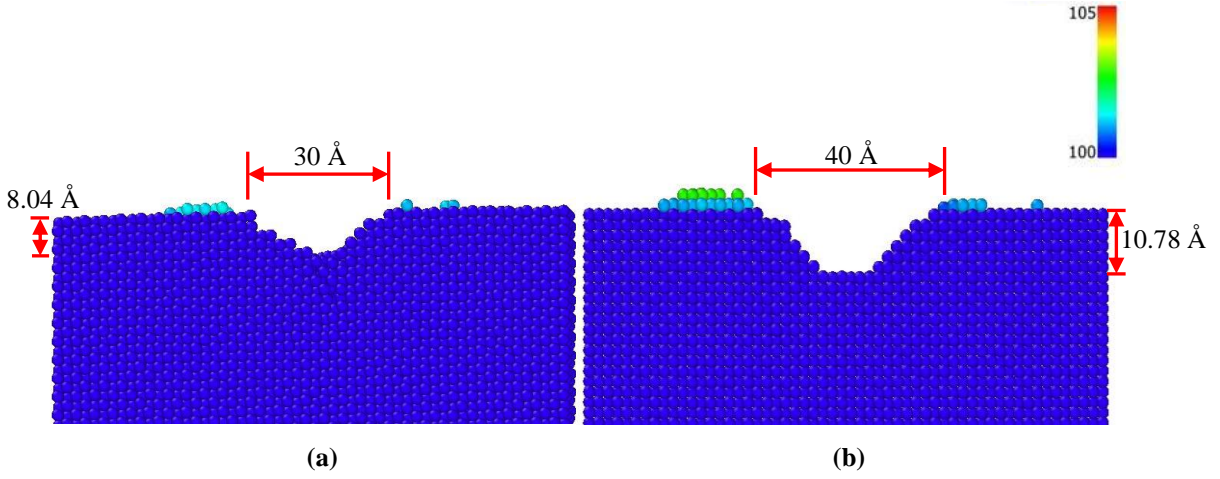


Fig. 3.7: Crater formation at spark energy (a) 0.165 μJ (b) 5 μJ

(in %) was obtained by calculating the number of atoms whose temperature were beyond melting and vaporisation respectively. It can be obtained by using **Eqs. 3.4 – 3.5**.

$$\text{Vaporisation (\%)} = \frac{\text{Total number of atoms } \geq T_{vap}}{\text{Total number of atoms } \geq T_{melt}} \quad (3.4)$$

$$\text{Melting (\%)} = 100 - \text{Vaporisation (\%)} \quad (3.5)$$

Fig. 3.4 shows the phenomenon of melting and vaporisation taking place simultaneously during single discharge at 2.5 ps. With constant spark radius and high specific energy in case of 5 μJ , higher number of atoms will be affected due to heat source leading to higher amount of material removal as compared to the one with lower discharge energy (0.165 μJ). Based on MDS results (**Fig. 3.5**), percentage of molten material removed by vaporisation is almost constant at both energy levels (40%). It indicates that irrespective of discharge energies in the range of 0.165 μJ to 5 μJ , mode of material removal is nearly constant i.e. 40% by vaporisation and 60% by melting out of which most of the molten material is being re-

solidified and remains on the workpiece as recast layer. The percentage of melting and vaporisation was calculated based on number of atoms which reached temperature above the melting point in each case (Eqs. 3.4 - 3.5). This is dependent on thermal properties of material and hence can vary with respect to different materials. It is not related to the amount of material removal but the percentage. A schematic of crater characteristics i.e. the crater diameter and the overall crater depth (the actual crater depth and the thickness of recast layer) obtained after a single discharge in EDM is shown in **Fig. 3.6**. **Fig. 3.7** depicts these crater characteristics obtained from MDS. Both crater diameter and overall crater depth increases with respect to high discharge energy. The increase in crater diameter is in the ratio 1.33 whereas the increase in crater depth is in the ratio 1.34.

3.2.3 Crystal structure distortion due to single discharge

Application of heat source on the workpiece leads to increase in temperature of atoms and this distorts the crystal structure of the workpiece. Conversion of FCC crystal structure to amorphous structure locally at discharge zone during melting and vaporisation for both energy levels can be seen in **Fig. 3.8 (a, c)**. At the end of discharge process (20 ps), most of the material

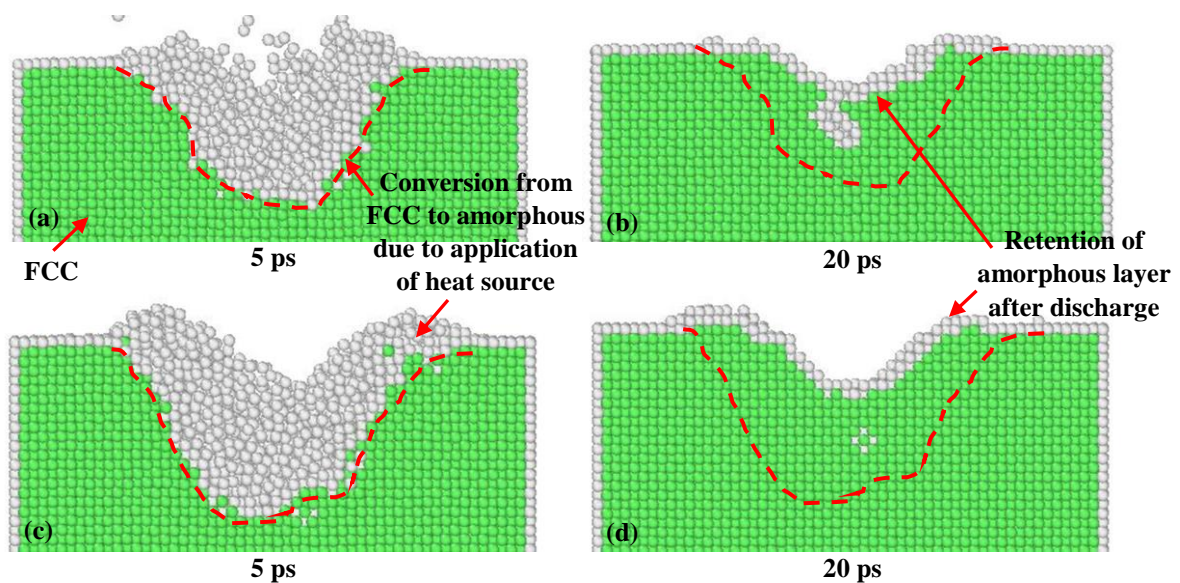


Fig. 3.8: Formation of amorphous layer during single spark at energy (a-b) 0.165 μJ (c-d) 5 μJ

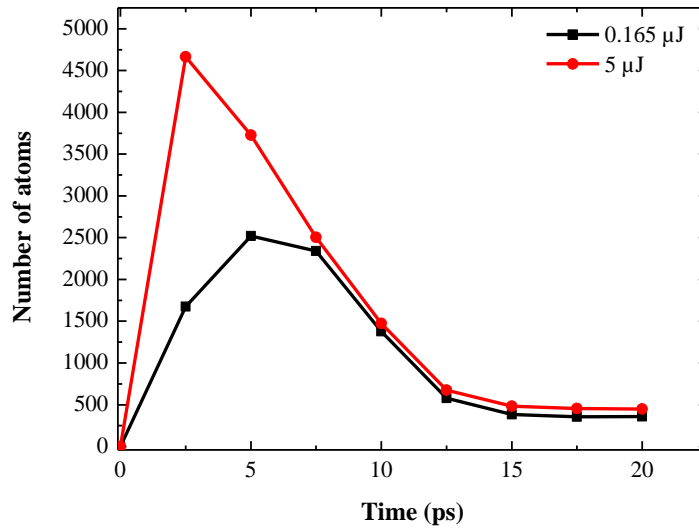


Fig. 3.9: Number of atoms in the amorphous layer

regains its crystalline form however, some amount of material still remains in amorphous phase (**Fig 3.8 (b, d)**). This is in conjunction with Murray et al. [106] and Cusanelli et al. [107] where characterisation of sample by TEM after electrical discharge by EDM revealed the presence of amorphous layer. **Fig. 3.9** shows a plot of number of atoms in the amorphous layer upon application of heat source. The number of atoms leaving the FCC crystal structure at each time step has been calculated using CNA in OVITO. At high discharge energy (5 μJ) and same discharge radius, increase in specific energy leads to affecting higher number of atoms. This leads to higher amount of distortion in crystal structure at high energy as compared to lower energies (0.165 μJ) during discharge. However, as soon as heat source is removed (after 5 ps), there is a steep decline in the number of atoms in the amorphous layer. This indicates that after the discharge ceases, the material starts regaining its original crystal structure. After 7.5 ps, the decrease in number of atoms follow a similar trend for both energy levels. Though behaviour of amorphisation during this phase is similar irrespective of discharge energies, the degree of distortion in case of higher discharge energy is marginally high (20 ps). Hence, it can be concluded that the amorphous layer is formed on the crater surface and it is slightly higher for higher discharge energy.

3.3 Molecular dynamics simulation of multiple discharges in RMEDM

During machining in RMEDM, numerous discharges occur leading to the formation of the desired micro feature. Three different discharge configuration are possible (**Fig. 3.10**) based on their location. They are listed below.

- (a) Discharges occurring at a gap of one discharge diameter (separate craters)
- (b) Discharges with their periphery coinciding with each other (craters coinciding)
- (c) Discharges overlapping by half of discharge radius (craters overlapping)

These three cases are simulated, analysed and the mechanism behind the formation of craters, recast layer and material removal mechanism are studied using MDS. Geometry used for this simulation (height of workpiece = 50 Å), potential function and heat source (0.165 μJ) are similar to the one described in *Section 3.2*. Simulation parameters are shown in **Table 3.2**. Though the spatiotemporal scale used in this study is significantly small as compared to actual

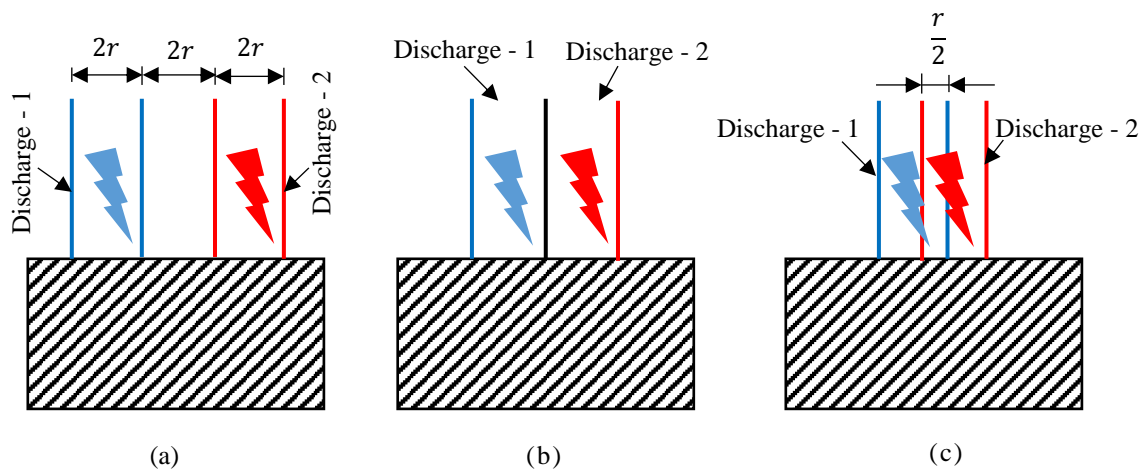


Fig. 3.10: (a) Discharges separated by spark diameter ($2r$) (separate craters) (b) Discharges coinciding at the periphery (craters coinciding) (c) Discharges overlapping (craters overlapping); Pulse energy: 0.165 μJ

Table 3.2: Computational parameters for simulation

Parameters	Values
Maximum heat flux density at the centre of arc column	0.02 GeV/ps (0.165 μJ)
Spark radius	12.5 Å
Discharge duration for each spark	5 ps
Relaxing time for each spark	15 ps
Total calculation time	40 ps
Time step	0.001 ps

RMEDM process, the simulation results will help in qualitative understanding of the effect of successive discharges on the surface of machined workpiece leading to variation in crater size.

3.3.1 Material removal mechanism during multiple discharges

Due to heat source applied to workpiece during pulse on time in each case, temperature rise at the discharge zone exceeded the melting and vaporisation temperature of the workpiece leading to material expulsion from the workpiece. Simulation results obtained from MDS is shown in **Fig. 3.11**

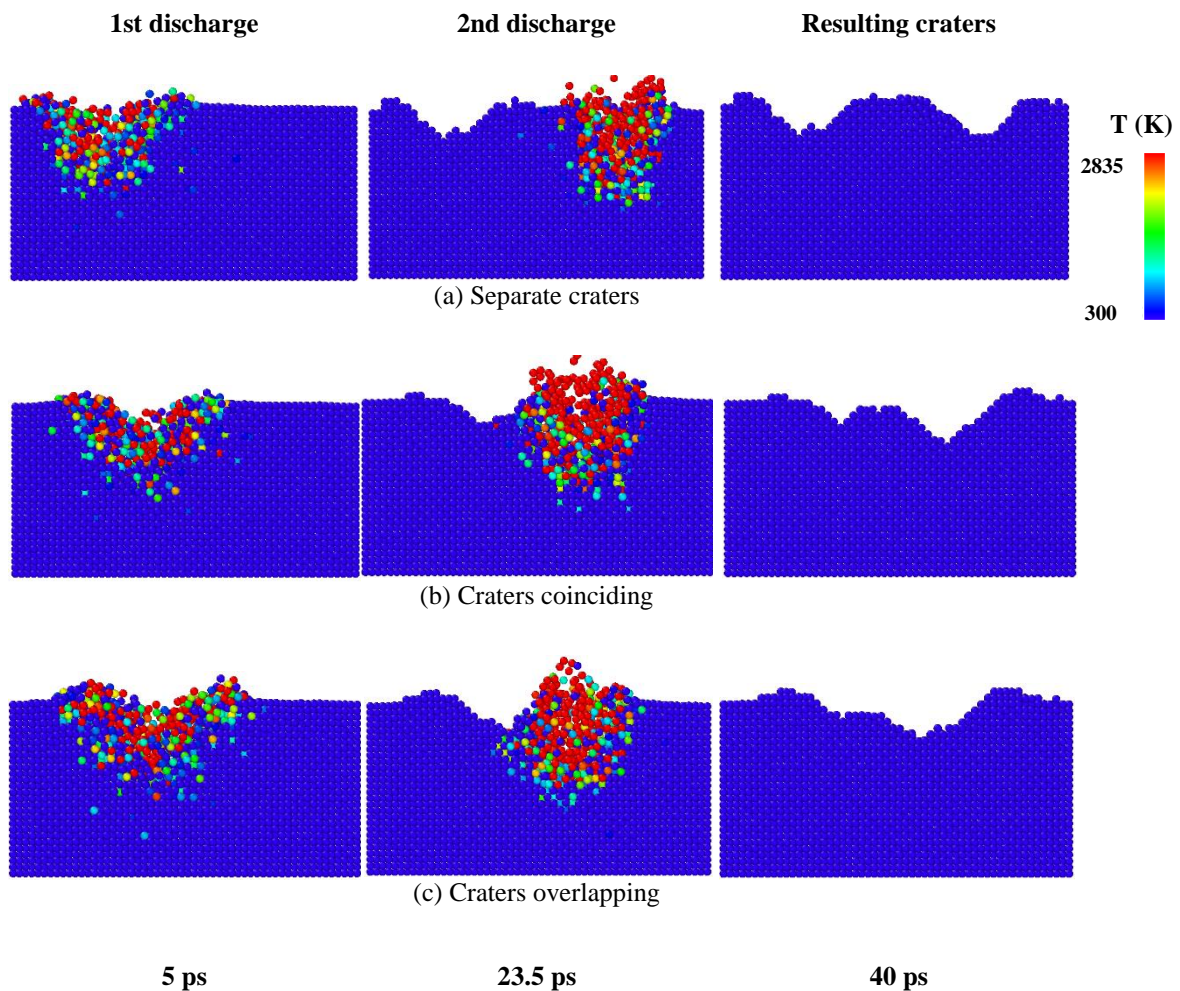


Fig. 3.11: Melting and vaporization taking place on (a) separate craters (b) craters coinciding (c) craters overlapping at time intervals 5 ps, 23.5 ps and 40 ps; Pulse energy: 0.165 μ J

Atomic clusters melting and vaporising during 1st and 2nd discharges are shown in all the three cases. After material removal and re-solidification of molten material takes place, a single crater is generated as shown at 23.5 ps. Also, 2nd discharge occurs which leads to formation of 2nd crater. Overlapping of craters is most common occurrence during actual machining. During this case, the occurrence of 2nd discharge adjacent to the already formed 1st crater interacts with its atoms leading to removal of atoms beneath the 1st crater (Fig. 3.12).

As discharge progresses, molten material expelled from the 2nd crater is deposited on the 1st crater. Hence, the 1st crater size reduces but the resulting overall crater obtained due to 2nd discharge increases. Fig. 3.13 shows the formation of recast layer on the top surface of the

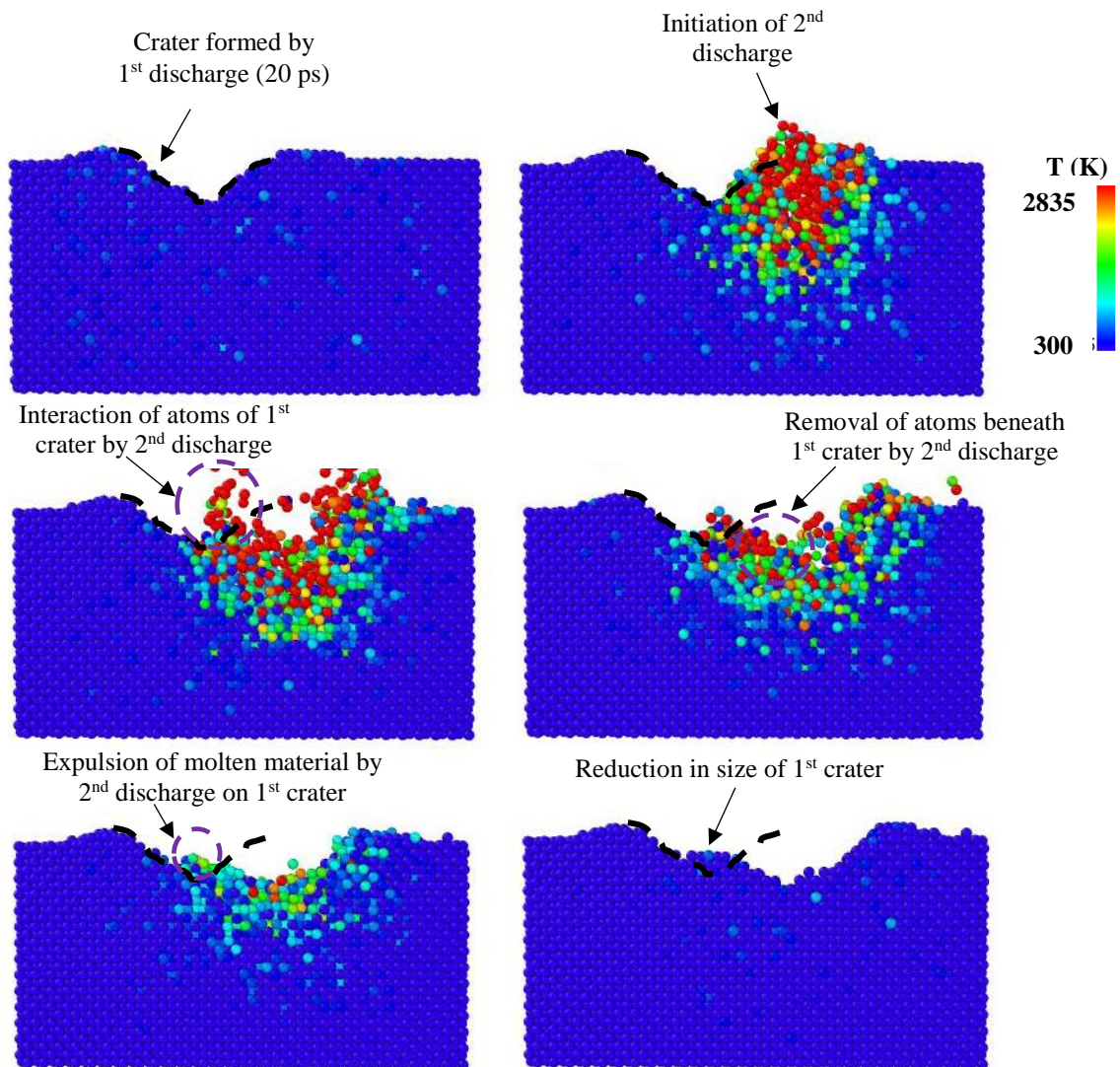


Fig. 3.12: Effect of 2nd discharge on 1st crater in case of overlapping craters

craters and the crater shapes obtained in three cases. Colouring scheme used to denote craters and recast layer in **Fig. 3.13** was variation in the depth (Z-axis). When discharges occur by some distance apart (**Fig. 3.13 (a)**), the gap between the craters is covered by recast layer formed by flow of molten material around the crater due to extremely high pressure generated in the workpiece during discharge and also due to accumulation of atomic clusters adhering on the surface [59]. The formation of recast layer is also observed at the gap between two craters on actual surface (**Fig. 3.13 (a)**). With craters coinciding (**Fig. 3.13 (b)**), the crater size corresponding to 1st discharge reduces in size as compared to crater formed by 2nd discharge. This is due to expulsion and deposition of molten material by the 2nd discharge on the already formed 1st crater. Formation of overlapping craters (**Fig. 3.13 (c)**) results in a larger overall crater and segregation of individual crater is difficult. It can be seen that both craters have merged into one another and the crater observed from 1st discharge after completion of both discharges has become a part of overall crater.

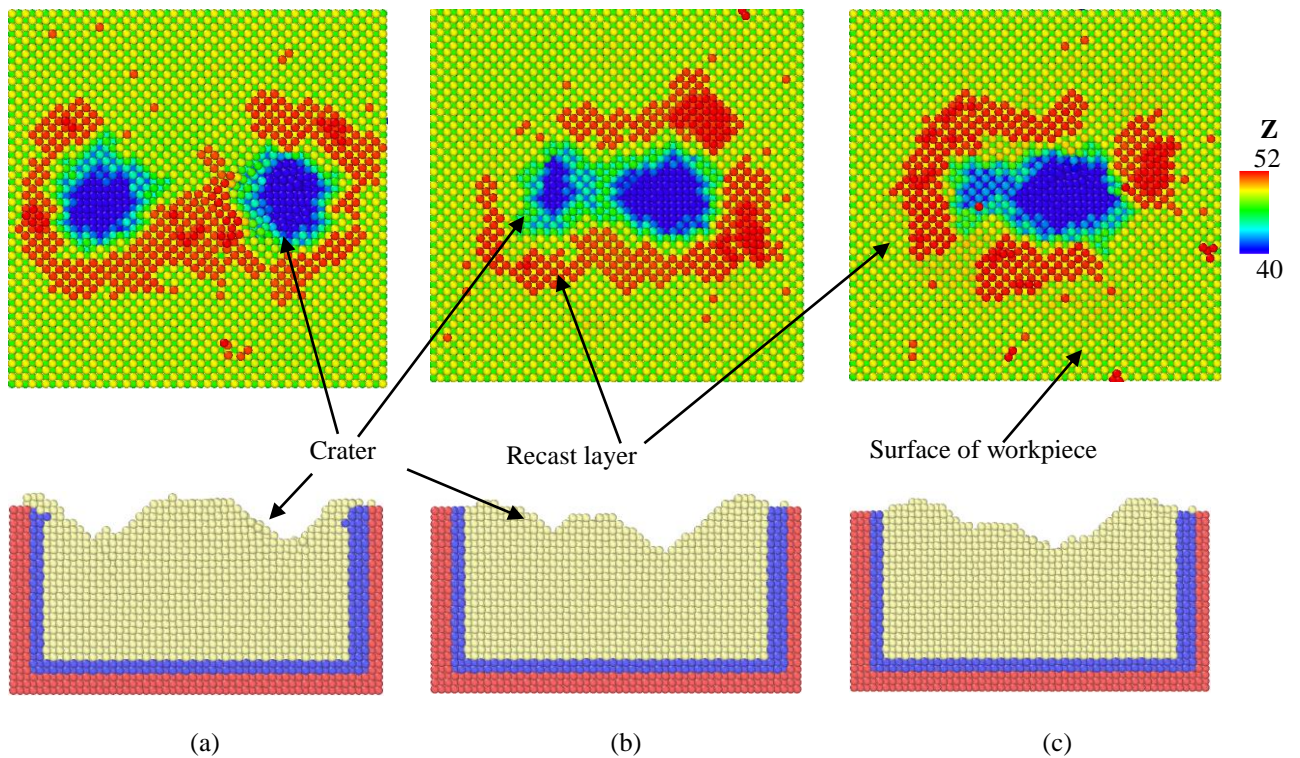


Fig. 3.13: Crater and recast layer formation in (a) separate craters (b) craters coinciding (c) craters overlapping

3.3.2 Size of craters during multiple discharges

A comparison of crater sizes viz. depth and diameter computed from MDS results is shown in **Fig. 3.14**. It can be seen that when craters are separated by some finite distance, the depth as well as diameter of crater (measured after 40 ps) resulting from 2nd discharge is marginally higher than the 1st due to the molten material from 2nd discharge partially thrown to the crater generated on the first discharge. As the distance between discharges decreases (starting from separate craters, craters coinciding and craters overlapping), it can be seen that the crater depth and diameter are higher throughout the 2nd discharge as compared to 1st discharge. The crater depth and diameter (measured at 40 ps) obtained from 1st discharge is the smallest in case of overlapped craters as most of the molten material expulsion from 2nd discharge gets deposited on the 1st crater leading to material re-solidification on the crater and decrease in crater depth and diameter.

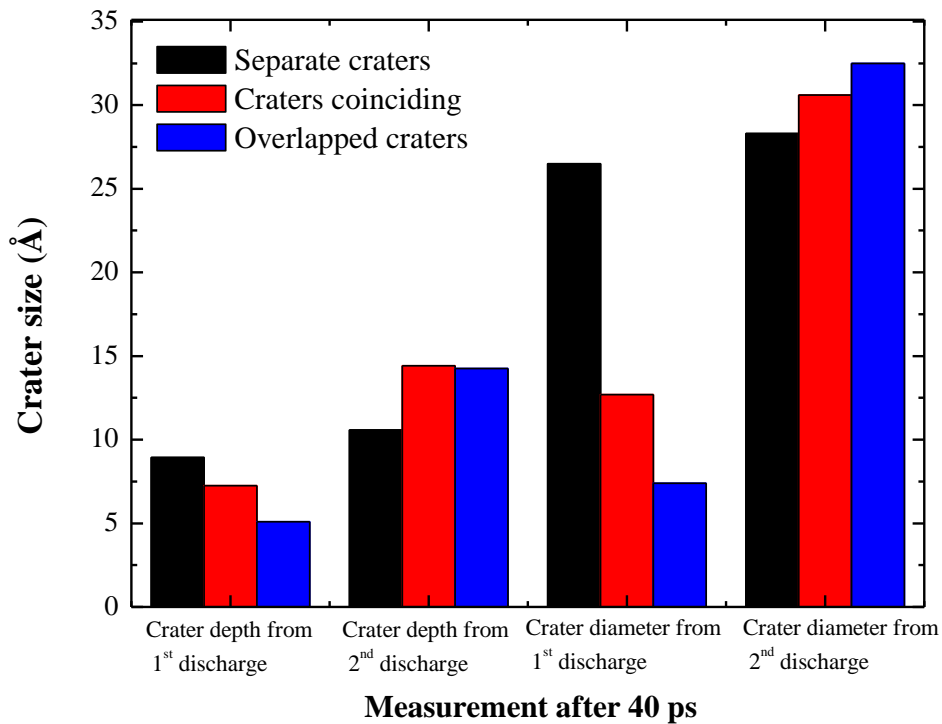


Fig. 3.14: Crater depth and diameter obtained after 2nd discharge in all three cases

3.3.3 Qualitative comparison of craters formation during multiple discharges in RMEDM

The surface of 3-D hemispherical micro feature generated by RMEDM (experimental procedure to be discussed later in Chapter 5 and experimental details mentioned in Table 4.3) is shown in **Fig. 3.15**. All the three possible cases simulated using MDS are also observed on actual surface. Considering the case with separate craters, the crater diameters are almost similar and are separated by recast layer. This is similar to **Fig. 3.13 (a)** where the crater diameter obtained by simulation is almost comparable (**Fig. 3.14**). With decrease in distance between discharges (craters coinciding and adjacent craters), the crater diameter due to 2nd

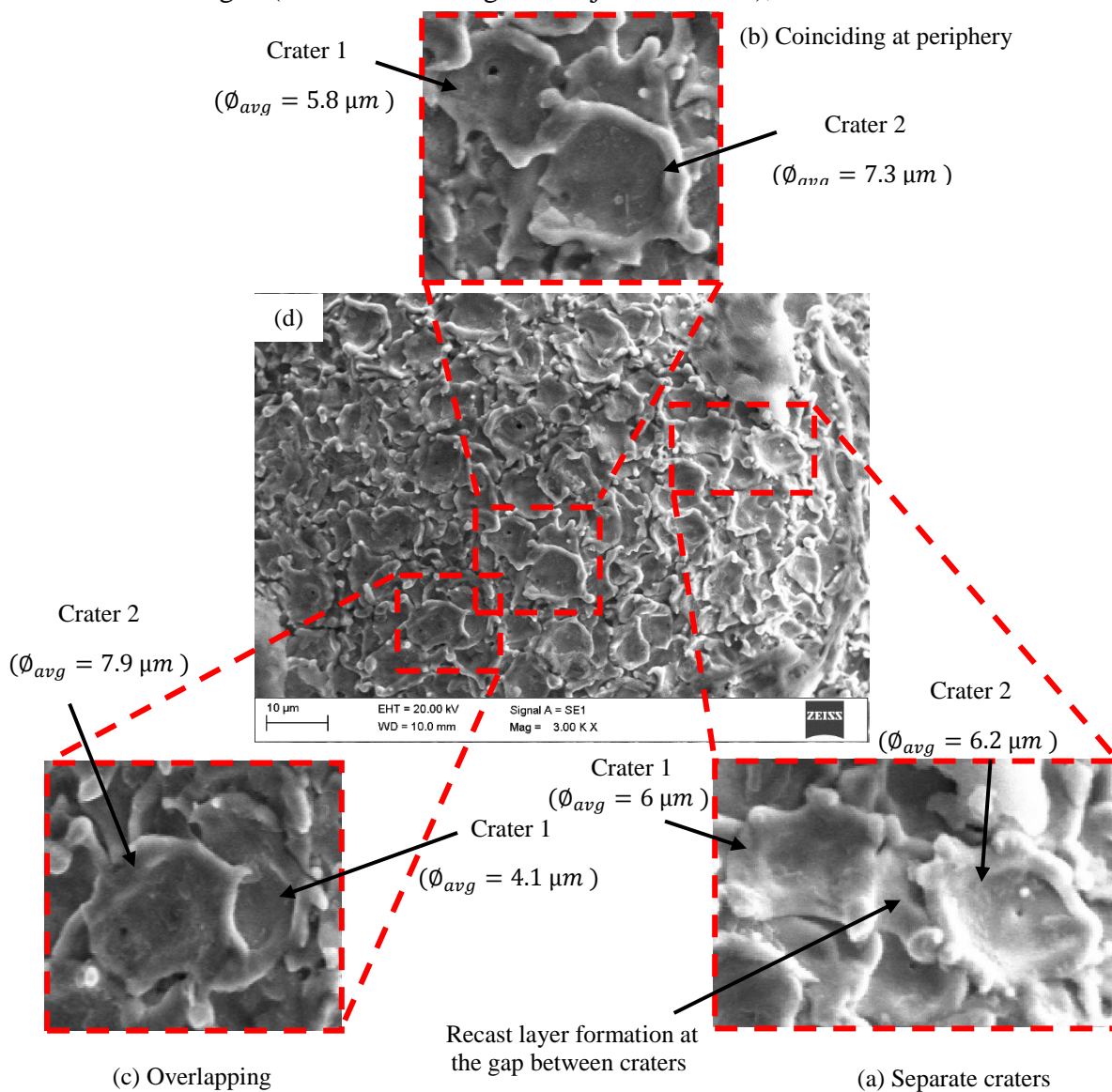


Fig. 3.15: (a) Separate craters (b) Craters coinciding (c) Overlapping of craters (d) SEM image of surface obtained from RMEDM, Pulse energy: 0.165 μJ

discharge increases as compared to 1st crater (**Fig. 3.15**). Similar results were also observed from MDS results. Simulation results obtained in the case of overlapping craters throws light on the fact that with the decrease in distance between discharges, molten material expulsion from the current discharge leads to reduction in size of the previous crater.

3.4 Dimensionless correlation between MDS and experimental results

MDS is extensively used to study mechanisms occurring at the atomic scale whereas actual experiments in RMEDM occur at the micro scale. Difference in the scale between the two makes it difficult to validate the simulation results with the results obtained from experiments. Therefore, the only possible way is to form a dimensionless correlation between the two and then predict the experimental results based on simulation. In this study, a dimensionless correlation between MDS and experimental results is obtained which is described in the following sub-sections.

3.4.1. Dimensionless ratio (R_{MDS}) of specific material removal from MDS

Amount of material removed (in nm³) using MDS for each discharge energy (0.13 μJ, 0.165 μJ, 4.5 μJ, 5 μJ and 10 μJ) was evaluated based on simulation results. The range of discharge energies selected was based on the input capabilities of the machine viz. voltage and

$$V_{MR} = \frac{m}{4} \times a_{Cu}^3 + (n - m) \times \frac{4}{3} \pi r_{Cu}^3 \quad (3.6)$$

n = total number of atoms removed from workpiece

$m = 4p$,

p = number of unit cells that contains exactly m atoms

$n - m = 1, 2, 3$

a_{Cu} = edge length of unit cell = 0.361 nm

r_{Cu} = radius of copper atom = 0.128 nm

$$R_{MDS} = \frac{\text{Specific material removal at higher energy (MDS)}}{\text{Specific material removal at lower energy (MDS)}} \quad (3.7)$$

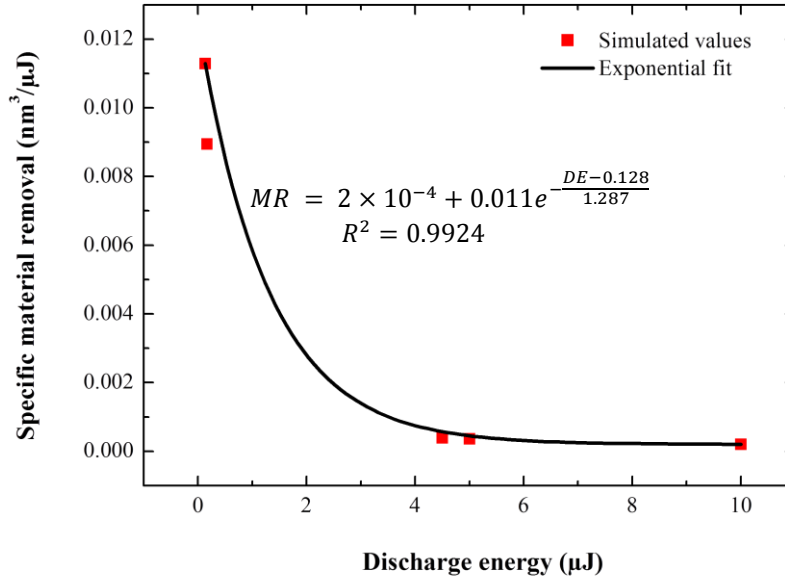


Fig. 3.16: Simulated specific material removal at different spark energies

capacitance ($DE = \frac{1}{2} CV^2$). **Eq. 3.6** was used for calculating the volume of material removed.

Fig. 3.16 shows the specific material removal i.e. material removal per unit of discharge energy

$\left(\frac{\text{Material removed (nm}^3\text{)}}{\text{Corresponding discharge energy (}\mu\text{J)}} \right)$ corresponding to each discharge energy. It was found that

the specific material removal during single discharge is an exponential function of the discharge energy with a very high correlation co-efficient. With decrease in discharge energy,

specific material removal increases. This is because with increase in discharge energy, amount

of molten/vaporised material re-depositing on the surface increases thereby reducing the total

amount of material removal and increasing the amount of recast layer. This can be verified

from **Figs. 3.2 - 3.3** (corresponding to 20 ps) wherein recast layer thickness in case of 0.165 μJ

is very less as compared to higher discharge energy i.e. 5 μJ. Based on results obtained for

specific material removal at different discharge energies, a dimensionless ratio, R_{MDS} is

determined as shown in **Eq. 3.7**. Ten different ratios were found out based on higher to lower

discharge energies namely 10 μJ/5 μJ, 10 μJ/4.5 μJ, 10 μJ/0.165 μJ and so on.

3.4.2. Dimensionless ratio (R_{expt}) of specific material removal from experiments

Single discharge experiments were carried out at five different discharge energies (0.13 μJ , 0.165 μJ , 4.5 μJ , 5 μJ and 10 μJ). This is in coherence with the discharge energies used during MDS for determining specific material removal. At each discharge energy, three experiments were conducted for repeatability. Though MDS was carried out on monocrystalline copper, for experimental study, polycrystalline copper was used. Spark radius at the highest of all energies used in this study i.e. 10 μJ was calculated [108] to be around 1 μm which is well below the single crystal range ($> 10 \mu\text{m}$) [109]. Hence, discharge is assumed to occur inside a single crystal and not across grain boundaries even though material as a whole is polycrystalline.

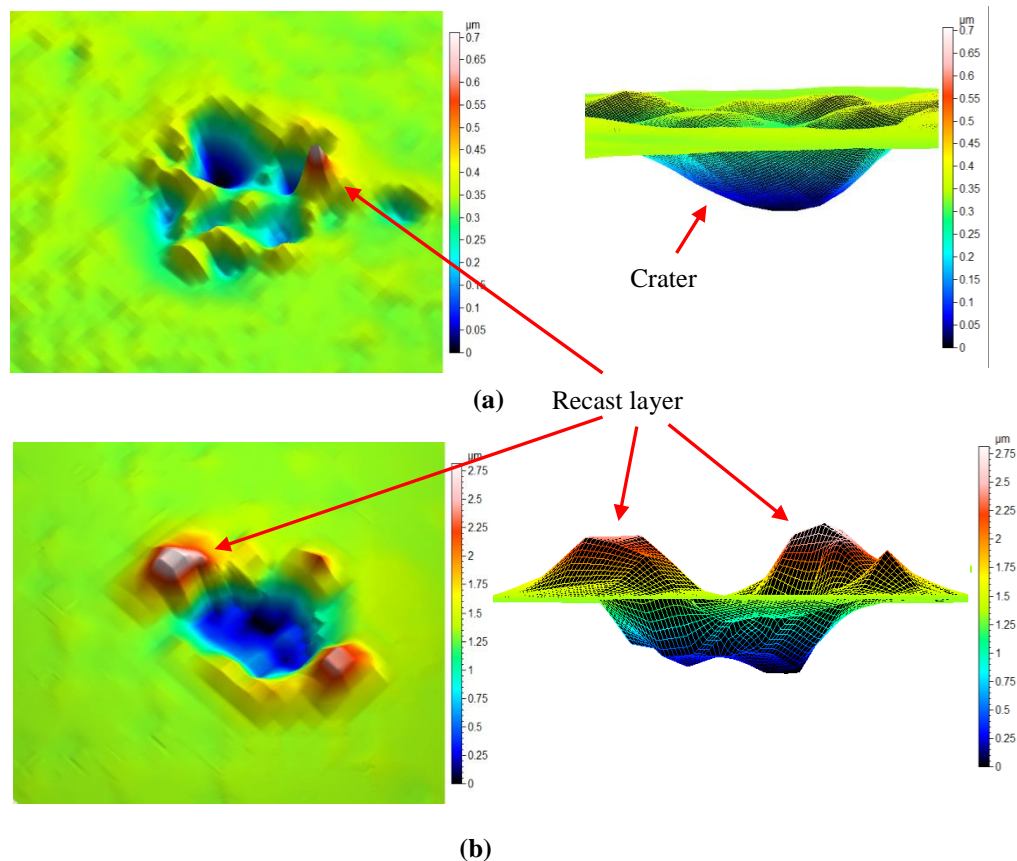


Fig. 3.17: Crater formation with spark energy (a) 0.165 μJ (b) 5 μJ

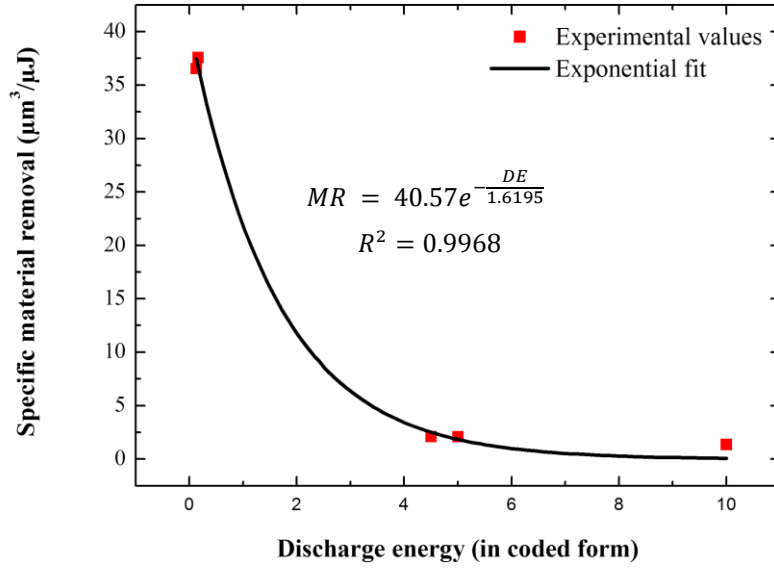


Fig. 3.18: Actual material removal at different spark energies

Amount of material removal during single discharge was measured using Taylor Hobson Make-Talysurf Coherent Correlation Interferometer (CCI). The crater dimensions viz. depth and diameter of crater were also measured using CCI.

Fig. 3.17 shows the actual crater formed after single discharge. Two cases have been shown that include discharge energies of 0.165 μJ and 5 μJ respectively. Crater diameter and recast layer formed in case of higher discharge energy are higher as compared to lower discharge energy. This observation was also obtained from MDS where crater diameter and recast layer thickness were more in case of higher discharge energy (**Figs. 3.2, 3.3 & 3.7**). Volume of material removed for each discharge energy was obtained using CCI. **Fig. 3.18** shows the specific material removal in experiments corresponding to each of the five discharge energies (0.13 μJ, 0.165 μJ, 4.5 μJ, 5 μJ and 10 μJ). Similar to MDS results (**Fig. 3.16**), an exponential relation between specific material removal $\left(\frac{\text{Material removed } (\mu\text{m}^3)}{\text{Corresponding discharge energy } (\mu\text{J})} \right)$ and discharge energy was also observed in this case with a very high correlation co-efficient. Similar to MDS results, a dimensionless ratio, R_{expt} was found out as shown in **Eq. 3.8**.

$$R_{expt} = \frac{\text{Specific material removal at higher energy (expt)}}{\text{Specific material removal at lower energy (expt)}} \quad (3.8)$$

3.4.3. Proposed dimensionless correlation (k')

Since specific material removal is found to be exponentially correlated with discharge energy in both MDS and experiments (Figs. 3.16 & 3.18) with very high correlation coefficients, a double Y-axis curve has been plotted with specific material removal found from MDS as well as from experiments (Fig. 3.19). The discharge energy along X-axis has been intentionally spaced equally as a qualitative comparison of specific material removal corresponding to each discharge energy is carried out here. Local slopes connected specific material removal obtained from each discharge energy with its neighbour. It is found that the specific material removal corresponding to MDS and experiments coincides for each discharge energy. This indicates that the simulated results are proportional to the experimental values.

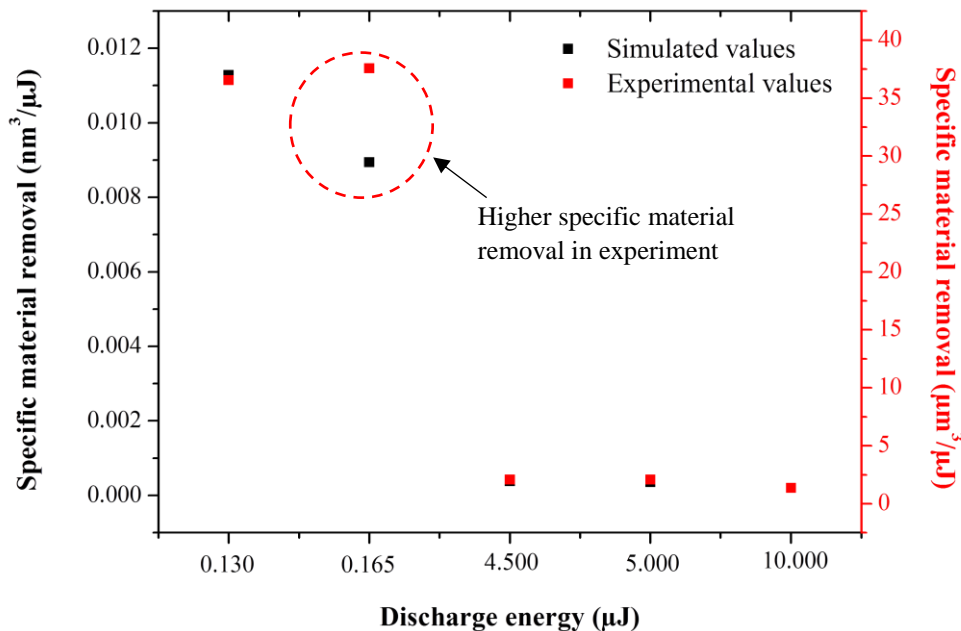


Fig. 3.19: Qualitative comparison of specific material removal between MDS and experiments (for equal spacing of different energies along X-axis)

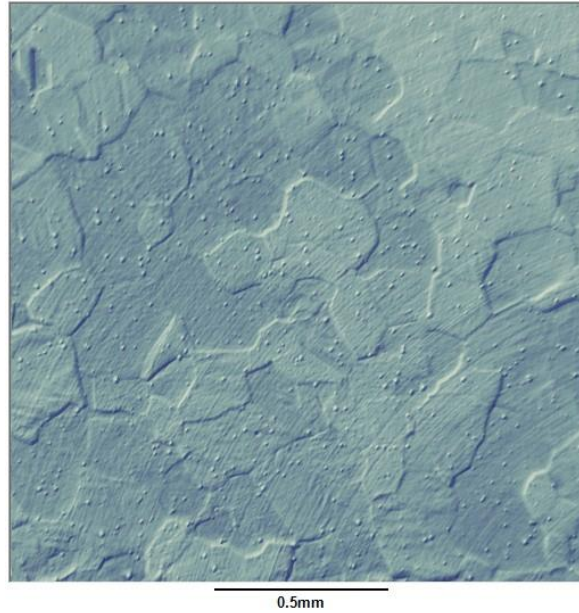


Fig. 3.20: Grain boundaries on workpiece

An exception to this is for discharge energy $0.165 \mu\text{J}$ wherein a higher specific material removal is observed in case of experiments. The higher material removal in actual experiment in this case can likely be attributed to discharge occurring at a grain boundary whereas the rest of the discharges occurred inside a grain [110,111] as verified by overlapping of specific material removal for all energies in MDS and experiments apart from discharge energy $0.165 \mu\text{J}$. This is quite possible as the size of grains are very large (**Fig. 3.20**) as compared to spark radius, hence, most of the discharges have occurred inside grains which is evident from proportional specific material removal.

Based on dimensionless ratios R_{MDS} and R_{expt} found from *Sections 3.4.1 and 3.4.2*, a linear or non-linear correlation is to be obtained. Both these ratios being dimensionless, this correlation, therefore, serves as the link between MDS and experiments. This method has been used in this study in order to determine dimensionless correlation between MDS and experiments in terms of specific material removal.

Table 3.3: Values of R_{MDS} and R_{expt} for different ratios of discharge energies

Ratio of discharge energies ($\mu\text{J}/\mu\text{J}$)	R_{MDS}	R_{expt}
0.165/0.13	0.793	1.028
4.5/0.13	0.034	0.058
5/0.13	0.032	0.057
10/0.13	0.018	0.037
4.5/0.165	0.043	0.056
5/0.165	0.040	0.056
10/0.165	0.023	0.036
5/4.5	0.940	0.995
10/4.5	0.539	0.644
10/5	0.573	0.648

Values of R_{MDS} and R_{expt} are shown in **Table 3.3**. A graph of R_{expt} vs R_{MDS} has been plotted in **Fig. 3.21**. Based on the values obtained for R_{expt} and R_{MDS} , a linear regression model was fitted between the two which showed a very high correlation co-efficient (0.9855) between the two. This indicates that ratio of specific material removed in experiments is linearly correlated with ratio of specific material removed in MDS as shown in **Eq. 3.9**. Two specific points (corresponding to ratio of discharge energies of 0.13 μJ – 0.165 μJ and 4.5 μJ – 5 μJ) are diverging towards the end of **Fig. 3.21**. This is due to the fact that the considered discharge energies are very close to each other at lower energy levels, hence, their ratios (R_{MDS} and R_{expt}) is very nearly equal to 1 (**Table 3.3**) and are away from the line.

$$R_{expt} = k' \times R_{MDS} \quad (3.9)$$

where, $k' = 1.1595$

Confirmation experiment was conducted by taking discharge energy (CE = 0.312 μJ) within the specified range used in this study. MDS was also conducted using CE as the input energy. k' obtained by using different combination of spark energies with CE are found to be well within 10% error.

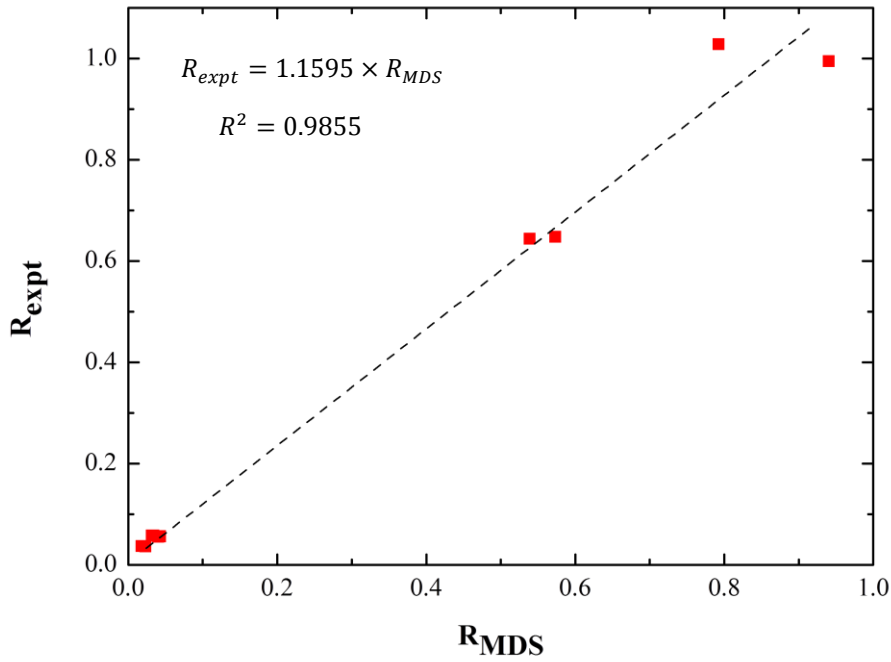


Fig. 3.21: Dimensionless correlation between MDS and experimental results

Hence, it can be concluded that specific material removal in a given range of discharge energies (in this study 0.13 μJ to 10 μJ) can be obtained without actual experimentation. A reference value of material removal at a discharge energy (e.g. 0.13 μJ) is only required. Specific material removal at this discharge energy can be easily calculated. Conducting MDS study for two spark energies i.e. reference discharge energy and discharge energy for which specific material removal is to be determined helps in determining R_{MDS} . Taking the value of R_{MDS} obtained and the reference specific material removal from experiment and using them in **Eq. 3.9** yields the value of specific material removal for the discharge energy whose material removal is to be determined. Multiplying this specific material removal with its corresponding discharge energy yields the actual material removal for discharge energy whose value is to be determined. Based on this method, material removal has been determined and used during numerical modelling and simulation of shape generation of 3-D hemispherical micro feature discussed later in *Chapter 5*. Alternatively, experimental values obtained from regression curve

in **Fig. 3.18** can also be used to determine material removal. However, in this research work the dimensionless correlation has been employed in *Chapter 5*. This proposed method can further be extended to macro/micro/nano/sub-nano scale manufacturing/finishing processes wherein phenomena occurring at the atomic scale is desired along with prediction of a single output parameter based on MDS results.

3.5 Summary

Molecular dynamics simulation (MDS) was carried out to study the material removal mechanism in RMEDM based on single discharge as well as multiple discharges. Important findings of this study are summarised below.

- Percentage of material removed by melting (~ 60%) and vaporisation (~ 40%) remains nearly constant at low spark energies (0.165 μJ and 5 μJ)
- Due to discharge, conversion of crystal structure from FCC to amorphous was observed on top of the surface of crater for both spark energies. Number of distorted atoms i.e. amorphisation in case of higher spark energy is slightly more as compared to lower energy.
- A new method is proposed based on which a dimensionless correlation between MDS and experimental results was obtained that connects the ratio between specific material removal at higher spark energy to that at lower spark energy for both MDS (R_{MDS}) and experiments (R_{expt}). This correlation minimizes the need for conducting rigorous experiments for determining the amount of material removal during single spark in RMEDM for the range of spark energies used in this study. This correlation has further been used in *Chapter 5* to determine amount of material removal during numerical modelling and simulation of shape generation of 3-D hemispherical micro feature
- Considering the case with multiple discharges, the resulting crater depth and diameter (measured at 40 ps) obtained from 2nd discharge is higher as compared to 1st discharge.

This increase in crater depth and diameter is found to increase with decrease in distance between the discharges. This increase in crater diameter with decrease in distance between the discharges were also observed on surfaces generated by RMEDM.

---x---

CHAPTER 4

SEGREGATION OF DISCHARGES USING FEA SIMULATION AND EXPERIMENTAL CORRELATION

4.1. Introduction

Presence of debris during machining in RMEDM process leads to abnormal discharges which affects the machining process. In order to have a thorough understanding of the effect of debris during machining, segregation of discharges based on debris is extremely important. This chapter discusses the segregation of debris during machining in RMEDM based on FEA simulation and experimental results. Also, the cause of occurrences of unusual discharges with high discharging points during machining is explained based on numerical model.

4.2. Segregation of discharges in RMEDM (numerical model and simulation)

With increase in machining time during RMEDM process, the presence of debris alters the discharge profiles. The discharge profiles at the beginning of machining when the dielectric is relatively free from debris are different than that towards the end of machining when the dielectric is filled with debris that cannot escape the machining zone. The discharge profiles are more crucial towards the end of machining as they are responsible for obtaining the desired form accuracy, surface finish and integrity of surface. **Fig. 4.1** shows the different types of discharges that occur during machining in RMEDM. The segregation of discharges and details governing their occurrences are discussed in detail below.

4.2.1 Primary, secondary and higher order discharges

Primary discharges, are ideal discharges that occur between walls of anode and walls of cathode. These discharges mostly occur during the beginning of machining when the dielectric is relatively free from debris. These discharges are the most favoured ones during machining (**Fig. 4.2 (a)**), where constant inter-electrode gap (IEG) is maintained. Further, it forms an equivalent capacitance (C) when there is no debris in the dielectric (**Fig. 4.2 (a)**).

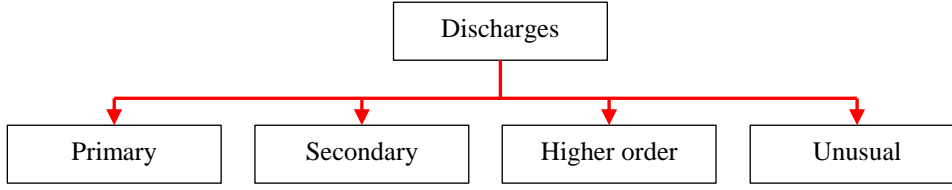


Fig. 4.1: Types of discharges in RMEDM

Secondary discharges occur when a debris particle adheres either to cathode or anode, or is located somewhere in the IEG and creates a different discharge profile (**Fig. 4.2 (b)**). During the presence of conductive debris in the dielectric as in Fig. 4.2 (b), each debris can form a capacitor with the anode/cathode. When debris is somewhere midway in the dielectric and not attached to the walls of anode/cathode, it can form two different capacitors in series. Equivalent capacitance in Eq. 4.1. can be calculated based on the arrangement of different capacitances (C_1, C_2, C_3, C_4) and so on in series or in parallel. C_1 refers to the case when a debris adhered to cathode forms a capacitor with the anode, C_2 refers to the case when a debris adhered to anode forms a capacitor with the cathode and C_3 & C_4 refers to the case when a debris midway forms two capacitors with anode and cathode. With the introduction of debris, the overall capacitance (C_{debris}) of the dielectric decreases. The presence of debris in dielectric can be considered equivalent to a single capacitor comprising of capacitors (C_1, C_2, C_3, C_4). The equivalent capacitance in this case can be written as given by **Eq. 4.1**.

$$C_{debris} = C_1 + C_2 + \frac{C_3 \times C_4}{C_3 + C_4} + \dots \quad (4.1)$$

Higher order discharges occur in situations where significantly large debris agglomerates float in the discharge channel and change the characteristics of the discharge significantly. This type of discharge is very complex in nature and occurs when debris particles adhere to both the electrodes. No interaction between walls of electrodes takes place during such type of discharge. **Fig. 4.2 (c)** shows the case when a single debris particle adheres to both the electrodes. However, during actual machining, more debris particles agglomerate and

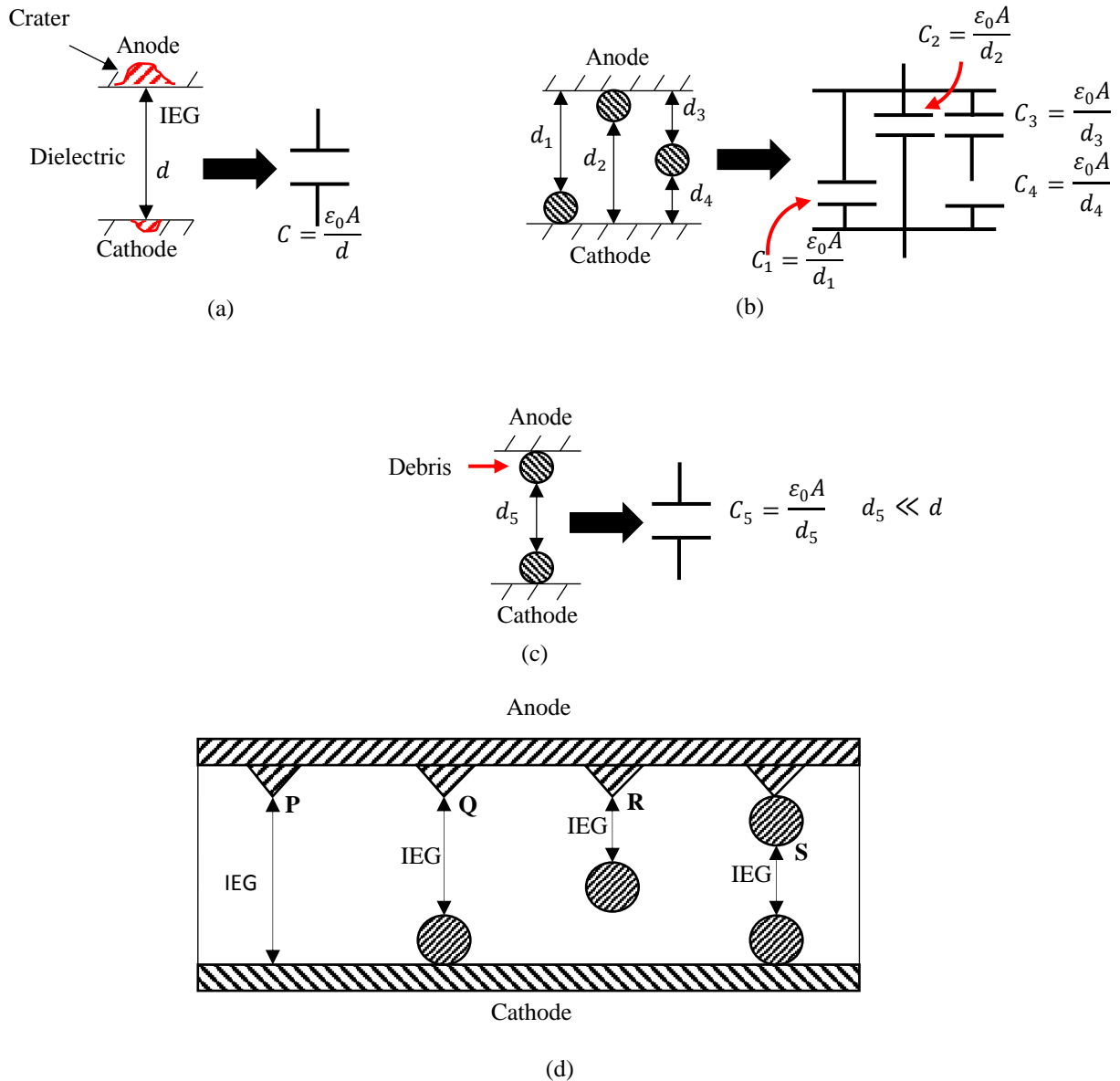


Fig. 4.2: Equivalent capacitance in case of (a) no debris (b) single debris adhered to either cathode or anode or in the discharge channel (c) debris adhering to both electrodes (d) multiple peaks with debris in dielectric

adhere to both the electrodes. The equivalent capacitance in this case is similar to the one shown in **Fig. 4.2 (a)**, however, IEG in this case is reduced drastically due to the presence of debris. Short circuit occurs when these agglomerates or debris from both electrodes join to form a chain of debris.

During machining, often, all the three cases occur simultaneously, however, the number of the occurrences change depending on the machining time. All the cases described above are collectively represented in **Fig. 4.2 (d)**.

4.2.1.1 Numerical model to study segregation of discharges

A numerical model was developed to identify various discharges that occur as a result of presence or absence of debris in the dielectric. Four different cases were considered as shown in **Fig. 4.2 (d)**. A discharge would occur whenever the electric field intensity (E) at any of the points (**P**, **Q**, **R** and **S**) cross the threshold value of dielectric (E_{th}); the dielectric behaves as a conducting path. The breakdown voltage, hence, refers to the voltage at which $E \geq E_{th}$. **P** represents occurrence of primary discharge, **Q**, **R** represents occurrences of secondary discharges and **S** represents occurrence of higher order discharges. The governing equations of the model are described by **Eqs. (4.2 – 4.4)**. **Eqs. 4.2 and 4.3** describe the equations for charging and discharging of a generalized RC circuit. Since micro EDM is based on RC circuit, the equations for charging and discharging used are the same that is used for a generalised RC circuit. The electric field (E) is calculated based on the change of the voltage (**Eq. 4.4**).

$$V = OCV \times \left(1 - e^{-\frac{t_{off}}{R \times C}}\right) \quad (\text{during charging}) \quad (4.2)$$

$$V = OCV \times e^{-\frac{t_{on}}{R \times C}} \quad (\text{during discharging}) \quad (4.3)$$

$$E = -\nabla V \quad (4.4)$$

Table 4.1: Parameters for simulation

Solver Configuration		Parameters	
Solver type	MUMPS	Resistance, R :	1000 Ω
Non-linear method	Constant (Newton)	Capacitance, C :	1000 pF
Simulation type model	Time dependent	Pulse on time, t_{on} :	50 ns
Geometry type	2-D	Pulse off time, t_{off} :	200 ns
Shape function	Lagrange (Linear)	Threshold electric field, E_{th} :	1.0 MV/cm
Type of mesh	Triangular	Density of debris, ρ :	8940 kg/m³
		Density of dielectric, ρ_f :	820 kg/m³
		Diameter of debris, d_p :	0.01 μm

Simulation parameters are shown in **Table 4.1**. COMSOL Multiphysics® was used for simulating the segregation of discharges based on electric field intensity. Values of averaged pulse on and off times were taken from experiments.

4.2.1.2 Simulation results for primary, secondary and higher order discharges

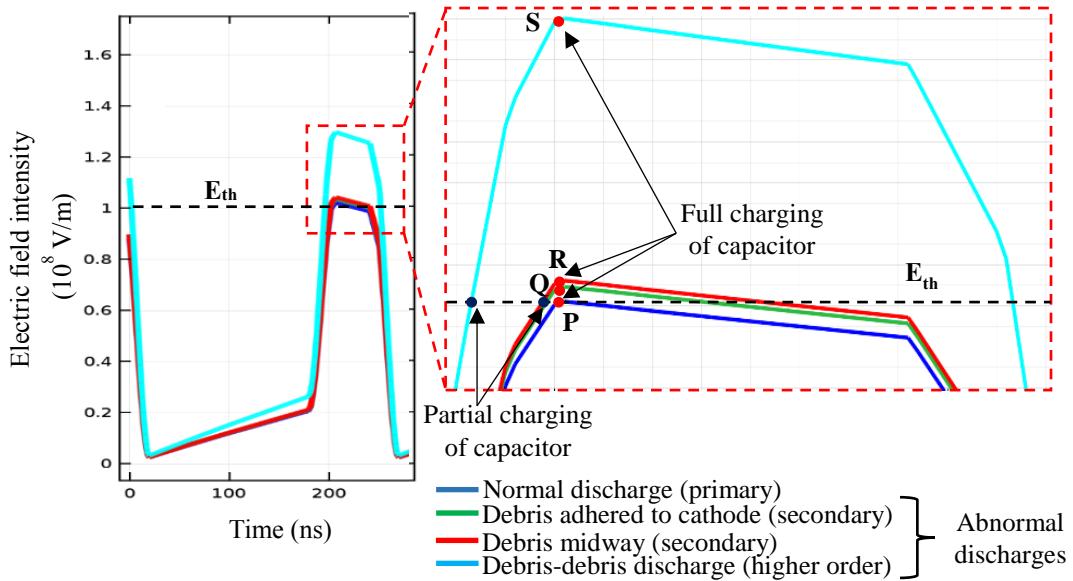


Fig. 4.3: Electric field intensity due to normal and abnormal discharges

The effect of electric field intensity at points **P**, **Q**, **R** and **S** on the anode (**Fig. 4.2 (d)**) were found out due to the absence (**P**) or presence (**Q**, **R** & **S**) of debris in dielectric. The electric field intensity calculated for each point from the simulation is shown in **Fig. 4.3**. A full discharge in all the cases is shown. A horizontal line here depicts the breakdown strength (E_{th}) of dielectric [112]. Whenever, the electric field value (E) reaches the threshold limit (E_{th}), the discharge occurs. It can be observed that in the case of fresh dielectric i.e. in the absence of debris (**P**), the capacitor is fully charged till the point it reaches the breakdown strength of dielectric. Hence, a full discharge takes place in the case of primary discharge. A full discharge implies that the discharge starts from rated open circuit voltage (OCV) and discharges till it reaches 0 V (**Fig. 4.4**). This type of discharge occurs mostly at the beginning of machining when the dielectric is free from debris. In case of secondary (**Q**, **R**) and higher order discharges

(S), breakdown strength of dielectric (E_{th}) is achieved well before the full charging of capacitor and hence partial discharging in these three cases takes place. Due to the partial discharge of capacitor in cases Q, R and S, the discharge occurring from OCV will cease at voltages well above 0 V (Fig. 4.4), depending on the amount of charge stored in the capacitor. It is observed from Fig. 4.3 that in the case of higher order discharge (S) i.e. discharges with high debris agglomerates, the amount of charge storage in the capacitor is the least before it reaches E_{th} . Therefore, the discharge will take place from OCV to such a point that the potential difference between OCV and the point at which discharge ends is the least among all the cases.

4.2.2 Discharges with unusually high discharging points

Apart from occurrences of primary, secondary and higher order discharges during machining in RMEDM, preliminary experiments also showed the occurrences of certain unusual discharges with very high discharging points (~130-170% of OCV). A typical schematic of unusual discharge is shown in Fig. 4.4. These type of discharges were also recorded by Thakur [83] during machining in wire EDM (~150-200% of OCV). To understand the physical phenomenon behind occurrence of these discharges, two different simulations were carried out incorporating the dissociation of dielectric into constituent ions and electrons during breakdown and subsequently analysing the voltage signals.

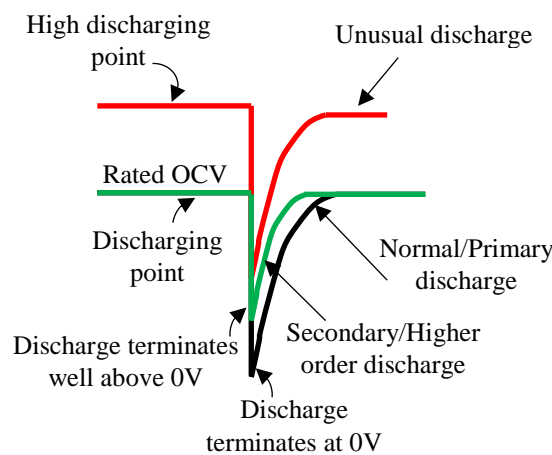


Fig. 4.4: Typical schematic of a discharge

During breakdown of dielectric, electrons from cathode are released and they travel towards anode with a very high velocity. These electrons collide with neutral molecules of dielectric and dissociation of neutral molecules into ions and electrons takes place (**Fig. 4.5**) [113]. A chain reaction thereby is initiated in which a large number of dissociation of neutral molecules take place inside the discharge channel. During the absence of debris in the dielectric, the discharge channel is mostly composed of ions, electrons and neutral molecules during discharge.

4.2.2.1 Presence of both ions and electrons in discharge channel

Primary discharges occur when the capacitor is charged upto the OCV, breakdown of dielectric starts at that instant and lasts till the instantaneous voltage reaches 0 V. The change in instantaneous voltage during a normal discharge is given by **Eqs. (4.2 – 4.3)**; the input values being taken from experiments and mentioned in **Table 4.2**.

During breakdown of dielectric, neutral molecules start dissociating into constituent ions and electrons. With each dissociation, certain amount of ions and equal amount of electrons are added to the discharge channel [114]. This leads to an increase in overall charge of the discharge channel, however total charge remains neutral since equal number of ions and

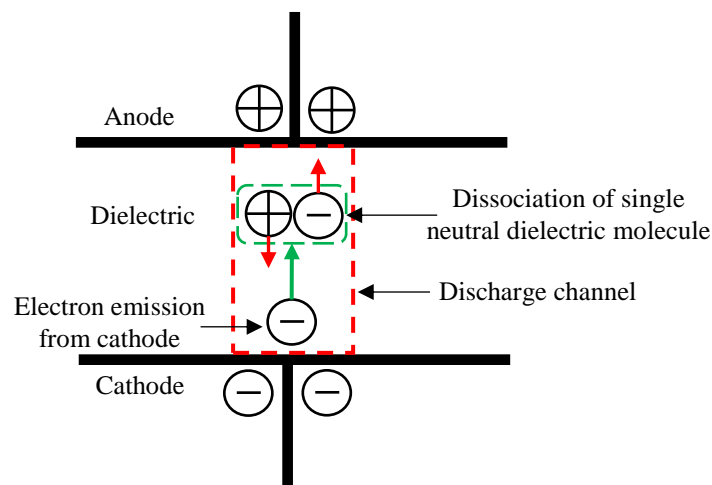


Fig. 4.5: Dissociation of neutral molecule of dielectric in discharge channel

electrons are added for each dissociation. The increase in charge density (ρ_V) is calculated based on the number of ions/electrons (n), charge of an ion/electron (z) and their position (**Eq. 4.5**). This increased charge density leads to change in electric field (**Eq. 4.6**) which in turn changes the voltage (**Eq. 4.4**). **Eqns. (4.4 – 4.6)** describe this change in voltage. A numerical model was developed to determine the change in voltage due to increased charge in the discharge channel. The following assumptions were used for simplifying the model.

- a) To explain the dissociation of large number of molecules occurring simultaneously inside the discharge channel, a single particle for each ion and electron was considered with high charge multiplication factor ($\sim 10^5$) on each. This factor was established after performing initial simulations for parametric optimization of occurrences of various discharges.

$$\rho_V = \sum_{j=1}^{N_t} nZe\delta(r - r_j) \quad (4.5)$$

$$\nabla \cdot \mathbf{E} = \frac{\rho_V}{\epsilon_0} \quad (4.6)$$

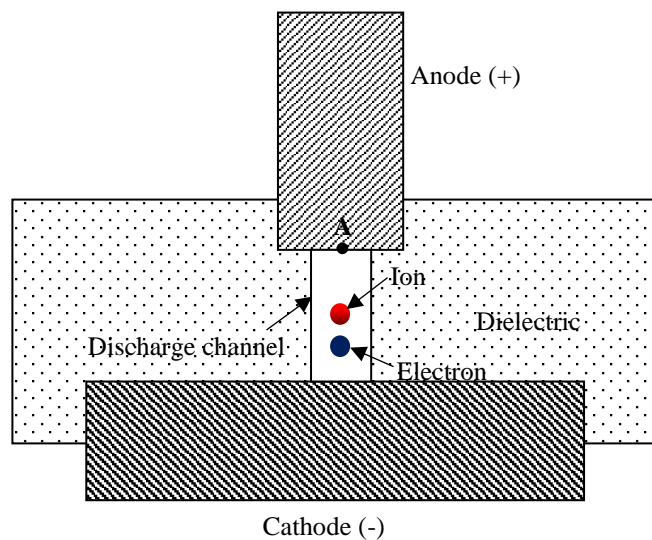


Fig. 4.6: Ion and electron in discharge channel

Table 4.2: Simulations parameters

Solver Configuration		Parameters	
Solver type	MUMPS	Resistance, R:	1000 Ω
Non-linear method	Constant (Newton)	Capacitance, C:	1000 pF
Simulation type model	Time dependent	Pulse on time, t_{on}:	50 ns
Geometry type	2-D	Pulse off time, t_{off}:	200 ns
Shape function	Lagrange (Linear)	Open circuit voltage, V:	125 V
Type of mesh	Triangular		

- b) A random velocity function was assigned to both the particles since the motion of ions and electrons is difficult to estimate due to multiple collisions inside the discharge channel.

The geometry of the model is shown in **Fig. 4.6**. **Table 4.2** provides the parameters used for simulation. The change in voltage at point **A** due to addition of charges is to be found out based on **Eqns. (4.2 – 4.6)**. Boundary condition on discharge channel walls was given in such a way that every time the particles collide with the walls, rebounding of particles from walls took place. Pulse on and off times recorded during machining were used as input to the model. Simulation was carried out with the help of COMSOL Multiphysics®.

4.2.2.2 Presence of ions in discharge channel

A fraction of total discharge energy ($E_T = \frac{1}{2}CV^2$) is transferred to discharge channel which is responsible for dissociation of neutral molecules (**Eq. 4.7**) as well as formation of debris and its ejection [113]. The right hand side of **Eq. 4.7** represents the total kinetic energy of ions and electrons. The total mass of ions being heavier as compared to electrons, the average velocity of ions are very less in magnitude as compared to that of electrons. Due to very high velocities of electrons as compared to ions, it can be assumed that after dissociation, by the time electrons reach the anode, ions will still be in the discharge channel. For a very short period of time (fraction of nanoseconds), the net positive charge in the discharge channel will

be higher as compared to the negative charge i.e. the number of ions are much higher as compared to the number of electrons in the discharge channel. Therefore, the discharge channel can be approximated to be free from electrons during this time period and it is considered that the discharge takes place at this time. Based on this assumption, a numerical model was developed considering the presence of ions only in the discharge channel (**Fig. 4.7**). Model assumptions, governing equations and simulation parameters are similar to **Section 4.2.2.1**.

$$p \cdot \left(\frac{1}{2} CV^2 \right) = \frac{1}{2} \cdot m_{total\ ions} \cdot (v_{avg\ ions})^2 + \frac{1}{2} \cdot m_{total\ electrons} \cdot (v_{avg\ electrons})^2 \quad (4.7)$$

where

p	Fraction of total energy going to discharge channel (= 0.74) [113]	m_{total}	Total mass of ions/ electrons (= $m \cdot n$)
C	Capacitance (= 1000 pF)	m	Mass of ion/electron
V	Open circuit voltage (= 125 V)	v_{avg}	Average velocity
n	Total number of ions/electrons (= 10^5)		

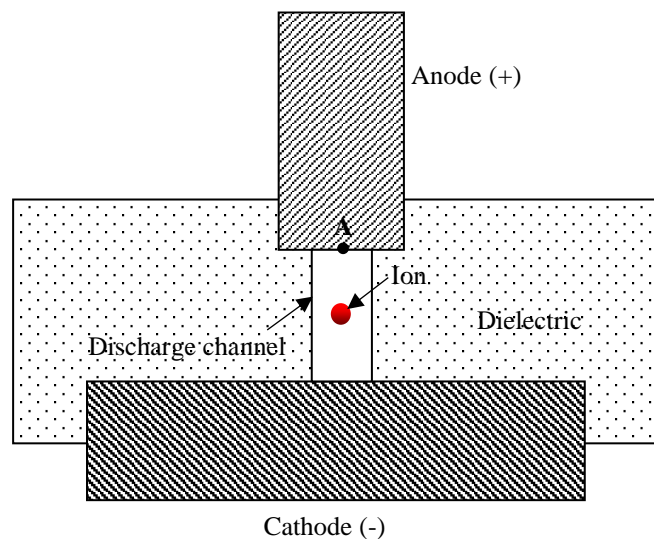


Fig. 4.7: Ion in discharge channel

4.2.2.3 Simulation results for unusual discharges

Simulations were carried out for a period of 1000 ns. The voltage profile obtained from simulation considering the presence of both ions and electrons in the discharge channel is shown in **Fig. 4.8**. The discharge obtained with high discharging point corresponds to 133% of OCV. Similar discharge profile was also observed for the case when the discharge channel consists of ions only. The results obtained are shown in **Fig. 4.9**. However, in the second case i.e. the case with presence of ions only in discharge channel, high discharging point occurred that corresponds to 170% of OCV. Though a random velocity function was assigned to the ions, this high discharging point (**Fig. 4.9**) was observed in all the cases when simulations were repeated.

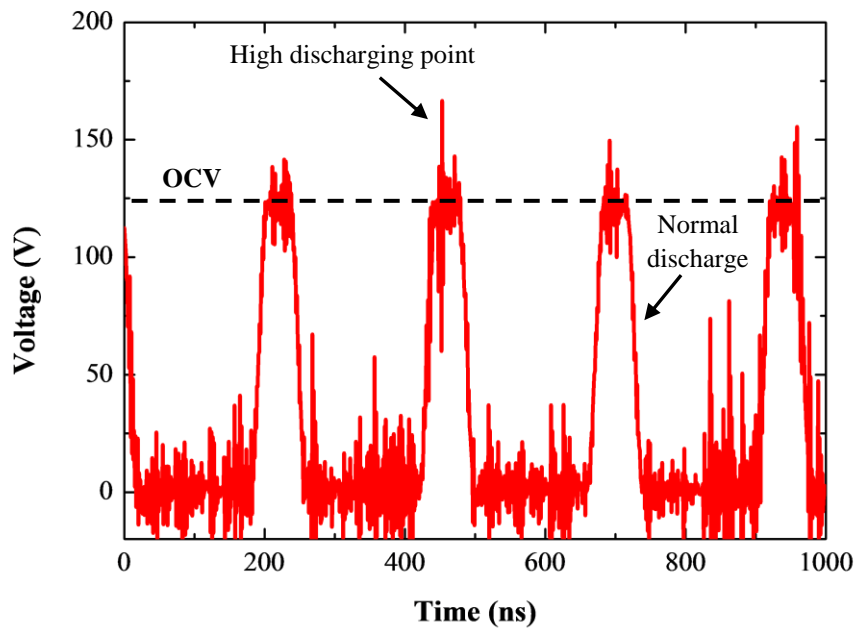


Fig. 4.8: Change in voltage at A due to presence of ions and electrons

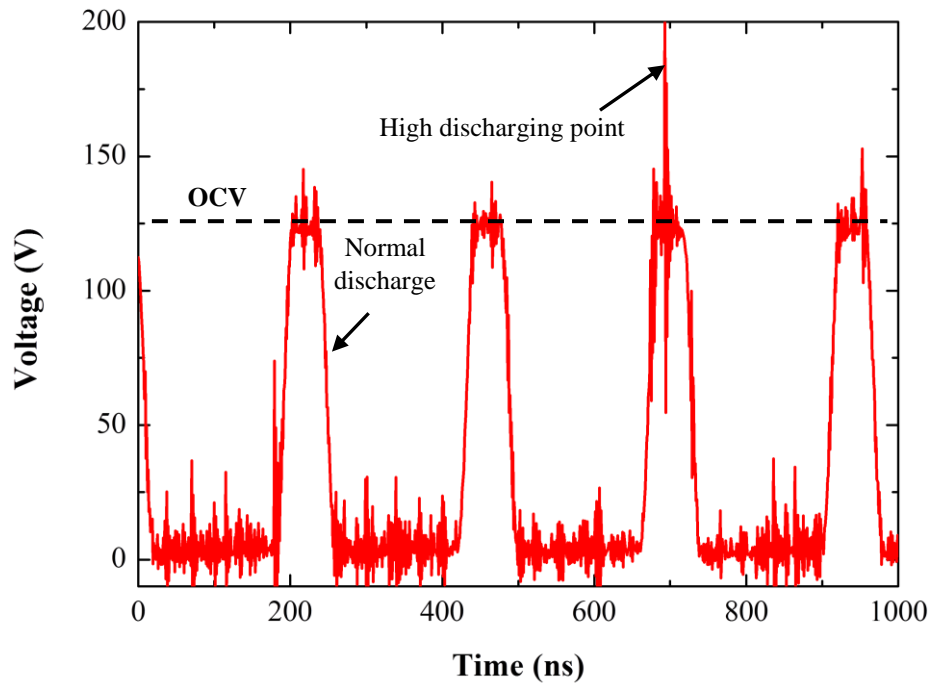


Fig. 4.9: Change in voltage at A due to presence of ions

4.3. Segregation of discharges in RMEDM (experimental)

Experiments for generating 3-D hemispherical micro features were carried out on a specially designed Make-Hybrid Precision, Model-ED-07 Micro EDM (**Fig. 4.10**). The cathode was mounted on the table and the anode was held vertically on the spindle. Each set of experiments were repeated three times.

The parameters used for experiments as well as materials for anode-cathode are shown in **Table 4.3**. The parameter levels used were established after performing initial experiments and optimising them.

Measurement of voltage signals during machining in RMEDM was carried out using Tektronix DPO 3014 oscilloscope (100 MHz, 2.5 GSPS, 5 Mega point record length, 3.5 ns). Voltage pulses were acquired at depths of 0.1-1.0 mm traverse of anode with steps of 0.1 mm. A total number of 100,000 data points were recorded for each measurement at a time interval

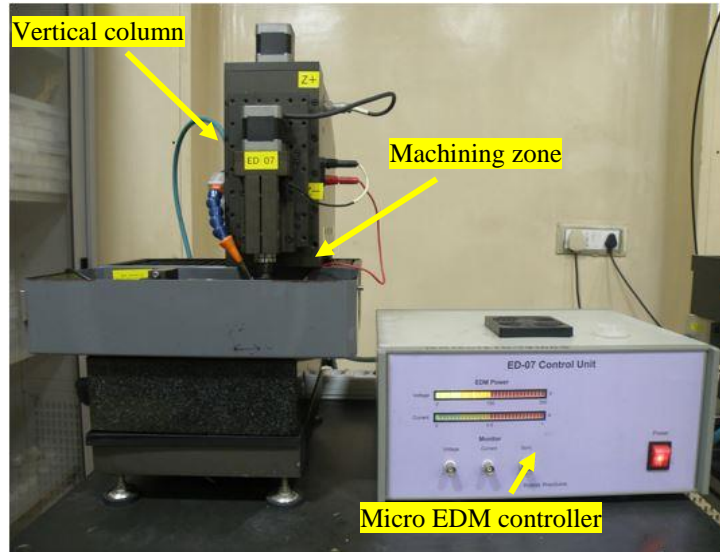


Fig. 4.10: ED-07 Micro EDM setup

of 10 ns. Based on the voltage signals captured during machining, discharges were segregated into primary, secondary, higher order (depending on the voltage at which the discharge ends) and unusual discharges (high discharging points).

Fig. 4.11 shows the voltage profiles obtained by oscilloscope at different traverse depths of anode. Unusual discharges (discharges with high discharging points, well above OCV) occur frequently during machining. Apart from unusual discharges, primary discharges (discharges occurring from OCV till 0 V) as well as abnormal discharges are also observed (discharges occurring from OCV and ends at a much higher value). **Fig. 4.12** segregates these abnormal/partial discharges into secondary (discharges discharge starting from OCV and ends at 50 V) and higher order discharges (discharge starting from OCV and ends well above 50 V).

Table 4.3: Materials and Operating Parameters

Material:				
Cathode (Plate)	Stainless Steel (grade AISI 304)			
Anode (Rod)	Copper and brass were used			
Parameters:		Values	Parameters	Values
Open circuit voltage	125 V	Capacitance	1000 pF	
Discharge pulses	RC circuit	Traverse feed rate	2 μm/sec	
Return time	100 μsec	Hold time	100 μsec	
Diameter of hole	0.2 mm			

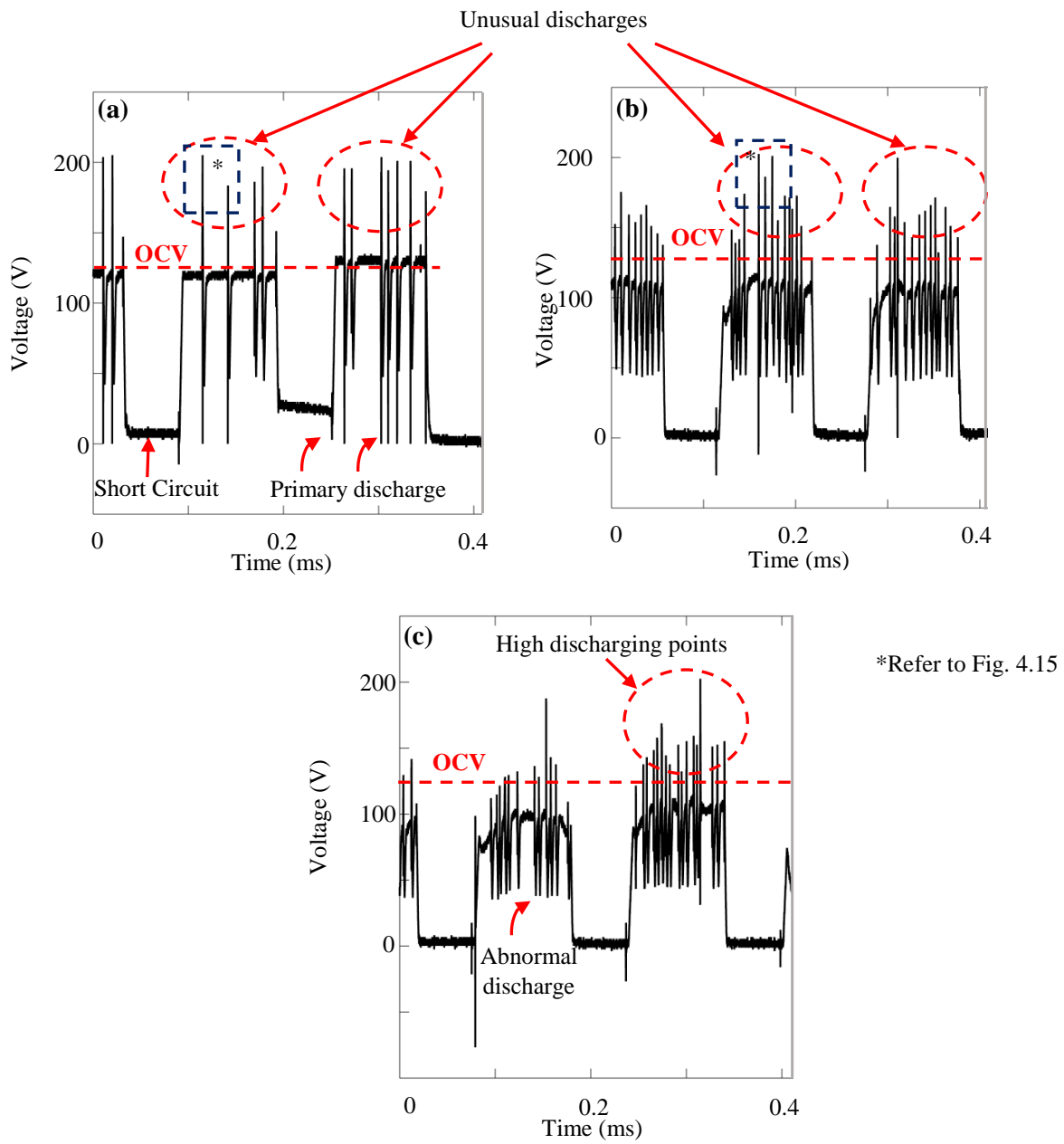


Fig. 4.11: Voltage profiles recorded at (a) 0.2 mm (b) 0.6 mm and (c) 1.0 mm traverse depth in RMEDM

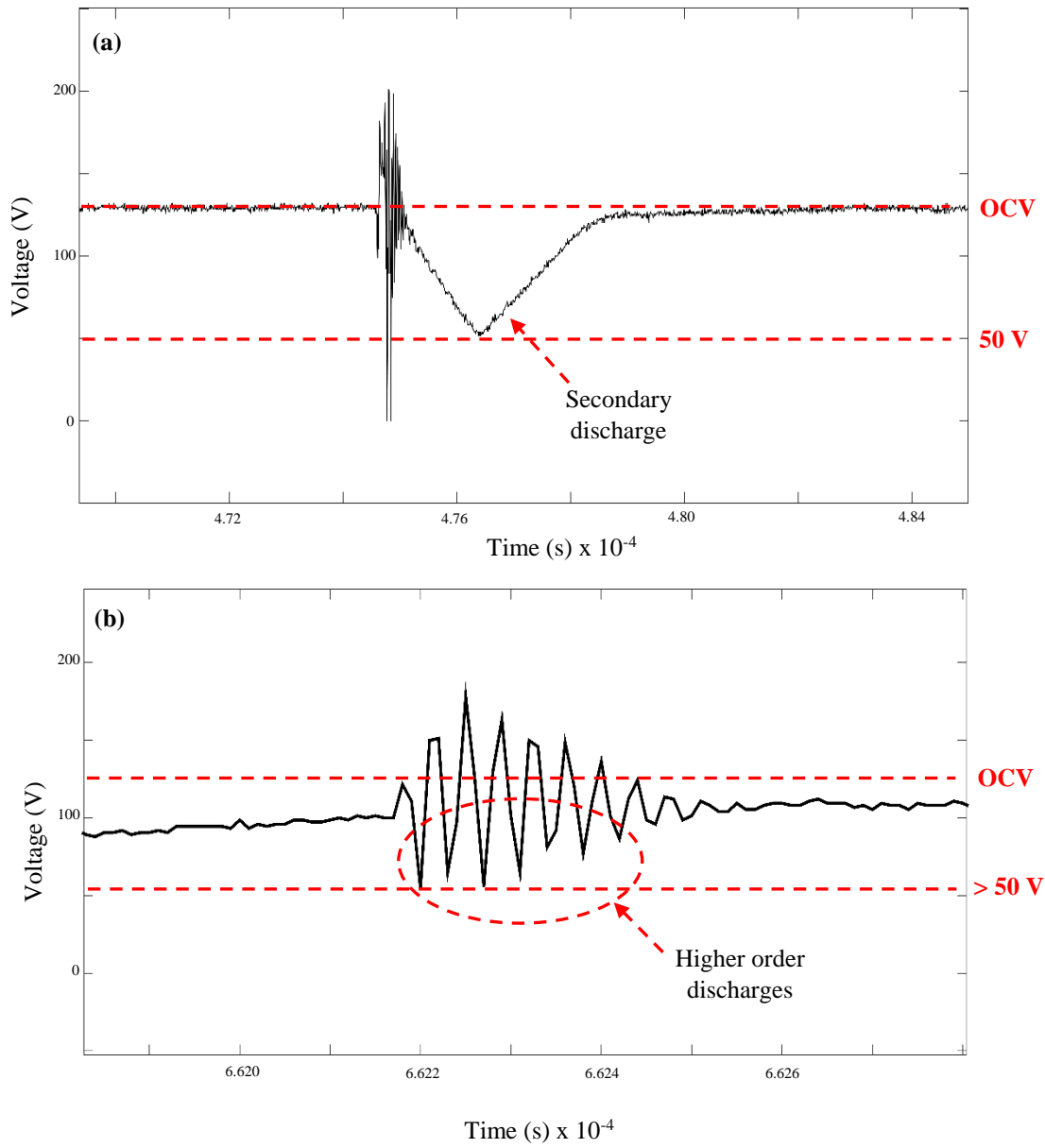


Fig. 4.12: (a) Secondary and (b) Higher order discharge obtained during machining in RMEDM

4.3.1 Number of primary, secondary and higher discharges and comparison with numerical model

A MATLAB[®] based computer program was used for determining the number of primary, secondary and higher order discharges at every step of anode traverse (Fig. 4.11). It was observed that primary discharges dominate at the beginning of machining since most of the debris produced are easily removed from the machining zone. With an increase in the machining time, the number of secondary and higher order discharges increase as compared to the primary discharges. The occurrence of higher order discharges increases with anode traverse depth. Also, at the high traverse depths > 0.4 mm, higher order discharges dominate the material removal. This could be due to larger entrapment of debris at these depths [23]. Also, frequent short circuit is observed during RMEDM as debris agglomerates to form a chain connecting both the electrodes. With more amount of debris – debris interaction leading to

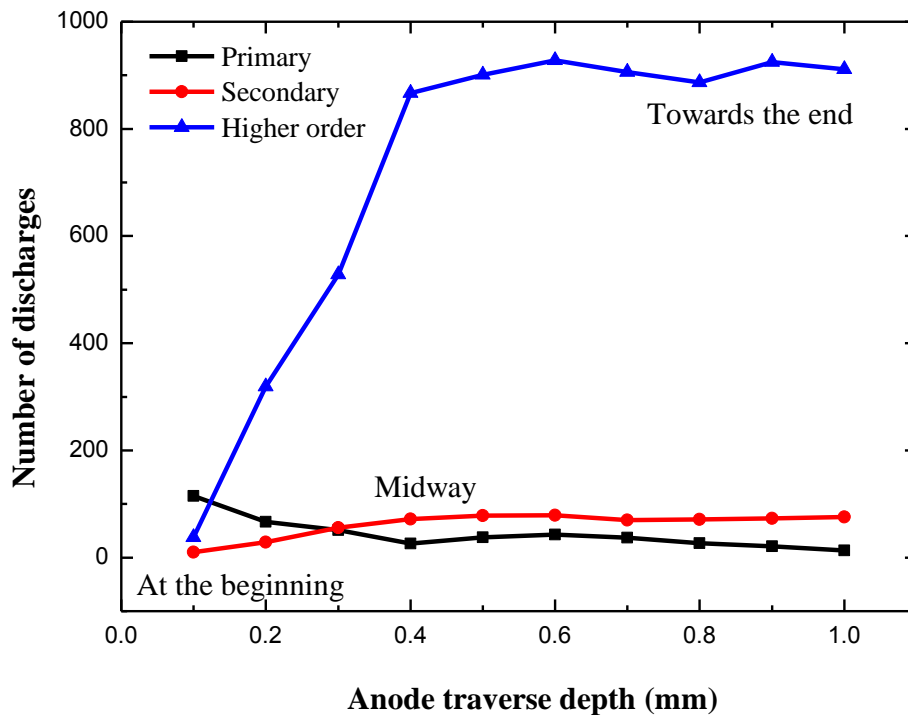


Fig. 4.13: Number of discharges during RMEDM at different traverse of anode

higher order discharges and short circuit, as the machining time increases. As a consequence, breakdown voltage reduces at increased machining depths, which in turn increases the total number of secondary and higher order discharges.

Segregation of discharges based on electrode-electrode (primary discharge), debris-electrode (secondary discharge) and debris-debris (higher order discharge) interaction was carried out using numerical modelling as well as experimental techniques (with respect to voltage). Segregation method in the case of numerical model was based on the electric field intensity (**Fig. 4.3**). Preliminary experiments were carried out and the data for OCV were recorded using oscilloscope. The number of primary/normal discharges occurring during initial machining were found out to be very high as compared to machining at later stages (also shown in **Fig. 4.11**). Primary discharges occurred from OCV to 0 V. This indicates that the capacitor was fully charged during a primary discharge. Based on preliminary experimental results, the model was constructed in line so that a primary discharge indicates full charging of the capacitor.

Simulation results showed that in case of primary discharges (in the absence of debris), capacitor is fully charged till it reaches E_{th} . Since the capacitor is fully charged, therefore, discharges can occur from rated OCV till 0 V. This discharge from rated OCV to 0V have also been experimentally observed in **Fig. 4.11** (primary discharges). This confirms that primary discharges occur in the absence of debris with full charge available on the capacitor to discharge till 0 V. With inclusion of debris in the machining zone, particularly considering the case of secondary discharges, the electric field intensity curve (**Fig. 4.3**) showed that the electric field due to debris-electrode interaction reached the threshold value i.e. E_{th} before full charging of the capacitor. This indicates that due to lack of full charge on capacitor, the discharge will be short and cannot reach 0 V. Therefore, a partial discharge is possible in the case of secondary discharge. This was also observed experimentally as discharge starting from

OCV ended at 50 V (**Fig. 4.12 (a)**) indicating a partial discharge during secondary discharge. This confirms that inclusion of debris changes the discharge behaviour from a full discharge to a partial discharge. Charge storage in capacitor in case of higher order discharges i.e. during debris-debris interaction was even lesser as compared to secondary discharge since the electric field intensity in case of debris-debris interaction reached E_{th} very early as compared to secondary discharge (**Fig. 4.3**). Hence, very low amount of charge is stored in this case which was also verified experimentally as discharge occurred from OCV till a value higher than 50 V (**Fig. 4.12 (b)**).

4.3.2 Unusual discharges during machining and its comparison with numerical model

The occurrences of unusual discharges are already shown in **Fig. 4.11**. **Fig. 4.14** compares the maximum discharging points observed from experiments (**Fig. 4.11**) and those obtained from simulation (**Figs. 4.8 – 4.9**). It can be seen that with the presence of both ions

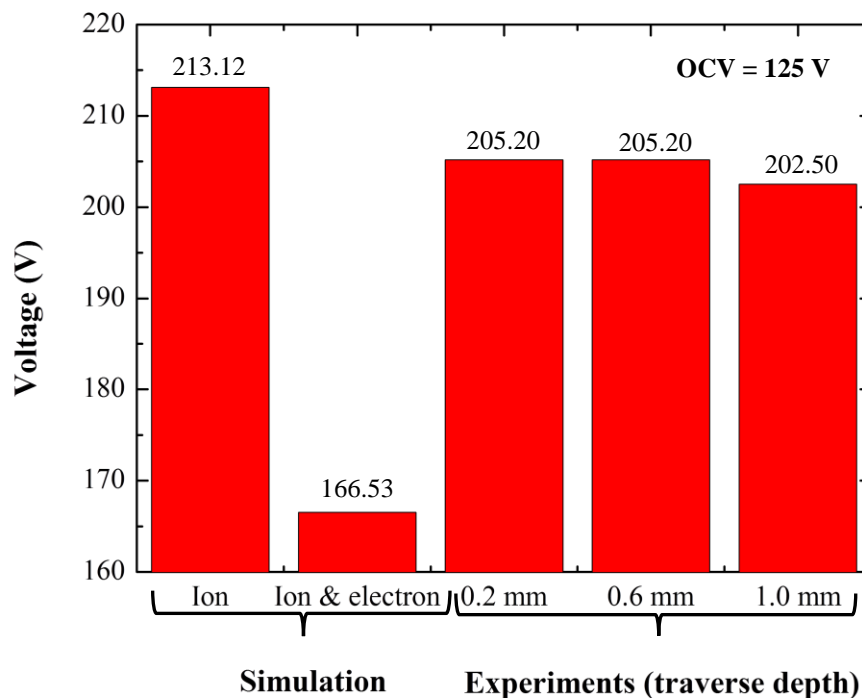


Fig. 4.14: Maximum discharging points obtained in simulation and experiments

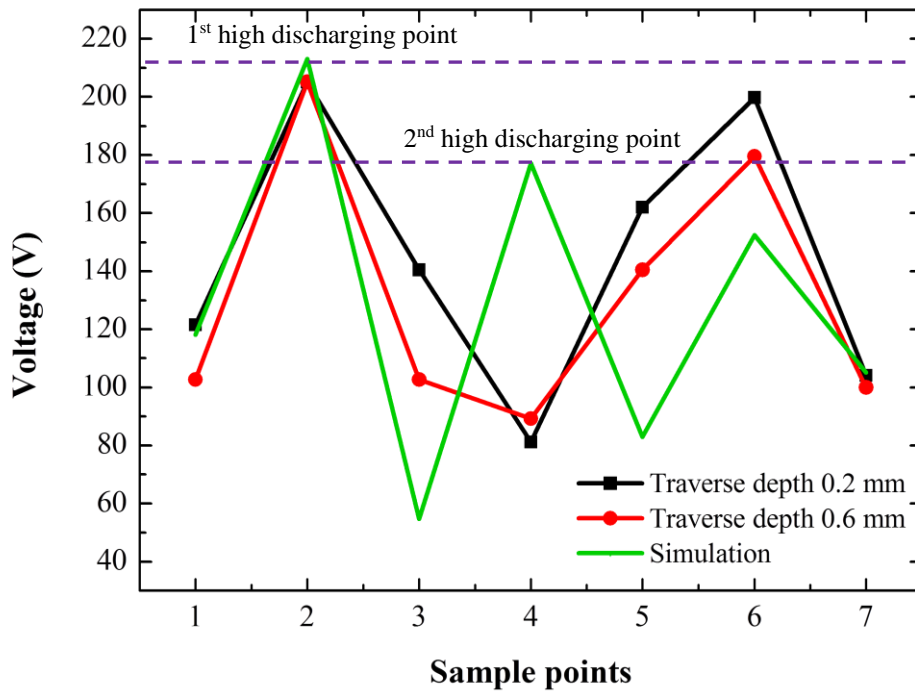


Fig. 4.15: Comparison of simulated and experimental results for voltage profiles (Magnified view of * in Fig. 4.11 (a & b))

and electrons in the discharge channel, though high discharging points occurs, however, the maximum value of high discharging point is 166.53 V (about 133% of OCV). However, considering the case of presence of ions in the discharge channel, the maximum value of high discharging point is 213.12 V (about 170% of OCV) which is very close to those observed from experiments 202.50 V - 205.20 V (162-164% of OCV). Therefore, the phenomena of increase of net positive charge in the discharge channel momentarily due to very high velocity of electrons as compared to ions is responsible for occurrences of unusual high discharging points (~170% of OCV). **Fig. 4.15** represents the comparison of voltage profiles obtained from experiments conducted at traverse depths of 0.2 mm and 0.6 mm with that obtained from simulation considering the case of presence of ions in discharge channel. The sample points refer to the data points obtained from the oscilloscope based on which high discharging points have been plotted (experiments). Corresponding points obtained from simulation have also been plotted. As observed from **Fig. 4.15**, the 1st high discharging point in all the three cases

are similar. The subsequent discharges in case of simulation is seen to start early as compared to experiments. This is due to random movement imparted to ions leading to very high electric field generation in a span of few nanoseconds and thereby discharging at a rapid rate. The voltage during 2nd high discharging point is very close to that of the discharge obtained in case of traverse depth of 0.6 mm. Hence, it confirms that unusual high discharging points (well above OCV) observed during machining in RMEDM is due to the influence of increase in the number of ions as compared to the number of electrons, thereby, creating a net positive charge in the discharge channel.

4.4. Summary

The effect of debris in changing the discharge phenomena during machining in RMEDM has been discussed in this chapter. Important findings of this chapter are summarised below.

- Depending on the magnitude of electric field intensity, discharge pulses were segregated into three stages: primary or normal discharges without any debris, secondary discharge with singular debris particles and higher order discharge with debris agglomerates. It was found that in case of abnormal discharges (secondary and higher order discharges), partial charging of capacitor takes places due to which a partial discharge occurs.
- Based on magnitude of voltage during experiments, it was found that during initial phase of machining primary discharges dominate. With increase of machining time, the number of secondary and higher order discharges increase as compared to the primary discharges. At traverse depths > 0.4 mm, higher order discharges dominate the process.
- Segregation of discharges based on magnitude of electric field intensity in the simulation and magnitude of voltage in the experiments have been correlated based on amount of charge stored in capacitor and the voltage where discharges end. A good agreement was

established between the two. Prior knowledge of this helped in determining material removal from abnormal discharges (secondary and higher order discharge) in *Chapter 5* which is otherwise very difficult to obtain from experiments.

- Two different simulations were carried out to understand the phenomena of occurrence of discharges with high discharging points. In the first simulation, dissociation of neutral molecules of dielectric into constituent ions and electrons were considered and the resulting change in voltage was simulated. The second simulation considered the case of momentary existence of ions alone in the discharge channel as electrons have comparatively higher velocity with respect to ions.
- First simulation showed that due to the presence of dissociated ions and electrons in the discharge channel leads to unusually high discharging point of around 130% of OCV. Second simulation showed that momentary increase of ions (positive charge) in the discharge channel leads to unusually high discharging point of around 170% of OCV.
- Simulated voltage profile obtained from both the simulations showed the presence of discharges viz. normal and abnormal in addition to the unusually high discharging points.
- Comparing the results obtained from simulations with those of experiments, it was observed that in the case of second simulation i.e. the case with presence of ions in the discharge channel, high discharging points of around 170% is very close to that obtained from experiments (162-164% of OCV).

---x---

CHAPTER 5

SHAPE GENERATION MECHANISM AND SURFACE ROUGHNESS ANALYSIS OF 3-D HEMISPHERICAL MICRO FEATURE

5.1 Introduction

This chapter explains the mechanism of shape generation of 3-D hemispherical micro feature based on FEA simulation and experimental validation. Subsequently surface roughness analysis based on piecewise de-trending of simulated shape is discussed and validated with the actual values. Moreover, the RMEDM process used for generating single 3-D hemispherical micro feature is extended to fabricate arrayed micro features of similar and dissimilar aspect ratios.

5.2 Numerical model and simulation of shape of 3-D hemispherical micro feature

Crookall and Moncrieff studied the concept of geometric relative duty in shape generation in EDM [115]. The method of relative duty was more inclined towards geometric modelling considering the ratio between volumetric material removal between electrode and workpiece, the current study is more inclined towards physics based modelling wherein multiple physical phenomena have been studied and cumulative effect of different forces have been analysed leading to shape generation of micro feature. The mechanism of shape generation of 3-D hemispherical convex micro feature using RMEDM process is described in this section. Few assumptions considered in the FEA simulation in order to simplify the model are as follows.

- a) Heat transfer to the surface of electrodes is dissipated only by conduction
- b) Convective and radiative heat losses are negligible
- c) Fraction of discharge energy imparted to anode and cathode is constant
- d) Dielectric fluid is homogeneous, incompressible and isotropic
- e) Debris particles are spherical in shape

5.2.1 Governing Equations

Voltage pulses in RMEDM is dependent on the charging and discharging of capacitor. **Eqs. 4.2 – 4.3** shows the voltage during charging and discharging. This gives rise to changing electric field (**Eq. 4.4**). Differential form of Gauss's law shows the correlation between instantaneous electric field strength and the charge density (**Eq. 4.6**).

Apart from considering the effect of change in electric field on debris movement, Navier-Stokes equation for momentum and continuity equation is solved simultaneously to study the flow of debris. **Eqs. (5.1 – 5.2)** incorporates the fluid flow behaviour. **Eq. 5.3** represents Fourier's heat conduction equation.

$$\rho_f \frac{d\mathbf{u}}{dt} + \rho_f (\mathbf{u} \cdot \nabla) \mathbf{u} = \nabla \cdot [-p\mathbf{I} + \mu(\nabla \mathbf{u} + (\nabla \mathbf{u})^T)] + \mathbf{F} \quad (5.1)$$

$$\rho_f \nabla \cdot (\mathbf{u}) = 0 \quad (5.2)$$

$$\rho C_p \frac{\delta T}{\delta t} - k \nabla^2 T = q_0 \quad (5.3)$$

5.2.2 Geometry of the model

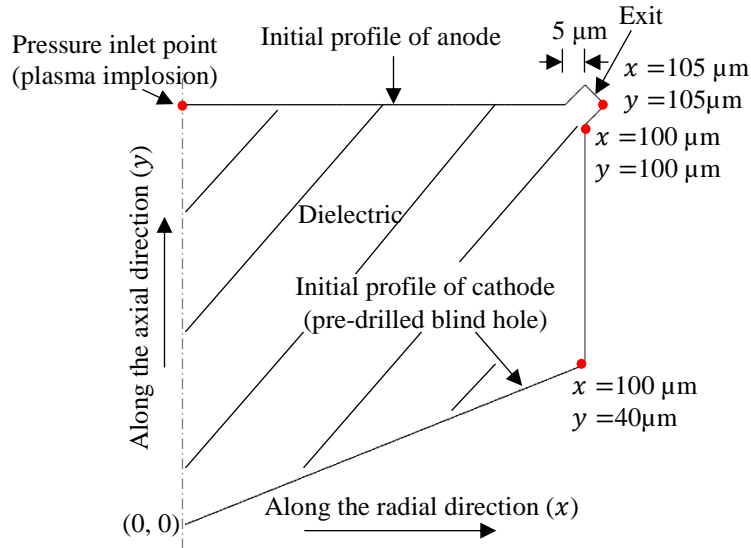


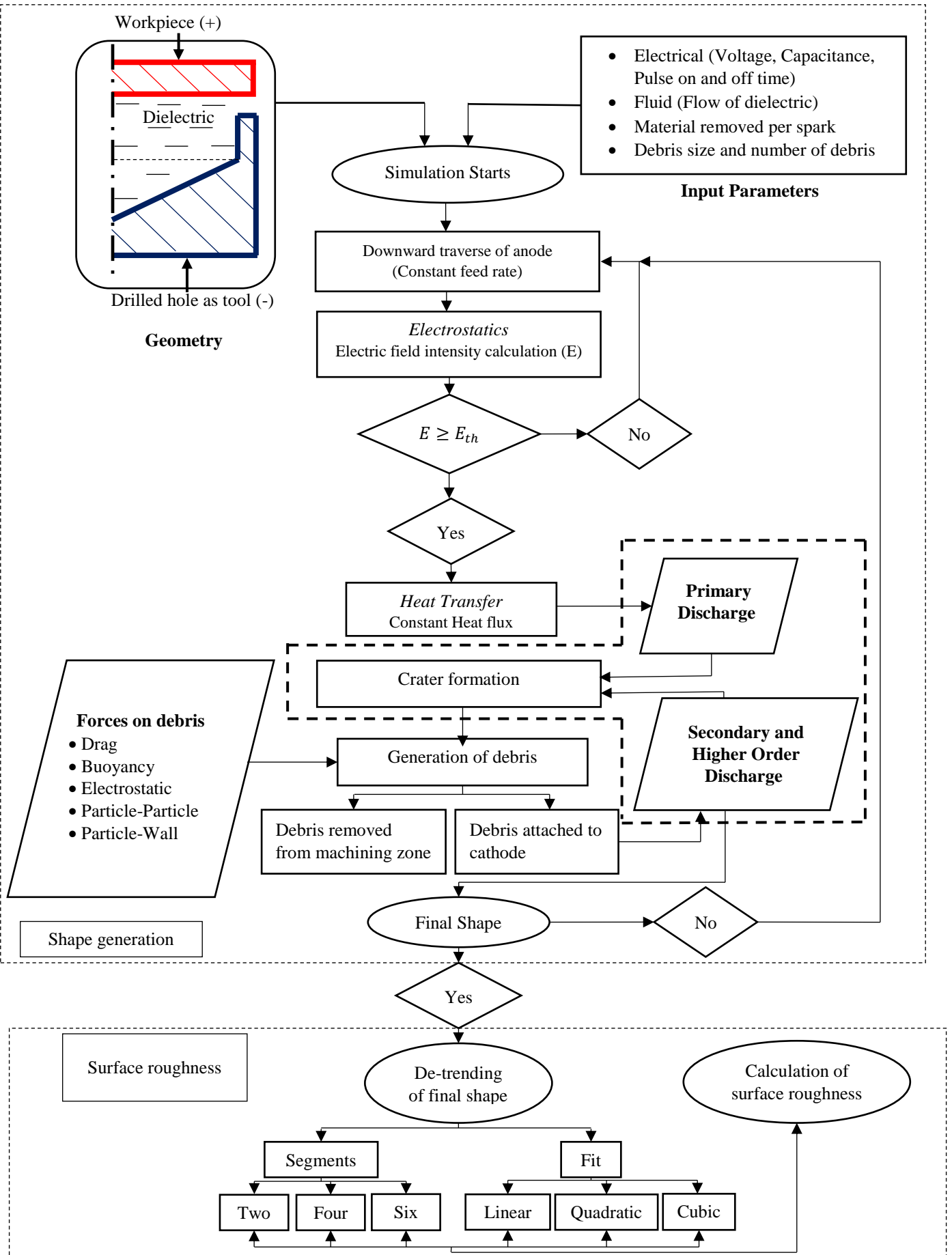
Fig. 5.1: 2-D axisymmetric geometry (obtained after $t = 0.1s$)

RMEDM process using a drilled hole is simplified by a 2-D axisymmetric geometry (**Fig. 5.1**). The top boundary is the anode (workpiece) whereas the bottom boundary is the cathode (tool). The initial side gap is maintained at 0.005 mm. The domain is filled with the

dielectric. The flowchart for simulation is shown in **Fig. 5.2**. The steps for simulation is described below:

1. Geometry has been constructed as per **Fig. 5.1** and input parameters (from experiments listed in *Section 5.4*) have been incorporated.
2. The anode is traversed with a constant feed rate.
3. Instantaneous electric field (**Eqs. 4.2 – 4.4**) is computed at every step during anode traverse.
4. At certain gap between anode and cathode (minimum IEG), instantaneous electric field E crosses the threshold value of electric field (breakdown strength of dielectric); E_{th} . A constant heat flux (**Eq. 5.3**) is applied on anode and cathode at locations wherever $E \geq E_{th}$.
5. This heat flux is responsible for creating a primary discharge (**Fig. 4.2 (a)**) that leads to material removal from both the electrodes and a crater is formed on each electrode.
6. Material removal leads to formation of debris. These debris move in the dielectric due to plasma implosion pressure at the end of discharge. Forces acting on debris are shown in **Fig. 5.2**.
7. These debris are either removed from the machining zone or attached to tool (cathode).
8. Debris adhering to cathode reduces local IEG leading to secondary and higher order discharge (**Fig. 4.2 (b-c)**).
9. Secondary and higher order discharge also leads to generation of crater similar to *Step 5*. However, material removal rate (MRR) by this is different than that by primary discharges and have been found out in this study.
10. These steps are continued until the desired shape is achieved. Once the 3-D hemispherical convex micro feature is observed, further processing for determining surface roughness of generated micro feature is carried out which will be discussed later in **Section 5.3**.

Fig. 5.2: Flowchart for simulation of shape and surface roughness of 3-D hemispherical convex micro feature



The data for input electrical parameters viz. voltage and capacitance have been taken from actual input data for experiments. As the numerical model incorporates multiphysics compilation, COMSOL Multiphysics® was used for simulating the shape of micro hemisphere generated by reverse micro-EDM. For deformation of anode, Arbitrary Lagrangian-Eulerian (ALE) method was used.

5.2.3 Boundary conditions

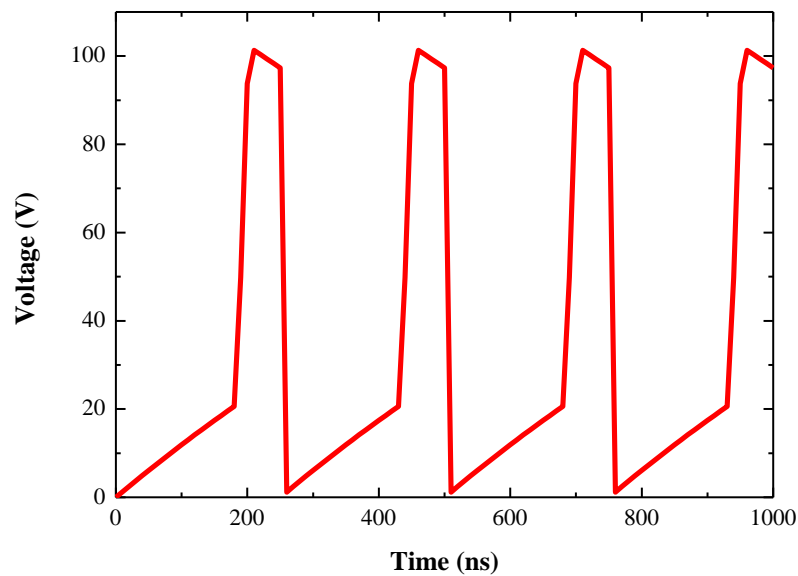


Fig. 5.3: Change in voltage with respect to time

As RMEDM process employs RC circuit, the pulse duration is determined by the charging and discharging of capacitor. The pulse on and off time were recorded using Tektronix DPO 3014 oscilloscope (100 MHz, 2.5 GSPS, 5 Mega point record length, 3.5 ns). Using the values of pulse on and off times obtained, the pulses generated due to potential difference between anode and cathode is shown in **Fig. 5.3**.

During pulse on time (t_{on}), spark occurs at the minimum IEG between anode and cathode as soon as the electric field intensity at the IEG crosses the breakdown strength of the

dielectric (E_{th}). This leads to melting and vaporization and subsequent removal of material takes place during the pulse off time (t_{off}). In case of MEDM/RMEDM, the pulse on and off time are in nanoseconds [116].

Due to the breakdown of dielectric ($E \geq E_{th}$), a plasma channel is formed that is responsible for removal of material from both the electrodes. This plasma channel can be approximated to be a disk heat source with a heat flux radius, r_{hf} (μm) [108], as shown in Eq.

5.4.

$$r_{hf} = 0.0284 \cdot t_{on}^{0.9115} \quad (5.4)$$

A constant heat flux is applied to the electrodes wherever electric field crosses the threshold value (**Eq. 5.5**) [117]. The constant, p has been taken as 0.39 for anode and 0.14 for cathode [118].

$$q_0 = p \cdot \frac{\frac{1}{2} \cdot CV^2}{\pi \cdot r_{hf}^2 \cdot t_{on}} \quad (5.5)$$

Due to this heat flux, material removal from workpiece takes place. The volume of the crater (V_c) formed per spark can be written as shown in Eq. (**5.6**). This has been calculated based on the dimensionless correlation obtained for MDS and experiments in *Section 3.4.3* (**Eq. 3.9**). The discharge energy (DE) used in this model was $7.8 \mu\text{J}$. To determine the crater volume, the already determined experimental value of specific material removal (SMR) at $0.165 \mu\text{J}$ (*Chapter 3*) and MDS results of SMR at $0.165 \mu\text{J}$ and $7.8 \mu\text{J}$ were used.

$$V_{c_{DE=7.8\mu\text{J}}} = k' \times R_{MDS} \times SMR_{expt_{0.165}} \times DE \quad (5.6)$$

Hence, material removal rate on anode by primary discharges (MRR_{PD}) per pulse can be written as (Eq. 5.7). Material removal rate on cathode has been calculated in proportion to the amount of heat transferred (Eq. 5.5) and is given by Eq. 5.8

$$MRR_{PD} = \begin{cases} \frac{V_c}{t_{on} + t_{off}}, & E \geq E_{th} \cap T \geq T_{melt} \\ 0, & E < E_{th} \end{cases} \quad (5.7)$$

$$MRR_{cathode} = \frac{0.14}{0.39} \times MRR_{PD} \quad (5.8)$$

The debris particles formed due to melting and vaporization are either carried away by the dielectric (flushing) due to plasma implosion or are attached to the walls of cathode and anode. The plasma implosion [66] acting at the pressurized inlet point (Fig. 5.1) can be written as shown in Eq. 5.9. This pressure originates from a point and spreads along the surface of anode.

$$p_{plasma} = a_1 e^{(-((t_{on}+t_{off}-b_1)/c_1)^2)} + a_2 e^{(-((t_{on}+t_{off}-b_2)/c_2)^2)} \quad (5.9)$$

where,

$$\begin{aligned} a_1 &= 4.598 \times 10^{11} & a_2 &= 8.28 \times 10^5 \\ b_1 &= -1.094 \times 10^{-6} & b_2 &= 5.928 \times 10^{-7} \\ c_1 &= 3.186 \times 10^{-7} & c_2 &= 2.115 \times 10^{-6} \end{aligned}$$

Debris particles were collected and images were taken using SEM. Average size of debris measured by using public domain image processing software (ImageJ 1.46r, NIH) was 0.5 μm . For simulation purpose, a uniform distribution of debris in the size range 0.1 μm – 1 μm have been considered. A total number of 100 debris particles were released in the domain containing dielectric after every discharge. These debris are weakly charged particles [119,120] and hence their presence in the dielectric increases the intensity of electric field at localised points on anode thereby decreasing the breakdown strength of dielectric. A two-way coupling

between the debris particles and the electric field has been considered to incorporate the reduction in breakdown strength of dielectric. The modified charge density due to increase in debris particles is shown in **Eq. 4.5**. It represents the charge density at a point, which is the sum of individual charges ($q_j = nZe$) at position r_j . This modified charge density leads to change in localised electric field distribution (**Eq. 4.6**) leading to breakdown of dielectric at spots where debris agglomeration and attachment to cathode take place.

The various forces that acts on a debris particle are shown in **Eq. 5.10** [120,121].

$$F_{total} = F_D + F_B + F_E + F_{P-P} + F_{P-W} \quad (5.10)$$

where,

$$F_D = 3\pi\mu d_p(u - u_p)$$

$$F_B = 4\pi r_p^3 \rho g$$

$$F_E = eZE$$

$$F_{P-P} = \frac{24\varepsilon}{\sigma} \sum_{j=1}^N \left[2 \left(\frac{\sigma}{|r - r_j|} \right)^{13} - \left(\frac{\sigma}{|r - r_j|} \right)^7 \right] \left(\frac{r - r_j}{|r - r_j|} \right)$$

Fig. 5.4 shows two cases in which a solid particle and a hollow particle (density ρ) are inside a fluid having density ρ_f . In **Fig. 5.4 (a)**, the volume of fluid displaced by solid (V_f) is exactly equal to the volume of the solid particle (V_{solid}). Since, the density of particle is greater than fluid, net force acting on the particle is downwards and the particle sinks. In **Fig. 5.4 (b)**, the volume of hollow particle (V_{hollow}) decreases considerably as compared to solid particle but the volume of fluid displaced remains the same. Under such conditions, buoyancy force dominates and the particle experiences a resulting upward force. Debris formed in the range of sub-microns to a few microns are hollow in nature [122,123]. Hence, buoyancy force on the debris can be considered and weight of debris can be ignored. Particle-wall interaction force has been simplified by considering an assumption that debris adheres to walls of cathode with

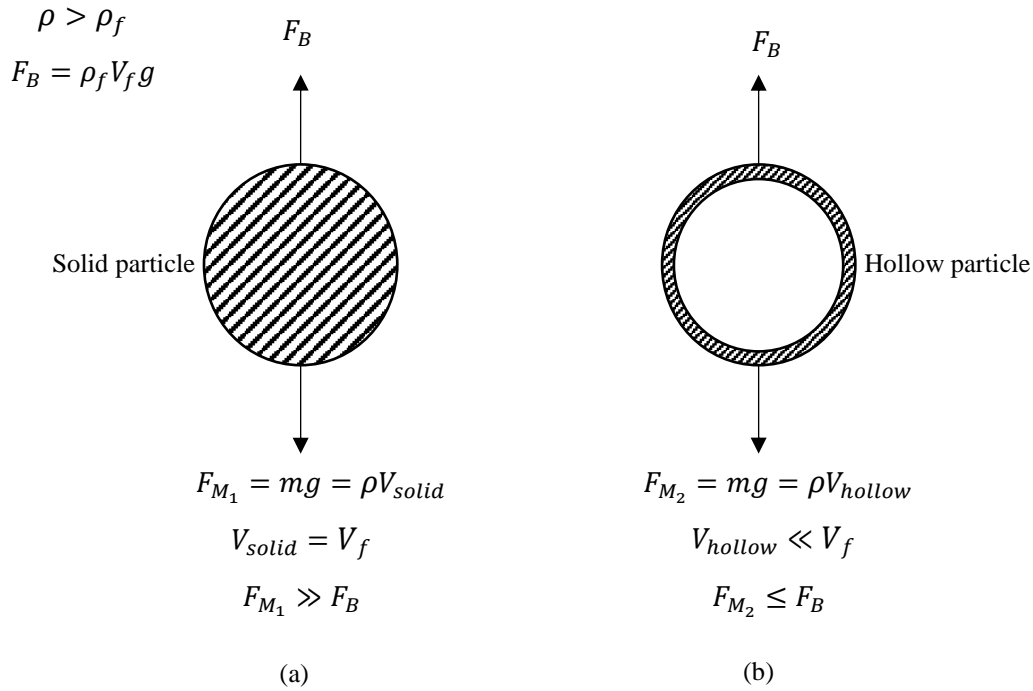


Fig. 5.4: Effect of buoyancy on debris

a probability of 0.5. Debris particles adhering to anode has been ignored. The parameters used for simulation are presented in **Table 5.1**.

5.2.4 Role of debris in shape generation

Simulations were performed for prediction of shape generation of 3-D hemispherical convex micro feature using non-conformal RMEDM. Ideally, the anode shape should be a

Table 5.1: Parameters for simulation

<i>Solver type</i>	MUMPS	ρ :	8940 kg/m³	R :	1000 Ω
<i>Non-linear method</i>	Constant (Newton)	ρ_f :	820 kg/m³	C :	1000 pF
<i>Simulation type model</i>	Time dependent	d_p :	0.5 μm	t_{on} :	50 ns
<i>Geometry type</i>	2-D axisymmetric	μ :	0.00164 Pa.s	t_{off} :	200 ns
<i>Shape function</i>	Lagrange (Linear)	Z :	10^{-6}	E_{th} :	1.0 MV/cm [112]
<i>Type of mesh</i>	Quadrilateral	σ :	3.3×10^{-10} m	n :	10^6
		ε :	1.6×10^{-21} J	C_p :	377 J/kg K
		k :	385 W/m K	T_{melt} :	1085 K

negative replica of the cathode. However, due to complex nature of abnormal random discharges occurring in RMEDM process that includes secondary and higher order discharges by debris in addition to primary discharges, the shape deviates from the ideal behaviour and is not conformal. Since, it is difficult to measure the amount of material removed by secondary and higher order discharges experimentally, a relation between material removal by secondary and higher order discharges (MRR_{SHD}) and material removal by primary discharges (MRR_{PD}) has been assumed to be of linear order as shown in **Eq. 5.11**. For different values of ' k_0 ' (averaged for entire machining depth), the shape generated numerically is presented in **Fig. 5.5**.

$$k_0 = \frac{\text{Material removal by secondary and higher order discharges } (MRR_{SHD})}{\text{Material removal by primary discharges } (MRR_{PD})}$$

$$MRR_{SHD} = k_0 \cdot MRR_{PD} \quad (5.11)$$

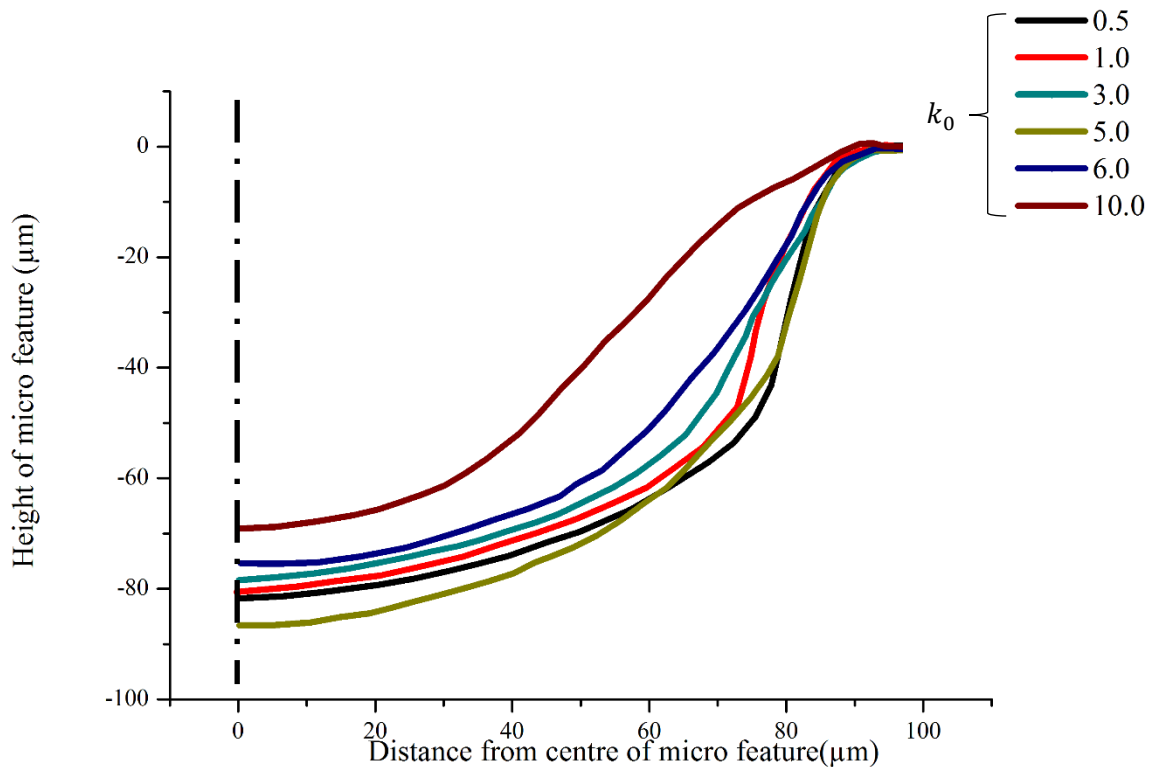


Fig. 5.5: Value of ' k_0 ' obtained through simulations

Least square fitting of the data of simulated hemispherical shape obtained from **Fig. 5.5** show minimum error when $k_0 = 5$. Anything below or above this value for k_0 , the error is high and the curve deviates from the desired hemispherical shape. Hence, the value of k_0 has been taken as 5.

Shape of micro feature generated by simulation at different traverse depth of anode is shown in **Fig. 5.6**. The eroded shape of cathode has not been studied in detail. Machining of 3-D hemispherical convex micro feature has been studied taking into account four different stages of machining namely:

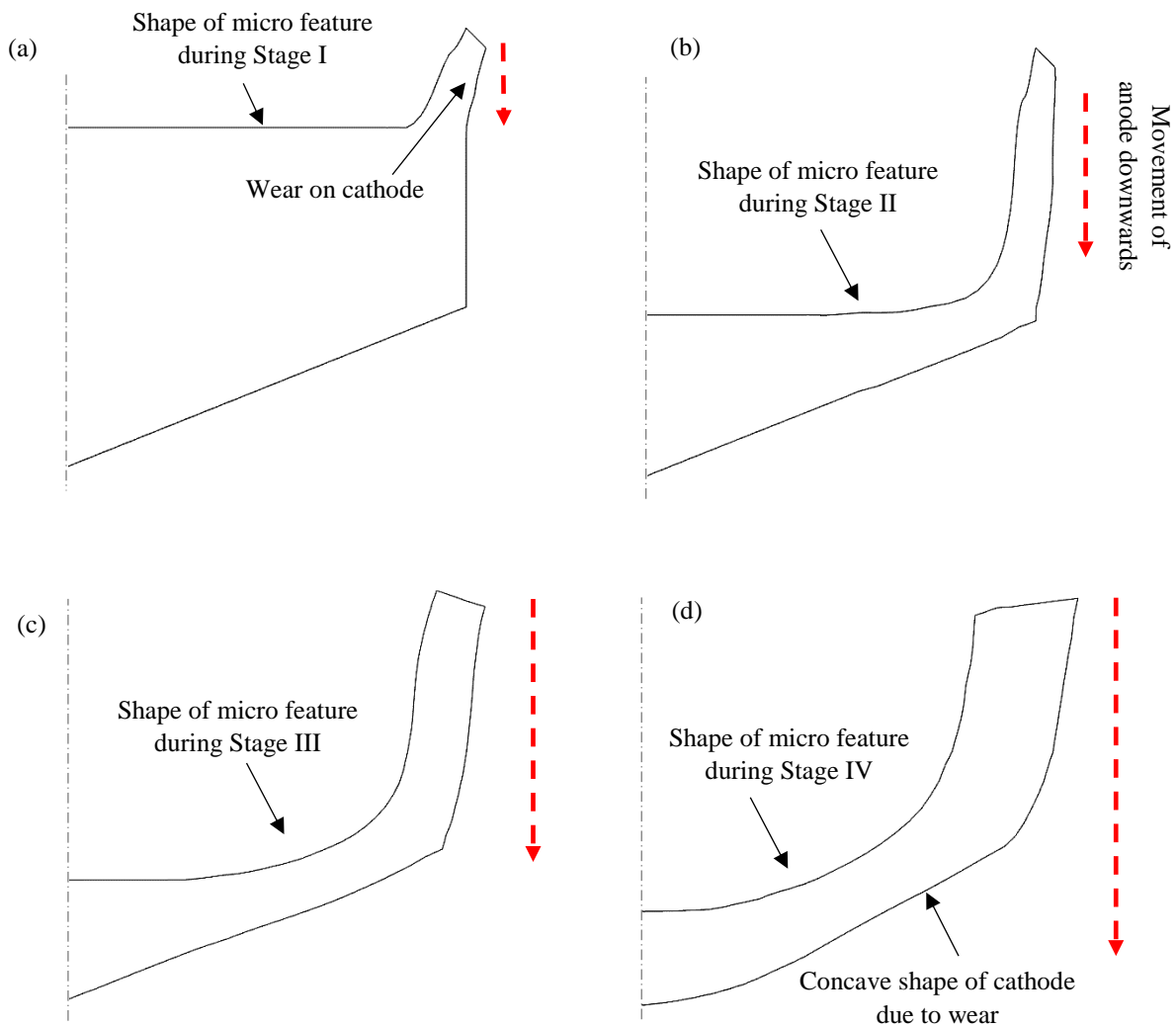


Fig. 5.6: Geometry during (a) Stage I (b) Stage II (c) Stage III (d) Stage IV of RMEDM process

- a) *Stage I (Fig. 5.6 (a))*: Initiation of discharges between tool and workpiece (Beginning of taper formation)
- b) *Stage II (Fig. 5.6 (b))*: Discharges occurring between the straight portion of tool and the workpiece (Maximum point at which the base of the micro feature remains flat)
- c) *Stage III (Fig. 5.6 (c))*: Discharges occurring between tapered portion of tool and workpiece (Curvature formation on the base of micro feature).
- d) *Stage IV (Fig. 5.6 (d))*: Towards the end of machining (Generation of 3-D hemispherical convex micro feature)

5.2.4.1 Stage I

As the workpiece (anode) starts moving downwards, discharges between the electrodes occur as soon as the electric field exceeds the breakdown strength of the dielectric. This leads to removal of material from both the electrodes. Most of the numerical models available in literature do not incorporate cathode wear (i.e. material removal on cathode) due to complexity [44,124]. This leads to formation of vertical walls on workpiece (**Fig. 5.7**). Secondary

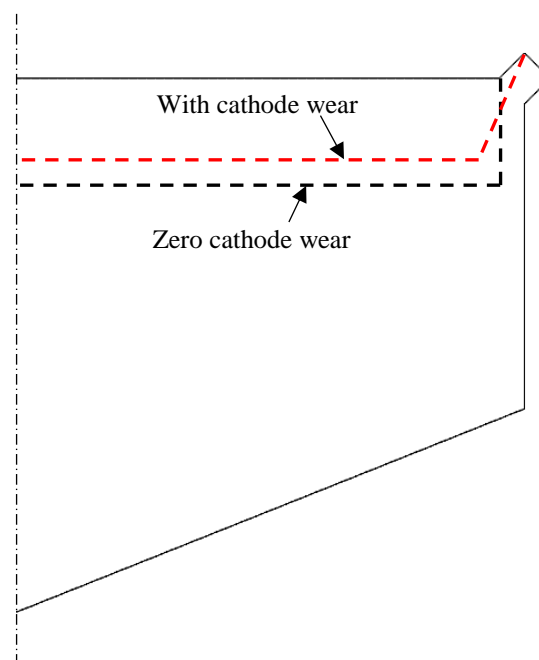


Fig. 5.7: Profile of micro feature during initial discharges (with and without cathode wear)

discharges between sides of tool and workpiece leads to initial taper generation on the workpiece. Incorporating cathode wear in the present numerical model along with presence of

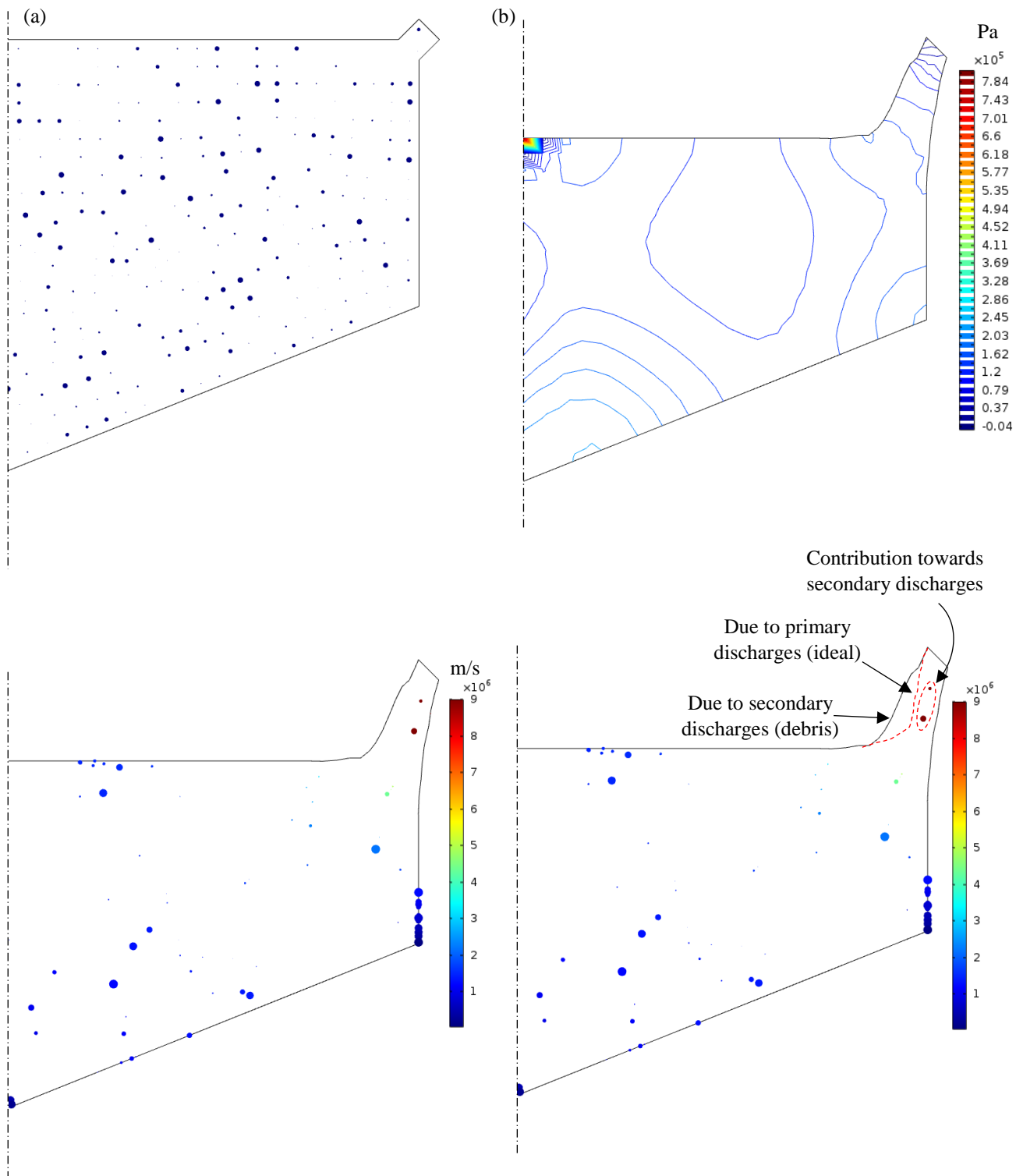


Fig. 5.8: Stage I (a) Uniform distribution of debris (b) Pressure contour for plasma implosion (c) Movement of debris (d) Electric field enhancement due to debris

debris in the dielectric, the taper on workpiece (**Fig. 5.7**) as well as little taper on tool can be observed (**Fig. 5.6 (a)**).

A uniform distribution of debris in the size range of $0.1 \mu\text{m} - 1 \mu\text{m}$ with average size of $0.5 \mu\text{m}$ was released in the dielectric (**Fig. 5.8 (a)**). Due to plasma implosion (**Fig. 5.8 (b)**), the debris particles are expelled towards the corners of the tool as well as the exit where the pressure is comparatively less as compared to the implosion pressure (**Fig. 5.8 (b, c)**). During the movement of debris, some of them escape through the exit, some adhere to cathode and the rest are suspended in the dielectric. Their movement is mainly governed by the pressure difference at different locations on the electrodes in addition to different forces acting on the debris particle (**Eq. 5.10**). The adhesion of debris on the tapered portion and straight walls of the cathode as well as those suspended between the workpiece and the tapered portion of the

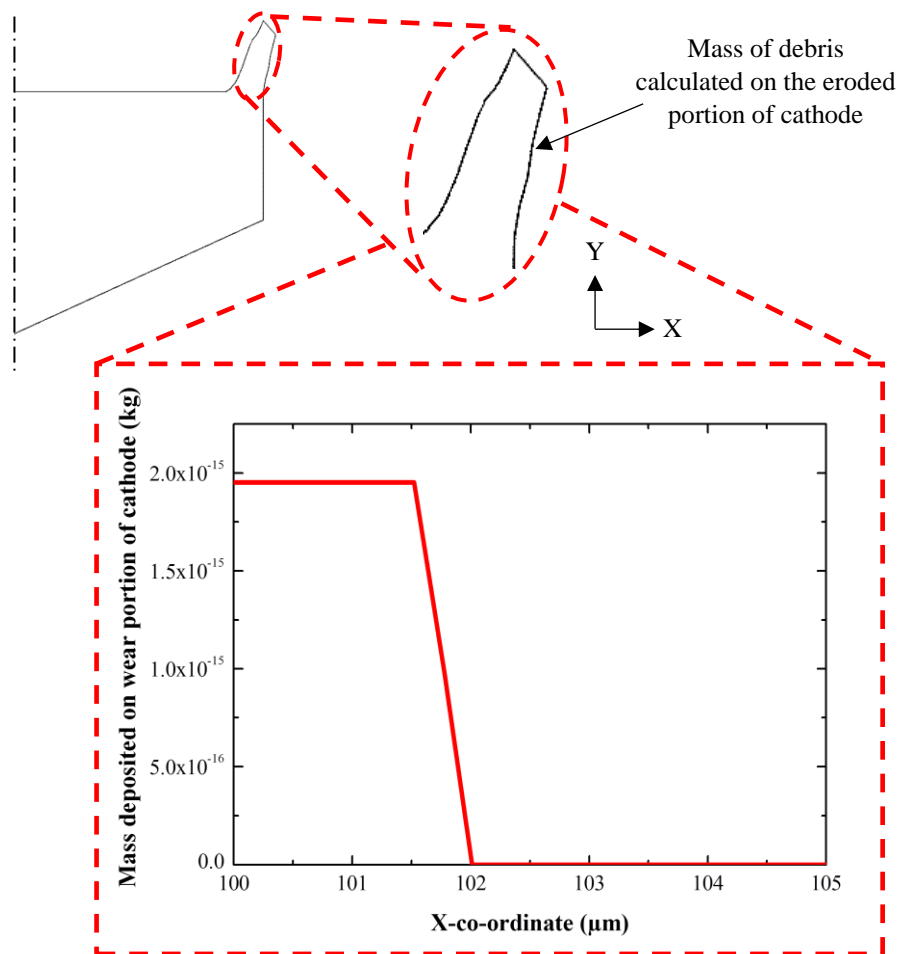


Fig. 5.9: Mass of debris deposited on eroded portion of cathode during Stage I

tool (**Fig. 5.8 (c)**) do not have any significant impact on the discharge process as the gap between the workpiece and the portion of cathode with adhered debris is very high in this stage.

The primary region of interest in this stage is the profile of micro feature generated due to material removal from anode due to discharges occurring between the electrodes as well as secondary discharges due to debris. In the absence of debris (i.e. no secondary discharges), the profile of micro feature should follow the profile of the cathode (**Fig. 5.8 (d)**). During actual machining, debris plays a key role in two aspects:

- Contribute to secondary discharges
- Reduction in breakdown strength of dielectric by increasing the localised electric field strength

Fig. 5.9 was constructed by determining the amount of mass deposited on the eroded portion of cathode and plotting it against the X-co-ordinate i.e. along the radial direction (or Y-co-ordinate i.e. along the axial direction) of the eroded portion of cathode; for instance in **Fig. 5.9**, the eroded portion ranges from $x = 100\mu\text{m}$ to $x = 105\mu\text{m}$; the mass deposited between this region is specified. The co-ordinate system is shown in **Fig. 5.1**. Mass deposition curves are also plotted for each stage (described later) and the procedure for construction is similar to the one described here.

From **Fig. 5.8 (d)**, it can be seen that the actual profile of micro feature matches with the ideal profile (only primary discharges) for some distance near the exit. Till this point, there is negligible mass of debris deposited on cathode (**Fig. 5.9**). Hence, only primary discharges occur in this zone. Beyond that, the profile of micro feature deviates from the ideal profile (**Fig. 5.8 (d)**). This is due to (a) presence of suspended debris that helps in reducing the breakdown strength of dielectric thereby allowing a larger IEG as well as (b) mass of debris deposited on cathode in this zone that leads to occurrences of secondary discharges.

5.2.4.2 Stage II

During machining, as the workpiece (anode) traverses downwards (**Fig. 5.6 (b)**), discharges between tool and workpiece occur and wear on both electrodes takes place. Stage II defines the instant at which the straight portion of cathode and workpiece have interacted with each other. Till this point, discharges between the tapered portion of cathode and the workpiece have not started yet. **Fig. 5.10** shows the pressure contour curve during this stage. With decrease in distance between the tapered portion of tool and base of workpiece as compared to Stage I, the pressure profile also changes. There is a continuous reduction in pressure from the origin of plasma implosion towards the exit. Because of this reduction in pressure, debris particles tend to move out of the machining zone. During their movement towards exit, some debris particles adhere to the walls of cathode. **Fig. 5.11** shows the amount of mass of debris deposited on cathode at different stages. Debris particles agglomerate at the corner of the tapered portion and this agglomeration increases with time. As a result of this, secondary and higher order discharges (abnormal discharges) occurs more in this zone and

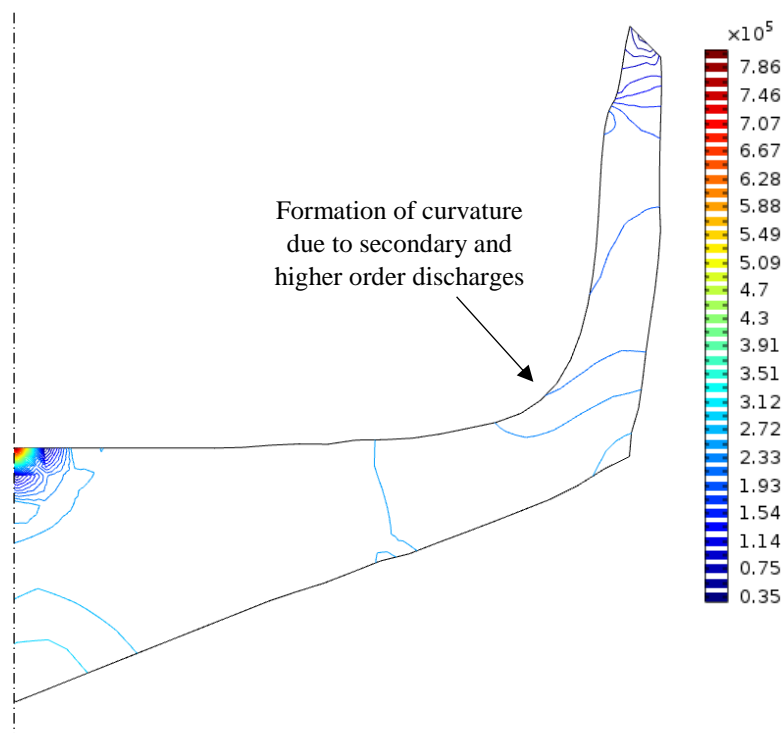


Fig. 5.10: Pressure contour during Stage II

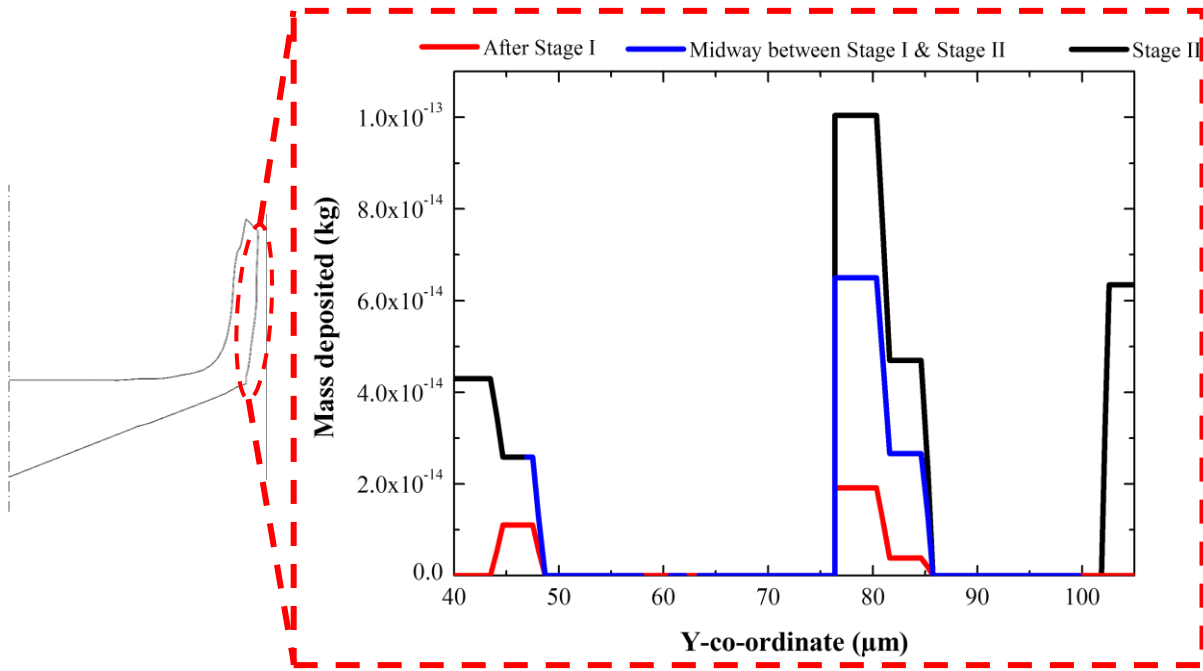


Fig. 5.11: Mass of debris deposited on straight portion of cathode during Stage II

causes a curvature formation at the corner of the workpiece (**Fig. 5.10**). Agglomeration of debris also occurs on the straight walls of cathode and it increases with increase in anode traverse. Due to this, secondary and higher order discharges increases and this in turn increases surface roughness of the micro feature. Towards the end, agglomeration of debris is mainly due to large amount of debris escaping out of the exit. Most of these debris are removed during successive flowing out of debris with increase in anode traverse.

5.2.4.3 Stage III

This stage refers to the case when discharges apart from occurring with respect to the straight portion of tool also occurs between tapered portion of tool and workpiece. Pressure contour along with the velocity field (in terms of arrow heads) are shown in **Fig. 5.12**. Due to higher velocity of dielectric near the centre arising due to pressure difference, expulsion of debris takes place near the centre (**Fig. 5.13 (b)**). Most of the debris move towards the exit while some debris adhere to the walls of cathode near the centre (**Fig. 5.13 (a-b)**). The distance

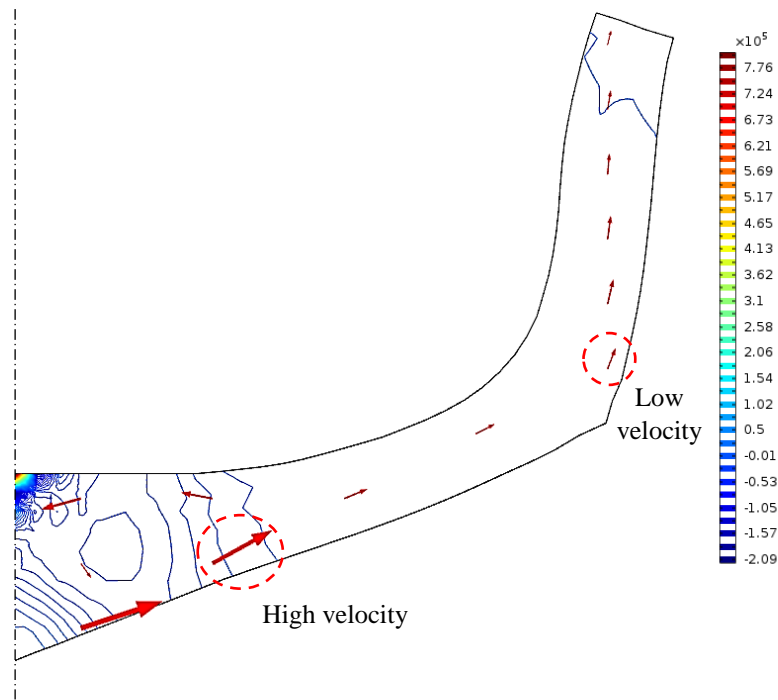


Fig. 5.12: Pressure contour and velocity field during Stage III

between the walls of cathode and walls of anode near the centre are comparatively high as compared to other portions in order to have a significant effect on the discharge profiles. Amount of mass deposited on the junction between straight and tapered portion of cathode in *Stage III* is higher as compared to other regions on the straight portion (**Fig. 5.14**). Due to this, higher number of discharges now occur near the tapered portion which increases the curvature on the micro feature (**Fig. 5.6 (c-d)**). This is in contrast to *Stage II* wherein higher mass deposition was midway in the straight portion (**Fig. 5.11**) and caused discharges that led to increase in surface roughness. Combining the amount of mass deposited on straight portion of cathode during *Stage II* and *Stage III* (**Fig. 5.14**), both phenomenon occurs simultaneously i.e. increasing the curvature near the base of micro feature and increase in surface roughness on the sides of micro feature.

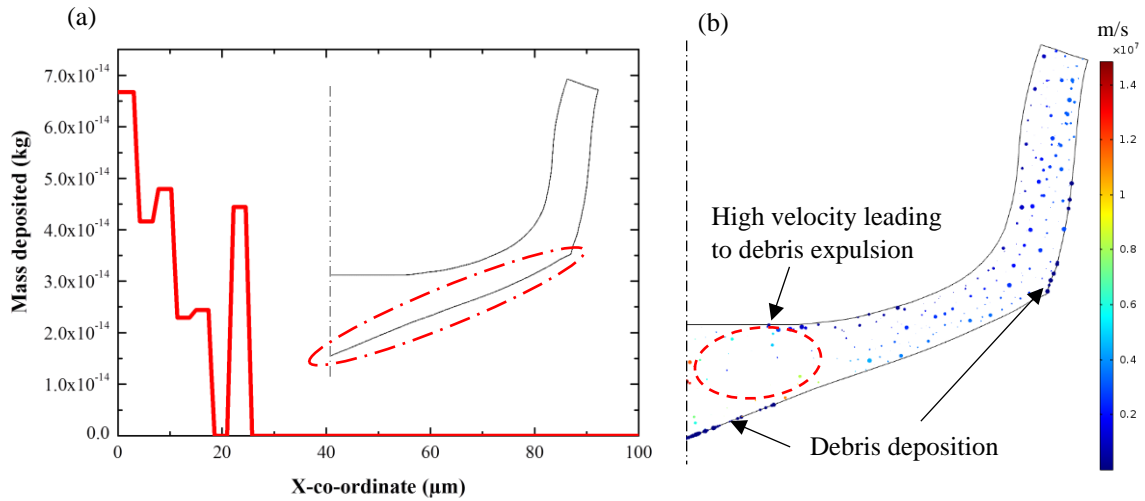


Fig. 5.13: Stage III (a) Mass of debris deposited on tapered portion of cathode (b) Velocity of debris

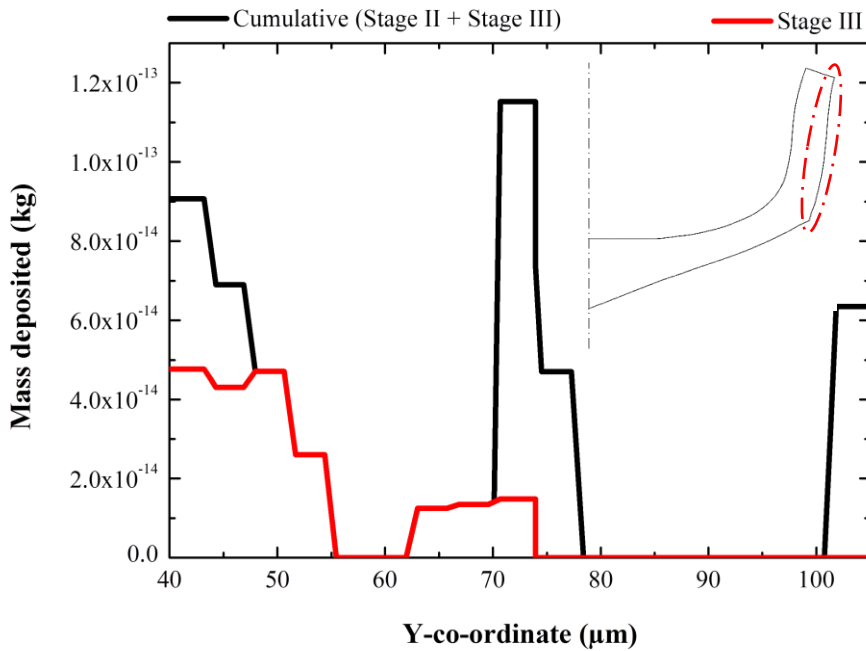


Fig. 5.14: Mass of debris deposited on straight portion of cathode during Stage III

5.2.4.4 Stage IV

As machining progresses, the amount of debris in the channel increases. This leads to further reduction in breakdown strength of dielectric as compared to earlier stages. Therefore, discharges occur at higher inter-electrode gaps as opposed to the case with a fresh dielectric.

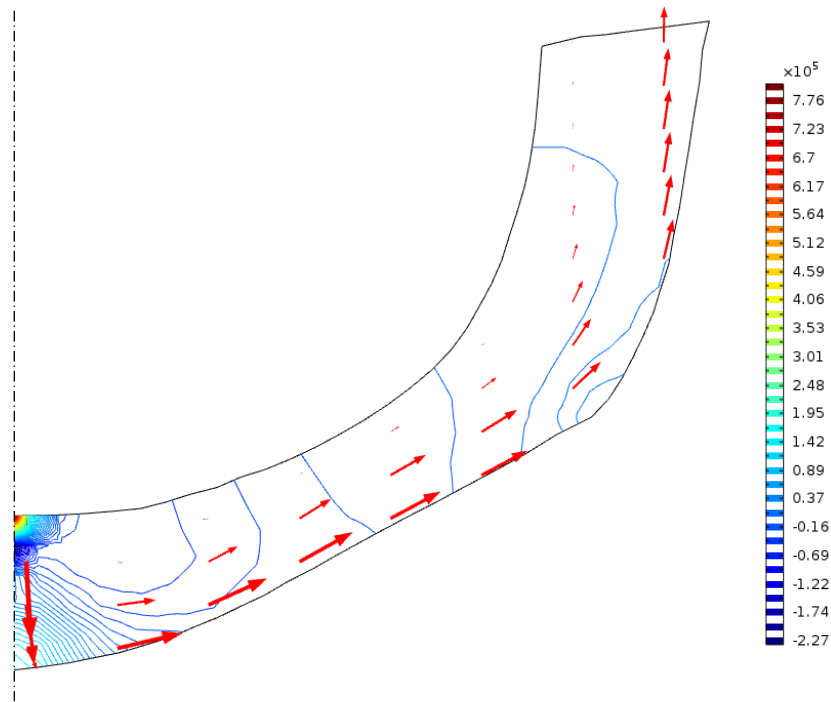


Fig. 5.15: Pressure contour and velocity field during Stage IV

Velocity field (**Fig. 5.15**) during this stage is directed from the pressure implosion point towards the base of tool. Due to this, debris agglomeration at the central portion of the tool increases as compared to *Stage III* (**Fig. 5.13 (a)**). This is evident from the amount of mass of debris deposited at the base of the tool. Repetitive number of discharges due to debris agglomeration near the centre helps in increasing the curvature of the micro feature finally

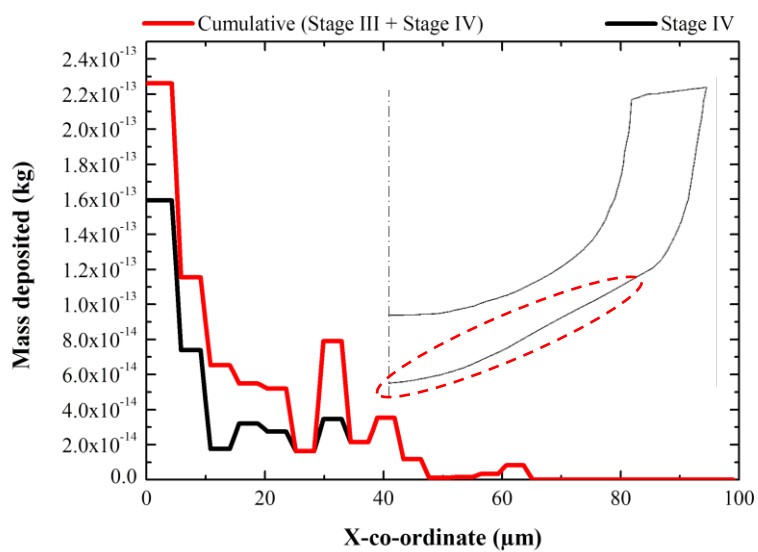


Fig. 5.16: Mass of debris deposited on tapered portion of cathode during Stage IV

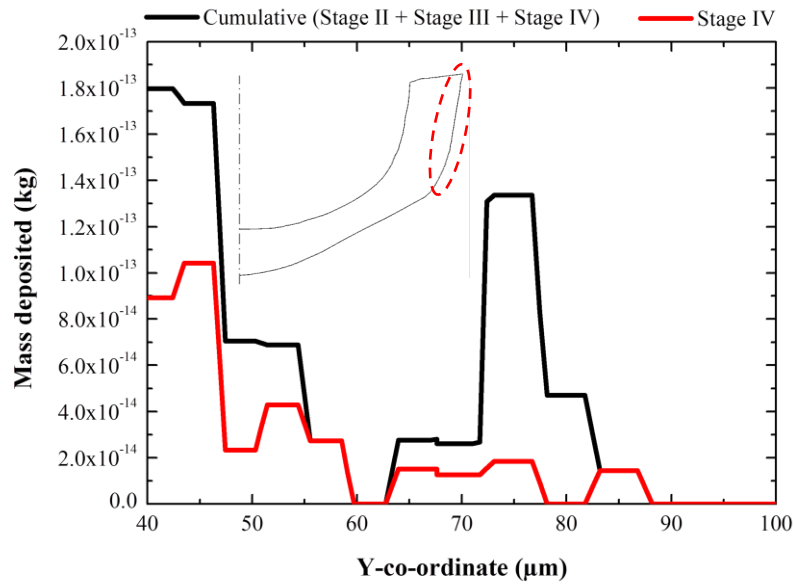


Fig. 5.17: Mass of debris deposited on straight portion of cathode during Stage IV

resulting in the formation of 3-D hemispherical convex micro feature. Velocity of fluid from the centre is further re-directed towards the junction of tapered and straight portion of tool (**Fig. 5.15**). The debris agglomeration, therefore, reduces from the centre to the junction between tapered and straight portion (**Fig. 5.16**) as most of the debris move towards the straight portion of cathode. On the straight portion of cathode, debris agglomeration has further increased at

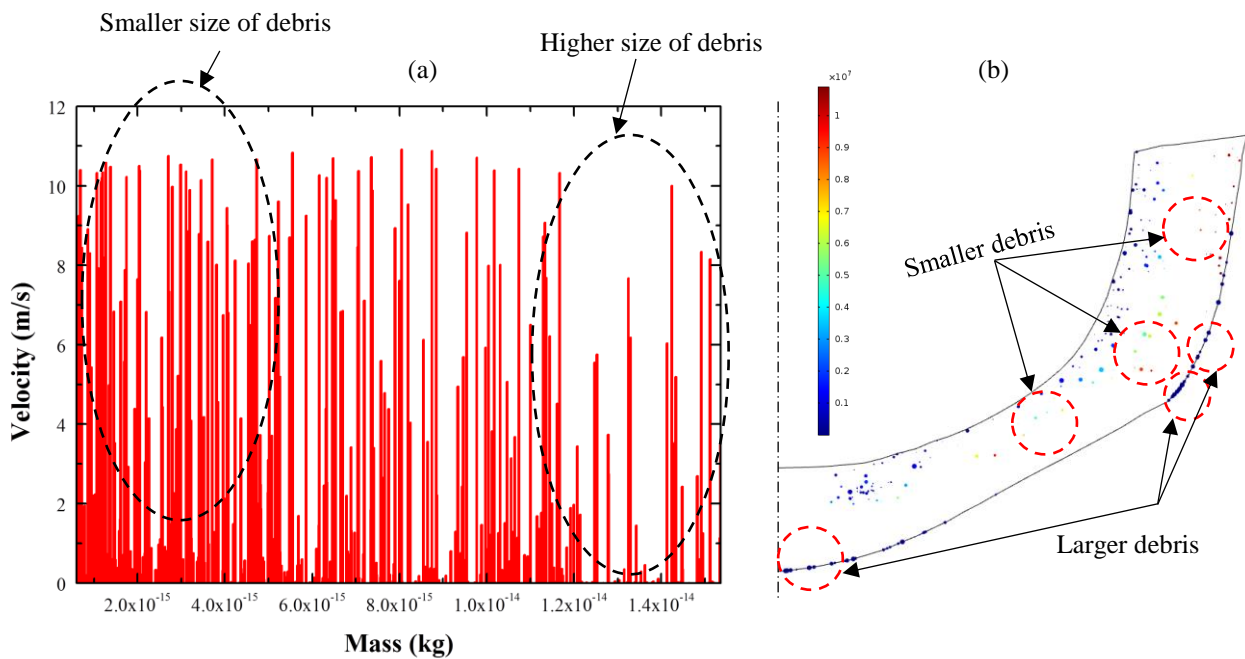


Fig. 5.18: (a) Debris particle velocity corresponding to its mass (diameter) (b) Velocity of debris during Stage IV

locations adjacent to tapered portion whereas midway on the straight portion has reduced (**Fig. 5.17**). Therefore, the discharge phenomena result in more number of discharges near the tapered portion which increases the curvature on the anode as compared to other three stages.

Since, the size of debris varies from few nm to few μm in diameters with an average diameter of $0.5 \mu\text{m}$ (collected and measured), uniform distribution of debris size in the range of $0.1 \mu\text{m}$ - $1 \mu\text{m}$ was considered for simulation. **Fig. 5.18 (a)** shows the plot of velocity of debris with their mass. Higher mass of debris indicates higher diameter. Simulation results show that larger size of debris will have lower velocities and hence they are more prone to adherence on walls as compared to smaller sized debris. **Fig. 5.18 (b)** shows the smaller debris moving towards the exit whereas most of the larger sized debris adhere to the walls resulting in higher amount of debris agglomeration as already seen in **Figs. 5.16 – 5.17**.

Wear on cathode was incorporated in this model which resulted in formation of concave shaped feature on the cathode due to material removal due to discharges. **Fig. 5.19 (a)** shows the concave shape of cathode obtained by simulation. Due to very smaller size of hole on cathode ($200 \mu\text{m}$), measurement of its form using touch probe form measurement technique was difficult. Also due to agglomeration of debris on the cathode, the surface was very rough

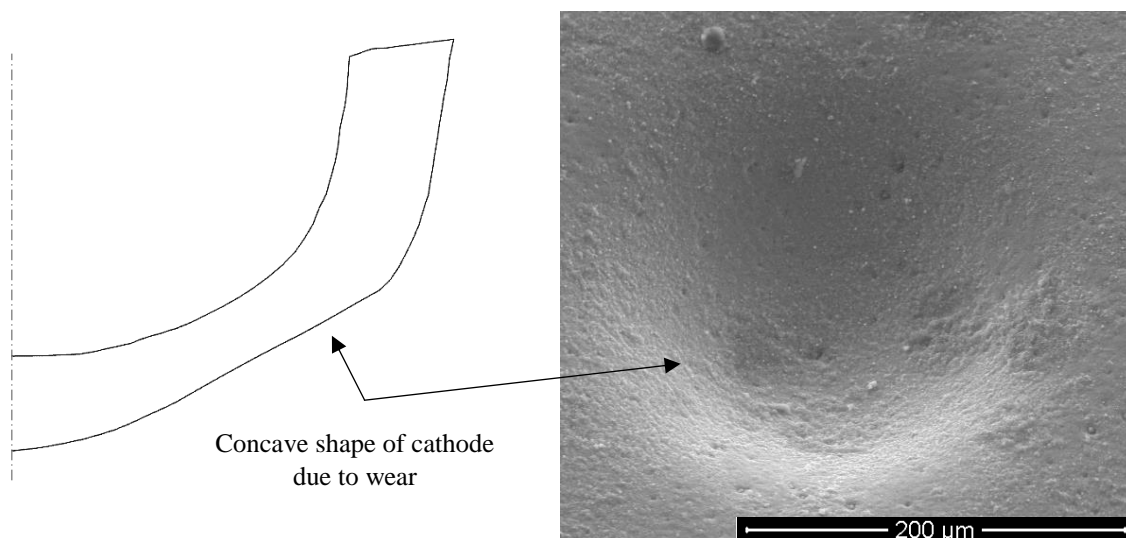


Fig. 5.19: (a) Simulated profile of cathode during Stage IV (b) SEM image of eroded cathode

in order to be accurately measured by optical measurement techniques. Qualitatively, it can be seen that both profiles resemble a near concave shaped feature arising due to conversion from an initial taper ended blind hole to a concave shaped blind hole (**Fig. 5.19 (b)**). This is because of secondary and higher order discharges arising due to debris agglomeration on cathode. Based on qualitative comparison of erosion on cathode, it can be concluded that the process is conformal since a convex hemispherical micro feature is generated by a concave shaped eroded hole.

5.2.4.5 Comparison between different stages of machining

To summarise the effect of different stages of machining in generation of 3-D hemispherical convex micro feature using a reverse micro EDM with an initial taper ended blind hole as tool, **Table 5.2** demonstrates the effect of each stage with respect to debris agglomeration, secondary and higher order discharge and contribution of each stage towards machining of 3-D hemispherical convex micro feature.

5.3 Surface roughness analysis based on piecewise de-trending of simulated shape

De-trending of final shape (**Fig. 5.6 (d)**) of 3-D hemispherical convex micro feature obtained through simulation is necessary to remove the effect of curvature in determining surface roughness (R_a). Since, material removal takes place by primary, secondary and higher order discharges, piecewise de-trending of surface is necessary to filter out waviness components from the surface. **Fig. 5.20** shows a magnified portion of the fabricated micro feature where a crater formation can be seen along with surface roughness on the micro feature. Piecewise de-trending was done by dividing the surface into two, four and six segments respectively. In each case, linear, quadratic and cubic best fit curves (**Fig. 5.21**) were plotted for each segment. The deviation of each data point from their respective best fit curve (z_n) was

Table 5.2: Comparative analysis of different stages of machining

	Debris agglomeration	Secondary and higher order discharges	Contribution towards machining
Stage I	Very low and at a little distance away from the exit	Secondary discharges near the exit	With secondary discharges near the exit, the shape obtained deviates from the ideal profile
Stage II	Occurs on the straight portion. Higher debris agglomeration is midway on the straight portion while some amount of debris is accommodated near the junction of tapered portion	Secondary and higher order discharges are higher somewhere in the middle of the straight portion of cathode. This results in increase in surface roughness	Secondary and higher order discharges helps in generating a small curvature at the corner of the workpiece
Stage III	<i>Straight portion of cathode:</i> Higher at locations adjacent to tapered portion as compared to Stage II <i>Tapered portion of cathode:</i> Debris agglomerated near the central portion of cathode	Cumulative debris agglomeration (secondary and higher order discharges) at midway of straight portion contributed to high surface roughness while that at the junction of tapered portion contributed to curvature formation	Curvature formation has increased as compared to Stage II
Stage IV	<i>Straight portion of cathode:</i> Very high at locations adjacent to tapered portion <i>Tapered portion of cathode:</i> Very high near the centre	Repeated discharges occur near locations where debris agglomerated.	High amount of repetitive discharges occurred near locations where debris agglomerated leading to curvature formation on anode finally resulting in 3-D hemispherical convex micro feature

calculated and the average of all the data points results in the average surface roughness of that segment (R_a). A total of 7500 data points were extracted from the simulated profile and the surface roughness obtained by dividing the surface into various segments is discussed below.

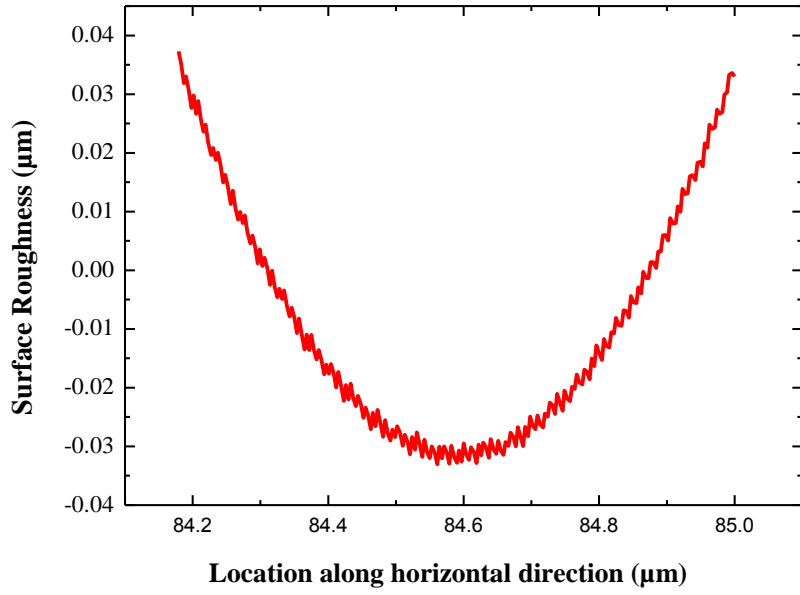
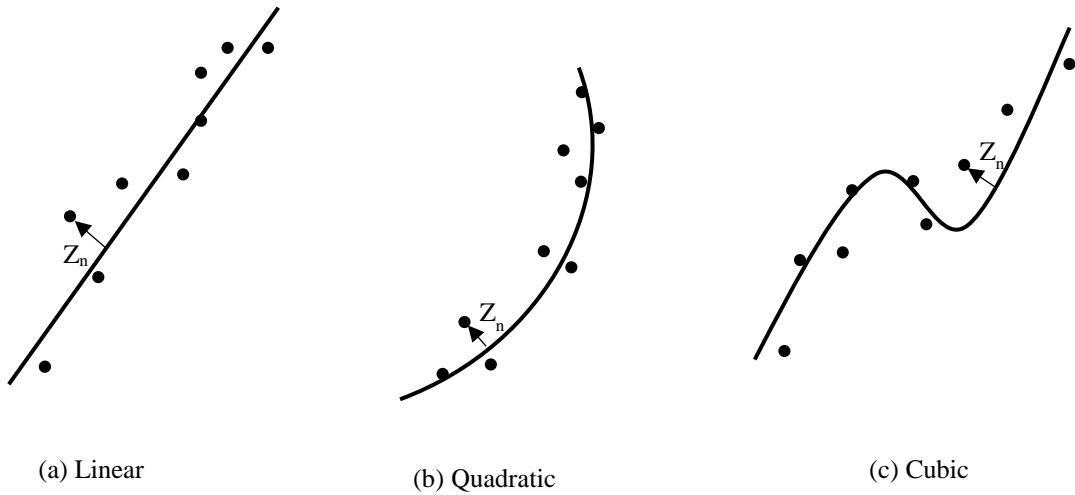


Fig. 5.20: Segment of simulated shape showing crater formation and surface roughness on the profile



$$R_a = \frac{\sum_1^n |z_n|}{n}$$

Fig. 5.21: Best fit curve for (a) linear (b) quadratic (c) cubic

5.3.1 Two equal segments

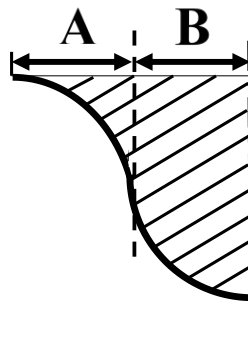


Fig. 5.22: Two equal segments of surface profile of anode

In the first case, the surface profile of anode was divided into two equal segments as shown in **Fig. 5.22**. The best fit curve based on linear, quadratic and cubic equations were found out for both the segments based on profile data. **Fig. 5.23** shows the variation of surface roughness with respect to location along horizontal direction on the surface. For all the three cases viz., linear, quadratic and cubic, surface roughness at the lower portion of micro feature containing the base is less as compared to the top half of micro feature with the tip. Dividing the surface into two segments cannot capture the effect of variation of surface roughness due to secondary and higher order discharges at the side of micro feature as compared to the tip and

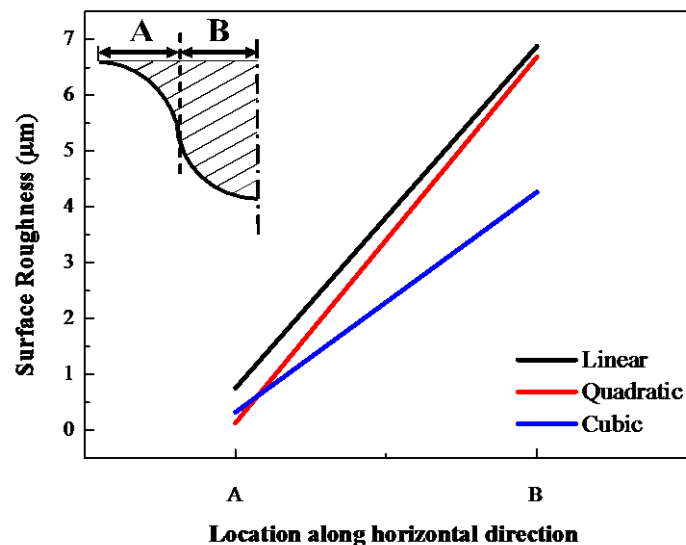


Fig. 5.23: Surface roughness prediction using two segments of profile of anode

base of micro feature where this effect is less due to debris expulsion by plasma implosion and removal of debris by dielectric respectively.

5.3.2 Four equal segments

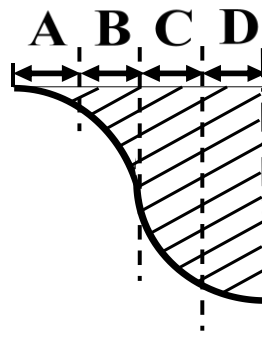


Fig. 5.24: Four equal segments of surface profile of anode

In this case, four equal segments of profile were taken into consideration as shown in **Fig. 5.24**. Similar to *Section 5.3.1*, best fit curves were obtained for each segment and surface roughness values are plotted in **Fig. 5.25**. Results indicate that there is a steep increase in surface roughness beyond the segment C. It indicates increase in surface roughness due to secondary and higher order discharges. However, it could not capture the

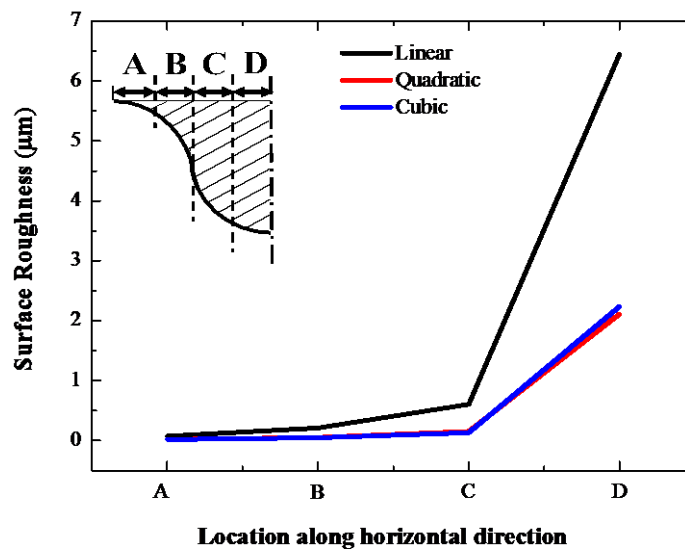


Fig. 5.25: Surface roughness prediction using four segments of profile of anode

reduction in surface at the tip of surface due to removal of debris by plasma implosion pressure.

5.3.3 Six equal segments

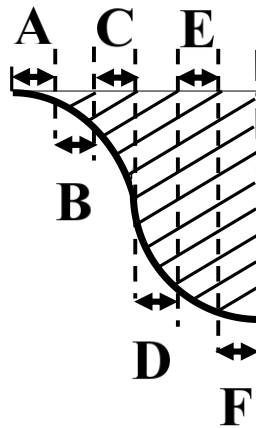


Fig. 5.26: Six equal segments of surface profile of anode

In this case, six equal segments of profile were taken into consideration as shown in **Fig. 5.26**. Best fit curves for linear, quadratic and cubic equations obtained from profile were found out for each segment and surface roughness values are plotted in **Fig. 5.27**. Surface roughness curve based on cubic best fit curve shows an abrupt value at Section B. The result

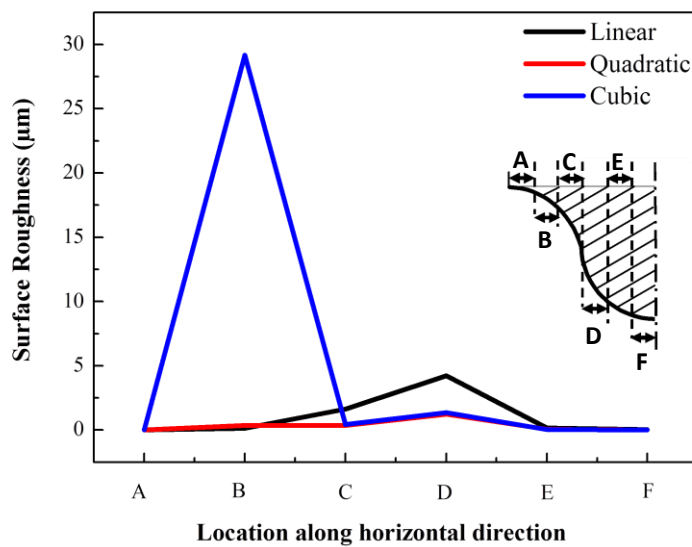


Fig. 5.27: Surface roughness prediction using six segments of profile of anode

for surface roughness in this case is erroneous. For both linear and quadratic best fit curves, trend of surface roughness curve captures the increase in surface roughness at the sides of micro feature as compared to base and tip of micro feature. However, surface roughness is generally of the order of $\leq 1 - 2 \mu\text{m}$ [43,125]. Linear best fit curve predicts a surface roughness value higher than the normal range. The surface roughness obtained in case of quadratic profile seems to be well within the limits of surface roughness. Quadratic best fit curve shows the best results for surface roughness in all the three cases described in *Sections 5.3.1-5.3.3*.

5.4 Experimental analysis of 3-D hemispherical micro feature using RMEDM

Experiments for generating 3-D hemispherical micro features are already described in *Section 4.3*. Size, shape and surface roughness measurements of generated micro features were carried out using different measuring devices that include SEM, optical microscope and interferometer. Size of the micro features were further verified using public domain image processing software (ImageJ 1.46r, NIH).

5.4.1 Shape generation of 3-D hemispherical convex micro feature

In order to generate a 3-D hemispherical convex micro feature using RMEDM, a pre-drilled tapered blind hole on plate (cathode) was employed as tool (**Fig. 5.28 (a)**). The dimension of the tapered blind hole was one of the most important factors in shaping of 3-D hemispherical convex micro feature. The depth of drilled hole was kept equal to its radius (0.1 mm). Apart from the hole dimensions, other important factors that contributed towards shaping of 3-D hemispherical convex micro feature were the debris adhesion and agglomeration on the electrodes which contributed in a constructive manner as opposed to the general trend wherein

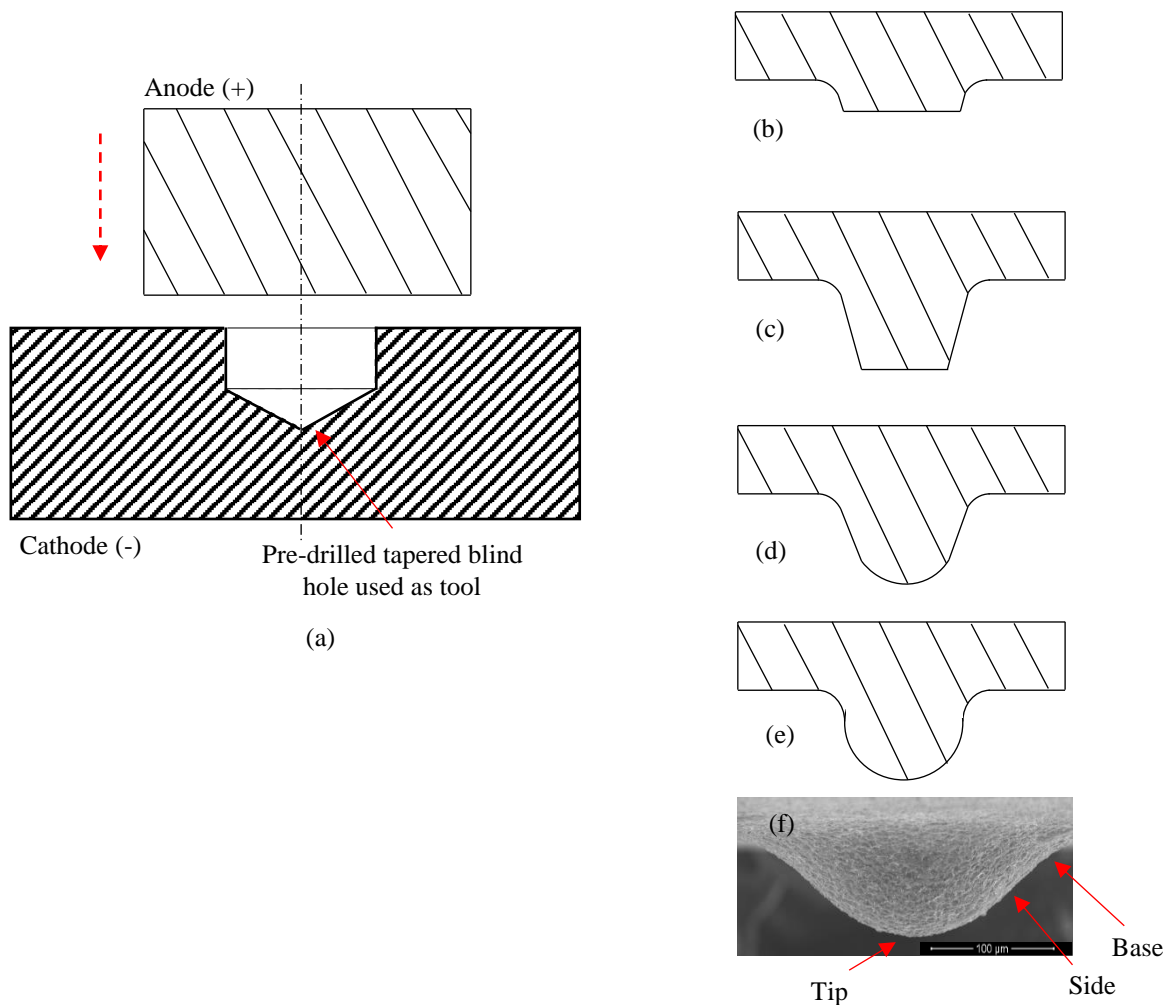


Fig. 5.28: Schematic of (a) RMEDM with modified tool and shape of micro feature during (b-e) Shapes of micro feature at different traverse of anode (f) Actual 3-D hemispherical convex micro feature

debris adhesion and agglomeration are considered to be hindrance to machining in case of discharge based machining processes. **Fig. 5.28 (b-e)** shows the shape of micro feature at different traverse of anode and **Fig. 5.28 (f)** depicts the SEM image of the fabricated 3-D hemispherical convex micro feature. Measurement of shape of micro feature were conducted at regular intervals of 0.1 mm for a total traverse of 1.2 mm. The axisymmetric shape of micro feature generated at different traverse of anode is shown in **Fig. 5.29**.

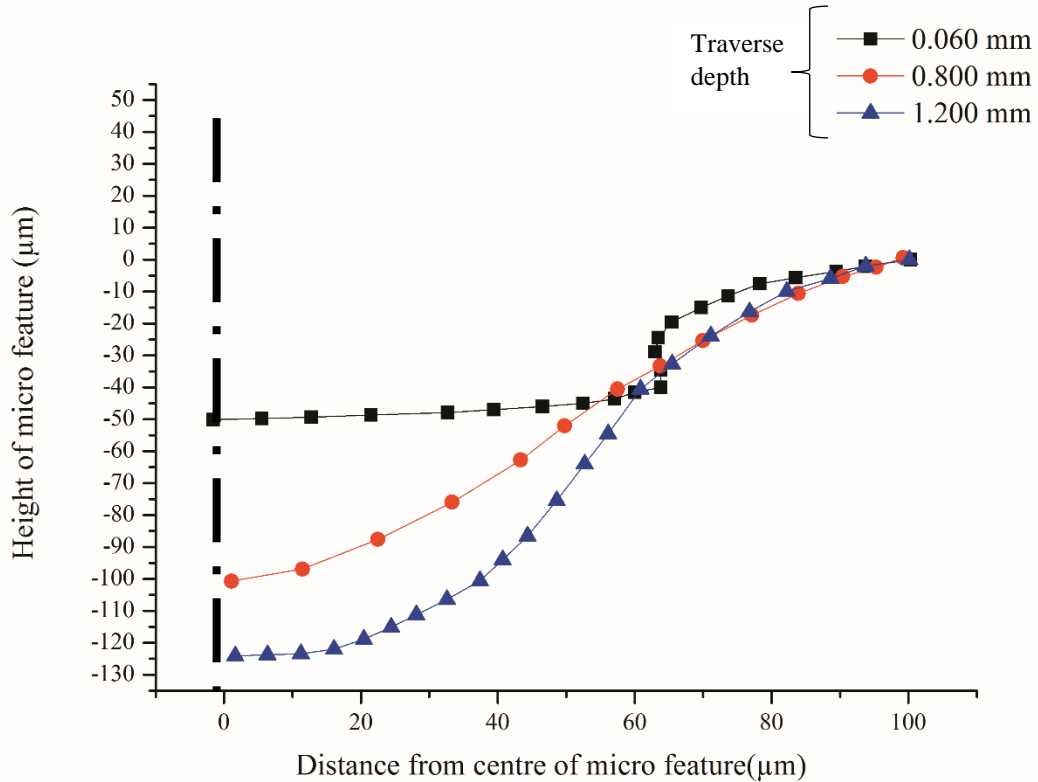


Fig. 5.29: Shape of anode generated due to various traverse of anode downwards

5.4.2 Surface roughness measurements on the 3-D hemispherical convex micro feature

Magnified images of the 3-D hemispherical convex micro feature (**Fig. 5.30**) were taken at three different locations (side, tip and base of the micro feature respectively). It can be seen from **Figs. 5.30 (b-c)** that the crater size remains constant throughout the region indicating that primary discharges mostly occurred in these regions. However, in **Fig. 5.30 (a)**, variation in crater size can be seen on the sides. This is primarily due to debris attachment on the corners of cathode that created secondary and higher order discharges at these locations. Also, re-solidified molten material can also be seen mostly on the sides of the micro feature and little at the tip of the surface. Experimental results thereby confirm the existence of secondary and higher order discharges leading to variation in crater size on the sides of 3- D hemispherical convex micro feature. This variation in crater size on the side of micro feature leads to higher surface roughness as compared to tip or base of micro feature (**Fig. 5.31**).

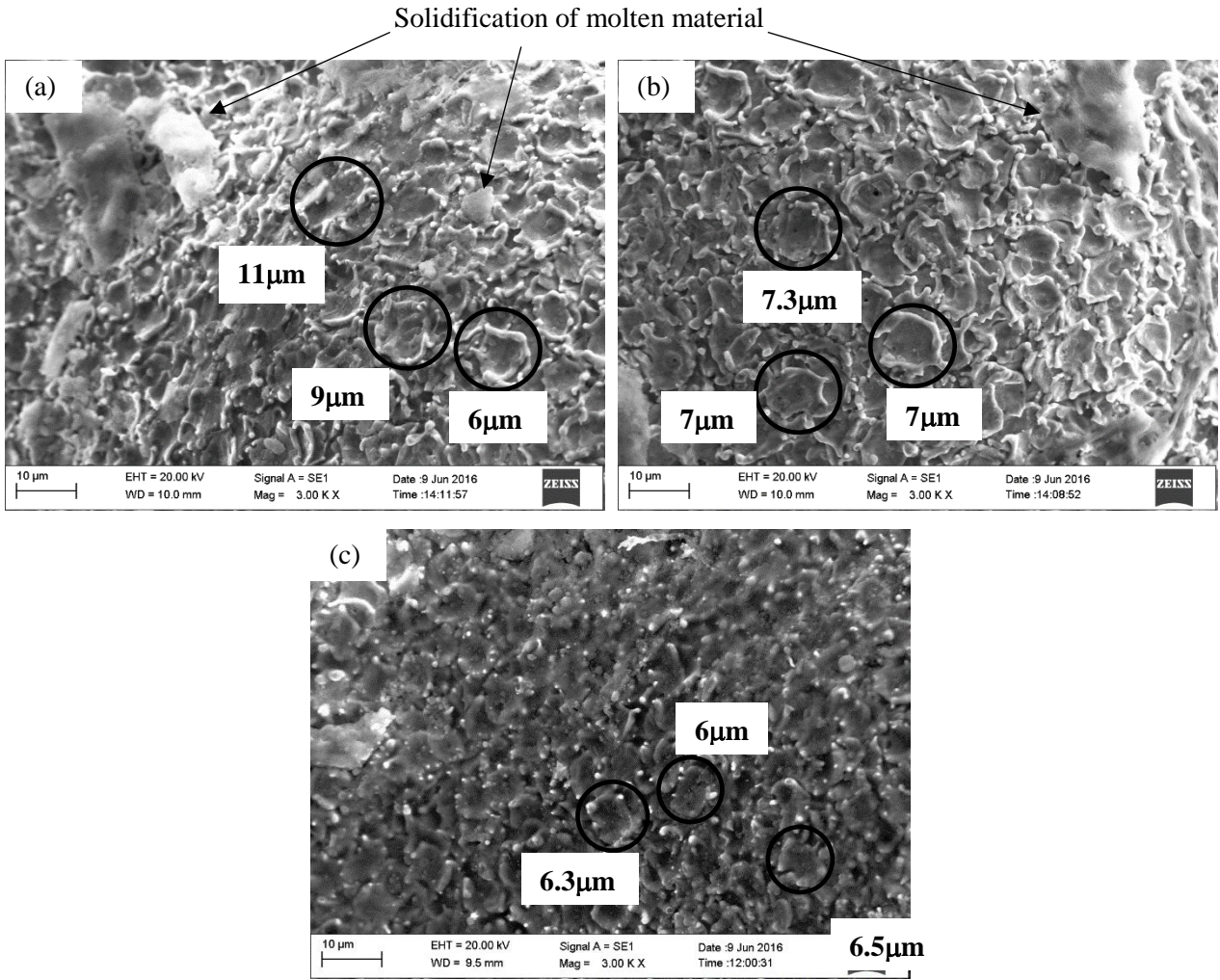


Fig. 5.30: SEM micrographs of (a) Side (b) Tip and (c) Base of the convex micro hemi-spherical profile

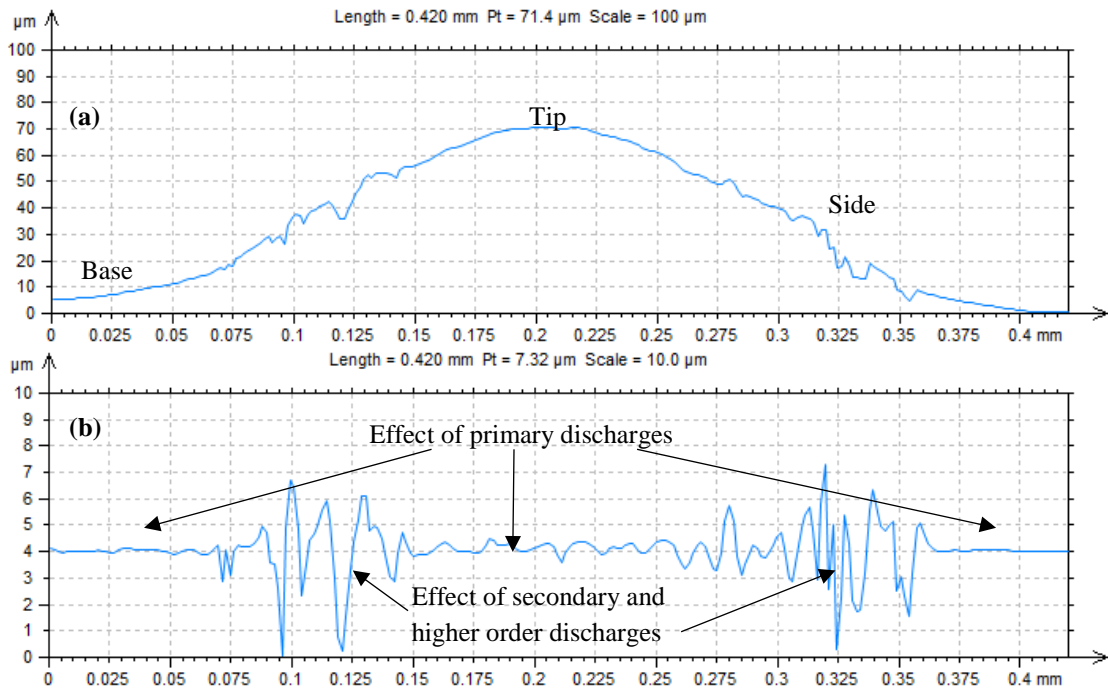


Fig. 5.31: (a) 3-D hemispherical convex micro feature (b) Surface roughness on the fabricated micro feature

5.5 Model validation for shape and surface roughness of 3-D hemispherical convex micro feature

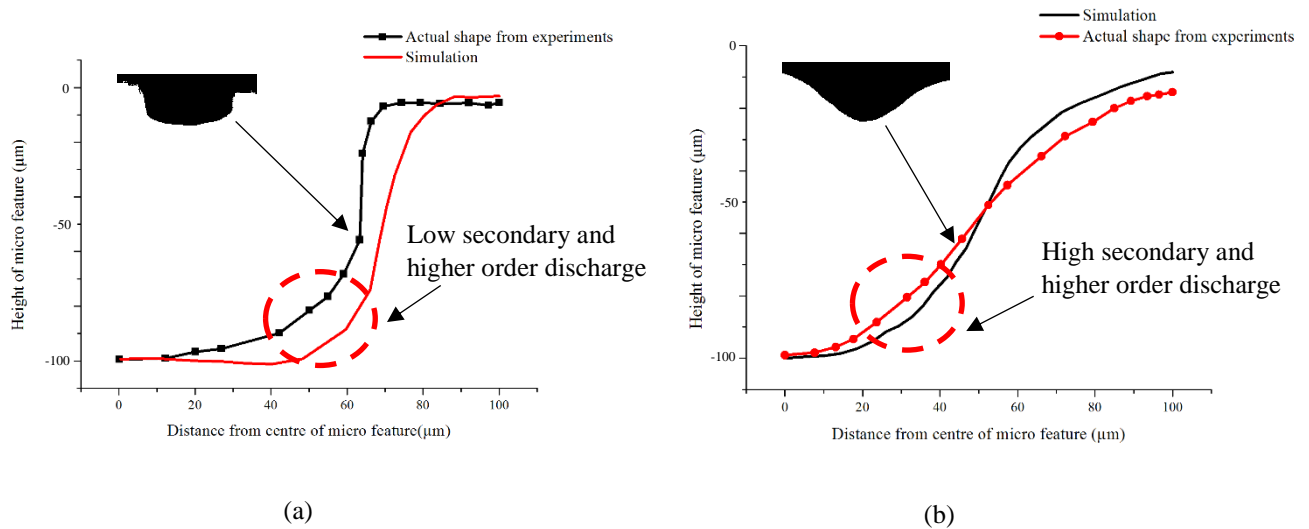


Fig. 5.32: Experimental and simulated shape of micro feature corresponding to anode traverse of (a) 0.095 mm (b) 0.8 mm

Fig. 5.32 shows the actual profile of micro feature obtained from experiments as well as that obtained from simulation when anode has traversed a distance of 0.095 mm and 0.8 mm respectively. During initial phase of anode traverse, the gap between the anode and cathode is large ($\gg 10 \mu\text{m}$). The extent of secondary and higher order discharges is comparatively less. Primary discharges dominate the erosion phenomena till the anode reaches the tapered portion of the hole (**Fig. 5.32 (a)**). As soon as the anode reaches the tapered portion of the hole, secondary and higher order erosion increases gradually (**Fig. 5.32 (b)**) due to reduced gap between the electrodes. Secondary and higher order discharges is maximum when the gap reduces to minimum IEG of $\leq 10 \mu\text{m}$. Initially, the amount of primary discharge will be more compared to secondary and higher order discharges due to ample space for debris to move out of the machining zone. A comparison of final shape of micro feature obtained is shown in **Fig. 5.33**. One of the assumptions considered by researchers is the absence of cathode wear [44,124]. A similar study was done to find out the deviation from the actual shape obtained. The error between simulation and experiments is quite large as evident from **Fig. 5.33**. Hence,

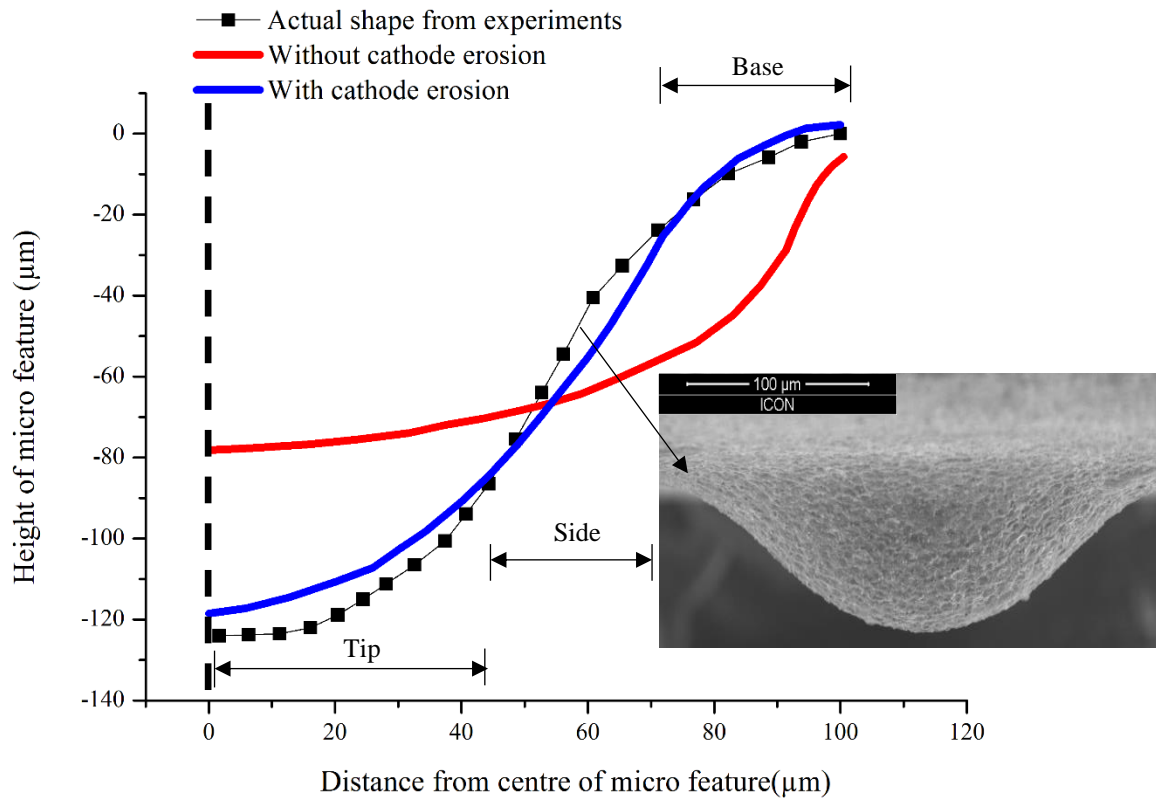


Fig. 5.33: Comparison of final shape of micro feature obtained with experiment and simulation

cathode wear was incorporated in our model which was also observed during experiments (**Fig. 5.19 (b)**). The material removal on cathode was considered in proportion to the ratio of energy distribution to anode and cathode. This ratio has been taken as 2.79 [108]. Incorporating cathode wear in our model improves the results and the simulated results matches well with the experimental results. Three distinct regions (tip, side and base) are marked in **Fig. 5.33**. Their corresponding SEM images are already shown in **Fig. 5.30**.

The entire surface of micro feature was divided into six equal segments to compare the results obtained in **Section 5.3.3**. The experimental data for surface roughness is plotted in **Fig. 5.34** along with the quadratic model obtained from **Fig. 5.27** for comparison. The phenomena of secondary and higher order discharges at the side of micro feature due to debris adhesion on walls of both electrode leads to variation in crater size. This in turn results in increased surface roughness on the sides as compared to the other portions of the micro feature. This can clearly be seen from the experimental plot of surface roughness in **Figs. 5.31**. Comparing the

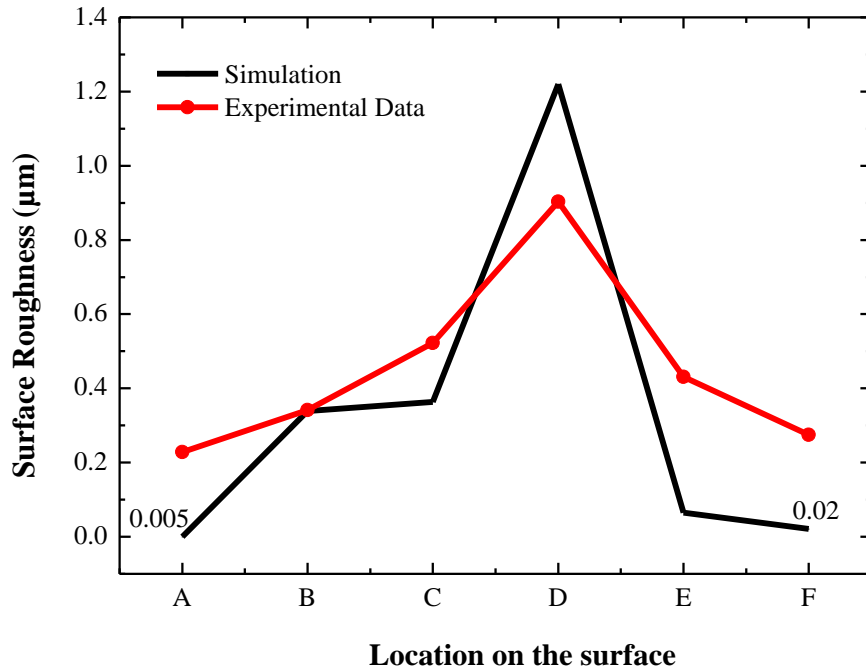


Fig. 5.34: Comparison of simulated and experimental results for surface roughness

experimental and simulated results of surface roughness, it can be seen that high amount of surface roughness is on the sides of micro feature (**D**) whereas surface roughness values are lower as we move away from the side of micro feature towards the tip (**F**) or base (**A**) of micro feature. The experimental results match well with the simulated results with a maximum error of 13%.

The phenomena for material removal due to secondary and higher order discharges and subsequent surface roughness can therefore be summarised by **Fig. 5.35**. The possible shapes of 3 – D hemispherical convex micro feature obtained by primary discharges alone as well as by incorporating secondary and higher order discharges along with primary discharges is shown. Due to tapered bottom drilled hole, equally larger radii at the base and at the sides are generated. In this case, initially a cylindrical shape is generated (shown by dotted lines on anode) till it reaches the tapered portion of the hole. Subsequently, the taper on the hole causes erosion at the corner of the generated cylinder. Furthermore, due to debris attachment to corners

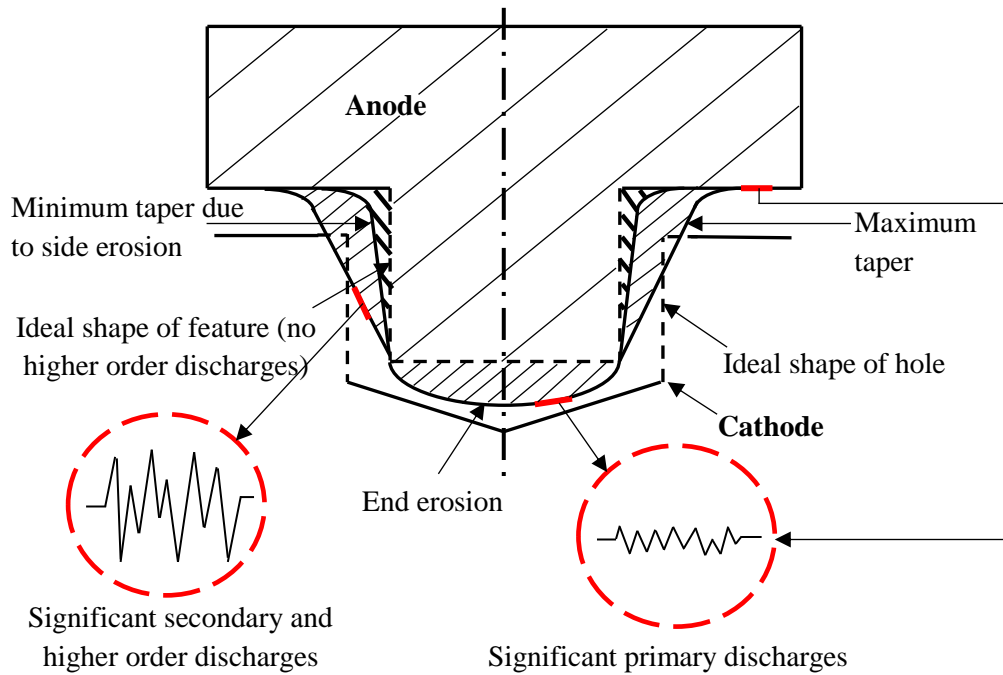


Fig. 5.35: Secondary and higher order erosion on 3 – D hemispherical convex micro feature

and walls of cathode as well as reduction in IEG due to debris agglomeration and suspension of debris in dielectric, secondary and higher order discharges take place which leads to increase in crater size at those areas increasing surface roughness and results in a hemi-spherical shaped micro feature. Both experimental and simulated results confirm the effect of secondary and higher order discharges leading to high surface roughness at the sides as compared to tip and base of the 3 – D hemispherical convex micro feature.

5.6 Fabrication of arrayed micro features

It has already been shown that suitable tool modification in RMEDM process can lead to generation of 3-D hemispherical micro feature. This section extends the capability of the process in generating of arrayed micro features of similar and dissimilar aspect ratios.

5.6.1 Array of 3-D hemispherical micro features

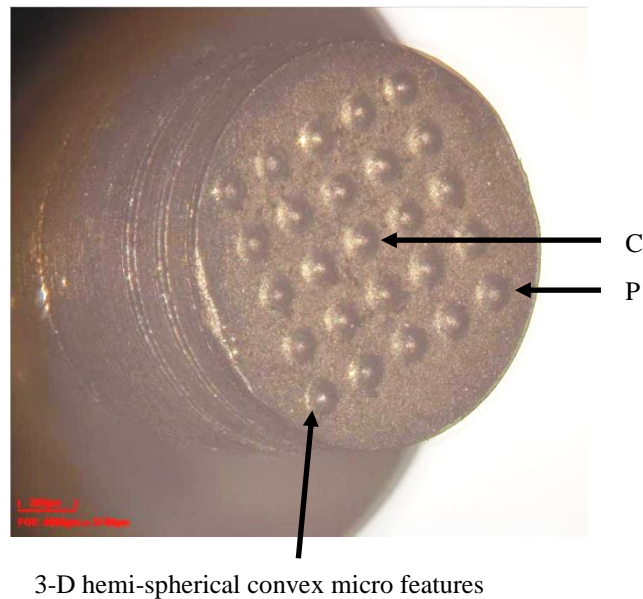


Fig. 5.36: Array of 5 by 5 3-D hemi-spherical convex micro features using RMEDM

The phenomenon of generating 3-D hemispherical convex micro features using RMEDM process was further extended to fabricate array of 3-D hemispherical convex micro features. Instead of a single tapered blind hole as tool in *Section 5.4.1*, the plate contained an array of 5 by 5 tapered blind holes. Experiments were conducted using constant hole diameter

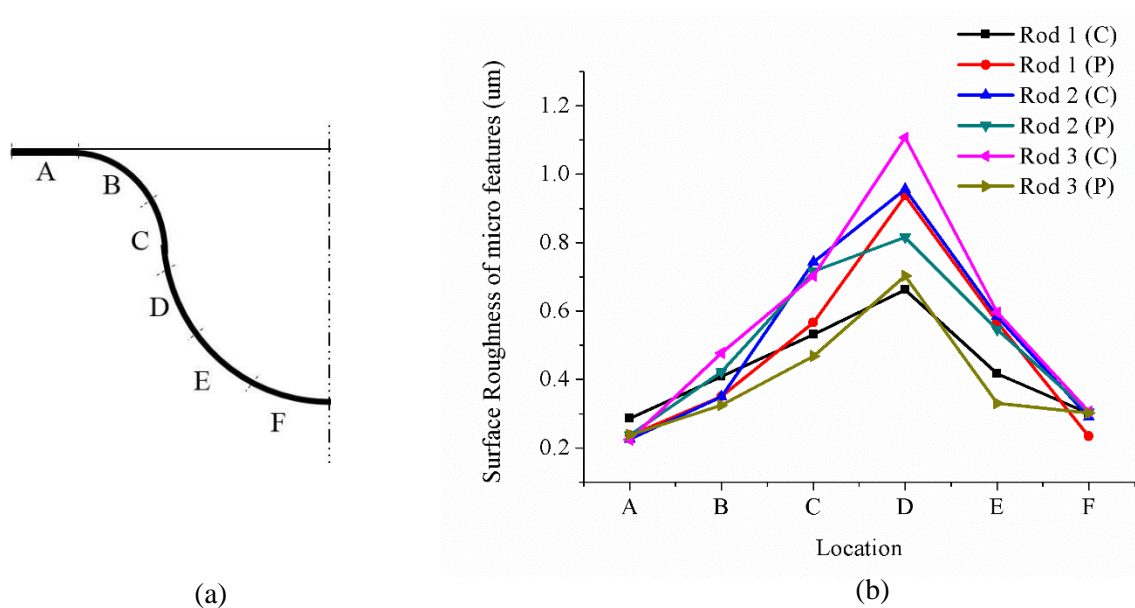


Fig. 5.37: (a) Symmetrical profile of 3-D hemi-spherical convex micro feature (b) Surface roughness obtained for various profile at different location

(0.2 mm) and constant hole depth of 0.1 mm. **Fig. 5.36** shows the fabricated array of 5 by 5 3-D hemispherical convex micro features. These experiments were repeated three times.

Surface Roughness (R_a) measurements were carried out at six different locations (A, B, C, D, E, and F) on each micro hemi-spherical feature as shown in **Fig. 5.37 (a)**. A total number of six micro features were measured on the three fabricated array. Two features per array were measured, one at the centre (C) of the array and other at the periphery (P) as indicated in **Fig. 5.36**. The results obtained are plotted in **Fig. 5.37 (b)**. It can be observed from the figure that surface roughness values are comparatively higher at the sides as compared to the flat or the end portion. It proves that irrespective of the number of 3-D hemispherical convex micro features fabricated on a surface, the surface roughness pattern is similar i.e. higher surface roughness at the sides while lower at the tip and base (**Figs. 5.34 & 5.37 (b)**). **Fig. 5.38** shows the profile of surface roughness obtained by plotting median values of R_a corresponding to each location. To obtain a relationship between surface roughness and location, a best fit curve was plotted that shows a third order polynomial relation between surface roughness and

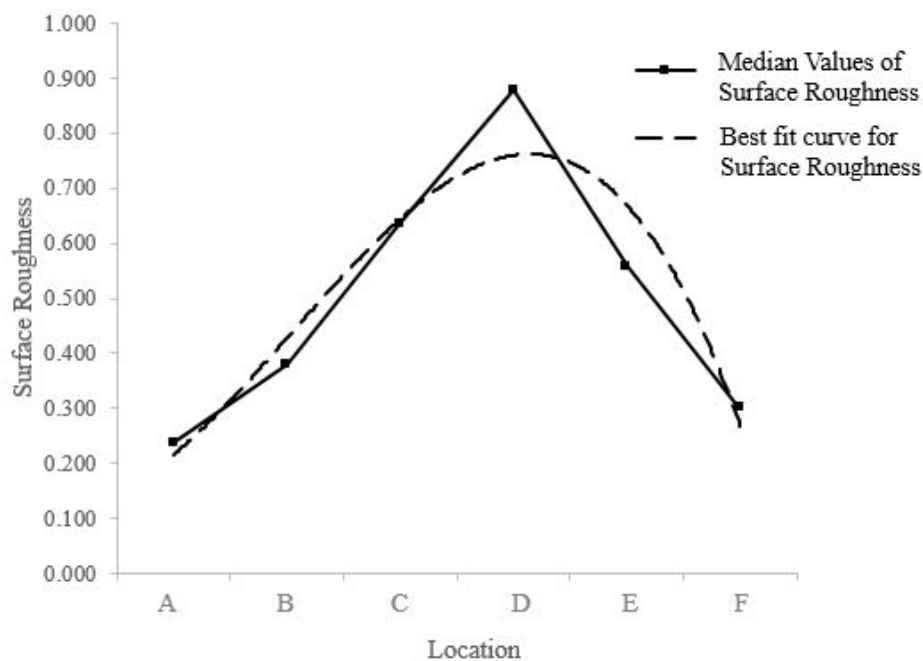


Fig. 5.38: Best fit curve for Surface Roughness

location (Eq. 5.12) with $R^2 = 0.89$.

$$y = 0.114 + 0.0126x + 0.1073x^2 - 0.0175x^3 \quad (5.12)$$

y = surface roughness (μm)

x = location on the micro feature (average) (μm)

A = 0-20 (average = 10 μm)

B=20-40 (average = 30 μm)

C=40-60 (average = 50 μm)

D=60-80 (average = 70 μm)

E=80-100 (average = 90 μm)

F=100-120(average = 110 μm)

5.6.2 Fabrication of protruded micro features with different shapes and heights

RMEDM process was further extended to generate micro features corresponding to different tapered blind hole depths. This was carried out to investigate the effect of the depth of blind holes on the shape and size of the generated micro features. Four tapered blind holes, each of diameter 0.2 mm were drilled on a plate with depths of 0.1 mm, 0.3 mm, 0.5 mm and 0.7 mm respectively. A schematic of the arrangement along with the final shape of features after traversing a depth of 1.2 mm is shown in Fig. 5.39. Fig. 5.40 shows the actual photograph of three of the machined micro features corresponding to tapered blind hole depths of 0.1 mm, 0.3 mm and 0.5 mm respectively.

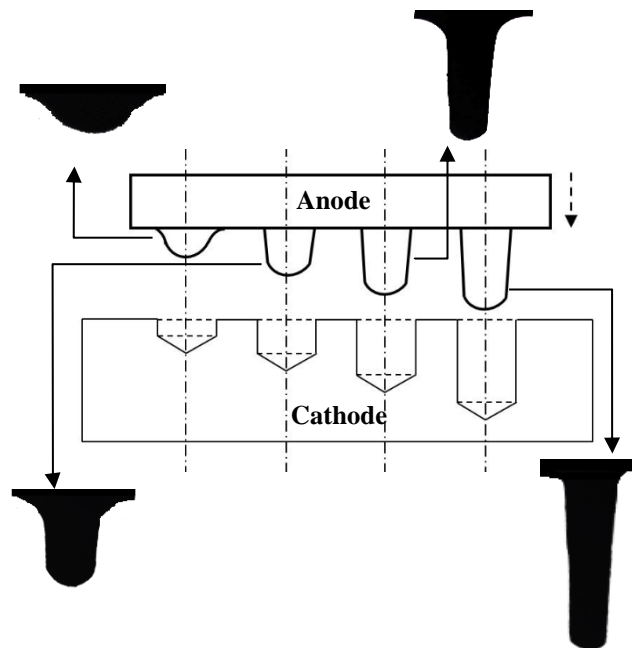


Fig. 5.39: Protruded micro features corresponding to different hole depths using RMEDM

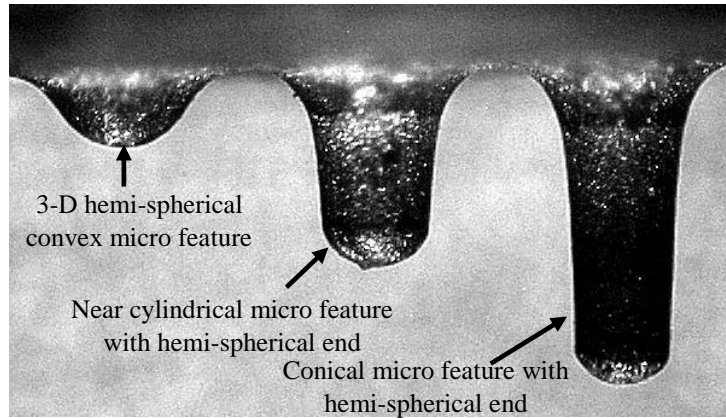


Fig. 5.40: Protruded micro features of different shape and height

Fig. 5.41 (a) shows the shapes and heights of the micro features at various traverse depths of anode (0.1, 0.5 and 1.2 mm) corresponding to hole depths of 0.1, 0.3 and 0.7 mm respectively. Micro feature corresponding to 0.5 mm hole depth has intentionally not been shown as it similar in shape to that corresponding to 0.7 mm hole depth. **Fig. 5.41 (b)** shows the 3-D image of one of the micro features using CCI. **Fig. 5.42** shows the height of micro features generated for various traverse for different hole depths. Hemi-spherical micro features are generated corresponding to hole depth of 0.1 mm at traverse of 1.2 mm (**Fig. 5.41 (a)**). In all other conditions, either near cylindrical or near cylindrical with hemi-spherical end or conical with hemi-spherical ends are generated. It is observed from **Fig. 5.41** that the achieved

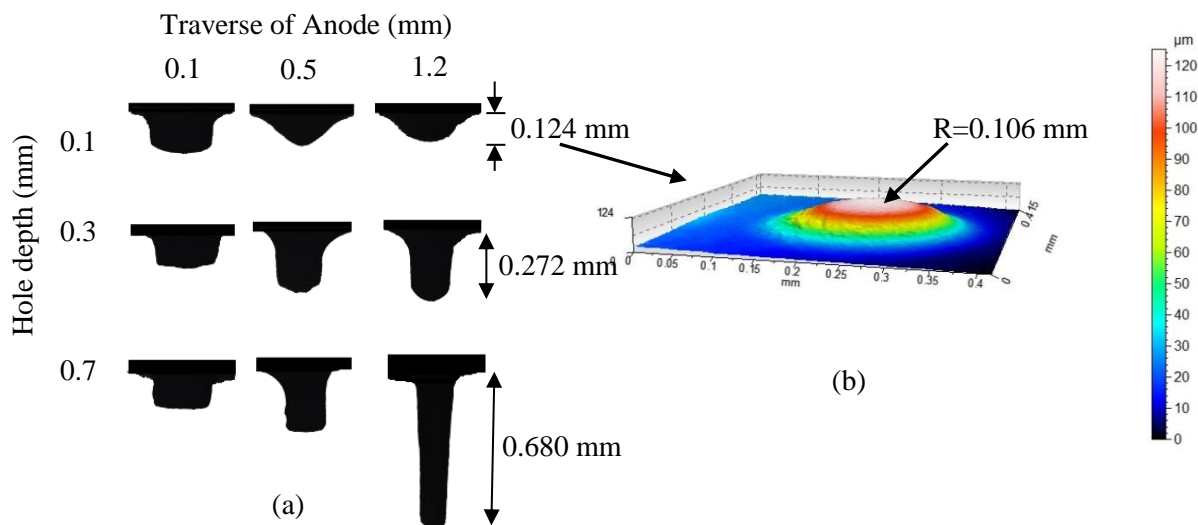


Fig. 5.41: (a) Shape of micro features generated using RMEDM (b) Shape of micro feature corresponding to 0.1 mm hole depth and 1.2 mm traverse

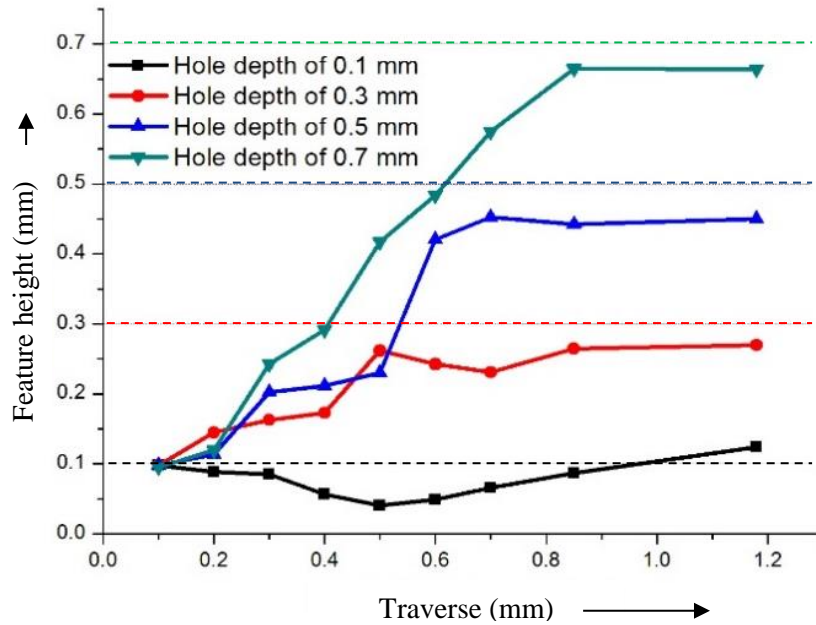


Fig. 5.42: Feature height vs Anode traverse

micro feature height (0.124 mm) for low aspect ratio hole (0.1 mm depth of hole) for a traverse of 1.2 mm is more than the hole depth. This is due to the easy escape passage available to the debris as well as erosion on cathode at low aspect ratio of the hole. Whereas in other cases, the feature height is always less than the hole depth indicating that the entrapped debris particles causes end erosion without causing high primary cathode erosion.

The process of fabrication of protruded micro features of different shapes and sizes simultaneously using RMEDM was also extended to array fabrication (**Fig. 5.43**) in which the central micro feature corresponds to tapered blind hole depth of 0.5 mm while the protruded micro features surrounding the central micro feature corresponds to 0.3 mm hole depth. The micro features at the periphery of the array of 5 by 5 micro features corresponds to 0.1 mm hole depth. Characterization of micro features were carried out using X-Ray computed micro tomography as well as SEM (**Fig. 5.43**).

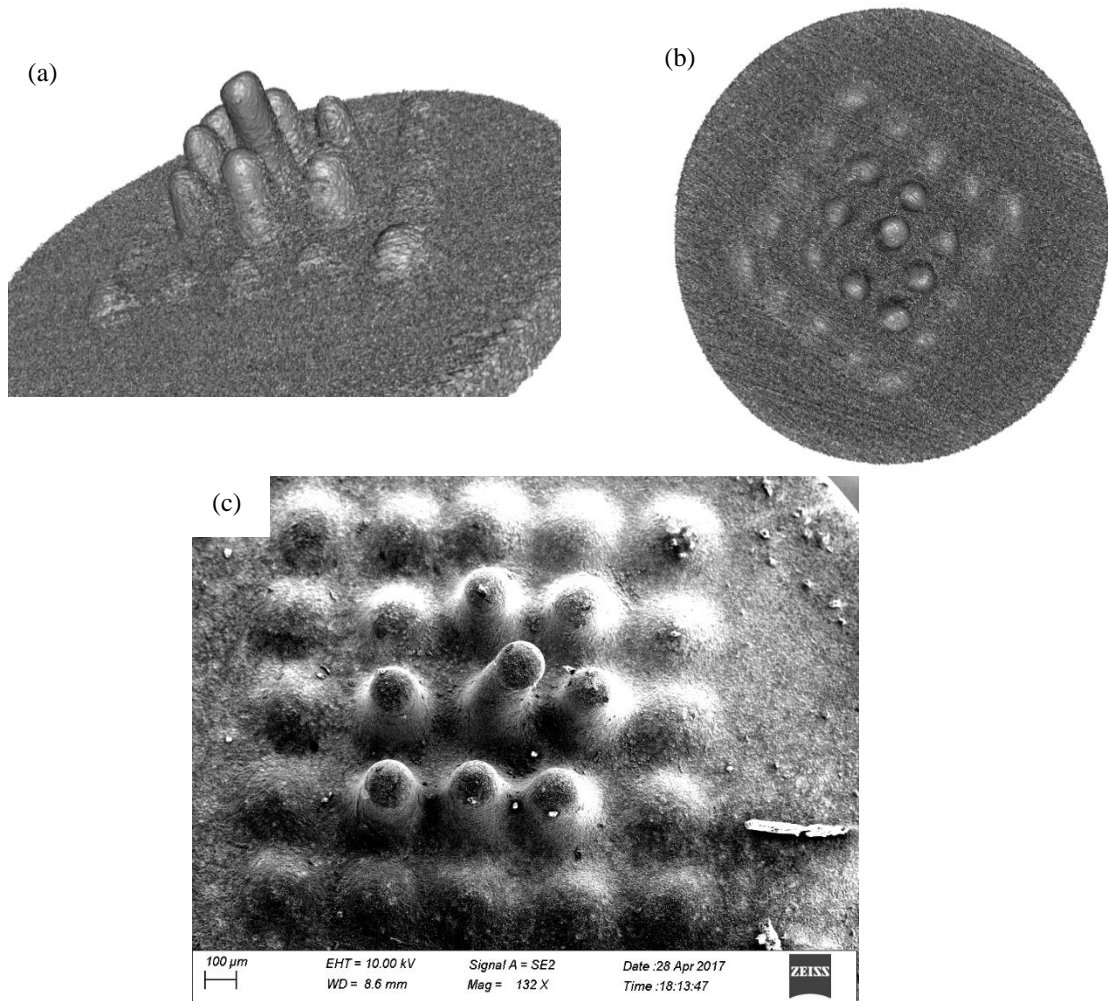


Fig. 5.43: (a) XMCT image of isometric and (b) top views (c) SEM image of 5 by 5 fabricated protruded micro features generated by non-conformal RMEDM

5.7 Summary

Based on FEA simulation and experiments, the mechanism of generation of 3-D hemispherical convex micro features has been described in detail in detail. Further, surface roughness analysis of the simulated shape was also carried out and validated with experiments. RMEDM process with tool modifications was used for generating single 3-D hemispherical micro feature as well as arrayed micro features of similar and dissimilar aspect ratios. The important findings from this study are as follows.

- A factor k_0 determined in this study relates the ratio of material removal by abnormal discharges to that by normal discharges. This ratio was found to be the most influential factor in determining the shape of micro feature by simulation.

- The machining process was divided into four stages depending on the occurrences of discharges between the cathode and anode. Steep decrease in plasma implosion pressure during *Stage I* helps in debris evacuation from machining zone and results in almost negligible amount of debris deposition on the tapered portion of the tool.
- Debris deposition during *Stage II* mostly occurred at the mid and end of the tapered portion. Abnormal discharge were very low in number which did not have substantial effect on the shape of micro feature.
- During *Stage III*, the smaller debris particles having higher velocity move out of the machining zone. The debris particles with higher size have comparatively lower velocity and thereby adhere to the walls of electrodes. Debris coming in contact with adhered debris reduces their velocity and agglomerate with these debris leading to increased mass of debris at the tapered portion of the tool. Very low pressure drop during Stage III is also contributes for higher adhesion and agglomeration of debris in this case.
- High amount of debris deposition in *Stage IV* is responsible for creating high amount of secondary and higher order discharges on the workpiece leading to formation of 3-D hemispherical convex micro feature.
- Pre-drilled hole as tool blocked the escape path of debris thereby allowing debris to adhere to walls of electrodes creating secondary and higher order discharges which was found to effect surface roughness. Surface roughness at the sides of micro feature was higher as compared to other regions due to occurrences of high amount of secondary and higher order discharges at the sides.
- Larger crater size on sides of micro feature confirms the occurrences of secondary and higher order discharges on sides leading to higher surface roughness as compared to base and tip of micro feature.

- Piecewise de-trending of simulated shape into six equal segments and fitting quadratic model on each segment for surface roughness matches closely with experimental results with a maximum error of 13%.
- Suitable tool modifications in RMEDM also enabled fabrication of arrayed micro features of similar aspect ratio as well as different aspect ratio of micro features.

CHAPTER 6

MECHANICAL AND MICROSTRUCTURAL CHARACTERIZATION OF MICRO FEATURES GENERATED BY RMEDM FOR RECAST LAYER AND HAZ

6.1 Introduction

This chapter investigates the extent of formation of recast layer and heat affected zone (HAZ) of 3-D hemispherical convex micro feature fabricated using RMEDM. Their mechanical properties (hardness, elastic modulus and residual stresses) are determined and compared to that of parent material. Mechanical properties determined for 3-D hemispherical convex micro feature were also compared with that of protruded micro feature having different heights fabricated by RMEDM process. Thickness of discharge affected layers of arrayed micro features with different heights were also found out using X-Ray micro computed tomography (XMCT).

6.2 Characterization by destructive testing method for determination of recast layer and HAZ of 3-D hemispherical micro feature

RMEDM generated micro features inevitably contains recast layer and HAZ. Due to low energy in RMEDM, the extent of recast layer and HAZ are less as compared to macro EDM process. This section determines extent of recast layer and HAZ formed on the 3-D hemispherical convex micro feature and also compares its mechanical properties to that of the parent material.

6.2.1 Preparation and characterization of samples for nano indentation

Preparation of sample for nano indentation tests was carried out with utmost care since little amount of force might lead to breakage of the micro feature from the surface making it unusable for characterization. Mounting press (Model - Citopress-10) was used for mounting the sample (micro feature) on a transparent polymeric mould for proper holding during polishing (**Fig. 6.1**). Polishing was carried out using specimen preparation unit (Model - Tegra Doser-1). The sample was cleaned after an interval of 1 minute and was observed through

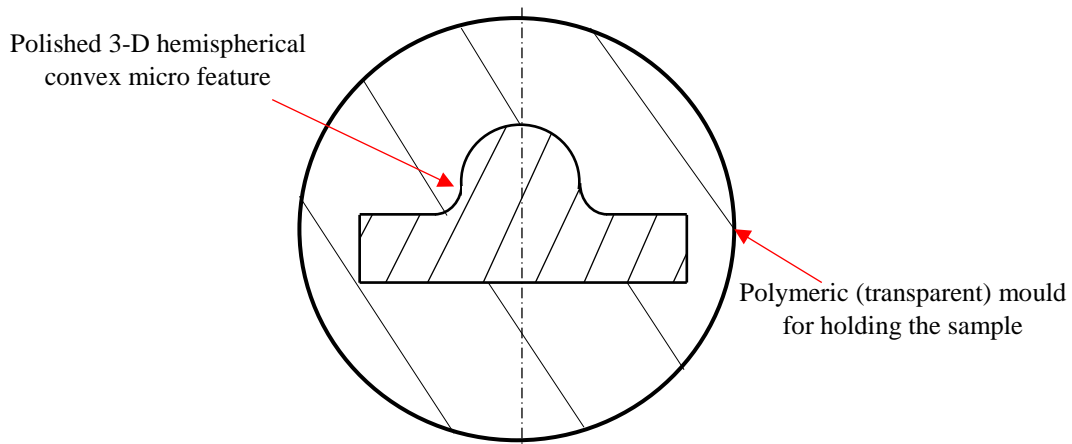


Fig. 6.1: Polished 3-D hemispherical convex micro feature mounted on polymeric transparent mould

optical microscope. This process was continued until the internal structure of the micro feature was clearly observed. Subsequent etching was carried out using concentrated nitric acid solution for approximately 5 seconds. By this process, the grain structure of the micro feature was exposed.

Grain structure visualization of the etched micro feature was carried out using electron back scattered diffraction (EBSD). Indentations were performed on the etched micro feature at different locations to determine the load-displacement curves and mechanical properties (hardness and elastic modulus) of the parent material, recast layer and heat affected zone.

6.2.2 Nano indentation system

Nano indentation experiments were performed on TI 900 TriboIndenter that has an integrated optical microscope with high magnification for observation of surfaces. It has the capability for both low (upto 10 μN) and high (upto 500 mN) indentation loads with a resolution of 1 nN. Z-axis displacement resolution is 0.04 nm and that of X-axis is upto 4 nm.

Three different sets of nano indents (a total of 18 nano indents) were made on the micro feature. Each set of 6 nano indentation and location of each nano indentation are shown in **Fig. 6.2**. The initial nano indent (N_1) was made near the periphery and subsequent nano indents (N_2 - N_6) were made at a distance of 5 μm interval respectively and each moved towards the centre

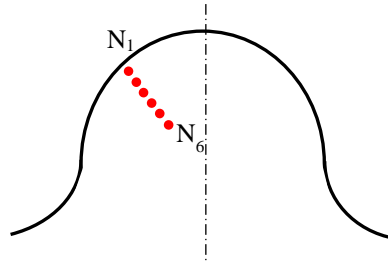


Fig. 6.2: Location of one set of nano indents on etched micro feature

of the micro feature until and unless the mechanical properties of parent material was found on any one of the nano indents. Two other sets of nano indents were performed for repeatability. Apart from that, a total of 6 nano indents were also made at locations far away from the micro feature (discharge locations) in order to find the mechanical properties of the parent material. The properties of parent material serve as reference for determining mechanical properties of the nano indents. Nano indentation experiments were performed using displacement controlled mode with a maximum indentation depth of 200 nm.

6.2.3 Microstructural characterization and determination of recast layer thickness

Fig. 6.3 shows the grain structure of the etched micro feature which has been segregated into two zones. The zone at the top represents the region wherein discharges occurred that led

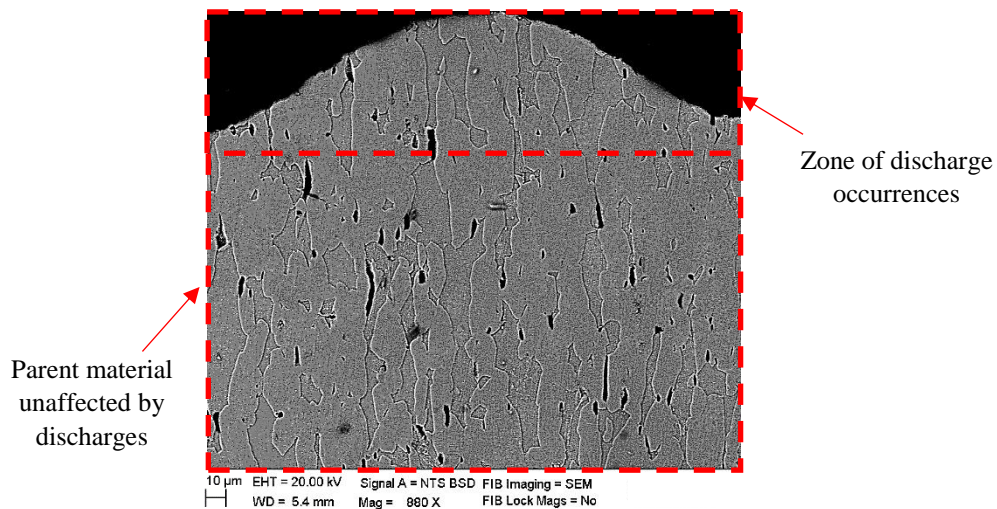


Fig. 6.3: Grain structure of etched micro feature

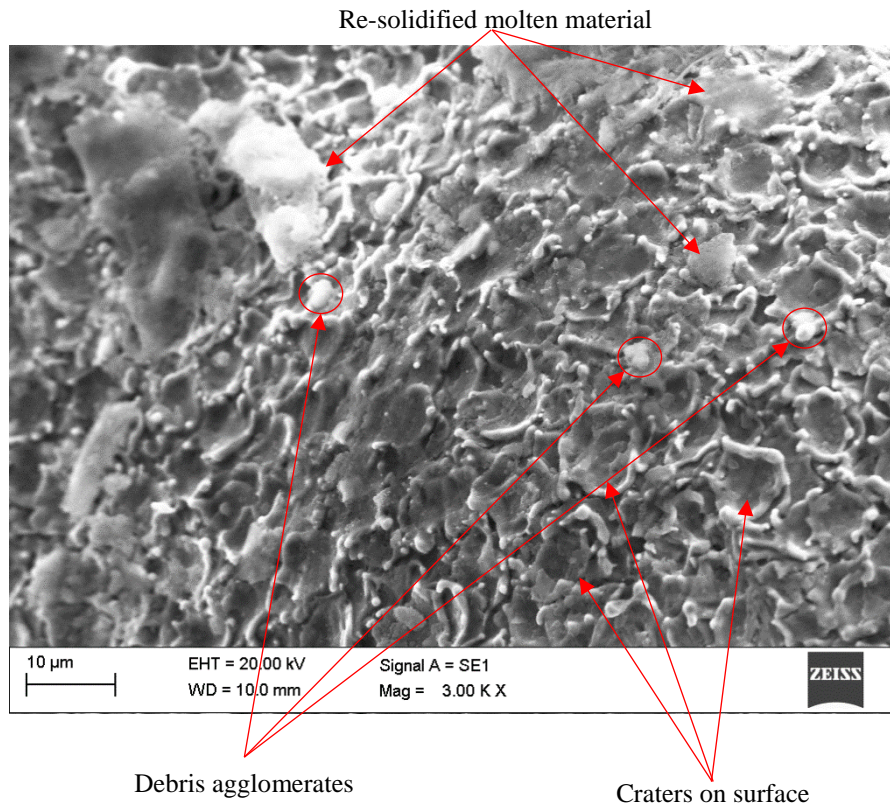


Fig. 6.4: Magnified view of a portion of the micro feature

to shaping of the micro feature. The bottom zone represents the region which was free from discharges and thereby constitutes the parent material.

Formation of recast layer is inevitable in case of material removal processes that uses energy beam as source viz. EDM, laser machining etc. The properties of the recast layer is different as compared to the parent or unaffected material [84]. Due to this, it is extremely important to determine the thickness of recast layer and its mechanical properties as compared

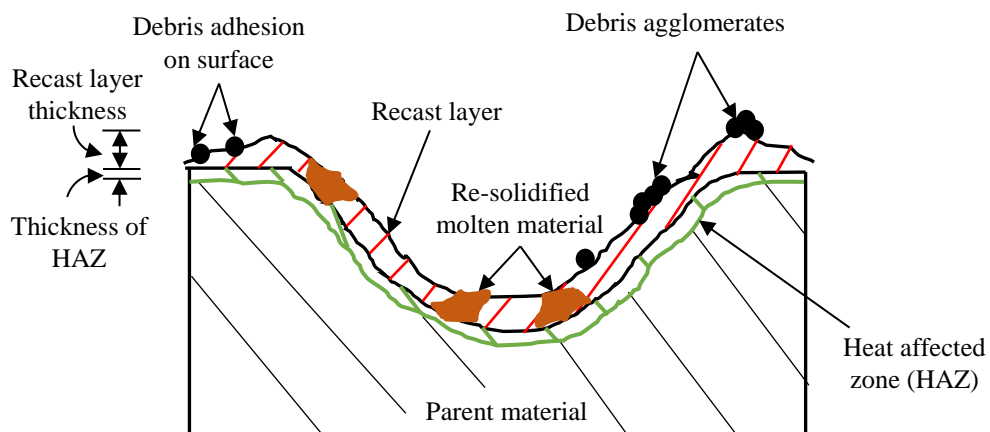


Fig. 6.5: Schematic of formation of recast layer and HAZ in a single crater

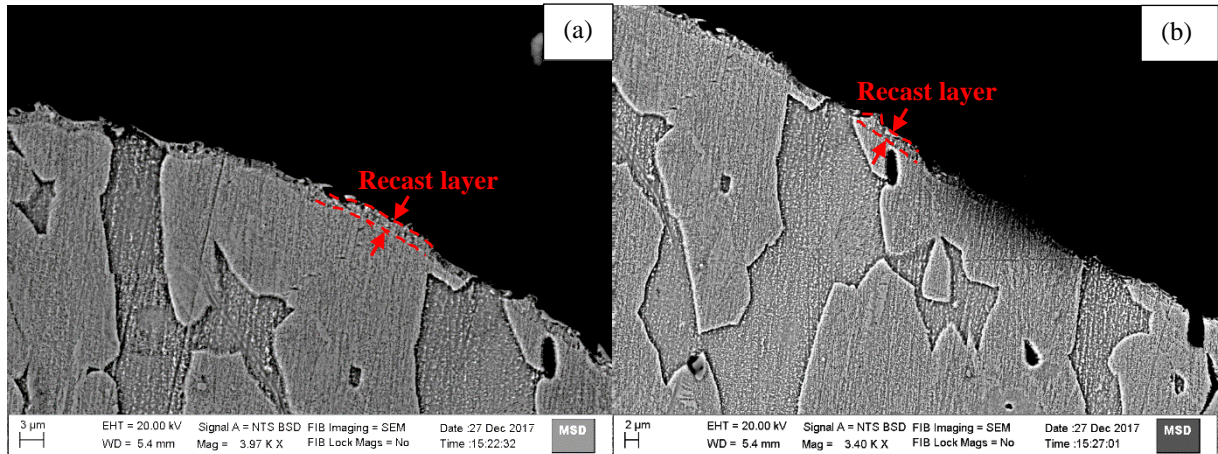


Fig. 6.6: Recast layer on micro feature (a) Near the tip (b) Near the base

to the parent material. **Fig. 6.4** shows a magnified view of a portion of the micro feature. The surface of micro feature consists of a large number of craters that were formed due to large number of discharges occurring during machining. These craters are accompanied by debris agglomerates as well as re-solidified molten material that were deposited on the surface. Recast layer is an accumulation of these debris agglomerates and the re-solidified material on the surface. A schematic of the formation of recast layer on a single crater is shown in **Fig. 6.5**. Discharge energy in case of micro EDM and its variants are very low as compared to EDM

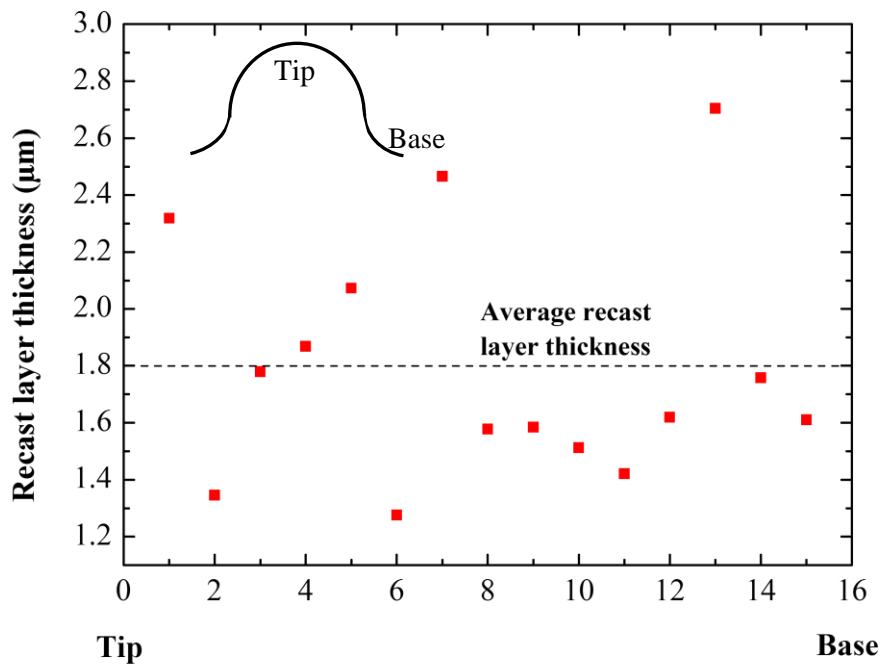


Fig. 6.7: Thickness of recast layer on the micro feature (16 sample points)

process, therefore, very small amount of material removal takes place from the surface after every discharge. The adverse effects such as cracks, voids etc. which are common in traditional EDM process due to high discharge energy are absent in this case. Grain structure of zone of discharge occurrences do not vary significantly as compared to parent material (**Fig. 6.3**).

Fig. 6.6 shows the EBSD images of recast layer near the tip as well as near the base of the micro feature. As compared to traditional EDM process where recast layer is of the order of 20-40 μm [126–128], the thickness of recast layer in this case is very small. This is due to comparatively smaller amount of discharge energy which leads to smaller amount of material removal from the surface. Measurement of thickness of recast layer was carried out at 15 different locations on the micro feature starting from the tip to the base. Public domain image processing software (ImageJ 1.46r, NIH) was used for measurement. The thickness of recast layer is plotted against its location and shown in **Fig. 6.7**. Thickness of recast layer varied from 2.7 μm to 1.3 μm . The average thickness of recast layer was found to be 1.8 μm .

6.2.4 Mechanical properties of recast layer and heat affected zone (HAZ)

Fig. 6.5 also shows the occurrence of heat affected zone (HAZ) just beneath the recast layer. As the grain structure of the micro feature do not show any significant effect of HAZ (**Figs. 6.3 & 6.5**), therefore, to determine the extent of HAZ, nano indentation experiments were carried out. Location of HAZ was identified by relating the hardness values obtained from nano indentation with that of the parent material and the recast layer (**Fig. 6.8**). Hardness of HAZ should be significantly different from both the recast layer as well as the parent material. In addition to hardness, elastic modulus for both recast layer and HAZ were also found out using nano indentation. Determination of these mechanical properties helps in estimating the life expectancy of these micro features particularly in tribological applications.

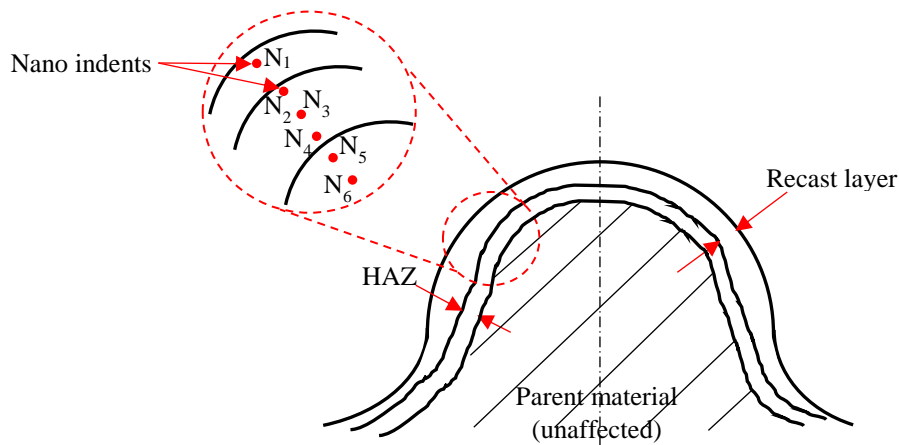


Fig. 6.8: Schematic of micro feature showing the location of nano indents with recast layer and HAZ

Typical loading-unloading curves for parent material and nano-indentations N₁ and N₆ have been plotted and shown in **Fig. 6.9**. It can be seen that loading-unloading curve for N₁ has higher loading values and lower final displacement as compared to parent material. The loading-unloading curve for N₆ is similar to the parent material confirming that it is unaffected by the discharges and forms a part of the parent material. Hence, indentations were limited to 6 for each case since N₆ shows the behaviour of parent material.

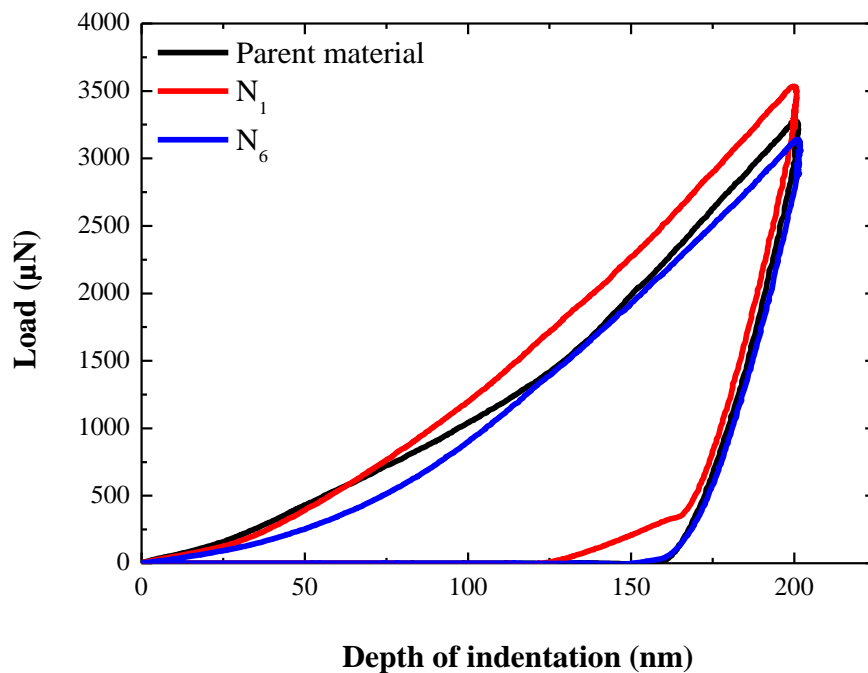


Fig. 6.9: Loading and unloading curves for nano-indentations made on parent material, recast layer (N₁) and near the centre (N₆) of the fabricated 3-D hemispherical protruded micro feature

Nano-indentation helps in determining the hardness, H and modulus of elasticity, E of the recast layer and HAZ as compared to the parent material. The following formulas are used for finding out H and E [129].

$$H = \frac{P_{max}}{A} \quad (6.1)$$

$$E_r = \frac{\sqrt{\pi}}{2} \frac{S}{\sqrt{A}} \quad (6.2)$$

$$\frac{1}{E_r} = \frac{1 - \nu^2}{E} + \frac{1 - \nu_i^2}{E_i} \quad (6.3)$$

Where, P_{max} : peak indentation load, A : projected area of the hardness impression, S : contact stiffness, H : hardness, E_r : reduced modulus of elasticity with consideration of the effect of non-rigid indenters, ν, E : Poisson's ratio and elastic modulus of material, ν_i, E_i : Poisson's ratio and elastic modulus of Berkovich indenter.

Based on **Eqs. 6.1 – 6.3**, hardness and elastic modulus have been calculated and shown in **Figs. 6.10 – 6.11** respectively. Referring to **Fig. 6.10**, the average hardness of the parent material has been found out to be 3.2 GPa. Localized heating of surface during discharge results in melting and vaporization leading to removal of small amount of material from the workpiece. Most of the molten material, however, re-solidifies and settles on the surface. Due to very short pulse on and off times during machining in RMEDM (of the order of tens of ns), there is a possibility of quenching on the surface that leads to formation of recast layer. Due to this, a hardened recast layer is formed which can be confirmed based on higher hardness values of recast layer (N_1) as compared to the parent material. The quenched zone is still present a little distance away from the recast layer as indicated by the higher hardness value (N_2). This marks the onset of HAZ which is composed of two layers (a) hardened layer and (b) annealed layer

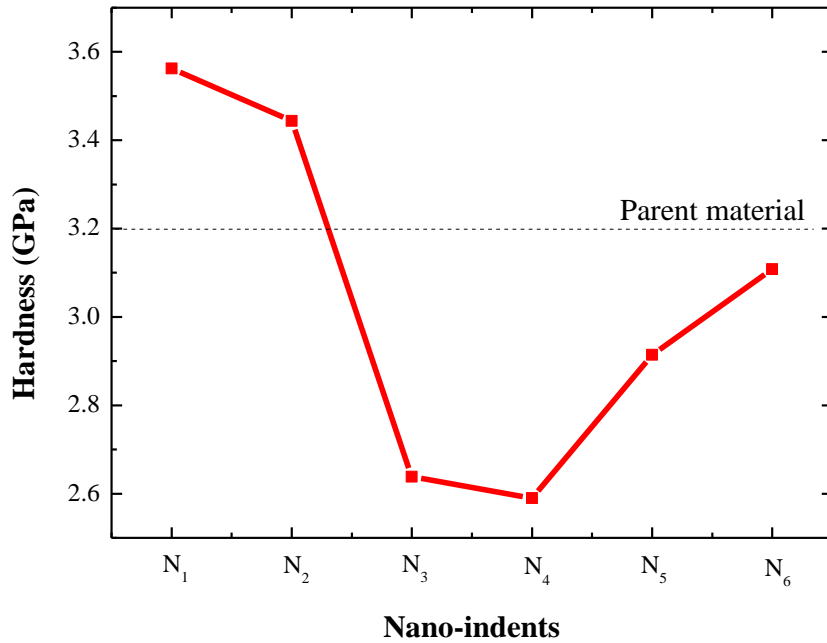


Fig. 6.10: Variation of hardness on the fabricated 3-D hemispherical protruded micro feature

[130]. N₂ denotes the hardened layer of HAZ, which is followed by a steep decline in hardness (N₃) at a distance of around 10 μm from the periphery. In this zone, relatively slower cooling of material takes place that leads to formation of soft layer with a lower hardness as compared to the parent material. The soft layer of HAZ extends to a length of approximately 10 μm (N₃, N₄) beyond which the material starts regaining its original hardness (N₅). The hardness at a distance of around 30 μm from the periphery (N₆) is approximately similar hardness as the parent material indicating that this zone is unaffected by the discharges.

During the unloading process, the load will be reduced at a constant rate. Pure elastic recovery occurs in this process. The reduced elastic modulus (**Eq. 6.2**) can be correlated to the slope of the displacement-unloading curve. Elastic modulus for recast layer, HAZ and parent material were determined using **Eq. 6.3**. The resulting elastic modulus for nano indents (N₁-N₆) is shown in **Fig. 6.11**. A horizontal line depicts the elastic modulus of the parent material.

Recast layer formation (N₁) leads to substantial increase in the elastic modulus as compared to the parent material. Beyond the recast layer, there is a reduction in elastic modulus

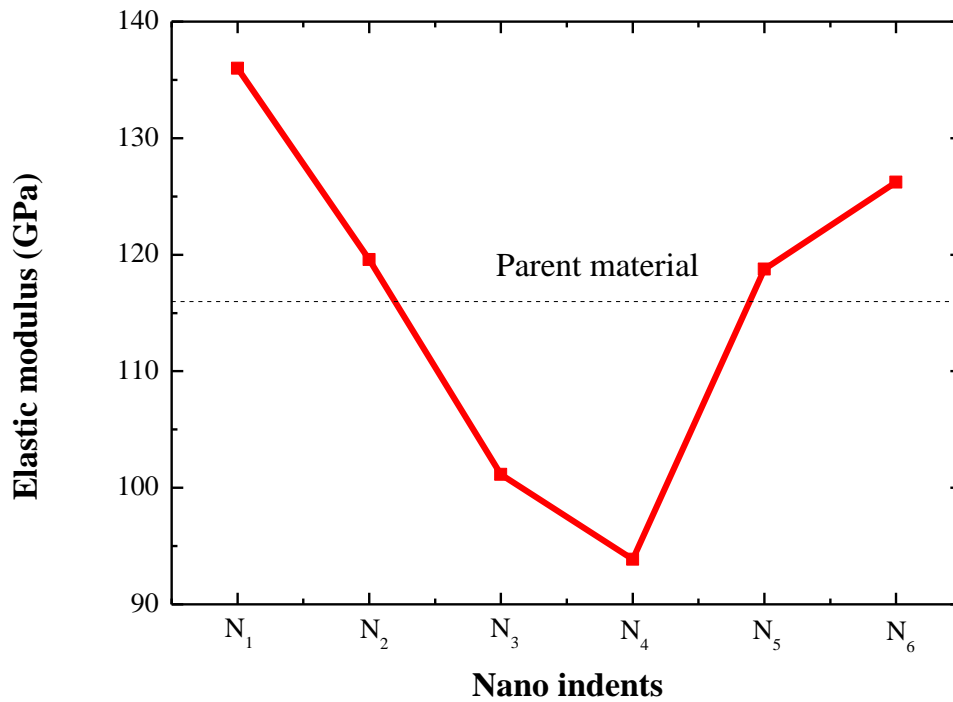


Fig. 6.11: Variation of elastic modulus on the fabricated 3-D hemispherical protruded micro feature

of the hardened layer of HAZ (N₂) and is close to that of the parent material. This decrease in elastic modulus from the recast layer to the hardened layer of HAZ is also observed for hardness (Fig. 6.10) [83,131]. The elastic modulus reduces further for the soft layer of HAZ (N₃, N₄). This variation in HAZ primarily arises due to hardening and softening of material due to

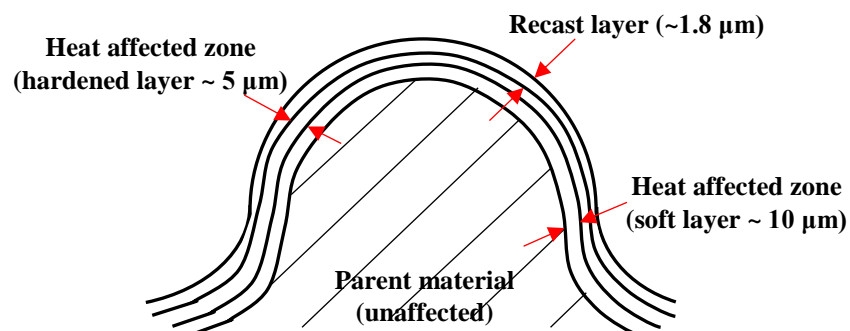


Fig. 6.12: Schematic of 3-D hemispherical protruded micro feature showing the recast layer, hardened and soft layer of HAZ

discharge leading to reduced elastic modulus in the soft layer. Beyond the HAZ, the material regains the original properties of the parent material.

Based on the above discussion, the recast layer, hardened layer and soft layer can be demarcated from the parent material as shown in **Fig. 6.12**. The thickness of each layer along with the height of micro feature is also indicated. The recast layer has the highest hardness and elastic modulus while the softened layer of HAZ has the least of all. The properties of parent material are intermediate between the two.

6.2.5 Qualitative analysis of residual stress

A qualitative comparison of residual stresses between the recast layer and heat affected zone with that of parent material is carried out based on loading and unloading curves obtained from nano indentation tests. Load-displacement curves are significantly affected by the presence of residual stresses in the material. For same penetration depth (200 nm in this case), higher loading values as compared to parent material indicates increase in compressive stresses whereas decrease in load indicates presence of tensile stresses. **Fig. 6.13** shows the effect of residual stress on loading curves for nano-indenters N_1 - N_6 as compared to the parent material. Recast layer (N_1) and hardened layer of HAZ (N_2) exhibits some amount of residual compressive stresses as the amount of load required for penetrating 200 nm is higher as compared to parent material. Residual compressive stresses constrain the indentation plasticity [132] and hence, higher loads are required for indentation as compared to parent material. High hardness on recast layer is due to presence of compressive residual stresses [133]. Soft layer of HAZ (N_3 - N_4), on the other hand, exhibits tensile residual stress, since, the amount of load requirement for same penetration is lower as compared to parent material. Hence, the hardness of soft layer of HAZ is also low. The presence of tensile residual stress enhances the indentation plasticity as compared to parent material [132] and hence, lower loads are required. Beyond

N₄, the material starts regaining its original strength as the loading curves (N₅- N₆) are shifted towards that of parent material.

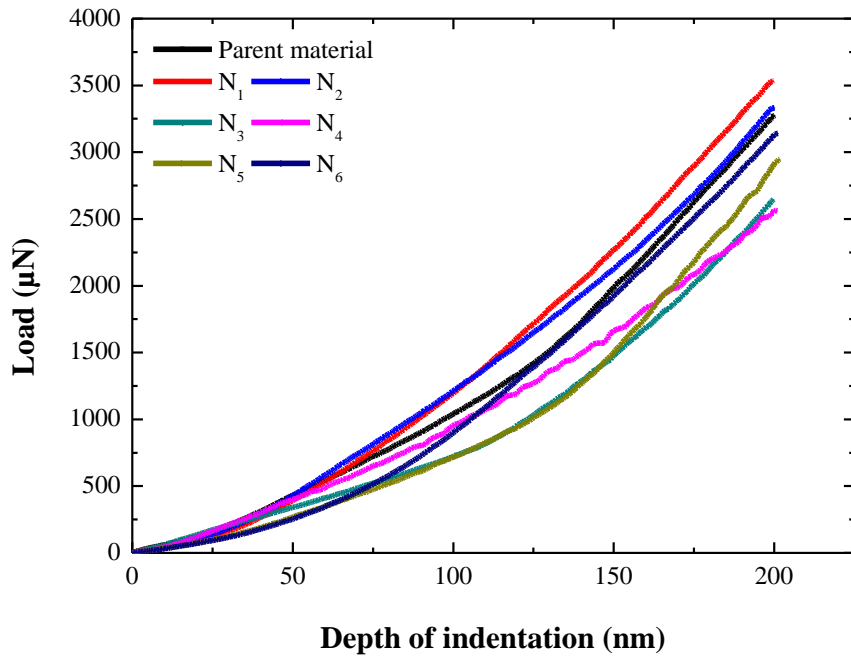


Fig. 6.13: Loading curves for indents made to a maximum depth of 200 nm with different residual stresses

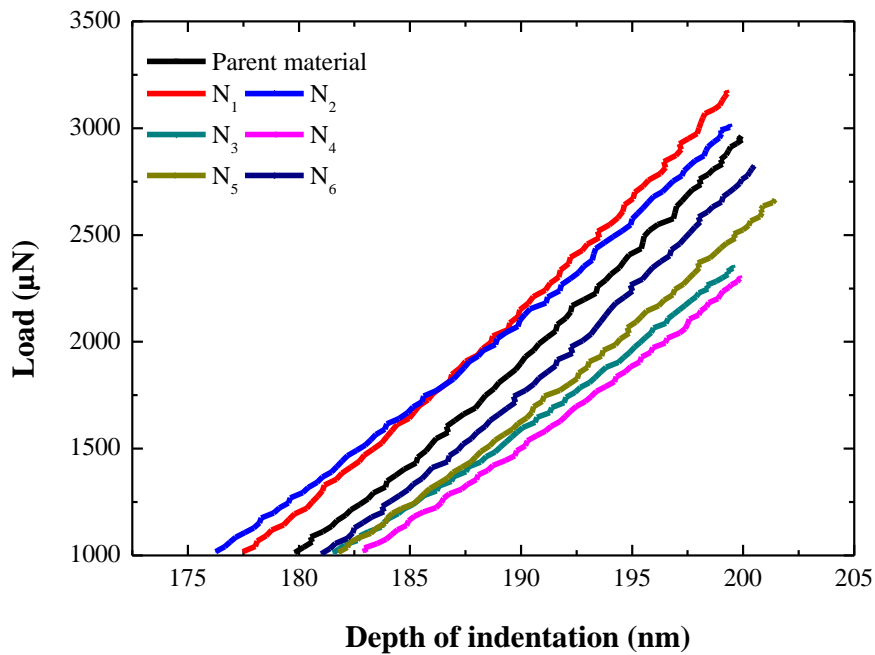


Fig. 6.14: Ending part of unloading curves for indents made to a maximum depth of 200 nm with different residual stress states

The presence of residual stress can also be confirmed based on unloading curves of material obtained from nano-indentation tests. The unloading curves undergo pure elastic recovery and no plastic recovery takes place [134]. The ending part of unloading curves (N_1 - N_6) is shown in **Fig. 6.14**. With respect to parent material, the unloading curves for recast layer (N_1) and hardened layer of HAZ (N_2) shift towards left. Since, presence of residual compressive stresses tend to lift the indenter higher as compared to parent material, more elastic recovery and smaller residual depths are induced in the recast layer. Corresponding to unloading curves for soft layer of HAZ (N_3 - N_4), an opposite effect i.e. lesser elastic recovery and larger residual depth is obtained indicating a tensile residual stress in this layer as compared to parent material.

6.2.6 Comparative analysis of mechanical properties of micro features

RMEDM process was extended to fabricate arrays of micro features as well as different shapes of micro features apart from 3-D hemispherical convex micro feature (*Section 5.5*). In this section, comparative analysis of mechanical properties of 3-D hemispherical convex micro feature is carried out with respect to micro feature generated corresponding to 0.3 mm tapered blind hole depth. Based on experimental procedures already described in *Chapter 5*, the micro

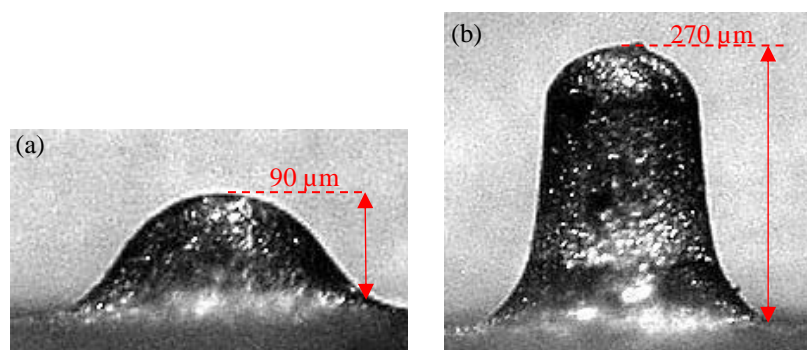


Fig. 6.15: Optical microscopic images of protruded micro features corresponding to tapered blind hole depth of (a) 0.1 mm (b) 0.3 mm

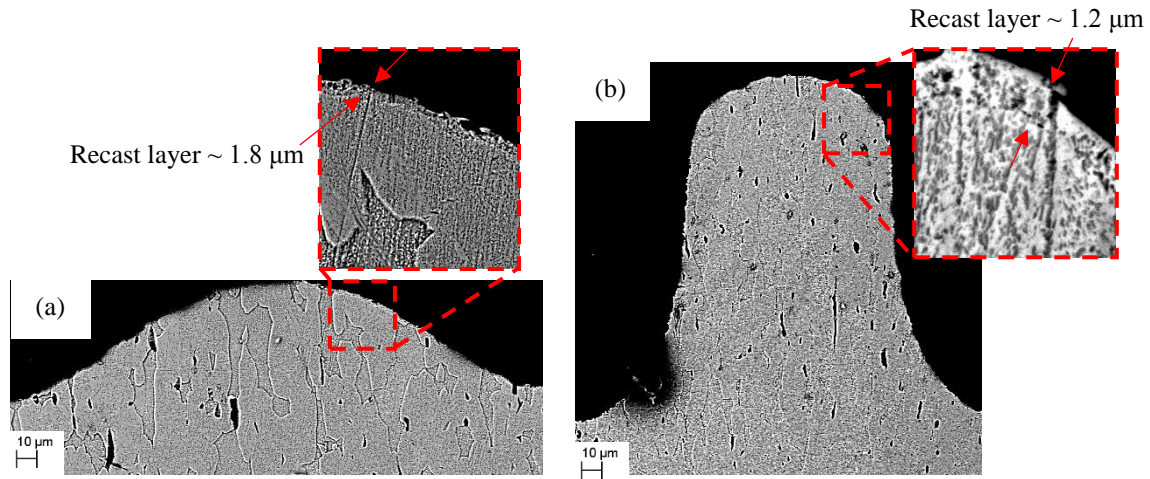


Fig. 6.16: EBSD images of protruded micro features corresponding to tapered blind hole depth of (a) 0.1 mm (b) 0.3 mm

features generated using RMEDM is shown in **Fig. 6.15**. The shape of micro feature obtained using tapered blind hole depth of 0.3 mm is cylindrical with hemispherical end. Polishing and etching processes and location of nano indents already described in *Sections 6.2.1-6.2.2* were also carried out on the micro feature corresponding to tapered blind hole depth of 0.3 mm. **Fig. 6.16** shows the EBSD images of the exposed grain structures of the micro features. A magnified image is also shown depicting the recast layer in each case.

6.2.6.1 Comparison of maximum load (P_{max})

The maximum load (P_{max}) obtained from loading – unloading curve is a very important factor that affects the mechanical properties viz. hardness and elastic modulus of the specimen. Typical loading-unloading curves for the parent material and the micro features is shown in **Fig. 6.17**. It can clearly be seen that the maximum load required for indenting 200 nm is different in all the three cases. The maximum load required in case of micro feature corresponding to hole depth of 0.3 mm is higher as compared to parent material. On the other hand, there is a reduction in maximum load for indenting a depth of 200 nm in case of 3-D hemispherical convex micro feature. This variation in maximum load is primarily due to

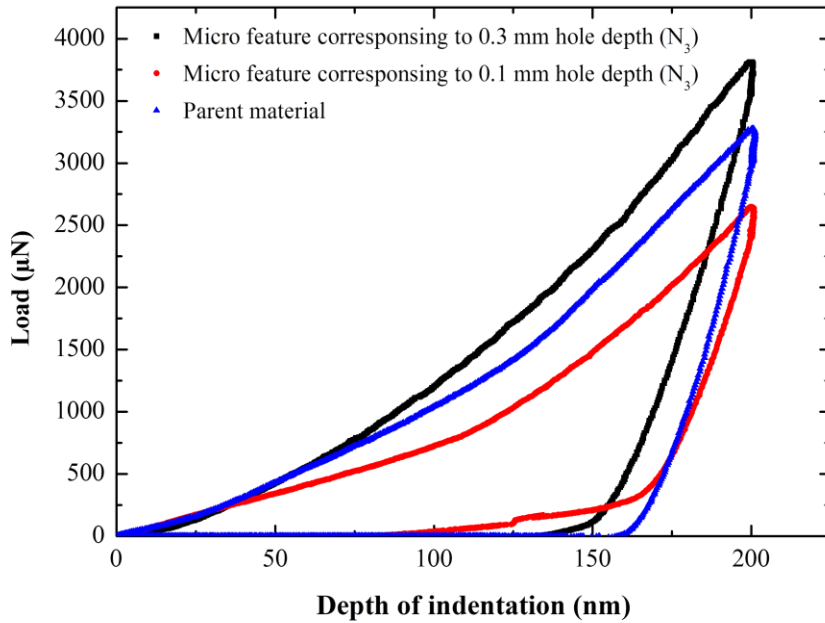


Fig. 6.17: Typical loading-unloading curves for protruded micro features corresponding to nano indent N_3

change in mechanical properties of the protruded micro features generated due to different hole depths as compared to the parent material. Hence, variation of depth of tapered blind hole is indirectly responsible for different load requirements for same indentation (200 nm).

Maximum load (P_{max}) for nano indents (N_1 - N_6) corresponding to both the micro features have been calculated and shown in **Fig. 6.18**. The horizontal line at 2925 μN depicts the maximum load corresponding to parent material measured at reference location shown in **Fig. 6.17**. With respect to 3-D hemispherical convex micro, it can be seen that there is an increase in P_{max} initially (N_1) indicating that higher loads are required to create permanent impression on the micro feature. On moving towards the centre (N_3 , N_4), the maximum load requirement decreases drastically indicating that very low loads are required for indenting the material. Beyond N_4 , maximum load requirement is similar to that of the parent material.

Considering the case of micro feature corresponding to hole depth of 0.3 mm, it can be seen that the maximum load increases and remains higher than parent material at all instants (N_1 - N_5). This is in contrary to the case with micro feature corresponding to 0.1 mm hole depth

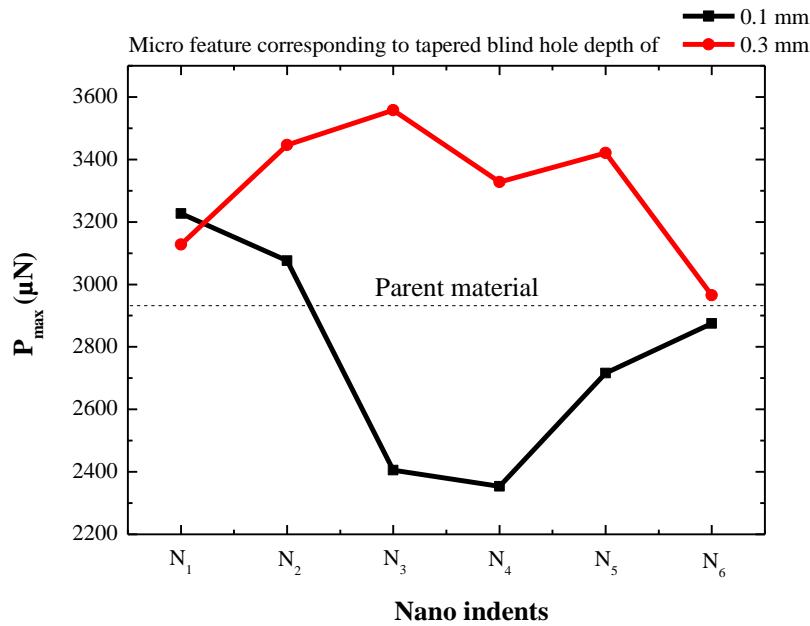


Fig. 6.18: Comparison of maximum indentation load of the protruded micro features

where comparatively lower loads are required for similar indentation. The variation in P_{max} suggests that there is a variation in mechanical properties due to which there is different load requirement at different location on each micro feature as well as on the protruded micro features with respect to the parent material.

6.2.6.2 Comparison of hardness

Eqs. 6.1 – 6.3 are used for determining the mechanical properties of the protruded micro features. Based on **Eq. 6.1**, hardness of the micro features was calculated and the values obtained are shown in **Fig. 6.19**. The hardness values for hemispherical convex micro feature in the recast layer, HAZ has already been explained in **Section 6.2.4**.

The initial value of hardness (N_1) of micro feature corresponding to 0.3 mm hole depth is similar with the 3-D hemispherical convex micro feature. This is the zone of recast layer which has similar hardness in both cases irrespective of hole depth. Beyond N_1 , there is a steep increase in hardness of micro feature corresponding to 0.3 mm hole depth. With increase in tapered blind hole depth, disposal of debris becomes difficult as the flushing of dielectric

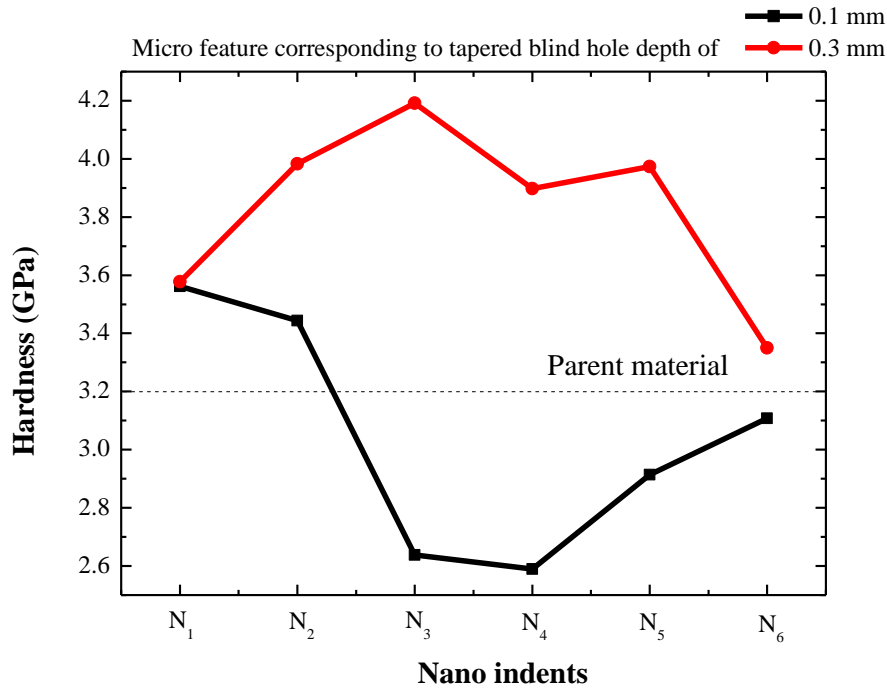


Fig. 6.19: Comparison of hardness of the protruded micro features

becomes inefficient at higher hole depths. Due to this, debris agglomeration increases inside the cavity. This leads to increase in the number of abnormal discharges in the machining zone on the micro feature corresponding to 0.3 mm hole depth. Due to higher amount of discharges, there is a significant reduction in the amount of time required for softening of material since

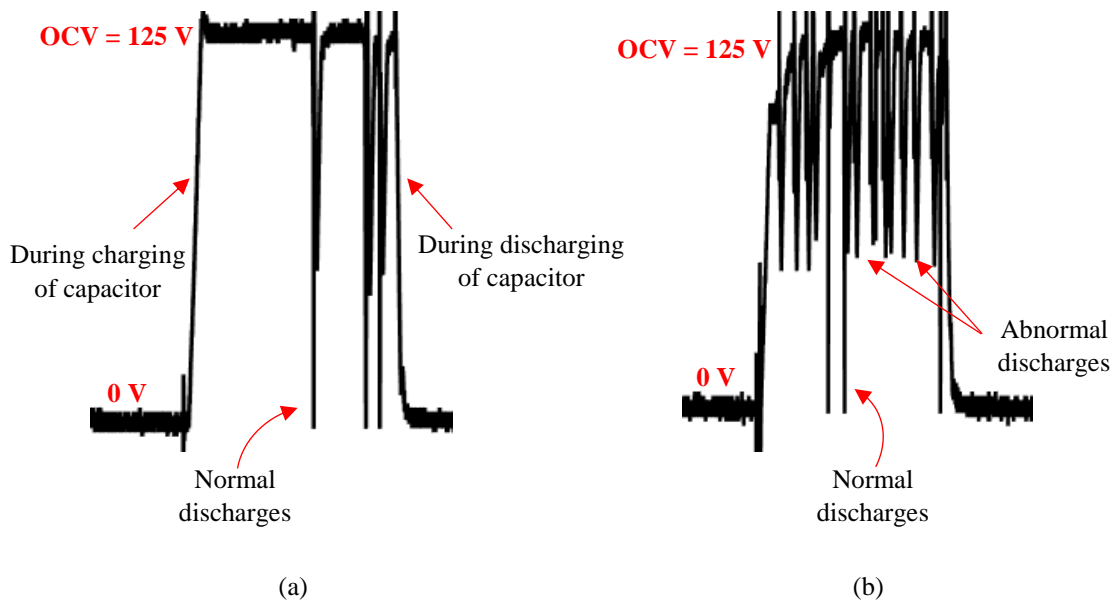


Fig. 6.20: Typical discharge profile for same time interval during machining of (a) 3-D hemispherical convex micro feature corresponding to 0.1 mm hole depth (b) micro feature corresponding to 0.3 mm hole depth

pulse off time between two subsequent discharges decrease in this case as observed from **Fig. 6.20**. The thermal softening of material on HAZ in micro feature corresponding to 0.3 mm hole depth is therefore, absent and the hardened layer of HAZ extends from about 10 μm from the periphery (N_2) and continues till 25 μm from the periphery (N_4) beyond which the material regains its original hardness.

6.2.6.3 Comparison of elastic modulus

Both elastic and plastic deformations during loading results in permanent impression on the material. During the unloading process, only elastic recovery takes place. The reverse plastic deformation is usually assumed to be negligible [134]. Typical loading and unloading curves for both the micro features for a particular indent are already shown in **Fig. 6.17**. Reduced elastic modulus (E_r) can be found out based on the gradient of the displacement-unloading curve (**Eq. 6.2**). The elastic modulus (E) of the material can be calculated (**Eq. 6.3**)

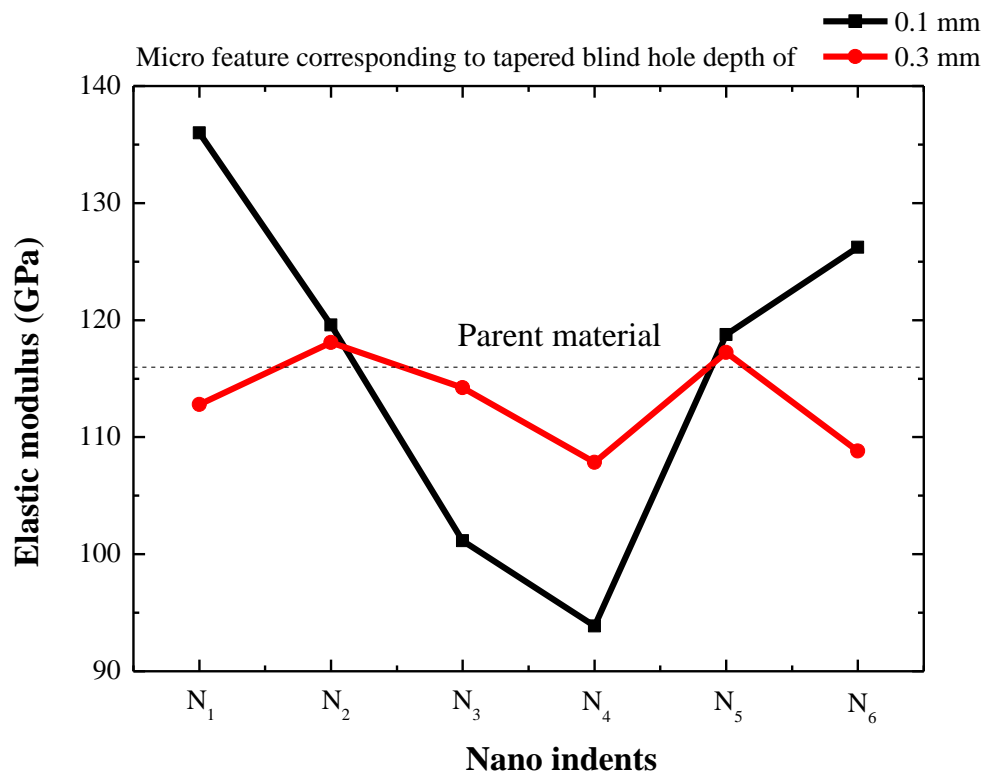


Fig. 6.21: Comparison of elastic modulus of the protruded micro features

if the Poisson's ratio (ν) of the material as well as elastic modulus (E_i) and Poisson's ratio (ν_i) of the Berkovich indenter are known.

Based on **Eqs. 6.2 – 6.3**, the elastic modulus (E) of both the micro features were calculated and is plotted in **Fig. 6.21**. A horizontal line depicts the elastic modulus of the parent material. The variation of elastic modulus corresponding to 3-D hemispherical convex micro feature is already described in **Section 6.2.4**.

Due to the absence of thermally softened layer in micro feature corresponding to 0.3 mm hole depth, the variation of elastic modulus in this case is very less as compared to 3-D hemispherical convex micro feature. With decrease in the depth of hole, the variation of elastic modulus of the micro feature increases. This is due to presence of hardened as well as softened layer that co-exist in the micro feature which leads to variation in the elastic modulus. Debris agglomeration at higher hole depths did not have much effect on the elastic modulus.

6.3 Characterization by non-destructive technique for determination of discharge affected layer

Destructive characterization (metallography) was used to determine the thickness of recast layer, HAZ and subsequently their mechanical properties were also found out based on nano indentation. This process is, however, limited to only a single micro feature and cannot be extended to array of micro features since simultaneous polishing of micro features is not possible. Therefore, a non-destructive characterization technique has to be employed for determining the discharge affected layers (recast layer + HAZ) on arrayed micro features using RMEDM.

XMCT is widely used as a non-destructive technique for characterization of samples of interest to material science, bio-medical and geological applications. This technique provides density map of the sample, in its three dimensional perspective, through volume reconstruction

Table 6.1: Parameters for conducting XMCT

Parameters:	Values
X-ray tube energy	120 KeV
Current	150 μ A
Number of projections	800
Voxel resolution in the reconstructed images	5 μ m

using two dimensional projection images. The details of the in-house developed XMCT system used for generating sliced images of array of positive micro features is described in detail by Sarkar et al. [135]. Once the 3D volume has been reconstructed, one can analyse the cross-sectional images to ascertain the density variation within the features. The XMCT was carried out to determine the discharge affected layer on array of micro features corresponding to **Fig. 5.45**. The discharge affected layer corresponds to recast layer and the HAZ. Segregation of recast layer and HAZ is not possible using XMCT. Parameters for conduction XMCT are shown in **Table 6.1**. Slicing of micro features were carried out as per schematic shown in **Fig. 6.22**. The sliced images for three different sections are shown in **Fig. 6.23**. The steps involved in measurement of discharge affected layer thickness is as follows:

- (a) 2-D stack of reconstructed slices (.tiff format) of array of 5 by 5 protruded micro features were produced by XMCT.
- (b) These sliced images were converted into .dicom format [136] using MIPAV (a cross-platform Java-based package supported by NIH [137]).
- (c) Building 3D model of array of 5 by 5 protruded micro features is carried out in 3D Slicer [138] with .dicom images as input. Once the 3D model is developed, slicing of the model at sections A-A, B-B, C-C is carried out (**Fig. 6.22**).
- (d) Discharge affected layer as observed from **Fig. 6.23** was carried out using public domain image processing software (ImageJ 1.46r, NIH). A correlation between distance in pixel (from image) and known dimension was carried out initially. Based on scale (distance (in μ m)/pixel), discharge affected layer thickness was measured.

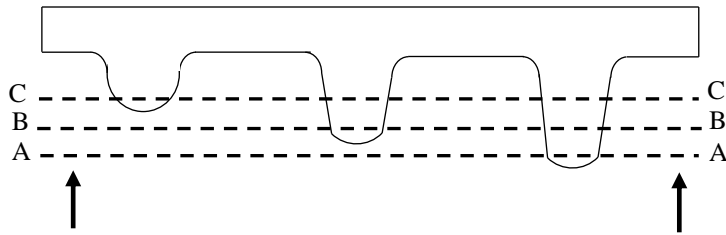


Fig. 6.22: Schematic of different slices of micro features for determining discharge affected layer thickness

Based on **Fig. 6.23**, the inner portion of micro feature cut section indicates the parent material and the periphery indicates the discharge affected layer. The thickness of the discharge affected layer found out for all three sections are shown in **Fig. 6.24**. The tip of micro feature corresponding to highest hole depth i.e. 0.5 mm has the highest layer thickness. On comparing the tip of each micro feature (**R**), there is a gradual decrease in discharge affected layer thickness with decrease in corresponding hole depth or height of micro feature. This is due to the fact that molten material expulsion from the tip in case of 0.1 mm hole depth is easier due to good flushing condition for low hole depth as compared to higher hole depth i.e. 0.5 mm. Hence, tendency of re-solidified layer reattaching on micro feature is low in case of micro feature with lower hole depth as compared to higher hole depths. Secondary and higher order discharges occur mostly at the sides (**Q**) of micro feature. Contrary to the trend in the case with layer thickness at the tip, the layer at the sides shows an increase in thickness for micro feature corresponding to 0.3 mm hole depth as compared to the one with higher hole depth i.e. 0.5 mm. This is because agglomeration of debris on the sides of micro feature corresponding to 0.3 mm hole depth is higher as compared to the micro feature corresponding to 0.5 mm hole depth. Considering micro feature corresponding to 0.5 mm hole depth, the layer thickness increases from base to tip. Similar phenomenon is also observed in case of 0.3 mm hole depth where the discharge affected layer thickness increased from sides to the tip of micro feature. This is due

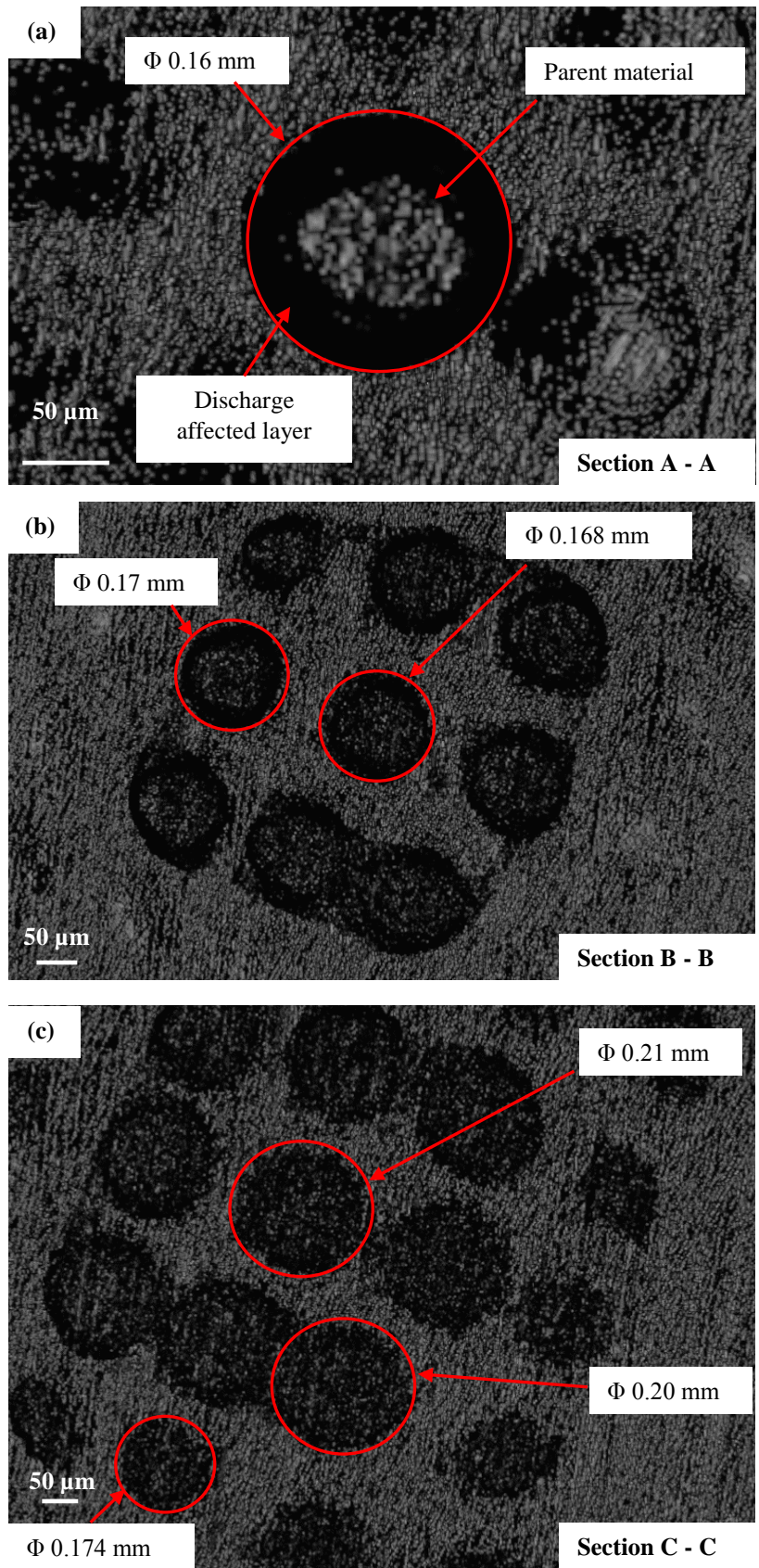


Fig. 6.23: Sliced images of micro features corresponding to (a) Section A-A (b) Section B-B (c) Section C-C

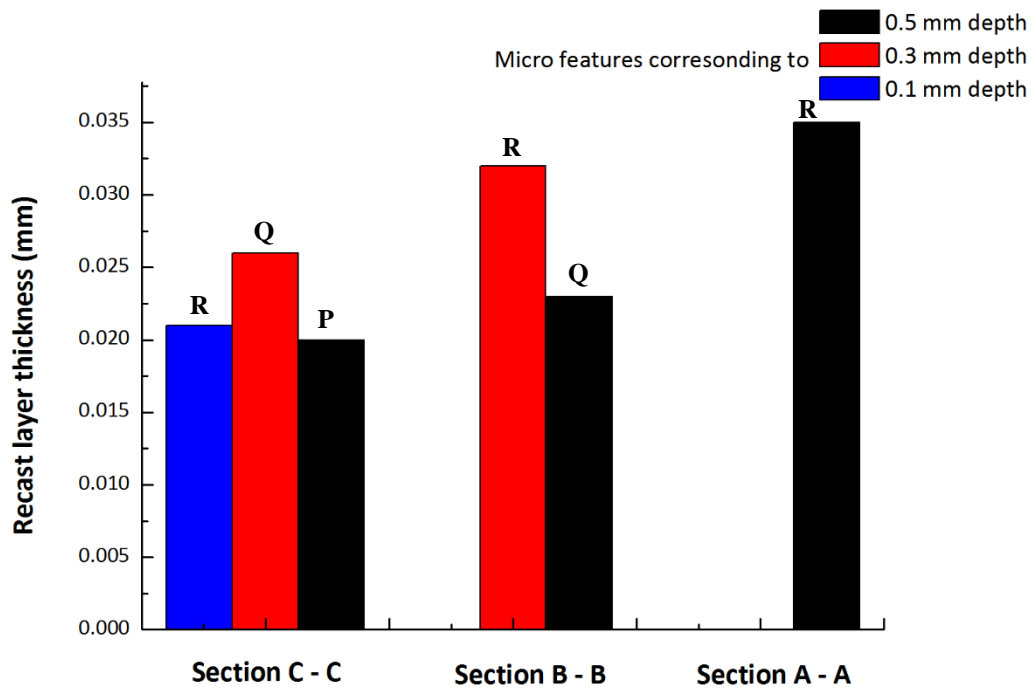


Fig. 6.24: Thickness of discharge affected layer at different sections

to the fact that the tip of all micro features is eroded more and hence high amount of molten material is produced near the tip that re-solidifies and adheres to the tip as compared to base/sides of micro feature.

Considering micro feature corresponding to 0.1 mm hole depth, destructive characterization showed that the discharge affected layer thickness (recast layer + HAZ) was around 16.8 μm (**Fig. 6.12**) which is close to that obtained by XMCT. Hence, it can be concluded that XMCT is an effective technique for determining discharge affected layer of arrayed micro features.

6.4 Summary

Mechanical and microstructural characterization of the 3-D hemispherical micro feature generated in *Chapter 5* is carried out in this chapter. Also, X-ray micro computed tomography was employed to determine the discharge affected layer on arrayed micro features. The important findings of this chapter are described below in brief.

- No adverse effect was observed on the internal grain structure of the 3-D hemispherical protruded micro feature and it remains uniformly distributed. However, a very thin layer of re-solidified molten material (recast layer) is uniformly formed around the periphery of the micro feature.
- Determination of hardness from the periphery to the centre of micro feature led to identification of hardened and soft layer of heat affected zone (HAZ). The recast layer had the highest hardness followed by the hardened layer of HAZ. The soft layer had the least hardness as compared to parent material.
- Elastic modulus of recast layer, hardened and soft layer of HAZ were determined using the slope of the unloading curve. Recast layer formation substantially increased the elastic modulus as compared to parent material. The soft layer of HAZ had the least elastic modulus.
- Qualitative analysis of residual stress using the loading and unloading portion of the load-displacement curves indicated that the recast layer comprises of compressive residual stresses while the soft layer of HAZ had tensile residual stresses as compared to the parent material.
- 3-D hemispherical micro feature contains heat affected zone (HAZ) with a hardened layer followed by a thermally softened layer which has a comparatively lower hardness as compared to the base material. However, the micro feature generated corresponding to 0.3 mm hole depth contains the hardened layer of the HAZ which has higher hardness throughout. There is no thermally softened layer possibly due to high amount of abnormal discharges occurring as a result of debris agglomeration at higher hole depths.
- Measurement of discharge affected layer thickness on arrayed micro features was carried out using non-destructive technique XMCT. It was found that thickness of discharge affected layer increases with increase in height of micro feature on the array.

CHAPTER 7

**CONCLUSIONS &
SCOPE FOR FUTURE WORK**

7.1. Conclusion

In the present work, atomistic and continuum scale modelling and simulation was carried out to understand the mechanism of shape generation of 3-D hemispherical micro feature using suitable tool modifications in RMEDM. Experiments were carried out to validate the simulation results. The following conclusions are derived from this study.

- Simulation results for shape generation using tapered blind hole as tool in RMEDM when divided into four stages depending on the occurrences of discharges between the cathode and anode, showed that high amount of debris deposition is responsible for creating high amount of secondary and higher order discharges on the workpiece leading to formation of 3-D hemispherical convex micro feature.
- Secondary and higher order discharges (abnormal discharges) due to debris leads to partial charging of the capacitor. Segregation of discharges with respect to debris carried out based on electric field intensity (numerical model) and correlated to voltage obtained during discharge (experiments) indicate that transition in discharge profiles from normal to abnormal discharges at increasing machining depth is due to presence of debris in the discharge channel.
- A factor k_0 determined in this study relates the ratio of material removal by abnormal discharges to that by normal discharges. This ratio was found to be the most influential factor in determining the shape of micro feature by simulation.
- Surface roughness evaluated based on piecewise de-trending of the simulated shape with six equal segments and quadratic fit for each segment matched closely with experimental results with a maximum error of 13%. The analysis of surface roughness indicated that larger crater sizes on sides of micro feature due to the occurrences of secondary and higher order discharges on sides leading to higher surface roughness as compared to base and tip of micro feature.

- MDS results shows that the percentage of material removed by melting (~ 60%) and vaporisation (~ 40%) during a single discharge remains nearly constant at low spark energies (0.165 μJ and 5 μJ). Change in crystal structure from FCC to amorphous takes place on the top surface of crater due to discharge.
- A dimensionless correlation has been found out between MDS and experimental results that connects the ratio between specific material removal at higher spark energy to that at lower spark energy for both MDS (R_{MDS}) and experiments (R_{expt}). This correlation was also used to determine the amount of material removal during numerical modelling and simulation of shape generation of 3-D hemispherical micro feature
- During multiple discharges, MDS results showed that the crater diameter increases as the distance between the discharges decreases. This was also observed on surfaces generated by RMEDM.
- RMEDM process has the capability to fabricate arrayed micro features of similar aspect ratio as well as different aspect ratio of micro features using suitable tool modifications.
- Recast layer on the 3-D hemispherical micro feature has the highest hardness followed by the hardened layer of HAZ. The soft layer has the least hardness as compared to parent material. Similar trend was also observed for elastic modulus i.e. substantially higher in the recast layer and the least in the soft layer of HAZ.
- Qualitative analysis of residual stress using the loading and unloading portion of the load-displacement curves indicated that the recast layer comprises of compressive residual stresses while the soft layer of HAZ had tensile residual stresses as compared to the parent material.
- Measurement of discharge affected layer thickness on arrayed micro features carried out using non-destructive technique XMCT indicated that the thickness of discharge affected layer increases with increase in height of micro feature on the array.

7.1.1. Scientific contributions

From the present work, it is also concluded that there are four major contributions that have been made, and they are listed as follows.

1. Constructive role of debris in RMEDM have been demonstrated and used for the generation of 3-D hemispherical micro feature.
2. A new dimensionless correlation of specific material removal in single electrical discharge between molecular dynamics simulation and experimental results has been developed to predict material removal rate.
3. A new factor, k_0 is defined (ratio of material removal by abnormal discharges to that by normal discharges) which influences the shape of micro feature
4. A mechanism for 3-D shape generation with RMEDM has been explained at atomic scale (for material removal) and continuum scale (for shape) for understanding the process and prediction of results.

7.2. Scope for future work

Though detailed numerical and experimental investigations were carried out in this research work to study the mechanism behind generation of 3-D shapes of micro features using RMEDM, there is a scope for further research in this area of shape generation which is listed as follows.

1. A factor, k_0 that was determined in this study was evaluated based on the average values of material removal by primary, secondary and higher order discharges. For each traverse depth, the amount of material removal is different due to difference in (a) number of type of discharges i.e. primary, secondary, higher order and (b) charge storage in the capacitor in presence or absence of debris. Therefore, the factor determined in this study can further be refined in future by incorporating a mathematical model that takes into account the

amount of material removal at each traverse depth. The instantaneous values of material removal at each traverse depth can improve the accuracy of the model and hence improved prediction of shape generation.

2. Even though wear on cathode was considered in the numerical model, it was not studied in this research work as the primary objective was to study the shape generation mechanism of micro feature. Therefore, future research work may be carried out by extensive experimentation with single as well as arrayed micro features and study the wear pattern for each. In this way, the role of wear on cathode on the shape generation can also be studied in detail.
3. Material removal in RMEDM is usually low due to low discharge energy. Future research can involve incorporating alternative methods to extract higher amount of material removal while retaining the desired shape. This can reduce the total machining time and cost.
4. Quantitative analysis of residual stress can also be one of the future scopes as a priori knowledge of the residual stress values can help in qualifying the micro feature as good or bad with respect to application point of view.

---X---

REFERENCES

- [1] T. Roy, R.K. Dutta, Integrated fuzzy AHP and fuzzy TOPSIS methods for multi-objective optimization of electro discharge machining process, *Soft Comput.* (2018). doi:10.1007/s00500-018-3173-2.
- [2] K.H. Ho, S.T. Newman, State of the art electrical discharge machining (EDM), *Int. J. Mach. Tools Manuf.* (2003). doi:10.1016/S0890-6955(03)00162-7.
- [3] El-Hofy, *Advanced machining processes Nontraditional and Hybrid Machining Processes*, 2005. doi:10.1036/0071466940.
- [4] M. Imran, A.S. Saragih, M.S.U. Sahar, T.J. Ko, Digital maskless lithography capabilities for surface texturing with biomachining, *Int. J. Adv. Manuf. Technol.* 89 (2017) 3709–3719. doi:10.1007/s00170-016-9317-6.
- [5] H. Yu, X. Wang, F. Zhou, Geometric Shape Effects of Surface Texture on the Generation of Hydrodynamic Pressure Between Conformal Contacting Surfaces, *Tribol. Lett.* 37 (2010) 123–130.
- [6] D.Z. Segu, S.S. Kim, Influence on friction behavior of micro-texturing under lubricated non-conformal contact, *Meccanica.* 49 (2014) 483–492.
- [7] T. Obikawa, A. Kamio, H. Takaoka, A. Osada, Micro-texture at the coated tool face for high performance cutting, *Int. J. Mach. Tools Manuf.* 51 (2011) 966–972. doi:10.1016/j.ijmachtools.2011.08.013.
- [8] Y. Wang, F. Houshmand, D. Elcock, Y. Peles, Convective heat transfer and mixing enhancement in a microchannel with a pillar, *Int. J. Heat Mass Transf.* 62 (2013) 553–561. doi:10.1016/j.ijheatmasstransfer.2013.03.034.
- [9] J. Yeo, M.J. Choi, D.S. Kim, Robust hydrophobic surfaces with various micropillar arrays, *J. Micromechanics Microengineering.* 20 (2010). doi:10.1088/0960-1317/20/2/025028.
- [10] C.Y. Chang, S.Y. Yang, L.S. Huang, J.H. Chang, Fabrication of plastic microlens array using gas-assisted micro-hot-embossing with a silicon mold, *Infrared Phys. Technol.* 48 (2006) 163–173. doi:10.1016/j.infrared.2005.10.002.
- [11] S. Bhattacharjee, C.-H. Ko, M. Elimelech, DLVO Interaction between Rough Surfaces, *Langmuir.* 14 (1998) 3365–3375. doi:10.1021/la971360b.
- [12] F. Zhang, L. Zhao, H. Chen, S. Xu, D.G. Evans, X. Duan, Corrosion resistance of superhydrophobic layered double hydroxide films on aluminum, *Angew. Chemie - Int. Ed.* 47 (2008) 2466–2469. doi:10.1002/anie.200704694.
- [13] A. V Il'inkov, V.G. Il'inkova, A. V Shchukin, Heat Transfer on Hemispherical Protrusions at Their Different Arrangement Density on the Channel Wall, *Russ. Aeronaut.* 54 (2011) 179–184.
- [14] S. Yadav, M. Kaushal, Varun, Siddhartha, Nusselt number and friction factor correlations for solar air heater duct having protrusions as roughness elements on absorber plate, *Exp. Therm. Fluid Sci.* 44 (2013) 34–41. doi:10.1016/j.expthermflusci.2012.05.011.
- [15] J.S. Li, Y.L. Li, D.Y. He, H.Y. Yu, X.B. Yan, Design and mechanism of cost-effective and highly efficient ultrathin (μm) GaAs solar cells employing nano-hemisphere surface texturing, *AIP Adv.* 3 (2014) 032145-1-032145-7. doi:10.1063/1.4799731.
- [16] J. Liu, Y. Song, G. Xie, B. Sunden, Numerical modeling flow and heat transfer in dimpled cooling channels with secondary hemispherical protrusions, *Energy.* 79 (2015) 1–19. doi:10.1016/j.energy.2014.05.075.
- [17] G.L. Chern, H.J. Lee, Using workpiece vibration cutting for micro-drilling, *Int. J. Adv. Manuf. Technol.* 27 (2006) 688–692. doi:10.1007/s00170-004-2255-8.

- [18] M.S. Cheong, D.W. Cho, K.F. Ehmman, Identification and control for micro-drilling productivity enhancement, *Int. J. Mach. Tools Manuf.* 39 (1999) 1539–1561. doi:10.1016/S0890-6955(99)00019-X.
- [19] K. Egashira, K. Mizutani, Micro-drilling of monocrystalline silicon using a cutting tool, *Precis. Eng.* 26 (2002) 263–268. doi:10.1016/S0141-6359(01)00113-1.
- [20] R. Kumar, P.K. Agrawal, I. Singh, Fabrication of micro holes in CFRP laminates using EDM, *J. Manuf. Process.* 31 (2018) 859–866. doi:10.1016/j.jmapro.2018.01.011.
- [21] U.S. Yadav, V. Yadava, Experimental investigation on electrical discharge diamond drilling of nickel-based superalloy aerospace material, *Proc. Inst. Mech. Eng. Part B J. Eng. Manuf.* 231 (2017) 1160–1168. doi:10.1177/0954405415592124.
- [22] P. Singh, V. Yadava, A. Narayan, Parametric study of ultrasonic-assisted hole sinking micro-EDM of titanium alloy, *Int. J. Adv. Manuf. Technol.* 94 (2018) 2551–2562. doi:10.1007/s00170-017-1051-1.
- [23] Z.Y. Yu, K.P. Rajurkar, H. Shen, High Aspect Ratio and Complex Shaped Blind Micro Holes by Micro EDM, *CIRP Ann. - Manuf. Technol.* 51 (2002) 359–362. doi:10.1016/S0007-8506(07)61536-4.
- [24] M.P. Jahan, Y.S. Wong, M. Rahman, A study on the quality micro-hole machining of tungsten carbide by micro-EDM process using transistor and RC-type pulse generator, *J. Mater. Process. Technol.* (2009). doi:10.1016/j.jmatprotec.2008.04.029.
- [25] Z.Y. Yu, Y. Zhang, J. Li, J. Luan, F. Zhao, D. Guo, High aspect ratio micro-hole drilling aided with ultrasonic vibration and planetary movement of electrode by micro-EDM, *CIRP Ann. - Manuf. Technol.* 58 (2009) 213–216. doi:10.1016/j.cirp.2009.03.111.
- [26] J.W. Byun, H.S. Shin, M.H. Kwon, B.H. Kim, C.N. Chu, Surface texturing by micro ECM for friction reduction, *Int. J. Precis. Eng. Manuf.* 11 (2010) 747–753. doi:10.1007/s12541-010-0088-y.
- [27] C.H. Jo, B.H. Kim, C.N. Chu, Micro electrochemical machining for complex internal micro features, *CIRP Ann. - Manuf. Technol.* 58 (2009) 181–184. doi:10.1016/j.cirp.2009.03.072.
- [28] G. Liu, Y. Li, Q. Kong, L. Yu, Impact Analysis of Electrolyte Pressure on Shape Accuracy of Micro Holes in ECM with Hollow Electrodes, in: *Procedia CIRP*, 2018. doi:10.1016/j.procir.2017.12.089.
- [29] D. Correa, J. Almeida, G. Almeida, M. Cardoso, L. De Boni, C. Mendonça, Ultrafast Laser Pulses for Structuring Materials at Micro/Nano Scale: From Waveguides to Superhydrophobic Surfaces, *Photonics.* 4 (2017) 8. doi:10.3390/photonics4010008.
- [30] U. Umer, M.K. Mohammed, A. Al-Ahmari, Multi-response optimization of machining parameters in micro milling of alumina ceramics using Nd:YAG laser, *Meas. J. Int. Meas. Confed.* 95 (2017) 181–192. doi:10.1016/j.measurement.2016.10.004.
- [31] C.A. Aguilar, Y. Lu, S. Mao, S. Chen, Direct micro-patterning of biodegradable polymers using ultraviolet and femtosecond lasers, *Biomaterials.* 26 (2005) 7642–7649. doi:10.1016/j.biomaterials.2005.04.053.
- [32] E.W. Becker, W. Ehrfeld, P. Hagmann, A. Maner, D. Münchmeyer, Fabrication of microstructures with high aspect ratios and great structural heights by synchrotron radiation lithography, galvanofarming, and plastic moulding (LIGA process), *Microelectron. Eng.* 4 (1986) 35–56. doi:10.1016/0167-9317(86)90004-3.
- [33] C.K. Malek, V. Saile, Applications of LIGA technology to precision manufacturing of high-aspect-ratio micro-components and -systems: A review, *Microelectronics J.* (2004).

doi:10.1016/j.mejo.2003.10.003.

- [34] A. Revzin, R.J. Russell, V.K. Yadavalli, W. Koh, C. Deister, D.D. Hile, M.B. Mellott, M. V Pishko, Fabrication of Poly(ethylene glycol) Hydrogel Microstructures Using Photolithography, *Langmuir*. 17 (2001) 5440–5447.
- [35] D. Qin, Y. Xia, G.M. Whitesides, Soft lithography for micro- and nanoscale patterning, *Nat. Protoc.* 5 (2010) 491–502. doi:10.1038/nprot.2009.234.
- [36] J. Rühle, And There Was Light: Prospects for the Creation of Micro- and Nanostructures through Maskless Photolithography, *ACS Nano*. 11 (2017) 8537–8541. doi:10.1021/acsnano.7b05593.
- [37] B.H. Kim, B.J. Park, C.N. Chu, Fabrication of multiple electrodes by reverse EDM and their application in micro ECM, *J. Micromechanics Microengineering*. 16 (2006) 843–850. doi:10.1088/0960-1317/16/4/022.
- [38] W. Zeng, Z. Wang, D. Dong, New micro-EDM reverse copying technology for microelectrode array fabrication, in: *Int. Technol. Innov. Conf. (ITIC 2006)*, 2006: pp. 1633–1636.
- [39] W.L. Zeng, Y.P. Gong, Y. Liu, Z.L. Wang, Experimental Study of Microelectrode Array and Micro-Hole Array Fabricated by Ultrasonic Enhanced Micro-EDM, *Key Eng. Mater.* (2008). doi:10.4028/www.scientific.net/KEM.364-366.482.
- [40] Y.L. Hwang, C.L. Kuo, S.F. Hwang, Fabrication of a micro-pin array with high density and high hardness by combining mechanical peck-drilling and reverse-EDM, *J. Mater. Process. Technol.* (2010). doi:10.1016/j.jmatprotec.2010.02.022.
- [41] Z.L. Peng, Z.L. Wang, Y.K. Wang, Y.H. Dong, H. Chen, Study on Micro Reversible Electrical Discharge Machining Method for the Fabrication of Micro Structures, *627* (2009) 279–284. doi:10.4028/www.scientific.net/MSF.626-627.279.
- [42] S.S. Mujumdar, S.A. Mastud, R.K. Singh, S.S. Joshi, Experimental characterization of the reverse micro-electrodischarge machining process for fabrication of high-aspect-ratio micro-rod arrays, *Proc. Inst. Mech. Eng. Part B J. Eng. Manuf.* 224 (2010) 777–794. doi:10.1243/09544054JEM1745.
- [43] S. Mastud, R.K. Singh, S.S. Joshi, Analysis of fabrication of arrayed micro-rods on tungsten carbide using reverse micro-EDM, *Int. J. Manuf. Technol. Manag.* 26 (2012) 176. doi:10.1504/IJMTM.2012.051430.
- [44] S.A. Mastud, N.S. Kothari, R.K. Singh, S.S. Joshi, Modeling Debris Motion in Vibration Assisted Reverse Micro Electrical Discharge Machining Process (R-MEDM), *J. Microelectromechanical Syst.* 24 (2014) 661–676. doi:10.1109/JMEMS.2014.2343227.
- [45] S. Mastud, M. Garg, R. Singh, J. Samuel, S. Joshi, Experimental Characterization of Vibration-Assisted Reverse Micro Electrical Discharge Machining (EDM) for Surface Texturing, in: *ASME 2012 Int. Manuf. Sci. Eng.*, 2012: pp. 1–10.
- [46] R. Balasubramaniam, P. Ranjan, V.K. Suri, Mapping the material removal behaviour of micro deep hole drilling EDM process, *Int. J. Mechatronics Manuf. Syst.* 5 (2012) 516–527. doi:10.1504/IJMMS.2012.049976.
- [47] Y.S. Wong, M. Rahman, H.S. Lim, H. Han, N. Ravi, Investigation of micro-EDM material removal characteristics using single RC-pulse discharges, *J. Mater. Process. Technol.* 140 (2003) 303–307. doi:10.1016/S0924-0136(03)00771-4.
- [48] F. Han, S. Wachi, M. Kunieda, Improvement of machining characteristics of micro-EDM using transistor type isopulse generator and servo feed control, *Precis. Eng.* 28 (2004) 378–385. doi:10.1016/j.precisioneng.2003.11.005.

- [49] S. Dhanik, S.S. Joshi, Modeling of a Single Resistance Capacitance Pulse Discharge in Micro-Electro Discharge Machining, *J. Manuf. Sci. Eng.* 127 (2005) 759. doi:10.1115/1.2034512.
- [50] S.H. Yeo, W. Kurnia, P.C. Tan, Electro-thermal modelling of anode and cathode in micro-EDM, *J. Phys. D. Appl. Phys.* 40 (2007) 2513–2521. doi:10.1088/0022-3727/40/8/015.
- [51] J. Tang, X. Yang, A Thermo-hydraulic Modeling for the Formation Process of the Discharge Crater in EDM, *Procedia CIRP.* 42 (2016) 685–690. doi:10.1016/j.procir.2016.02.302.
- [52] Y.H. Jeong, B.K. Min, Geometry prediction of EDM-drilled holes and tool electrode shapes of micro-EDM process using simulation, *Int. J. Mach. Tools Manuf.* 47 (2007) 1817–1826. doi:10.1016/j.ijmachtools.2007.04.011.
- [53] K.P. Somashekhar, S. Panda, J. Mathew, N. Ramachandran, Numerical simulation of micro-EDM model with multi-spark, *Int. J. Adv. Manuf. Technol.* 76 (2013) 83–90. doi:10.1007/s00170-013-5319-9.
- [54] P.C. Tan, S.H. Yeo, Modelling of overlapping craters in micro-electrical discharge machining, *J. Phys. D. Appl. Phys.* 41 (2008) 205302. doi:10.1088/0022-3727/41/20/205302.
- [55] X. Feng, Y.S. Wong, G.S. Hong, Characterization and geometric modeling of single and overlapping craters in micro-EDM, *Mach. Sci. Technol.* 20 (2016) 79–98. doi:10.1080/10910344.2015.1085317.
- [56] S. Kotake, M. Kuroki, Molecular dynamics study of solid melting and vaporization by laser irradiation, *Int. J. Heat Mass Transf.* 36 (1993) 2061–2067. doi:10.1016/S0017-9310(05)80137-1.
- [57] Shoichi Shimada, Naoya Ikawa, Giichi Ohmori, Hiroaki Tanaka, Unichi Uchikoshi, Molecular Dynamics Analysis as Compared with Experimental Results of Micromachining, *Precis. Eng.* 41 (1992) 117–120.
- [58] H.Y. S. Shimada, N. Ikawa, H. Tanaka, G. Ohmori, J. Uchikoshi, Feasibility Study on Ultimate Accuracy in Microcutting Using Molecular Dynamics Simulation, *CIRP Ann. - Manuf. Technol.* 42 (1993) 91–94.
- [59] X. Yang, J. Guo, X. Chen, M. Kunieda, Molecular dynamics simulation of the material removal mechanism in micro-EDM, *Precis. Eng.* 35 (2011) 51–57. doi:10.1016/j.precisioneng.2010.09.005.
- [60] X. Yue, X. Yang, Molecular dynamics simulation of single pulse discharge process : clarifying the function of pressure generated inside the melting area in EDM, *Mol. Simul.* 43 (2017) 935–944. doi:10.1080/08927022.2017.1306649.
- [61] Yue X , Yang X, Molecular dynamics simulation of material removal process and crystal structure evolution in EDM with discharge on different crystal planes, *Int J Adv Manuf Technol.* (2017) 1–11. doi:10.1007/s00170-017-0415-x.
- [62] X. Yue, X. Yang, Molecular dynamics simulation of the material removal process and gap phenomenon of nano EDM in deionized water, *RSC Adv.* 5 (2015) 66502–66510. doi:10.1039/C5RA11419E.
- [63] X. Yang, X. Han, F. Zhou, M. Kunieda, Molecular dynamics simulation of residual stress generated in EDM, *Procedia CIRP.* 6 (2013) 432–437. doi:10.1016/j.procir.2013.03.037.
- [64] S. Mastud, R.K. Singh, J. Samuel, S.S. Joshi, Comparative analysis of the process mechanics in micro electrical discharge machining and reverse micro EDM, *Proc. ASME 2011 Int. Manuf. Sci. Eng. Conf. June 13-17, 2011, Corvallis, Oregon, USA.* (2011) 1–10. <http://proceedings.asmedigitalcollection.asme.org/proceeding.aspx?articleid=1623511>.
- [65] M. Mahardika, K. Mitsui, A new method for monitoring micro-electric discharge machining

- processes, *Int. J. Mach. Tools Manuf.* 48 (2008) 446–458.
doi:10.1016/j.ijmachtools.2007.08.023.
- [66] J. Wang, Y.G. Wang, F.L. Zhao, Simulation of Debris Movement in Micro Electrical Discharge Machining of Deep Holes, *Mater. Sci. Forum.* 626–627 (2009) 267–272.
doi:10.4028/www.scientific.net/MSF.626-627.267.
- [67] M. Tanjilul, A. Ahmed, A.S. Kumar, M. Rahman, A study on EDM debris particle size and flushing mechanism for efficient debris removal in EDM-drilling of Inconel 718, *J. Mater. Process. Technol.* 255 (2018) 263–274. doi:10.1016/j.jmatprotec.2017.12.016.
- [68] Y.S. Liao, P.S. Wu, F.Y. Liang, Study of debris exclusion effect in linear motor equipped die-sinking EDM process, *Procedia CIRP.* 6 (2013) 123–128. doi:10.1016/j.procir.2013.03.058.
- [69] J. Wang, F. Han, Simulation model of debris and bubble movement in electrode jump of electrical discharge machining, *Int. J. Adv. Manuf. Technol.* 74 (2014) 591–598.
doi:10.1007/s00170-014-6008-z.
- [70] S. Cetin, A. Okada, Y. Uno, Effect of Debris Distribution on Wall Concavity in Deep-Hole EDM, *JSME Int. J. Ser. C.* 47 (2004) 553–559. doi:10.1299/jsmec.47.553.
- [71] J. Wu, M. Zhou, X. Xu, J. Yang, X. Zeng, D. Xu, Fast and stable electrical discharge machining (EDM), *Mech. Syst. Signal Process.* 72–73 (2016) 420–431.
doi:10.1016/j.ymsp.2015.11.006.
- [72] M. Zhou, J. Wu, X. Xu, X. Mu, Y. Dou, Significant improvements of electrical discharge machining performance by step-by-step updated adaptive control laws, *Mech. Syst. Signal Process.* 101 (2018) 480–497. doi:10.1016/j.ymsp.2017.06.041.
- [73] Y.S. Liao, T.Y. Chang, T.J. Chuang, An on-line monitoring system for a micro electrical discharge machining (micro-EDM) process, *J. Micromechanics Microengineering.* 18 (2008) 035009. doi:10.1088/0960-1317/18/3/035009.
- [74] M. Zhou, F. Han, I. Soichiro, A time-varied predictive model for EDM process, *Int. J. Mach. Tools Manuf.* 48 (2008) 1668–1677. doi:10.1016/j.ijmachtools.2008.07.003.
- [75] A. Goodlet, P. Koshy, Real-time evaluation of gap flushing in electrical discharge machining, *CIRP Ann. - Manuf. Technol.* (2015). doi:10.1016/j.cirp.2015.04.068.
- [76] A. Klink, M. Holsten, S. Schneider, P. Koshy, Acoustic emission signatures of electrical discharge machining, *CIRP Ann. - Manuf. Technol.* (2016). doi:10.1016/j.cirp.2016.04.082.
- [77] C. Smith, P. Koshy, Applications of acoustic mapping in electrical discharge machining, *CIRP Ann. - Manuf. Technol.* (2013). doi:10.1016/j.cirp.2013.03.106.
- [78] K. Ter Pey Tee, R. Hosseinnzhad, M. Brandt, J. Mo, Pulse Discrimination for Electrical Discharge Machining With Rotating Electrode, *Mach. Sci. Technol.* 17 (2013) 292–311.
doi:10.1080/10910344.2013.780559.
- [79] C.C. Kao, A.J. Shih, Sub-nanosecond monitoring of micro-hole electrical discharge machining pulses and modeling of discharge ringing, *Int. J. Mach. Tools Manuf.* 46 (2006) 1996–2008.
doi:10.1016/j.ijmachtools.2006.01.008.
- [80] C.K. Nirala, P. Saha, Development of an algorithm for online pulse discrimination in micro-EDM using current and voltage sensors and their comparison, *Souvenir 2015 IEEE Int. Adv. Comput. Conf. IACC 2015.* (2015) 496–500. doi:10.1109/IADCC.2015.7154758.
- [81] C.K. Nirala, D.R. Unune, H.K. Sankhla, Virtual Signal-Based Pulse Discrimination in Micro-Electro-Discharge Machining, *J. Manuf. Sci. Eng.* 139 (2017) 094501. doi:10.1115/1.4037108.
- [82] S.A. Mastud, N.S. Kothari, R.K. Singh, J. Samuel, S.S. Joshi, Analysis of debris motion in

- vibration assisted reverse micro electrical discharge machining, in: Proc. ASME 2014 Int. Manuf. Sci. Eng. Conf. MSEC 2014, 2014.
- [83] T.R. Newton, Investigation of the effect of process parameters on the formation of recast layer in wire-EDM of Inconel 718, Georgia Institute of Technology, 2008.
- [84] Y. Yildiz, M.M. Sundaram, A. Rajurkar, Kamlakar P, Altintas, Correlation of surface roughness and recast layer thickness in electrical discharge machining, Proc IMechE Part E J Process Mech. Eng. 0 (2015) 1–11. doi:10.1177/0954408915600949.
- [85] M. Gostimirovic, P. Kovac, M. Sekulic, B. Skoric, Influence of discharge energy on machining characteristics in EDM, J. Mech. Sci. Technol. 26 (2012) 173–179. doi:10.1007/s12206-011-0922-x.
- [86] B. Lauwers, J.P. Kruth, W. Liu, W. Eeraerts, B. Schacht, P. Bleys, Investigation of material removal mechanisms in EDM of composite ceramic materials, J. Mater. Process. Technol. 149 (2004) 347–352. doi:10.1016/j.jmatprotec.2004.02.013.
- [87] O. Thao, S.S. Joshi, Analysis of heat affected zone in the micro-electric discharge machining, Int. J. Manuf. Technol. Manag. 13 (2008) 201. doi:10.1504/IJMTM.2008.016771.
- [88] Y. Zhang, Y. Liu, R. Ji, B. Cai, Study of the recast layer of a surface machined by sinking electrical discharge machining using water-in-oil emulsion as dielectric, Appl. Surf. Sci. 257 (2011) 5989–5997. doi:10.1016/j.apsusc.2011.01.083.
- [89] H. Ramasawmy, L. Blunt, K.P. Rajurkar, Investigation of the relationship between the white layer thickness and 3D surface texture parameters in the die sinking EDM process, Precis. Eng. 29 (2005) 479–490. doi:10.1016/j.precisioneng.2005.02.001.
- [90] Y. Yildiz, Prediction of white layer thickness and material removal rate in electrical discharge machining by thermal analyses, J. Manuf. Process. 23 (2016) 47–53. doi:10.1016/j.jmapro.2016.05.018.
- [91] Y.H. Guu, H. Hocheng, C.Y. Chou, C.S. Deng, Effect of electrical discharge machining on surface characteristics and machining damage of AISI D2 tool steel, Mater. Sci. Eng. A. 358 (2003) 37–43. doi:10.1016/S0921-5093(03)00272-7.
- [92] R. Gil, J.A. Sanchez, S. Plaza, N Ortega, B. Izquierdo, I. Pombo, Modeling recast layer and surface finish in the manufacturing of high – aspect ratio micro-tools using the inverse slab electrical discharge milling process, Proc IMechE Part B J Eng. Manuf. 0(0). 228 (2013) 553–562. doi:10.1177/0954405413502024.
- [93] A. Kumar, V. Kumar, J. Kumar, Surface crack density and recast layer thickness analysis in WEDM process through response surface methodology, Mach. Sci. Technol. 20 (2016) 201–230. doi:10.1080/10910344.2016.1165835.
- [94] S. Vignesh, B. Mohan, T. Muthuramalingam, S. Karthikeyan, Evaluation of Recast Layer Thickness of Electrical Discharge Machined AISI 202 Stainless Steel with Various Pulse Generators, Appl. Mech. Mater. 766–767 (2015) 518–522. doi:10.4028/www.scientific.net/AMM.766-767.518.
- [95] K. Kensei, F. Katsushi, Crack-Less Electrical Discharge Machining of Molybdenum with Titanium Electrode, Appl. Mech. Mater. 510 (2014) 101–105. doi:10.4028/www.scientific.net/AMM.510.101.
- [96] M.P.S. Krishna Kiran, S.S. Joshi, Modeling of Surface Roughness and the Role of Debris in Micro-EDM, J. Manuf. Sci. Eng. 129 (2007) 265. doi:10.1115/1.2540683.
- [97] K. Salonitis, A. Stournaras, P. Stavropoulos, G. Chryssolouris, Thermal modeling of the

- material removal rate and surface roughness for die-sinking EDM, *Int. J. Adv. Manuf. Technol.* 40 (2009) 316–323. doi:10.1007/s00170-007-1327-y.
- [98] W. Kurnia, P.C. Tan, S.H. Yeo, Q.P. Tan, Surface roughness model for micro electrical discharge machining, *Proc. Inst. Mech. Eng. Part B J. Eng. Manuf.* 223 (2009) 279–287. doi:10.1243/09544054JEM1188.
- [99] J.A. Abbasi, M. Jahanzaib, M. Azam, S. Hussain, A. Wasim, M. Abbas, Effects of wire-Cut EDM process parameters on surface roughness of HSLA steel, *Int. J. Adv. Manuf. Technol.* 91 (2017) 1867–1878. doi:10.1007/s00170-016-9881-9.
- [100] M. Kiyak, B.E. Aldemir, E. Altan, Effects of discharge energy density on wear rate and surface roughness in EDM, *Int. J. Adv. Manuf. Technol.* 79 (2015) 513–518. doi:10.1007/s00170-015-6840-9.
- [101] Takeuchi H, Kunieda M, Effects of volume fraction of bubbles in discharge gap on machining phenomena of EDM, in: *Proc. 15th Int. Symp. Electromachining, 2007*: pp. 63–68.
- [102] S.M. Foiles, M.I. Baskes, M.S. Daw, Embedded-atom-method functions for the fcc metals Cu, Ag, Au, Ni, Pd, Pt, and their alloys, *Phys. Rev. B.* 33 (1986) 7983–7991. doi:10.1103/PhysRevB.33.7983.
- [103] S. Plimpton, Fast Parallel Algorithms for Short-Range Molecular Dynamics, *J. Comput. Phys.* 117 (1995) 1–19. doi:http://dx.doi.org/10.1006/jcph.1995.1039.
- [104] A. Stukowski, Visualization and analysis of atomistic simulation data with OVITO—the Open Visualization Tool, *Model. Simul. Mater. Sci. Eng.* 18 (2010) 015012. doi:10.1088/0965-0393/18/1/015012.
- [105] D. Faken, H. Jónsson, Systematic analysis of local atomic structure combined with 3D computer graphics, *Comput. Mater. Sci.* 2 (1994) 279–286. doi:http://dx.doi.org/10.1016/0927-0256(94)90109-0.
- [106] J.W. Murray, M.W. Fay, M. Kunieda, A.T. Clare, TEM study on the electrical discharge machined surface of single-crystal silicon, *J. Mater. Process. Technol.* 213 (2013) 801–809. doi:10.1016/j.jmatprotec.2012.11.028.
- [107] G. Cusanelli, A. Hessler-Wyser, F. Bobard, R. Demellayer, R. Perez, R. Flükiger, Microstructure at submicron scale of the white layer produced by EDM technique, *J. Mater. Process. Technol.* 149 (2004) 289–295. doi:10.1016/j.jmatprotec.2003.11.047.
- [108] S.H. Yeo, W. Kurnia, P.C. Tan, Electro-thermal modelling of anode and cathode in micro-EDM, *J. Phys. D. Appl. Phys.* 40 (2007) 2513–2521. doi:10.1088/0022-3727/40/8/015.
- [109] N. Taniguchi, *Nanotechnology: Integrated Processing Systems for Ultra-precision and Ultra-fine Products*, Oxford University Press, 1996.
- [110] Q.Y. Liu, Q.H. Zhang, J.H. Zhang, M. Zhang, Influence of Grain Size and Grain Boundary of Workpiece on Micro EDM, *Adv. Mater. Res.* 941–944 (2014) 2116–2120. doi:10.4028/www.scientific.net/AMR.941-944.2116.
- [111] Q. Liu, Q. Zhang, M. Zhang, J. Zhang, Effects of grain size of AISI 304 on the machining performances in micro electrical discharge machining, *Proc. Inst. Mech. Eng. Part B J. Eng. Manuf.* 231 (2015) 359–366. doi:10.1177/0954405415573062.
- [112] V. Naidu, M S; Kamaraju, *HIGH VOLTAGE ENGINEERING*, Second Edi, McGraw-Hill, 2009.
- [113] C. Xuyang, Z. Kai, W. Chunmei, H. Zhipeng, Z. Yiru, A Study on Plasma Channel Expansion in Micro-EDM, *Mater. Manuf. Process.* 6914 (2015) 150615134315006. doi:10.1080/10426914.2015.1059445.

- [114] IIT Kharagpur, NPTEL, Module 9: Electro discharge machining, 2009. <http://nptel.ac.in/courses/112105127/pdf/LM-39.pdf>.
- [115] J.R. Crookall, A.J.R. Moncrieff, A Theory and Evaluation of Tool-Electrode Shape Degeneration in Electro-Discharge Machining, *Proc. Inst. Mech. Eng.* 187 (1973) 51–61.
- [116] F. Han, L. Chen, D. Yu, X. Zhou, Basic study on pulse generator for micro-EDM, *Int. J. Adv. Manuf. Technol.* 33 (2007) 474–479. doi:10.1007/s00170-006-0483-9.
- [117] B. Shao, Modeling and simulation of micro electrical discharge machining, University of Nebraska-Lincoln, 2015. <http://digitalcommons.unl.edu/cgi/viewcontent.cgi?article=1094&context=mechengdiss>.
- [118] W.K. and P.C.T. S H Yeo, Electro-thermal modelling of anode and cathode in micro-EDM, *J. Phys. D. Appl. Phys.* 40 (2007) 2513–2521. doi:10.1088/0022-3727/40/8/015.
- [119] K. Takahata, Y.B. Gianchandani, Batch mode micro-electro-discharge machining, *J. Microelectromechanical Syst.* 11 (2002) 102–110. doi:10.1109/84.993444.
- [120] K. Yanatori, M. Kunieda, Study on Debris Movement in EDM Gap., *J. Japan Soc. Electr. Mach. Eng.* 29 (1995) 19–27. doi:10.2526/jseme.29.61_19.
- [121] J. Wang, F. Han, Simulation model of debris and bubble movement in consecutive-pulse discharge of electrical discharge machining, *Int. J. Mach. Tools Manuf.* 77 (2014) 56–65. doi:10.1016/j.ijmachtools.2013.10.007.
- [122] A. Gatto, E. Bassoli, L. Denti, L. Iuliano, Bridges of debris in the EDD process: Going beyond the thermo-electrical model, *J. Mater. Process. Technol.* 213 (2013) 349–360. doi:10.1016/j.jmatprotec.2012.10.020.
- [123] G. Monastyrsky, Nanoparticles formation mechanisms through the spark erosion of alloys in cryogenic liquids, *Nanoscale Res. Lett.* 10 (2015) 503. doi:10.1186/s11671-015-1212-9.
- [124] M.P.S. Krishna Kiran, S.S. Joshi, Modeling of Surface Roughness and the Role of Debris in Micro-EDM, *J. Manuf. Sci. Eng.* 129 (2007) 265. doi:10.1115/1.2540683.
- [125] C. Diver, J. Atkinson, H.J. Helml, L. Li, Micro-EDM drilling of tapered holes for industrial applications, *J. Mater. Process. Technol.* 149 (2004) 296–303. doi:10.1016/j.jmatprotec.2003.10.064.
- [126] J.W. Lee, Microstructural evaluation and phase transformation of recast layers in electrical discharge machined dual phase Fe-Mn-Al alloy, *J. Mater. Sci.* 38 (2003) 1679–1687. doi:10.1023/A:1023215424025.
- [127] B. Jabbaripour, M.H. Sadeghi, S. Faridvand, M.R. Shabgard, Investigating the effects of edm parameters on surface integrity, mrr and twr in machining of Ti-6Al-4V, *Mach. Sci. Technol.* 16 (2012) 419–444. doi:10.1080/10910344.2012.698971.
- [128] H. Sidhom, F. Ghanem, T. Amadou, G. Gonzalez, C. Braham, Effect of electro discharge machining (EDM) on the AISI316L SS white layer microstructure and corrosion resistance, *Int. J. Adv. Manuf. Technol.* 65 (2013) 141–153. doi:10.1007/s00170-012-4156-6.
- [129] W.C. Oliver, G.M. Pharr, An improved technique for determining hardness and elastic modulus using load and displacement sensing indentation experiments, *Journals Mater. Res.* 7 (1992) 1564–1583.
- [130] A.A. Khan, Role of heat transfer on process characteristics during electrical discharge machining, in: *Dev. Heat Transf., InTech (Open Access Book)*, 2011: pp. 417–436. doi:10.1016/0017-9310(65)90060-8.
- [131] G. Zamfirova, V. Lorenzo, R. Benavente, J.M. Perena, On the relationship between modulus

- of elasticity and microhardness, *J. Appl. Polym. Sci.* 88 (2003) 1794–1798.
doi:10.1002/app.11788.
- [132] L.-N. Zhu, B.-S. Xu, H.-D. Wang, C.-B. Wang, Measurement of Residual Stresses Using Nanoindentation Method, *Crit. Rev. Solid State Mater. Sci.* 40 (2015) 77–89.
doi:10.1080/10408436.2014.940442.
- [133] L.N. Zhu, B.S. Xu, H.D. Wang, C.B. Wang, Effect of residual stress on the nanoindentation response of (100) copper single crystal, *Mater. Chem. Phys.* 136 (2012) 561–565.
doi:10.1016/j.matchemphys.2012.07.026.
- [134] G.M. Pharr, A. Bolshakov, Understanding nanoindentation unloading curves, *J. Mater. Res.* 17 (2002) 2660–2671.
- [135] P.S. Sarkar, N.K. Ray, M.K. Pal, R. Baribaddala, A. Agrawal, Y. Kashyap, A. Sinha, S.C. Gadkari, Development of X-ray CCD camera based X-ray micro-CT system, *Rev. Sci. Instrum.* 88 (2017). doi:10.1063/1.4975376.
- [136] P. Mildenerger, M. Eichelberg, E. Martin, Introduction to the DICOM standard, *Eur. Radiol.* 12 (2002) 920–927. doi:10.1007/s003300101100.
- [137] M.J. McAuliffe, F.M. Lalonde, D. McGarry, W. Gandler, K. Csaky, B.L. Trus, Medical Image Processing, Analysis and Visualization in clinical research, in: *Proc. 14th IEEE Symp. Comput. Med. Syst. CBMS 2001*, 2001: pp. 381–386. doi:10.1109/CBMS.2001.941749.
- [138] A. Fedorov, R. Beichel, J. Kalpathy-Cramer, J. Finet, J.C. Fillion-Robin, S. Pujol, C. Bauer, D. Jennings, F. Fennessy, M. Sonka, J. Buatti, S. Aylward, J. V. Miller, S. Pieper, R. Kikinis, 3D Slicer as an image computing platform for the Quantitative Imaging Network, *Magn. Reson. Imaging.* 30 (2012) 1323–1341. doi:10.1016/j.mri.2012.05.001.

---x---